Distributed Photonic Sensing for Monitoring, Protection and Control of HVDC Networks

PhD Thesis

Alfred E. Amiolemen

Advanced Electrical Sensors Group
Electrical and Electronic Department
University of Strathclyde, Glasgow

April 24, 2026

Abstract

The increasing penetration of renewable energy sources is driving the deployment of high-voltage direct current (HVDC) systems for efficient long-distance power transmission. However, HVDC networks present significant challenges in fault detection, protection, and system observability due to the absence of natural current zero-crossings and the rapid rise of fault currents. These constraints necessitate high-speed, distributed sensing solutions capable of providing accurate real-time measurements along transmission infrastructure.

This thesis presents the design, development, and validation of a distributed optical current sensing (OCS) system for HVDC applications, enabling enhanced monitoring, fault detection, and localisation. The proposed approach integrates a low-resistance shunt with a piezoelectric transducer and fibre Bragg grating (FBG) sensing, facilitating the conversion of electrical current into optical signals for high-speed transmission and interrogation. The sensing architecture is embedded within HVDC cable infrastructure, enabling in-situ measurement and improved network observability.

The main contributions of this thesis are summarised as follows:

- Design and implementation of an instrumented HVDC cable butt splice joint, transforming a passive component into an active distributed sensing node.
- Development of a self-powered optical current sensing architecture, enabling electrically isolated operation under ultra-low-power conditions.
- Design of a nonlinear signal conditioning circuit, enhancing sensitivity for low-level signals while preventing saturation under high-current conditions.
- Proposition of a segregated piecewise calibration methodology, improving measurement accuracy across a wide dynamic range, particularly near the interrogation noise floor.
- Development of a distributed sensing framework enabling fault localisation and insulation condition monitoring based on transient signal propagation.

- Derivation of an analytical formulation for fault localisation, accounting for transient propagation effects in HVDC transmission media.

Experimental validation demonstrates that the proposed system can capture fast transient fault signals and achieve measurement performance consistent with IEC 61869-14 Class 1 requirements under representative conditions. The results confirm the feasibility of integrating distributed optical sensing within HVDC cable systems, providing a scalable pathway toward enhanced network observability, faster fault detection, and improved operational reliability in future HVDC grids.

Acknowledgements

First and foremost, I express my sincere gratitude to Professor Paweł Niewczas for the invaluable opportunity to undertake this research under his supervision. His commitment to excellence, clarity of vision, and strategic guidance were instrumental throughout this work. His insightful mentorship and steady leadership provided direction at every stage, while his sense of humour helped maintain a positive and supportive research environment.

I am also deeply grateful to Dr Grzegorz Fusiek for his consistent support and rigorous technical guidance. His emphasis on high standards, precision, and critical thinking significantly contributed to the quality of this research.

I would like to acknowledge, with sincere appreciation, the Department of Electrical and Electronic Engineering for its support, conveyed through my supervisor in August 2022 during a particularly challenging period.

My thanks extend to my research colleagues at the University of Strathclyde for their collaboration, technical discussions, and collegial support, all of which contributed meaningfully to this work.

I am profoundly grateful to my children, Shirley and Harry, whose patience and understanding were a constant source of motivation. I also extend my heartfelt thanks to my mother for her unwavering prayers and encouragement, and to my brothers and sister for their support during the most challenging moments of this journey.

Above all, I give thanks to God, from whom all knowledge, wisdom, strength, and blessings flow.

Contents

List of Figures

List of Figures

List of Tables

List of Abbreviations

AC	Alternating Current
AI	Artificial Intelligence
DAQ	Data Acquisition
DC	Direct Current
DCCB	DC Circuit Breaker
DP	Degree of Polymerisation
EMI	Electromagnetic Interferrence
FBG	Fibre Bragg Grating
FFT	Fast Fourier Transform
FSM	Frequency Sensitive Mode
GUM	Guide to the Expression of Uncertainty in Measurement
HDCCB	Hybrid Direct Current Circuit Breaker
HVAC	High Voltage Alternating Current
HVDC	High Voltage Direct Current
HSS	High Speed Switch
IEC	International Electrotechnical Commission
IGBT	Insulated Gate Bipolar Transistor
LCC	Line Commutated Converter
LVT	Low Voltage Transducer
MDCCB	Mechanical Direct Current Circuit Breaker
M&E	Mechanical and Electrical
MTDC	Multi-Terminal Direct Current
NI	National Instruments
OCS	Optical Current Sensor
OHL	Overhead Line
PZT	Piezoelectric Transducer
RC	Resistor-Capacitor

SFCL	Superconducting Fault Current Limiter
SG	Savitzky–Golay Filter
TCR	Temperature Coefficient of Resistance
TDR	Time Domain Reflectometry
TIV	Transient Interruption Voltage
VSC	Voltage Source Converter
WAMPAC	Wide Area Monitoring, Protection and Control
XLPE	Cross-Linked Polyethylene

Chapter 1

Introduction, Research Objectives and Contributions

1.1 Background and Motivation

The global power system is undergoing a rapid and unprecedented transformation driven by technological advancement, the escalating demand for clean energy, and global decarbonization initiatives. Historically, power systems were centrally planned and vertically integrated, relying predominantly on synchronous rotating machines powered by carbon-intensive fuels. However, international frameworks such as the Kyoto Protocol have accelerated the shift toward net-zero emissions, prompting a fundamental reconfiguration of the generation, transmission, and distribution landscape [1]. In contrast to traditional power networks, which follow a centrally controlled, vertically hierarchical structure, the modern paradigm emphasises decentralisation, decarbonisation, and digitalisation, leveraging diverse, geographically dispersed renewable energy sources. This shift has resulted in a generation portfolio increasingly composed of variable renewable sources such as wind, solar, and hydro. Consequently, transmission networks have evolved from conventional, vertically integrated AC architectures to hybrid AC–DC topologies, in which high-voltage direct current (HVDC) links serve as efficient interconnection corridors for bulk power transfer and the integration of remote renewable

resources.

The depletion of carbon-based energy reserves, whose reserve-to-production ratios indicate limited future availability, further underscores the urgency of alternative, sustainable, and low-carbon generation pathways (Table 1.1). Simultaneously, electricity's share in total global energy consumption, which is currently about 21%, continues to rise (Fig. 1.2 and Fig. 1.3), driving accelerated diversification of supply sources. The abundance and global distribution of renewable resources (Table 1.2) make them viable long-term substitutes for fossil-based generation.

Global electricity demand is projected to increase substantially by 2030, even as electricity production is projected to rise to 32,127 TWh by 2030, as shown in Fig. 1.1, with data centres emerging as one of the largest single end-use sectors. According to the International Energy Agency (IEA), data centres are expected to consume approximately 945 TWh by 2030, and 1200 TWh by 2035, of which renewable sources are projected to supply nearly 450 TWh [2]. The increasing reliance on geographically remote renewable generation accentuates the need for long-distance, high-efficiency transmission technologies. In this regard, HVDC systems play a pivotal role in enabling bulk power transfer while maintaining the network stability and reliability, particularly vital for energy-intensive infrastructures such as data centres.

The growing prominence of HVDC and medium-voltage direct current (MVDC) systems has also spurred significant global investment in engineering, procurement, and construction (EPC) projects. A notable example is the United Kingdom's $3.2 billion HVDC subsea interconnector, which exemplifies the trend toward large-scale, cross-border energy exchange [3].

At the distribution level, network topology has transitioned from centralized control to distributed configurations, integrating embedded generation and prosumer (producers and consumers) participation. Existing networks are also been transitioned from AC operated to DC form; pilot projects such as Angle-DC demonstrate the feasibility of repurposing existing AC infrastructure for DC operation to exploit DC's superior power-transfer capability [4]. Nonetheless, most distribution systems remain predominantly AC due to their operational simplicity, cost effectiveness, and mature protection

and voltage transformation schemes [5], [6], [7]. Conversely, transmission networks face distinct challenges, primarily the need to transmit power from remote renewable plants over long distances with minimal losses. The inherent impedance and reactive power constraints of AC systems reduce transmission efficiency and economic viability at such scales, reinforcing the global transition toward HVDC [8], [9]. However, the stochastic and intermittent characteristics of renewable generation introduce volatility in system frequency and voltage stability. The asynchronous nature of these sources necessitates an interface technology capable of harmonizing variable power outputs. HVDC converters inherently decouple generation from frequency constraints, providing controllable and stable transmission channels even under fluctuating operating conditions.

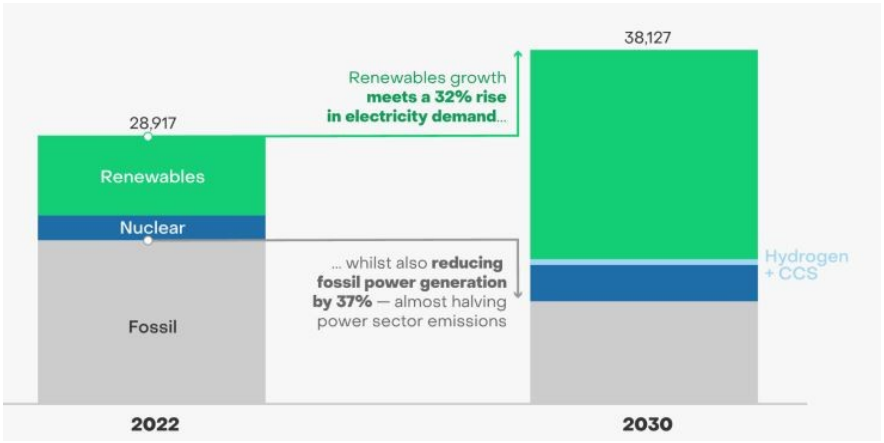

Figure 1.1: Global electricity production and projection (TWh) [10]

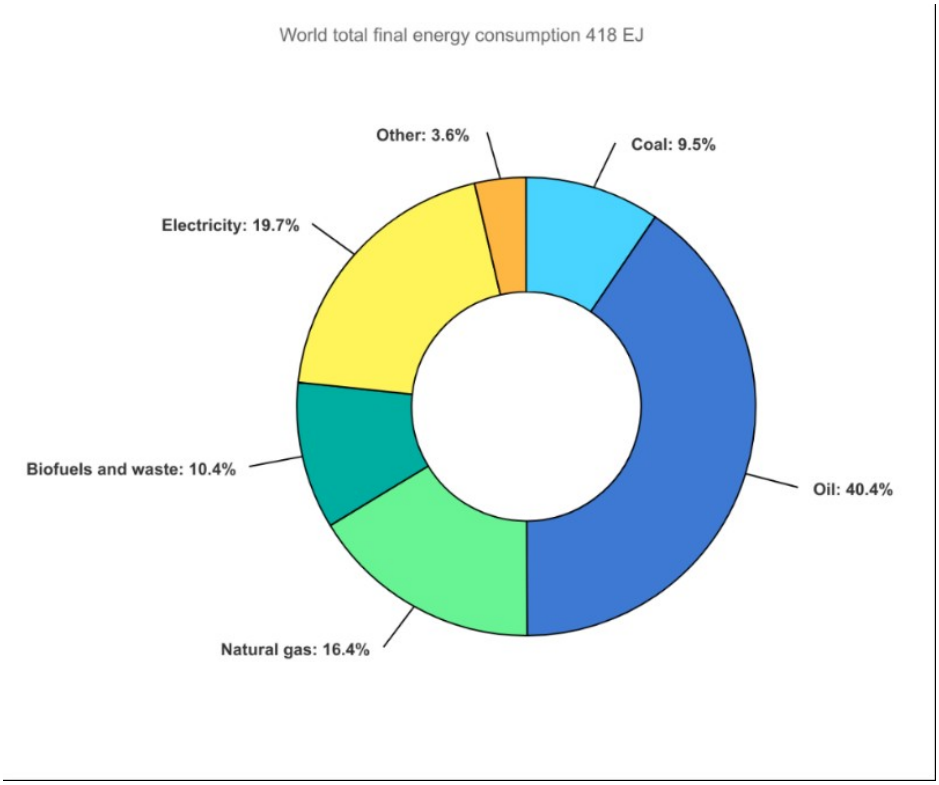

Figure 1.2: World total energy consumption in 2019 (418 EJ/year) [10], [11]

Table 1.1: Global Distribution of Coal, Oil, and Natural Gas Resources [12]

Regions	**Coal**			**Oil**			**Natural Gas**		
	Remaining Proven Recoverable Reserves (billion tons)	**Percentage**	**R/P ratio (year)**	**Remaining Proven Recoverable Reserves (billion tons)**	**Percentage**	**R/P ratio**	**Remaining Proven Recoverable Reserves (trillion m^3)**	**Percentage**	**R/P ratio (year)**
North America	245.1	27.5	250	35.0	13.6	37	12.0	6.3	13
Central and South America	14.6	1.6	149	51.1	19.5	> 100	8.0	4.1	44
Europe and the Eurasian Continent	310.5	34.8	254	19.8	8.8	23	57.0	30.6	55
Middle East	1.1	0.1	> 500	109.4	47.9	78	80.0	43.2	> 100
Africa	31.8	3.6	122	17.3	7.7	41	14.0	7.6	70
Asia-Pacific	288.4	32.4	54	5.6	2.5	14	15.0	8.2	31
Total	**891.5**	**100**	**113**	**238.2**	**100**	**53**	**186**	**100**	**55**

Table 1.2: Global Distribution of Hydro, Wind, and Solar Energy Resources [12]

Regions	**Hydropower**		**Wind Energy**		**Solar Energy**	
	Theoretical Reserves (TWh/year)	%	**Theoretical Reserves (TWh/year)**	%	**Theoretical Reserves (TWh/year)**	%
Asia	18,000	46	500,000	25	37,500,000	25
Europe	2,000	5	150,000	8	3,000,000	2
North America	6,000	15	400,000	20	16,500,000	11
South America	8,000	21	200,000	10	10,500,000	7
Africa	4,000	10	650,000	32	60,000,000	40
Oceania	1,000	3	100,000	5	22,500,000	15
Total	**39,000**	**100**	**2,000,000**	**100**	**150,000,000**	**100**

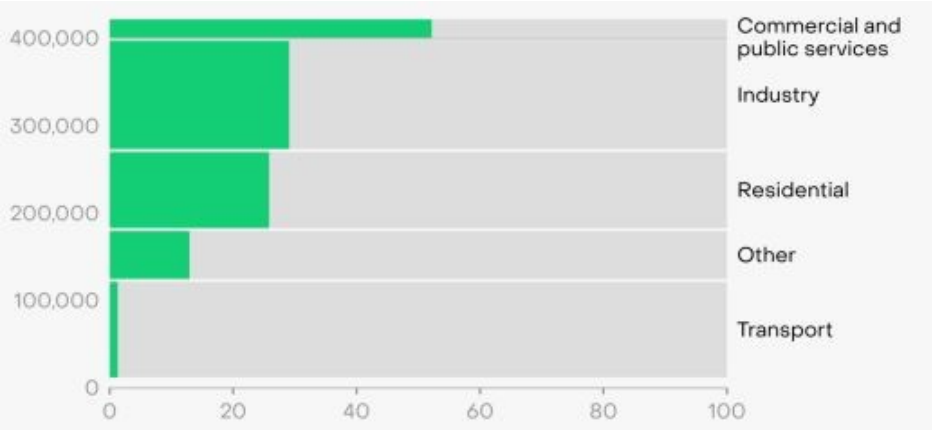

Figure 1.3: Share of electricity in final global consumption in 2021 (%). Energy use in petajoules (PJ) [10]

Although both AC and DC transmission systems will continue to coexist, the superior controllability, efficiency, and scalability of HVDC for bulk power transmission position it as the preferred technology for future grid expansion and cross-border interconnections. Consequently, HVDC is expected to attract increasing investment and operational involvement within modern and future power systems.

1.1.1 Development in HVDC network systems

Conventionally, electrical current can be classified into two forms: AC and DC. Whereas AC is produced by interaction between a coil of wire and a rotating magnetic field, which produces current with a periodic change of direction at a particular frequency, DC is produced by a battery, fuel cell and solar cell with a static direction of flow; it can also be produced by a conversion process from AC using rectifying components and a circuit. AC has the advantage of ease of voltage transformation between levels via transformers and of fault-condition management, since the current waveform crosses zero. On the other hand, DC current offers lower losses and higher energy density for the same cable dimensions and an unconstrained transmission distance, compared to AC. It is also more economical to operate over longer distances. An example of comparative analysis of power that can be transferred with the same cable dimension and distance between AC and DC transmission lines is shown in Table 1.3 [13], and a

technical comparison between HVAC and HVDC is shown in Table 1.4.

Table 1.3: HVDC Advantage in Power Density

	Length (km)	**Power (MW)**	**Voltage (kV)**	**Losses (%)**
AC	1000/2000	3000	800	6.7/10
DC	1000/2000	6400	800	3.5/5

Prior to the renewed interest in HVDC, AC mode of transmission had established the standard for power generation, transmission, and distribution. However, the rekindled interest in DC transmission led to the discovery of vacuum thyristors, which improved the methods for converting and transmitting DC power in bulk. It led to the installation of the first DC transmission system in the 1950s [14], [16], [18], [19]. HVDC has transitioned from isolated use to a major component of modern power system infrastructure. As at 2023, the total global installed capacity of the HVDC transmission is above 300 GW and projected to get to 500 GW by 2028 [20], [21].

The growth has catalysed innovation in diverse generation assets, each with its own peculiarities, including asynchronous generation and intermittent power flow. In the UK, there is a plan for renewable generation with significant capital outlay; it is expected that by 2030 the offshore wind industry will achieve a strategic target of 40 GW and 75 GW by 2050 [17]. HVDC transmission will enable power from these assets to be transmitted. Although generation assets are increasing in capacity, the transmission side of the network segment, traditionally dominated by overhead lines (OHL) and underground cables (UGC), is also expanding, albeit at a slower pace than generation. Nonetheless, cable assets are growing in volume of installed capacity, requiring high level of reliability; however, real-time monitoring of the cable condition is challenging [22]. Although cable failure rates are low, the unavailability of cable condition monitoring technology, and the difficulty in locating faulty segments leave the cable system vulnerable to defects and longer mean time to repair as reported in [22], [23]. Notwithstanding, the advantages of the adoption of the HVDC system far outweigh these setbacks, which are currently undergoing research for solutions.

Table 1.4: Technical Comparison Between HVAC and HVDC [8]

Transmission Type	**HVAC**	**HVDC**
Cables/Lines		
Number of Conductors	Higher (3-phase conductors, lower individual ratings, cumulatively more expensive)	Lower (2 conductors with higher individual rating)
Utilisation	Limited by skin-effect (although bundled conductors are used to limit it)	Full up to thermal limits
Losses	Higher (mainly resistive and reactive, requiring expensive line-capacitance compensators)	Lower (mainly resistive and corona losses)
ROW (right of way)	Higher (could exceed $\times 3$ times of HVDC [14])	Lower
Distance	Lower [14], [15]	Higher [9], [16]
Meshed Grids Availability	Widespread on a global scale	Currently limited with significant predicted growth
Protective Equipment	Well-developed UHV circuit breakers	Extensive R&D effort to develop HVDC breakers and/or converter fault blocking capability
Substations Cost	Significantly lower	Higher (converter stations)
Losses [17]	Low transformer and HV equipment losses (0.3% in AC double circuit)	Higher station losses (could exceed 1% for VSC)
Economic Viability	UG cables $<$ 50–100 km; overhead line $<$ 300–800 km	Beyond HVAC limits (point-to-point links)

1.2 Reason and Justification for Research

Although HVDC networks have advantages in bulk power transmission over HVAC and have become the go-to option, they are also blighted by challenges of fault management, instrumentation and measurement, cable condition monitoring challenges, and difficulty in locating compromised cable sections [22], [24].

Another challenge that HVDC faces is its intolerance to sustained fault and fault management that can easily be implemented in AC networks. In an AC network, a fault can easily be mitigated at a zero crossing. The increased amplitude and frequency during fault condition oscillate around the zero reference; mitigation strategies can be implemented at that point, such that the latent magnetic and capacitive energy released during fault is limited to almost zero. The same cannot be said of HVDC, which lacks this capability. There is a tendency for the fault current to rise exponentially above the line's operating capacity within a very short time, releasing a large amount of energy that could be detrimental to HVDC equipment. The energy dissipated that the network will theoretically have to cope and absorb can be quantified as per the following relationship [24]:

$$E = \frac{1}{2} L I^2 \tag{1.1}$$

where E is the latent magnetic energy in a conductor in Joules, L is the inductance in Henries, and I is the current in amperes.

For illustration, consider a 100 km HVDC cable with a cross-sectional area of 1000 mm^2 and an inductance of 0.97 mH/km [24], [25] carrying a fault current of 15 kA. Theoretically, the magnetic energy stored in the cable inductance and released during a fault can be expressed by (1.1): Substituting the parameters gives:

$$E = \frac{1}{2} \times 0.97 \times 10^{-3} \times 100 \times 15000^2 = 11 \text{ MJ} \tag{1.2}$$

A similar consideration applies to the electrostatic energy stored within the cable insulation due to charge accumulation during a fault or transient event, and can be

expressed using the capacitive energy relation:

$$E = \frac{1}{2}CV^2 \tag{1.3}$$

The absence of natural current zero crossings in DC systems introduces additional complexity in fault detection, isolation, and interruption. As a result, the effective operation of HVDC networks relies on rapid fault detection and timely mitigation. To provide context for the severity of DC fault conditions, the energy released during a high-current fault, such as a 15 kA event in a 100 km HVDC cable, can be comparable in magnitude to the kinetic energy associated with large-scale mechanical systems, for example, a 110-ton heavy freight train moving at 100 km/h, brought to an abrupt stop. This comparison illustrates the substantial energy levels that HVDC protection and interruption mechanisms must handle during fault events [24]. These are some of the challenges and the severe energy stress imposed on HVDC equipment during DC faults. Nonetheless, research is ongoing to address these gaps and accelerate mitigation strategies against some of the identified problems in HVDC networks. Hence, monitoring, detecting, and mitigating these occurrences in a timely manner will limit the extent of damage that could result from the fault condition.

The unique technical challenges of long-distance cable systems, particularly in fault detection, protection, and condition monitoring, have driven the need for innovative sensing and monitoring solutions to ensure secure, reliable, and resilient network operation. Accordingly, the following research questions are formulated to define and guide the scope of this work:

1. What are the conventional sensing technologies being deployed in HVDC monitoring?

2. What is the technology that currently supports wide area monitoring, protection and control (WAMPAC) in HVDC network monitoring?

3. How is fault occurrence detected in a long-distance cable?

4. How is the rise in current mitigated over a long-distance cable?

5. How is cable condition monitoring implemented in HVDC cable?

6. What are the current technologies to achieving that?

The answers to these questions will establish the basis for evaluating existing solutions, identifying their limitations, and justifying the need for the novel protection and sensing framework proposed in this research.

1.3 Problem Statement

Conventional current measurement sensors used for DC measurements, such as Hall-effect and fluxgate devices, are magnetic-based and inherently non-passive, requiring a local power supply [4], [5], [6], [7], [26]. As a result, their application for monitoring current within HVDC cables is limited, since remote interrogation, signal multiplexing, and stable operation under varying environmental conditions become impractical with them. Moreover, these sensors exhibit intrinsic drawbacks, including offset drift, core saturation, and thermal instability near their Curie temperature. For example, a standard 20 A Hall-effect sensor can experience offset drift of up to 300 mA over a moderate temperature range of 0 °C to 70 °C [27], while for hall effect sensors like Allegro micro A1324, A1325, A1326, there is a drift as much as 8.5% error of the measured current at maximum temperature can be observed [28]. However, these figures refer to uncompensated commercial sensors operating near thermal limits. Other sensing methods, such as photonic crystal fibre (PCF) and Sagnac interferometer, are effective for sensing DC at a single location but are very limited in distributed sensing and remote interrogation, and are constrained by their power requirements [29].

Beyond measurement constraints, HVDC systems face significant reliability challenges arising from DC fault-current behaviour. Following fault inception, the current initially rises due to the discharge of distributed line and DC-link capacitances, after which it is sustained by diode freewheeling and subsequent contribution from the AC network through the converter. In the absence of natural current zero crossings, as found in AC systems, passive interruption of DC fault currents is not possible, making

timely fault detection and interruption critical. If faults are not detected and interrupted within stringent time frames, typically on the order of a few milliseconds, the resulting high current and associated energy can impose severe electrical and thermal stress on protective devices and increase the risk of equipment damage [30]. The limitations in sensing and protection capabilities form a major barrier to the realisation of WAMPAC strategies within HVDC networks. In particular, the lack of distributed sensing technologies capable of providing comprehensive condition monitoring of HVDC cables further complicates fault localisation and system health diagnostics. The gaps that persist in the measurement and quantification of key state variables, such as voltage and current in HVDC, as outlined in Table 1.5, demand further research and innovation, which this study aims to address [31], [32], [33], [34].

Addressing these challenges is essential to enhance the resilience, stability, and reliability of HVDC systems, which are foundational to the ongoing transition away from conventional, carbon-intensive rotating machinery towards a cleaner, zero-carbon power infrastructure.

Table 1.5: Gaps in Measurement in HVDC [31], [32], [33], [34], [35], [36]

Aspect	**Identified Gaps**	**Implication/Research Need**
Fault Detection Speed, Selectivity, and Latency	Conventional single-ended and double-ended protection methods suffer from acquisition latency and poor selectivity. Current sensors lack the response speed required for fast detection [37]. Most fault detection methods rely on travelling waves. Travelling-wave propagation speed depends on line LC parameters and can be distorted at junctions with impedance discontinuity, termination points, and transition points between overhead lines and underground cables [38]. Line LC parameters can result in propagation velocities that are only a fraction of the speed of light, sometimes as low as 30% in some XLPE cables [39]. This can delay fault signal acquisition.	This undermines real-time fault location and jeopardises the protection system's rapid response. There is a need for ultrafast sensors and advanced detection schemes to reduce latency in HVDC fault identification. It also leads to delay in fault detection and contributes to fault current escalation, thereby placing HVDC equipment at risk.

Aspect	**Identified Gaps**	**Implication/Research Need**
Condition Monitoring of Cables	Cable condition monitoring remains a major challenge, particularly in long HVDC links where early degradation signals are weak and difficult to localise [40], [41], [42].	Absence of reliable condition monitoring increases the risk of undetected insulation deterioration. Novel multiple-point sensing and multiplexing technologies are required for detection and proactive fault prevention.
Thermal Stability	Many conventional current and voltage transducers, such as Hall-effect sensors, are susceptible to temperature-induced measurement drift. For example, a typical Hall-effect current sensor can exhibit a drift of up to approximately 300 mA when measuring a 20 A signal at temperatures approaching 70 °C, leading to significant degradation in measurement accuracy under elevated thermal conditions [28], [43]. The power requirement and form factor of sensors such as fluxgate devices make them unsuitable for low-power solutions in confined spaces [44].	This compromises measurement accuracy under dynamic operating conditions, rendering such devices unsuitable for certain HVDC applications. Research into temperature-compensated or thermally robust sensor designs is therefore critical.

Aspect	**Identified Gaps**	**Implication/Research Need**
Long-Term Reliability and Maintenance	The inclusion of energy sources, such as batteries, in most current measurement devices necessitates frequent maintenance, thereby limiting long-term reliability.	These requirements conflict with the need for continuous, maintenance-minimal operation in HVDC systems. Development of durable, low-maintenance sensing technologies is essential.
Electromagnetic Interference (EMI)	Most HVDC sensors such as Hall-effect and fluxgate sensors are susceptible to EMI [45].	This degrades accuracy in HVDC environments with strong electromagnetic fields. Robust EMI-resilient designs or alternative optical sensing technologies are needed.
Current Measurement	Currently, distributed measurement of current in HVDC is not possible due to a lack of mature solutions [46]. AC-based CTs and VTs remain widely used in HVDC networks due to the lack of a mature solution for direct-current measurement in HVDC. Hence, there remains significant reliance on AC CTs and VTs [13].	It impairs rapid response to fault conditions and puts HVDC equipment at risk.

Consequently, reliable measurement of current and voltage is essential for condition monitoring and the early detection of abnormal states in HVDC networks.

1.4 Research Contributions

Throughout this research, several contributions to the body of knowledge have been made, as outlined below.

1. **Design of an innovative instrumented butt splice joint sensor**

   The instrumented butt splice joint sensor represents a significant advancement in HVDC network monitoring. The sensor is designed to be embedded at cable splice joints, which are critical points in transmission lines where monitoring is often challenging, while simultaneously serving as both a cable joint connection point and an instrumentation device. By supporting data acquisition at multiple locations, it enhances the granularity of network monitoring and provides real-time information that is valuable for Wide-Area Monitoring, Protection, and Control (WAMPAC) strategies. This design allows seamless integration into existing HVDC infrastructure and offers the potential for early fault detection and predictive maintenance, thereby improving the reliability and safety of the transmission system.

2. **Design and implementation of an ultra-low-power non-linear amplifier without additional circuitry for gain-setting selection**

   This non-linear amplifier is engineered to operate at ultra-low power levels, making it suitable for power-constrained environments such as HVDC sensing applications. Its ability to function without additional circuitry for gain-setting selection simplifies the architecture and reduces both cost and complexity. The amplifier nonlinearity is tailored for the amplification of low-level signals, which is important in current-sensing and condition-monitoring applications where signal integrity must be preserved at very low amplitudes. This design provides a pathway towards more energy-efficient, compact, and robust HVDC monitoring systems.

   - Development and analytical derivation of a closed-form expression describing the output voltage of a non-linear amplifier configured with multiple paral-

lel feedback paths, combining resistive gain-setting networks with diode-induced non-linear behaviour.

3. **Development of a novel segregated piecewise calibration method in the quadratic regression family**

   This contribution introduces a piecewise calibration method that improves the accuracy of signal measurement near the error floor of interrogation equipment. By combining a piecewise approach with quadratic regression and straight-line fitting, the method improves handling of very low-level signals, which are typically difficult to measure due to noise and instrumentation limitations. This calibration technique is particularly beneficial for HVDC monitoring systems, where reliable measurement of small signal variations is critical for detecting early signs of cable deterioration or faults. The method, therefore, enhances both the resolution and the reliability of the sensing system.

4. **Design of a self-powered signal conditioning circuit for an HVDC optical current sensor**

   The self-powered signal-conditioning circuit is an important innovation for HVDC optical current sensors, particularly in remote or difficult-to-access locations. By eliminating the need for external power sources, the circuit simplifies sensor deployment and reduces operational costs. It also ensures that the sensor produces a clean and accurate output signal, even in the presence of noise or environmental disturbances. This design improves both the scalability and the reliability of HVDC monitoring systems.

5. **Specific contributions concerning power network protection and control**

   a. **Enhanced fault localisation using distributed photonic sensing as an alternative to conventional time-domain reflectometry**

      - Analytical formulation that captures the combined influence of sampling frequency, sensing-device resonance, and material-dependent signal-propagation

characteristics on fault-distance resolution.

b. **Determination of fault type and fault location using phase-shift and inverted-polarity signals from adjacent sensors**

- Analytical derivation of a fault-localisation formulation that accounts for transient signal propagation in homogeneous and inhomogeneous transmission media.

c. **Determination of insulation condition by monitoring the speed of signal propagation through the insulation**

1.5 Publications

The following publications have been produced from this research.

1.5.1 Journal Publications

I. A. Amiolemen, G. Fusiek, and P. Niewczas, "Self-Powered Signal Conditioning Circuit for an HVDC Optical Current Sensor," *IEEE Sensors Letters*, vol. 7, no. 11, Nov. 2023, doi: 10.1109/LSENS.2023.3311676.

II. A. Amiolemen, G. Fusiek, and P. Niewczas, "Improved Calibration Method of the Photonic Current Sensor for Monitoring HVDC Networks," *IEEE Sensors Letters*, vol. 8, no. 10, pp. 2–4, 2024, doi: 10.1109/LSENS.2024.3441228.

III. A. Amiolemen, G. Fusiek, P. Niewczas, and A. Dyśko, "Accelerated Fault Location and Detection in HVDC Networks Using Cable Joints Instrumented with Photonic Current Sensors," *IEEE Transactions on Instrumentation and Measurement*, under review.

1.5.2 Conference Publications

I. A. Amiolemen, G. Fusiek, and P. Niewczas, "Self-Powered Signal Conditioning Circuit for an HVDC Optical Current Sensor," in *Proceedings of the 22nd IEEE Sensors Conference*, Vienna, Austria, Oct. 29–Nov. 1, 2023, doi: 10.1109/LSENS.2023.3311676.

II. A. Amiolemen, G. Fusiek, and P. Niewczas, "Towards the Development of a Photonic Current Sensor for HVDC Networks," in *2024 IEEE International Instrumentation and Measurement Technology Conference (I2MTC)*, IEEE, May 2024, doi: 10.1109/I2MTC60896.2024.10560732.

III. A. Amiolemen, G. Fusiek, P. Niewczas, and A. Dyśko, "Accelerated Fault Detection in HVDC Networks Using Cable Joints Instrumented with Photonic Current Sensors," in *2025 IEEE International Instrumentation and Measurement Technology Conference (I2MTC)*, IEEE, May 2025, pp. 1–6, doi: 10.1109/I2MTC62753.2025.11079022.

1.6 Thesis Overview

1.6.1 Brief Overview of Each Chapter

This thesis is organised to first highlight the critical role of HVDC networks in enabling the reliable delivery of bulk power from diverse generation sources. The discussion then places this within the broader global energy outlook, emphasising the associated challenges. It further outlines the limitations of existing current-sensing methods, protection and control approaches, and condition-monitoring practices for HVDC cables, as well as the inherent difficulties in accurately locating fault points within HVDC networks.

Chapter 2 provides an overview of HVDC systems, beginning with their historical development and a technical review of the various configurations, including the advantages of HVDC over AC transmission. The chapter then examines protection mechanisms employed in HVDC networks and highlights the current state of the art in current and voltage measurement in HVDC systems. A detailed discussion of the underlying FBG technology is also presented, covering its sensing principles and advantages, before concluding with the current challenges of current sensing in HVDC networks.

Chapter 3 addresses HVDC fault characterisation, fault types, and the mechanisms of current release, fault dynamics, and propagation. It introduces the distributed optical current sensor for monitoring, protection, and control. The operating principles

of FBG sensors, their response to physical parameters, and the signal-processing techniques used for FBG sensors are discussed. The chapter also analyses protection stages, fault-detection algorithms based on FBG data, and strategies for fault mitigation.

Chapter 4 focuses on distributed photonic sensing, including fabrication, interrogation, and measurement applications. It introduces the principles of Bragg gratings, their different types, and methods of production.

Chapter 5 addresses the sensor system design, component evaluation, and the characterisation of each stage within the sensor building blocks. It presents the architecture of the proposed optical current sensor (OCS).

Chapter 6 presents the simulation and experimental results. It begins with a description of the software tools used for sensor analysis, followed by the experimental setup adopted for testing. The chapter then compares calculated and analytical results with simulated and experimental findings and analyses system performance under different fault conditions.

Chapter 7 deals with calibration and error analysis. It introduces a novel calibration-curve strategy based on a semi-piecewise segregated-polynomial formulation for constructing the calibration equation.

Chapter 8 focuses on the use-case application of the proposed sensing scheme. It demonstrates the deployment of the sensor within an HVDC network and highlights its effectiveness in fault detection and localisation. The discussion further emphasises the practical relevance of the sensing solution by illustrating how it enhances the monitoring and protection capabilities of HVDC systems under real operating conditions.

Chapter 9 discusses the key research findings, the original contributions to knowledge, and potential areas for further investigation.

Chapter 1 References

[1] United Nations, *Kyoto protocol to the united nations framework convention on climate change*, pp. 3–8, 1998.

[2] IEA, *Global investment in ai electricity need*, pp. 2–7.

[3] M. Čavčić. "Uk's subsea electricity superhighway." pp. 1–4, Accessed: Mar. 20, 2023. [Online]. Available: https://www.offshore-energy.biz.

[4] SP Networks, "ANGLE-DC 2015 electricity network innovation competition," Tech. Rep., 2015, pp. 6–18.

[5] S. M. Ismael, S. H. E. A. Aleem, A. Y. Abdelaziz, and A. F. Zobaa, "State-of-the-art of hosting capacity in modern power systems with distributed generation," *Renewable Energy*, vol. 130, pp. 1002–1020, Jan. 2019. DOI: 10.1016/j.renene.2018.07.008.

[6] T. Skoczkowski, S. Bielecki, M. Wołowicz, L. Sobczak, A. Weglarz, and P. Gilewski, "Participation in demand side response. are individual energy users interested in this?" *Renewable Energy*, vol. 232, pp. 2–5, Oct. 2024. DOI: 10.1016/j.renene.2024.121104.

[7] M. S. Bakare, A. Abdulkarim, M. Zeeshan, and A. N. Shuaibu, "A comprehensive overview on demand side energy management towards smart grids: Challenges, solutions, and future direction," *Energy, Sustainability and Society*, pp. 2–17, Dec. 2023. DOI: 10.1186/s42162-023-00262-7.

[8] A. Alassi, S. Bañales, O. Ellabban, G. Adam, and C. MacIver, "HVDC transmission: Technology review, market trends and future outlook," *Renewable and Sustainable Energy Reviews*, vol. 112, pp. 4–19, Sep. 2019. DOI: 10.1016/j.rser.2019.04.062.

[9] M. P. Bahrman and B. K. Johnson, "ABC of HVDC transmission," *IEEE Power and Energy Magazine*, 2007, pp. 2–12.

[10] M. Wiatros-Motyka et al., "Global electricity review 2024," Ember, London, Tech. Rep., 2024, pp. 20–62.

[11] International Energy Agency, "Key world energy statistics 2021," IEA, Tech. Rep., 2021, pp. 33–37.

[12] Z. Liu, *Global Energy Interconnection*. New York et al.: Elsevier, 2015, pp. 11–13, [Online]. Available: www.elsevier.com/permissions. Accessed: Sept. 15, 2023.

[13] M. Ardelean and P. M. Forename, *HVDC submarine power cables in the world: State-of-the-art knowledge*, 2015. DOI: 10.2790/023689.

[14] D. V. Hertem, O. Gomis-Bellmunt, and J. Liang, *HVDC Grids*. IEEE-Wiley, 2016, pp. 88–95.

[15] Scottish and Southern Electricity Network. "HVDC technology capability." pp. 8–10, Accessed: Jun. 18, 2023. [Online]. Available: https://www.ssen.co.uk.

[16] M. Barnes, D. van Hertem, S. P. Teeuwsen, and M. Callavik, "HVDC systems in smart grids," *Proceedings of the IEEE*, vol. 105, no. 11, pp. 9–16, 2017.

[17] Offshore Wind Industry Council, "Grid-access technologies for GB offshore wind industry executive summary," Offshore Wind Industry Council, Tech. Rep., 2020, pp. 3–8.

[18] ABB, "Special report: 60 years of HVDC," ABB, Tech. Rep., 2015, pp. 63–64.

[19] M. Eremia, C.-C. Lu, and A.-A. Edris, *Advanced Solutions in Power Systems: HVDC, FACTS, and Artificial Intelligence*. IEEE-Wiley, 2016, pp. 224–228.

[20] Hitachi Energy, "High voltage direct current (HVDC) transmission: Enabling the energy transition," Hitachi Energy, Tech. Rep., 2024, Enguerrand Ducene, Regional Sales Manager MEA, pp. 15–22.

[21] B. Group et al., *The operational and market benefits of HVDC to system operators*, 2023.

[22] O. E. Mountassir. "HVDC transmission cables in the offshore wind industry: Reliability and condition monitoring." pp. 1–6, Accessed: Sep. 4, 2023. [Online]. Available: http://www.tennet.eu/nl/news/article/tennet-and-mitsubishi-corporation-extend-partnership-in-ger-.

[23] ENTSO-E, "Recommendations to improve HVDC cable systems reliability," ENTSO-E AISBL, Tech. Rep., 2019, pp. 5–7.

[24] R. P. P. Smeets and N. A. Belda, "High-voltage direct current fault current interruption: A technology review," *High Voltage*, pp. 2–6, Apr. 2021. DOI: 10.1049/hve2.12063.

[25] NEXANS Cables, *6–36 kV medium voltage underground power cables: XLPE insulated cables*.

[26] M. A. Paun, J. M. Sallese, and M. Kayal, "Hall effect sensors design, integration and behavior analysis," *Journal of Sensor and Actuator Networks*, vol. 2, no. 1, pp. 85–97, Mar. 2013. DOI: 10.3390/jsan2010085.

[27] M. Crescentini, S. F. Syeda, and G. P. Gibiino, "Hall-effect current sensors: Principles of operation and implementation techniques," *IEEE Sensors Journal*, vol. 22, no. 11, pp. 8–10, Jun. 2022. DOI: 10.1109/JSEN.2021.3119766.

[28] Allegro MicroSystems. "Low-noise linear hall-effect sensor ICs with analog output." pp. 1–3, Accessed: Jun. 13, 2025. [Online]. Available: https://www.allegromicro.com.

[29] H. Huang et al., "A highly magnetic field sensitive photonic crystal fiber based on surface plasmon resonance," *Sensors*, vol. 20, no. 18, pp. 1–15, Sep. 2020. DOI: 10.3390/s20185193.

[30] CIGRE, "Protection and local control of HVDC-grids, B4/5.59 N739," CIGRE, Tech. Rep., 2018, pp. 14–30.

[31] W. Xiang, S. Yang, G. P. Adam, H. Zhang, W. Zuo, and J. Wen, "DC fault protection algorithms of MMC-HVDC grids: Fault analysis, methodologies, experimental validations, and future trends," *IEEE Transactions on Power Electronics*, vol. 36, no. 10, pp. 1–11, Oct. 2021. DOI: 10.1109/TPEL.2021.3071184.

[32] C. Zhang, Y. Li, G. Song, and X. Dong, "Fast and sensitive nonunit protection method for HVDC grids using levenberg-marquardt algorithm," *IEEE Transactions on Industrial Electronics*, vol. 69, no. 9, pp. 1–8, Sep. 2022. DOI: 10.1109/TIE.2021.3116570.

[33] D. Jovcic and K. Ahmed, *High-Voltage Direct-Current Transmission*. Wiley, 2015.

[34] A. Pragati, M. Mishra, P. K. Rout, et al., *A comprehensive survey of HVDC protection system: Fault analysis, methodology, issues, challenges, and future perspective*, pp. 3–6, 2023.

[35] D. Tzelepis et al., "Voltage and current measuring technologies for high voltage direct current supergrids," *IEEE Access*, vol. 8, pp. 7–12, 2020.

[36] A. Amiolemen, G. Fusiek, P. Niewczas, and A. Dyśko, "Accelerated fault detection in HVDC networks using cable joints instrumented with photonic current sensors," in *2025 IEEE International Instrumentation and Measurement Technology Conference (I2MTC)*, IEEE, May 2025, pp. 1–6. DOI: 10.1109/I2MTC62753.2025.11079022.

[37] M. Muniappan, "A comprehensive review of DC fault protection methods in HVDC transmission systems," *Protection and Control of Modern Power Systems*, vol. 6, no. 1, pp. 2–11, Dec. 2021. DOI: 10.1186/s41601-020-00173-9.

[38] P. M. B. Garcia, G. Chaffey, and D. V. Hertem, *HVDC fault detection performance in mixed overhead line and cable systems*, pp. 4–6, 2024.

[39] ABB. "XLPE submarine cable systems: Attachment to XLPE land cable systems – user's guide rev. 5." [Online]. [Online]. Available: https://www.abb.com/cables.

[40] O. E. Mountasir. "HVDC transmission cables in the offshore wind industry: Reliability and condition monitoring." pp. 1–6, Accessed: Sep. 4, 2023. [Online]. Available: http://www.tennet.eu/nl/news/article/tennet-and-mitsubishi-corporation-extend-partnership-in-ger-.

[41] ENTSO-E, "ENTSO-E AISBL recommendations to improve HVDC cable systems reliability," ENTSO-E, Tech. Rep., 2019, pp. 6–7.

[42] R. R. Tiferes, V. A. Lacerda, M. Cheah-Mane, and O. Gomis-Bellmunt, "A review on condition monitoring for XLPE-insulated subsea DC dynamic export cables," *IEEE Transactions on Dielectrics and Electrical Insulation*, pp. 11–15, 2025. DOI: 10.1109/TDEI.2025.3619448.

[43] Texas Instruments. "Comparing shunt- and hall-based current-sensing solutions in onboard chargers and DC/DC converters." pp. 3–7, Accessed: May 20, 2024. [Online]. Available: https://www.ti.com.

[44] Danisense, *DS200ID fluxgate sensor datasheet*, pp. 2–6.

[45] L. Zafari, Y. Liu, A. Ukil, and N. K. C. Nair, "Advances in HVDC systems: Aspects, principles, and a comprehensive review of signal processing techniques for fault detection," *Energies*, pp. 28–31, Jun. 2025. DOI: 10.3390/en18123106.

[46] J. Laninga, A. N. Esfahani, G. Ediriweera, N. Jacob, and B. Kordi, "Monitoring technologies for HVDC transmission lines," *Energies*, vol. 16, no. 13, pp. 4–6, Jul. 2023. DOI: 10.3390/en16135085.

Chapter 2

Technologies Underpinning HVDC Systems and Fibre-Optic Sensing

2.1 Technical Overview of HVDC

Modern high-voltage direct current (HVDC) transmission systems have evolved largely in response to advances in power semiconductor devices [1]. Two converter technologies dominate contemporary HVDC implementation: the line-commutated converter (LCC), which is based on thyristor valves, and the voltage-source converter (VSC), which is based on insulated-gate bipolar transistors (IGBTs). The transition from mercury-arc valves to thyristor-based converters in the late 1950s enabled reliable large-scale HVDC power transmission, while the later development of IGBT-based converters introduced substantially greater controllability, thereby facilitating more flexible point-to-point links and the emergence of multi-terminal HVDC grid architectures.

In a conventional HVDC converter station, shown schematically in Fig. 2.1, the AC system is interfaced with the converter station through an AC busbar incorporating transformers, switching apparatus, filters, and associated measurement and protection equipment. On the DC side, the principal components include the converter valves,

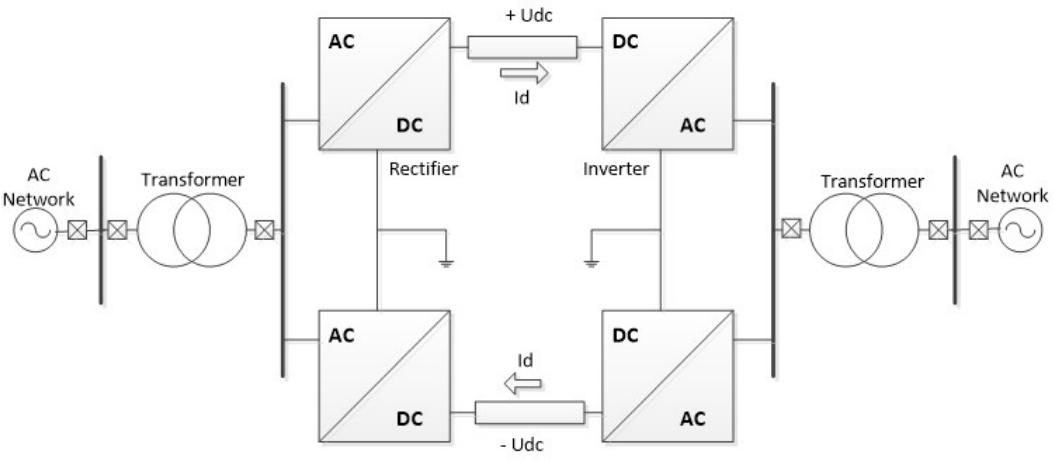

Figure 2.1: Bipolar HVDC link with ground return [2]

smoothing reactors, DC filters, overhead lines or cables, and the corresponding sensing, monitoring, and protection infrastructure. Since this thesis is concerned with HVDC cable monitoring and current measurement, particular emphasis is placed on the DC transmission path and its associated instrumentation requirements.

This chapter establishes the technical foundation for the sensing architecture proposed in this thesis by reviewing the principal technologies underpinning HVDC transmission and current measurement. Particular attention is given to current sensing approaches relevant to HVDC applications, including shunt-based methods, magnetic-field-based sensors, and fibre-optic sensing techniques. These technologies are critically assessed with respect to the requirements of HVDC monitoring, including electrical isolation, measurement bandwidth, deployment scalability, long-distance signal transmission, and suitability for distributed installation.

The principal contribution of this chapter is the systematic identification of the limitations of conventional HVDC current sensing technologies, particularly in relation to distributed monitoring, low-power operation, remote interrogation, and multiplexed deployment over long cable distances. Through this comparative assessment, it is shown that existing approaches do not simultaneously satisfy the requirements for high accuracy, galvanic isolation, scalability, and spatially distributed sensing. These limitations

define the research gap addressed in this thesis and motivate the development of the distributed optical current sensing architecture introduced in the subsequent chapters.

2.2 HVDC Converter Technologies

Converters are the defining functional element of an HVDC scheme and typically represent one of the most technically complex and capital-intensive components within a converter station. Their primary role is to perform power conversion between alternating current (AC) and direct current (DC), operating as rectifiers during AC-to-DC conversion and as inverters during DC-to-AC conversion. Broadly, HVDC converters may be classified into two main categories: line-commutated converters (LCCs) and voltage-source converters (VSCs).

2.2.1 LCC-Based HVDC

Line-commutated converters (LCCs) constitute the classical form of HVDC conversion technology and have historically formed the backbone of long-distance, high-power HVDC transmission. LCC-HVDC systems employ thyristors as the principal switching devices. A thyristor is a unidirectional semiconductor device that can be triggered into conduction and remains in the conducting state until the current through it naturally falls below its holding value. In LCC operation, this turn-off process is achieved through the alternating nature of the connected AC system, and for this reason the converter is described as line-commutated [3], [4].

In an LCC-HVDC scheme, the converter at the sending terminal operates in rectifier mode, converting AC power into DC power for transmission, while the converter at the receiving terminal operates in inverter mode, converting the transmitted DC power back to AC. The firing sequence of the thyristor valves is synchronised with the phase angle of the AC system, such that current is transferred from one valve to the next by the natural zero-crossing behaviour of the AC voltage. Consequently, successful commutation depends directly on the strength, waveform quality, and voltage support of the connected AC network [3].

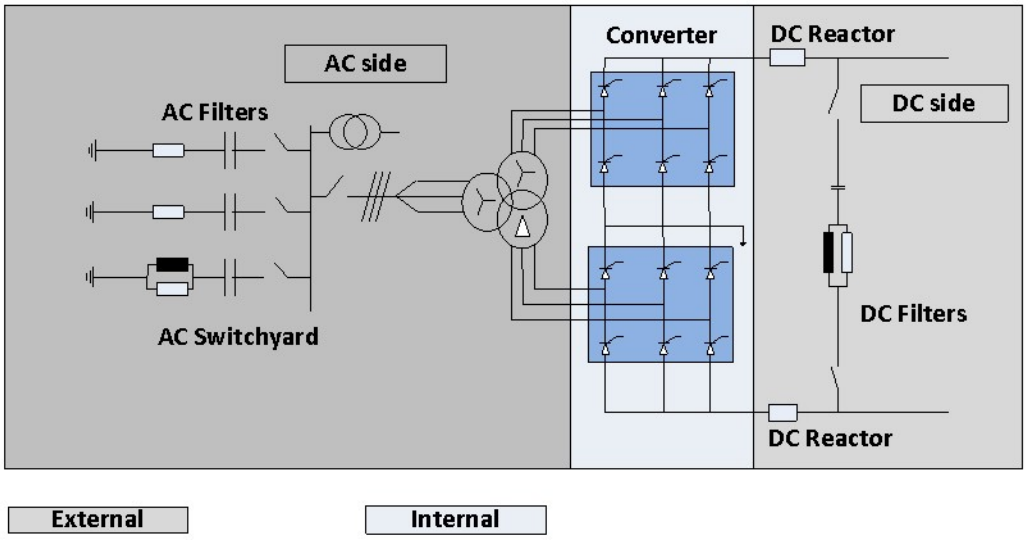

Figure 2.2: LCC-HVDC configuration [2]

A major limitation of LCC-HVDC is its dependence on the AC system for commutation. In weak grids, or during AC voltage depression, the converter becomes vulnerable to commutation failure. In addition, LCC stations consume reactive power and generate significant harmonic distortion, necessitating the installation of reactive compensation equipment and harmonic filters [3], [4]. Despite these limitations, LCC-HVDC remains widely deployed for bulk power transmission due to its high power rating, proven reliability, and favourable economics in long-distance applications.

2.2.2 VSC-Based HVDC

Voltage-source converter (VSC)-based HVDC represents a major advancement in HVDC transmission technology, particularly for applications requiring enhanced controllability, compact installation, and connection to weak or passive AC systems. VSC-HVDC employs insulated-gate bipolar transistors (IGBTs), enabling independent and rapid control of active and reactive power [3], [5].

An IGBT combines the high-input-impedance gate structure of a metal-oxide-semiconductor field-effect transistor (MOSFET) with the high-current and high-voltage handling capability of a bipolar device. Because switching is controlled electronically

rather than by the AC system waveform, VSC converters do not rely on external voltage zero-crossings for commutation.

This capability allows VSC-HVDC systems to operate effectively in weak or passive networks, making them particularly suitable for offshore wind integration, islanded systems, and multi-terminal HVDC grids. The principal components of a VSC-HVDC system include converters, DC transmission infrastructure, AC interface components, and advanced control systems.

The main advantages of VSC-HVDC include:

- independent control of active and reactive power;
- black-start capability;
- reduced station footprint;
- suitability for multi-terminal HVDC networks.

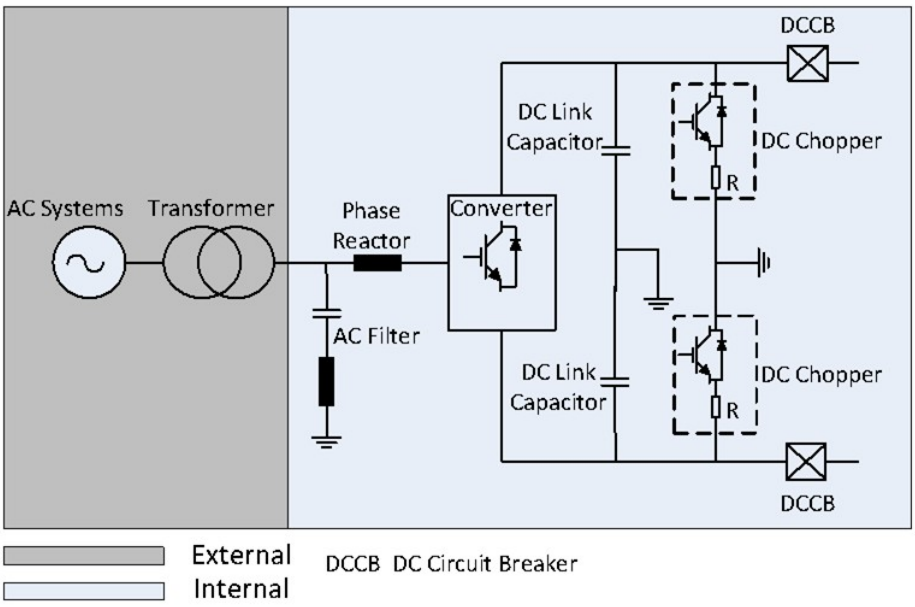

Figure 2.3: VSC-HVDC configuration [2]

Power electronic devices such as DC circuit breakers and DC choppers are commonly installed within the converter station building in order to provide environmental

protection and facilitate close integration with control, monitoring, and protection systems.

2.2.3 HVDC Configurations

VSC-based HVDC transmission can be realised in several network configurations, including monopolar, bipolar, back-to-back, and multi-terminal arrangements. Each configuration offers different levels of redundancy, operational flexibility, and power transfer capability. These alternatives allow HVDC systems to be tailored to a wide range of applications, from conventional point-to-point transmission schemes to more complex multi-terminal DC networks, as illustrated in Figs. 2.4 and 2.5.

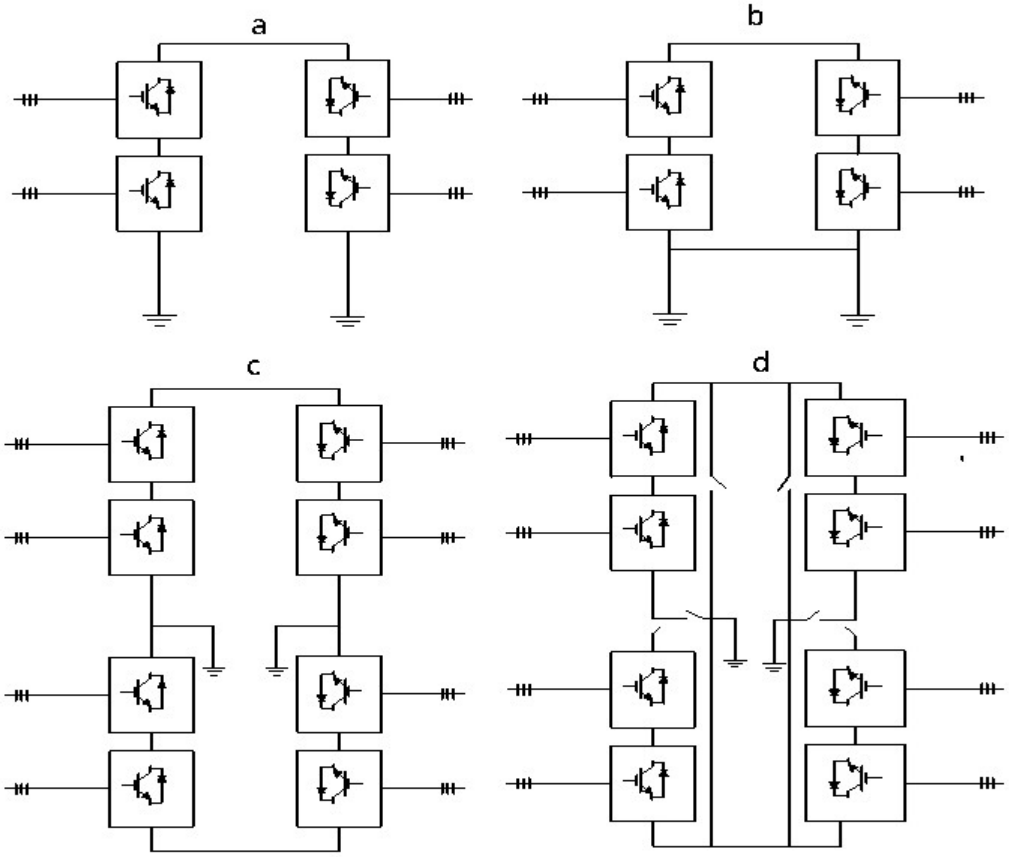

Figure 2.4: Basic HVDC configurations: (a) monopole with ground return, (b) monopole with metallic return, (c) bipole, and (d) bipole with metallic return

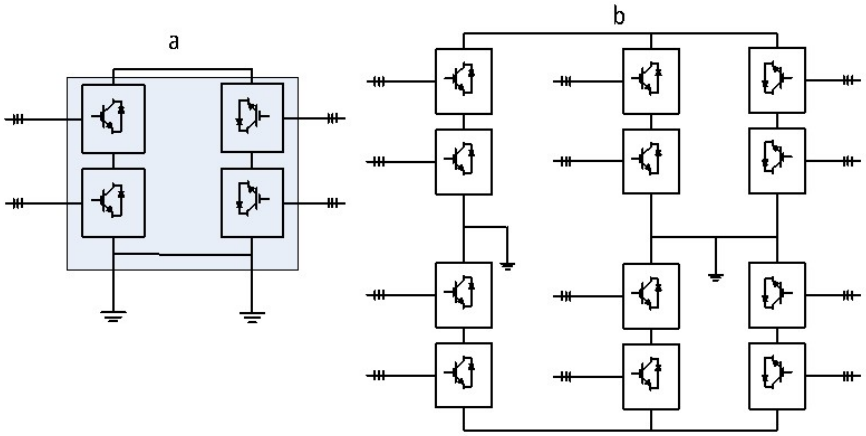

Figure 2.5: Advanced HVDC configurations: (a) back-to-back and (b) multi-terminal

2.3 HVDC Transmission Lines and Cables

HVDC transmission networks employ both overhead lines and underground or submarine cables for long-distance power transfer. Overhead lines are commonly used for land-based transmission, whereas underground and submarine cables are preferred in densely populated areas, offshore applications, and environmentally sensitive locations [3], [4], [5], [6].

2.3.1 Overhead Lines

HVDC overhead lines typically use aluminium or copper conductors supported by transmission towers. Compared with AC transmission, HVDC overhead lines can transmit higher power for a given conductor size because reactive power transfer constraints are absent. For the same transmission corridor and comparable conductor arrangement, DC transmission can provide higher power transfer capability than its AC counterpart [3].

However, overhead lines remain exposed to environmental disturbances such as lightning strikes, pollution-induced flashover, and severe weather conditions. Despite this vulnerability, they retain an important operational advantage: faults are generally easier to detect, access, and repair than in buried or submarine transmission systems. This relative ease of inspection and maintenance continues to make overhead lines

attractive for long-distance terrestrial transmission.

2.3.2 Underground and Submarine Cables

Underground and submarine HVDC cables are increasingly deployed where overhead transmission is technically, environmentally, or socially impractical. Their main advantages include reduced visual impact, narrower right-of-way requirements, and immunity to weather-related disturbances. Unlike overhead lines, underground cables preserve the surrounding landscape and avoid many of the mechanical risks associated with wind, ice loading, and conductor galloping.

They are also less exposed to contamination-related insulation problems and can offer greater public acceptance in urban or environmentally constrained regions. These advantages have contributed significantly to the growing adoption of cable-based HVDC transmission. Structurally, an HVDC cable consists of a central conductor surrounded by multiple functional layers, including semiconducting screens, insulation, metallic sheath or shield layers, and outer protective coverings.

A notable example of the vulnerability of overhead lines to climatic stress is the collapse of a 420 kV transmission line in Hardanger Fjord, Norway, during the 2013–2014 winter due to severe ice accumulation, as shown in Fig. 2.6 [7], [8].

Figure 2.6: Accumulated ice on a broken ground wire, January 2014 [7]

The principal HVDC cable technologies include [9]:

- mass-impregnated non-draining (MIND) cables;
- extruded XLPE cables; and
- thermoplastic elastomer-based cables.

Mass-Impregnated Non-Draining Cables

Mass-impregnated non-draining (MIND) cables have been used extensively in HVDC installations since the 1950s, particularly for submarine interconnections. Their long operational history has resulted in well-documented performance and reliability characteristics. MIND cables have recently been qualified for voltage levels up to approximately ±600 kV [3], [4], [9].

A major advantage of MIND technology is its tolerance to polarity reversal, which makes it particularly suitable for LCC-HVDC systems in which reversal of power flow is commonly achieved through reversal of DC polarity. In addition, MIND cables remain highly attractive for deep-water installations because of their robust moisture resistance and good water-tight performance at joints and terminations [3].

Extruded HVDC Cables

Extruded HVDC cables are predominantly insulated using cross-linked polyethylene (XLPE). With the development of VSC-HVDC technology, extruded cable systems have been deployed at voltage levels up to approximately ±540 kV, while manufacturers and standardisation bodies have targeted ratings up to 800 kV [8], [10]. These higher voltage classes have been considered in CIGRÉ guidance relating to testing procedures for extruded HVDC cable systems [10].

Despite these advantages, extruded HVDC cables remain susceptible to space-charge accumulation, particularly under polarity reversal. Space-charge build-up can distort the electric field distribution within the insulation, increase local electrical stress, and accelerate insulation degradation [11]. For this reason, conventional ex-

truded HVDC cable systems have historically been more closely associated with VSC applications than with LCC systems requiring polarity reversal.

A more recent development is the introduction of high-performance thermoplastic elastomer cable technology, such as high-performance polypropylene thermoplastic elastomer (HPTE), an example of which is shown in Fig. **??**. According to manufacturer data, HPTE-based cables can operate at voltage levels up to ±600 kV and power ratings of approximately 3400 MW, while offering improved suitability for both LCC and VSC applications [12]. Compared with XLPE cables of similar voltage class, HPTE cables offer improved thermal capability, reduced susceptibility to space-charge accumulation, and recyclability [13].

Figure 2.7: ±600 kV HVDC HPTE cable technology [14]

Figure 2.8: ±600 kV HVDC XLPE cable technology [14]

2.4 Protection Requirements in HVDC

Protection is fundamental to the reliable operation of HVDC systems. Because fault currents in DC networks can rise extremely rapidly, typically within a few milliseconds, detection and isolation must be achieved within similarly short timeframes in order to limit electrical and thermal stress on system components. Effective protection therefore depends strongly on accurate and fast measurement of key state variables, particularly current and voltage [2], [3], [15], [16].

2.4.1 Equipment Protection in HVDC Stations

Protection in an HVDC station is typically organised into several functional zones covering both the AC and DC subsystems.

DC-Side Protection

The DC protection zone of an HVDC station commonly includes:

- valve and ancillary system protection;
- DC smoothing reactor, DC filter, harmonic filter, and grounding switch protection;
- converter or pole protection;
- HVDC transmission link, cable, and DC busbar protection; and
- circuit breaker protection.

AC-Side Protection

The AC protection zone commonly includes:

- AC busbar and line protection;
- AC filter protection; and
- converter transformer protection.

As indicated above, HVDC station protection is inherently comprehensive because it combines conventional AC protection, which is relatively mature and well established, with DC protection, which remains more technically demanding due to the absence of natural current zero-crossings and the rapid growth of fault current. The overall protection architecture is therefore arranged to detect and isolate faults across all critical sections of the station, on both the AC and DC sides.

For DC-side protection in particular, fault detection commonly relies on sensors installed at terminal locations. In long cable systems, however, the propagation of fault-induced disturbances is influenced by the distributed inductance and capacitance of the line. Consequently, signal propagation delay and the resulting response time of the protection system become important constraints, especially where very fast fault clearance is required. These limitations provide part of the motivation for the distributed sensing approach investigated in this thesis.

2.5 Current and Voltage Measurement for Protection of HVDC Networks

Accurate measurement of current and voltage is fundamental to the protection, monitoring, and control of HVDC networks. Faults in HVDC systems are characterised by extremely rapid current rise, requiring protection systems to detect, classify, and initiate mitigation within very short timeframes [17]. In protection-oriented measurement systems, the total permissible delay, including sensing, signal conditioning, acquisition, and processing, is often constrained to the millisecond range [18], [19]. These requirements highlight the importance of fast and reliable measurement technologies for HVDC protection.

According to the ENTSO-E network code for HVDC systems, control and protection functions may be prioritised according to their relative importance as follows [20]:

1. protection of the HVDC network;

2. active power control for emergency support;

3. synthetic inertia, where applicable;
4. automatic remedial actions;
5. limited frequency sensitive mode (LFSM);
6. frequency control and frequency sensitive mode (FSM); and
7. power gradient constraint.

Within this hierarchy, HVDC network protection is assigned the highest priority. Central to this protection function is the accurate measurement of voltage and current, since these quantities are used as the principal trigger variables for fault detection and protective action. Current sensing technologies relevant to HVDC applications may be broadly classified into:

- resistive shunt-based measurement;
- magnetic-field-based sensing, including Hall-effect, fluxgate, and magnetoresistive devices;
- optical sensing based on the Faraday effect; and
- hybrid sensing approaches, which combine multiple transduction principles to improve performance under specific operating conditions.

Each sensing method offers different trade-offs in terms of bandwidth, accuracy, thermal stability, power consumption, galvanic isolation, and immunity to electromagnetic interference. Consequently, sensor selection is strongly application-dependent and must be matched to the requirements of the protection scheme and the operating environment [17], [19], [20].

2.5.1 Resistive Current Measurement (Shunt Sensors)

Shunt resistors measure current by exploiting the voltage drop developed across a precision resistor according to Ohm's law. This approach offers high linearity, wide bandwidth, and good measurement accuracy [21]. Since the primary sensing mechanism

is resistive, the intrinsic frequency dependence of the shunt itself is small, and any bandwidth limitation is typically imposed by the associated signal-conditioning and acquisition circuitry rather than the sensing element.

Despite these advantages, shunt-based current measurement requires galvanic contact with the current-carrying conductor, which introduces several practical limitations [10]:

- power dissipation due to Joule heating;
- possible electrochemical degradation at conductor interfaces;
- insulation and high-voltage integration constraints; and
- parasitic inductance, particularly under fast transient conditions.

Nevertheless, shunt sensors remain widely used because of their structural simplicity and high accuracy. Their performance can, however, degrade when the temperature rises significantly, since thermal effects may alter the resistance value and introduce departure from the assumed linear current–voltage relationship. Under such conditions, the reliability and accuracy of the measurement may be compromised [22].

2.5.2 Magnetic-Field-Based Sensors

Magnetic-field-based sensors infer current by detecting the magnetic field produced around a current-carrying conductor. Their operation is grounded in classical electromagnetic theory. Ampère's circuital law states that the line integral of magnetic field intensity around a closed path is proportional to the enclosed current, while the Biot–Savart law describes the magnetic flux density produced by an elemental current segment at a given observation point. These principles form the theoretical basis of magnetic current sensing technologies [10], [17], [23].

In practical implementations, the sensing element is positioned close to the conductor so that the generated magnetic field can be detected and converted into a proportional electrical signal. Because no direct electrical contact with the conductor is required, magnetic sensors offer galvanic isolation, which is particularly advantageous

in high-voltage environments such as HVDC systems. Common magnetic-field-based sensing technologies include:

- Hall-effect sensors;
- fluxgate sensors; and
- magnetoresistive sensors.

Although these technologies provide electrically isolated and non-intrusive measurement, their use in distributed HVDC monitoring is constrained by factors such as temperature sensitivity, power consumption, limited multiplexing capability, and susceptibility to external magnetic interference [17], [24]. These limitations reduce their suitability for large-scale distributed sensing over long transmission distances.

Hall-Effect Current Sensors

Hall-effect sensors measure magnetic field by exploiting the Hall effect, whereby a transverse voltage is generated when a current-carrying conductive or semiconductive material is subjected to a magnetic field. When the magnetic field intersects the conducting medium, charge carriers experience a Lorentz force, causing them to accumulate on one side of the material and thereby generating a measurable Hall voltage, as illustrated in Fig. 2.9 [25], [26], [27].

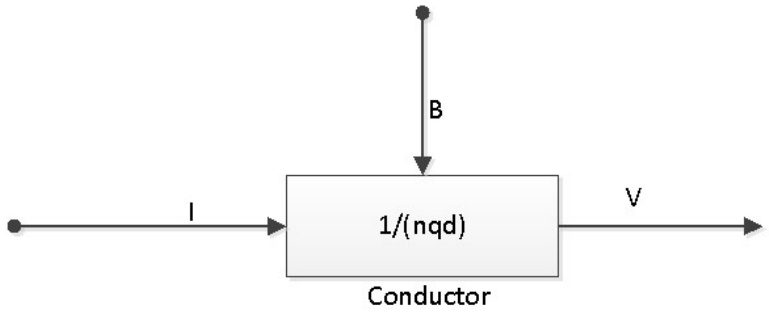

Figure 2.9: Principle of Hall-effect sensor input and output.

The Hall voltage may be expressed as

$$V = \frac{IB}{nqd} \tag{2.1}$$

where B is the magnetic flux density, I is the bias current, n is the charge carrier density, q is the electronic charge, and d is the thickness of the Hall material.

Equation (2.1) shows that the sensor output is directly proportional to magnetic flux density and inversely proportional to charge carrier density and material thickness. This explains why semiconductors, which have relatively low carrier densities, are generally preferred for Hall-effect sensing. Hall-effect sensors are widely used because they offer:

- galvanic isolation;
- the ability to measure both AC and DC current; and
- compact integration into electronic systems.

However, their use in HVDC monitoring is limited by several drawbacks [28]:

- sensitivity to temperature variation;
- offset drift and linearity error;
- susceptibility to electromagnetic interference; and
- limited sensitivity to weak magnetic fields.

Hall-effect current transducers are typically implemented in either open-loop or closed-loop form. In the open-loop configuration, a magnetic core concentrates the flux produced by the primary conductor and guides it across an air gap containing the Hall sensing element. While structurally simple, this arrangement is more vulnerable to magnetic nonlinearity and other error sources. In contrast, the closed-loop configuration uses the Hall sensor output within a feedback loop to drive a compensating current through a secondary winding. This compensating current cancels the magnetic flux generated by the primary current, thereby maintaining an approximately zero-flux operating condition. Such transducers, often referred to as zero-flux current sensors, provide improved linearity, bandwidth, and accuracy relative to open-loop designs [28].

Fluxgate Current Sensors

Fluxgate sensors operate by periodically driving a ferromagnetic core into saturation using an excitation current. In the absence of an external magnetic field, the magnetisation cycle of the core is symmetric. When an external magnetic field is present, this symmetry is disturbed, producing harmonic components in the output signal, particularly the second harmonic, which can be extracted and used to infer the field magnitude [17], [24], [29].

Fluxgate sensors are realised in several configurations, including single-core, dual-core, and multi-core structures. In the single-core arrangement, a single magnetic core is periodically excited into saturation, and the output is derived directly from the resulting nonlinear magnetic response. Although simple, this configuration is more susceptible to offset, excitation asymmetry, and temperature drift.

The dual-core configuration, which is more common in precision sensing, employs two matched cores driven in opposite directions. Under zero external field, the responses of the two cores are symmetric and cancel, thereby reducing offset. When an external field is present, the symmetry is broken, and the resulting second-harmonic component becomes proportional to the measured current. This configuration provides improved linearity, greater sensitivity, and lower offset compared with the single-core arrangement.

In more advanced implementations, three-core or multi-core structures may be used, in which separate magnetic cores are assigned to excitation, sensing, and compensation functions. This functional separation can improve stability, reduce coupling between excitation and sensing paths, and enhance noise immunity, albeit at the expense of increased structural complexity and calibration requirements.

The general operating principle of a closed-loop fluxgate transducer is shown in Fig. 2.10 [17], [24], [29].

In the configuration shown in Fig. 2.10, the primary current I_p produces a magnetic flux in the sensing cores. Excitation windings periodically drive the cores into saturation, while sensing and compensation windings detect and counteract the flux associated with the measured current. The magnetic system contains two principal

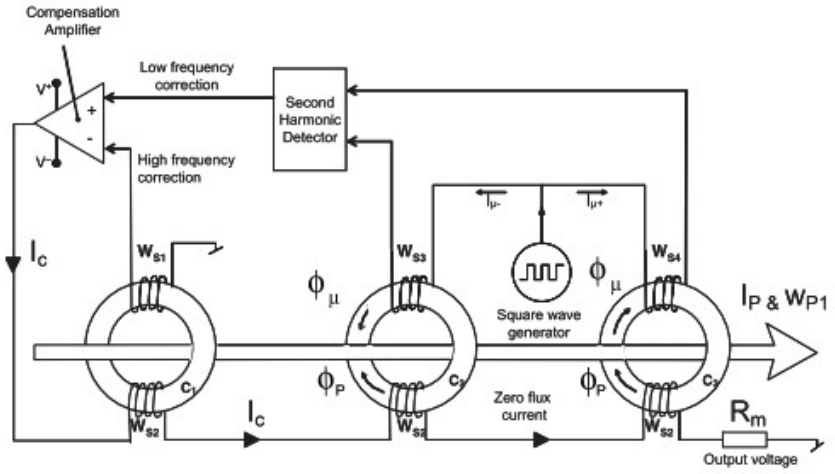

Figure 2.10: Closed-loop fluxgate current transducer [17], [24], [29].

flux components: the excitation-induced flux and the flux generated by the primary current. The latter disturbs the symmetry of the magnetic response and introduces harmonic components in the output signal. A second-harmonic detector extracts the relevant component, and the resulting signal is processed by a compensation amplifier, which drives a compensating current to restore the zero-flux condition. The voltage developed across the measuring resistor is therefore proportional to the compensating current and, by extension, to the primary current [29].

Fluxgate sensors offer several attractive features, including:

- high sensitivity;
- excellent accuracy; and
- low noise performance.

However, they also exhibit important limitations in HVDC monitoring applications [27], [30]:

- relatively high power consumption due to the excitation circuitry;
- bulky sensor structure;
- more complex calibration requirements;

- limited scalability for distributed deployment; and
- sensitivity to temperature variation.

Because continuous excitation current is required to maintain operation, fluxgate sensors are generally unsuitable for low-power or self-powered sensing applications, particularly where distributed monitoring is required along long HVDC cable systems.

Magnetoresistive Sensors

Magnetoresistive (MR) sensors operate by exploiting the change in electrical resistance induced by a magnetic field in a suitably engineered material. This field-dependent resistance change can be used to construct magnetic sensor heads for indirect DC current measurement. The principal forms of MR sensors are anisotropic magnetoresistive (AMR), giant magnetoresistive (GMR), and tunnelling magnetoresistive (TMR) devices.

Anisotropic Magnetoresistive Sensors AMR sensors rely on the change in resistance of a ferromagnetic material as the angle between the direction of current flow and the material magnetisation changes. The applied magnetic field modifies the magnetisation orientation and thereby the measured resistance [31], [32].

Giant Magnetoresistive Sensors GMR sensors typically comprise alternating ferromagnetic and non-ferromagnetic conductive layers. One magnetic layer is held in a fixed orientation, while the other rotates in response to the external magnetic field. The device resistance is lower when the magnetisations are parallel and higher when they are antiparallel, enabling high magnetic sensitivity [32].

Tunnelling Magnetoresistive Sensors TMR sensors are structurally similar to GMR devices, but employ an insulating barrier between ferromagnetic layers, such that electron transport occurs via quantum tunnelling. This structure yields higher resistance variation and typically greater sensitivity than GMR devices [32]. Although

MR sensors offer compactness and high sensitivity, their application in HVDC monitoring remains influenced by temperature dependence, offset drift, magnetic biasing requirements, and long-term stability considerations [33], [34].

Although MR sensors offer compactness and high sensitivity, their application in HVDC monitoring remains influenced by temperature dependence, offset drift, magnetic biasing requirements, and long-term stability considerations [33], [34].

2.5.3 Optical Magnetic-Field Current Sensing Based on the Faraday Effect

Optical magnetic-field sensors commonly operate on the Faraday magneto-optic effect, whereby the plane of polarisation of linearly polarised light rotates as the light propagates through a medium subjected to a magnetic field. This phenomenon arises from magnetically induced circular birefringence, in which the right- and left-circularly polarised components of the optical wave propagate with different phase velocities. The resulting phase difference causes rotation of the overall polarisation state of the transmitted light.

When the light exits the sensing medium and passes through an analyser, this polarisation rotation is converted into a measurable intensity variation, which can then be detected using a photodetector and processed electrically. The rotation angle is proportional to the magnetic field strength and therefore provides a direct means of estimating the current responsible for generating the field [35].

The Faraday-induced optical phase shift may be expressed as

$$\beta = V \int \vec{H} \cdot d\vec{s} \tag{2.2}$$

where V is the Verdet constant of the transmission medium, $\vec{H}$ is the magnetic field intensity, and $d\vec{s}$ is the differential path element vector.

From a physical perspective, the magnetic field modifies the phase velocity of the two circularly polarised components of the optical wave. One component experiences a slight increase in velocity, while the other experiences a corresponding decrease, re-

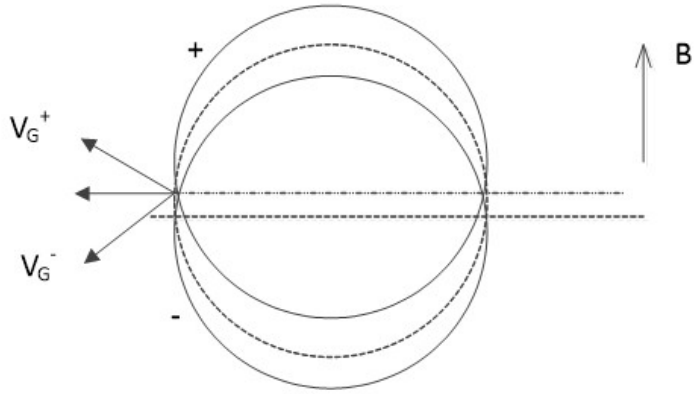

Figure 2.11: Deflection of polarised light under magnetic field [35].

sulting in a net phase difference and hence rotation of the polarisation plane. The corresponding group velocity of the two components may be expressed as [36]

$$v_G^{\pm} = \frac{C_0}{n}\hat{k} \pm \frac{VC_0^2}{\omega n^2}B_0 \tag{2.3}$$

where $v_G^{\pm}$ represents the group velocity of the right- and left-circularly polarised components, C_0 is the speed of light in vacuum, n is the refractive index of the medium, $\hat{k}$ is the unit vector in the direction of propagation, V is the Verdet constant, ω is the angular frequency of the optical wave, and B_0 is the applied magnetic flux density.

Experimental observations reported by Rikken and van Tiggelen confirm that the deflection or rotation of the polarised beam varies with the applied magnetic field, thereby demonstrating the suitability of the Faraday effect for optical magnetic-field sensing in current measurement applications [36].

As illustrated in Fig. 2.12, the beam displacement in the $\mathbf{k} \times \mathbf{B}$ direction can be detected experimentally. By rotating the photodiode assembly by 90° about the propagation direction $\mathbf{k}$, the displacement along the magnetic-field axis can also be resolved.

Another important relationship relevant to optical sensing is the electromagnetic wave propagation expression, which shows that the speed of light in a medium depends

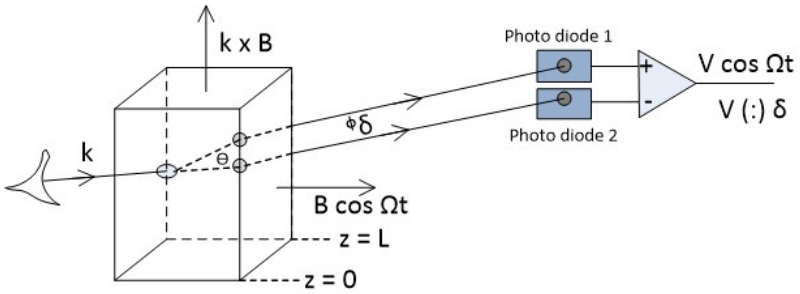

Figure 2.12: Difference between the deflection signal for two different polarisation states [35], [36].

on the electromagnetic properties of that medium:

$$C = \frac{1}{\sqrt{\mu\varepsilon}} \tag{2.4}$$

where C is the speed of light in the medium, μ is the permeability of the medium, and ε is its permittivity.

In practical implementations, Faraday-effect current sensors commonly employ an optical fibre wound around the current-carrying conductor so that the magnetic field generated by the conductor induces a measurable polarisation rotation in the propagating light. This arrangement provides excellent electrical isolation and strong immunity to electromagnetic interference. However, because the sensing fibre typically has to be wound around the conductor, the approach is less suitable for applications requiring embedded sensing within compact cable structures or joints.

2.5.4 Hybrid-Based Current Sensing Methods

Hybrid current sensing methods are based on multi-stage transduction, in which the primary electrical quantity is not measured directly, but inferred through successive conversions across multiple physical domains. This strategy enables complementary sensing mechanisms to be combined in order to overcome the limitations of individual technologies.

At the most fundamental level, current flowing through a conductor gives rise to

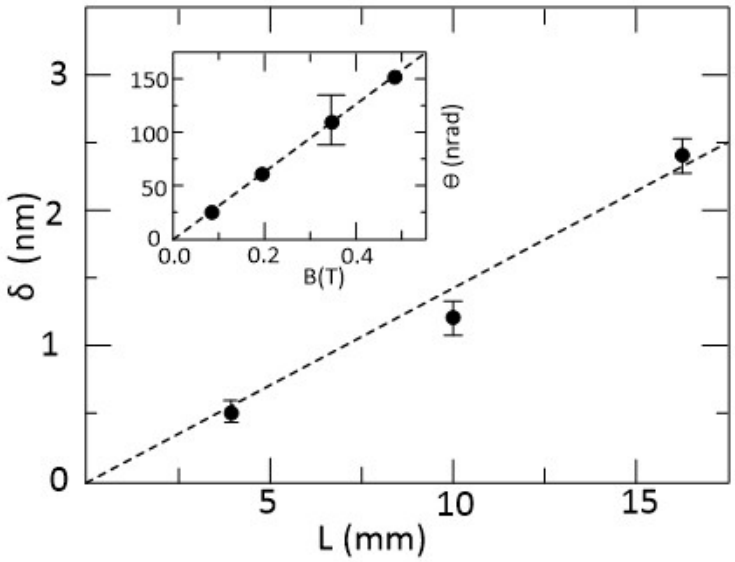

Figure 2.13: Displacement of light particles in response to magnetic field [36].

either:

- a magnetic field, as described by electromagnetic theory; or
- a voltage drop across a known impedance, as in resistive shunt measurement.

Conventional current sensors typically exploit one of these effects in isolation. For example, current transformers and Rogowski coils rely on magnetic coupling, whereas shunt resistors and voltage dividers rely on electrical potential differences. Each of these methods exhibits trade-offs in bandwidth, isolation, linearity, power consumption, and suitability for distributed deployment in high-voltage environments.

Hybrid sensing architectures address these limitations by combining multiple transduction stages within a unified measurement chain. In a typical implementation, a primary stage such as a Rogowski coil, current transformer, or precision shunt converts the current into a proportional electrical signal. This signal is then interfaced with a secondary transduction stage, often involving an optical sensing element such as a fibre Bragg grating (FBG), which converts the electrical response into an optical wavelength shift [17], [37].

In such architectures, the measurement pathway may be expressed conceptually as

$$\begin{aligned} \text{electrical current} &\rightarrow \text{electromagnetic or resistive effect} \\ &\rightarrow \text{electrical signal} \rightarrow \text{mechanical strain} \\ &\rightarrow \text{optical wavelength shift} \end{aligned} \tag{2.5}$$

This layered transduction pathway allows the system to retain the sensitivity of conventional electrical measurement while exploiting the intrinsic advantages of optical sensing, including galvanic isolation, immunity to electromagnetic interference, and suitability for multiplexed and distributed interrogation over long distances.

Hybrid systems can also be configured to combine multiple sensing elements according to the measurement objective. For example, Rogowski coils may be used for wide-band transient detection, current transformers for steady-state measurement accuracy, and optical sensing elements for remote interrogation. Such combinations can improve dynamic range, transient sensitivity, and spatial monitoring capability. Consequently, hybrid sensing methods provide an advanced measurement platform in which current is inferred through coupled physical domains rather than measured directly by a single sensing mechanism. This approach is particularly attractive for HVDC systems, where high operating voltage, fast transients, and the need for distributed monitoring impose stringent sensing requirements.

2.5.5 Voltage Measurement in HVDC

RC Voltage Divider Technique

Voltage measurement using an RC divider is a well-established approach in HVDC systems. In practice, a resistive–capacitive divider is used to provide accurate voltage measurement under both steady-state and transient conditions. The arrangement shown in Fig. 2.14 consists of two divider arms, each formed by a resistor and capacitor in parallel, thereby creating a frequency-dependent impedance network capable of maintaining an approximately constant division ratio over a broad frequency range.

Under steady-state DC conditions, where $\omega \rightarrow 0$, the capacitors behave effectively

as open circuits because

$$Z_C = \frac{1}{j\omega C} \to \infty.$$

The divider therefore reduces to a purely resistive network, and the output voltage becomes

$$V_{\text{out}} = \frac{R_2}{R_1 + R_2} V_{\text{dc}} \tag{2.6}$$

During transient conditions or at high frequency, the capacitive reactance decreases, and the capacitors provide a lower-impedance path. In the limiting high-frequency case, the network behaves as a capacitive divider:

$$V_{\text{out}} = \frac{C_1}{C_1 + C_2} V_{\text{dc}} \tag{2.7}$$

To ensure that the division ratio remains independent of frequency, the time constants of the two divider arms must be matched:

$$R_1 C_1 = R_2 C_2 \tag{2.8}$$

This condition ensures that the impedance ratios of both branches scale identically with frequency, thereby maintaining a consistent voltage division ratio from DC to transient operation.

The time constant $\tau = RC$ of each branch determines the dynamic response of the divider. Physically, it represents the rate at which the capacitor charges or discharges in response to a changing input voltage. A smaller time constant improves transient tracking, whereas a larger time constant generally improves stability and reduces high-frequency sensitivity. The design therefore involves a trade-off between bandwidth and robustness.

In practical HVDC applications, the resistor values are chosen to:

- limit current flow and power dissipation under high-voltage conditions; and
- satisfy insulation coordination and thermal stability requirements.

Once the resistor values are established, the capacitor values are selected to satisfy

the matching condition in (2.8). In addition, capacitor selection is influenced by:

- the required transient response or bandwidth;
- dielectric stability and voltage withstand capability; and
- minimisation of parasitic effects.

The RC divider therefore operates as a frequency-compensated voltage measurement network in which equality of time constants is the key design condition ensuring accurate voltage scaling under both steady-state and dynamic operating conditions **zhang2015measurement**, [17].

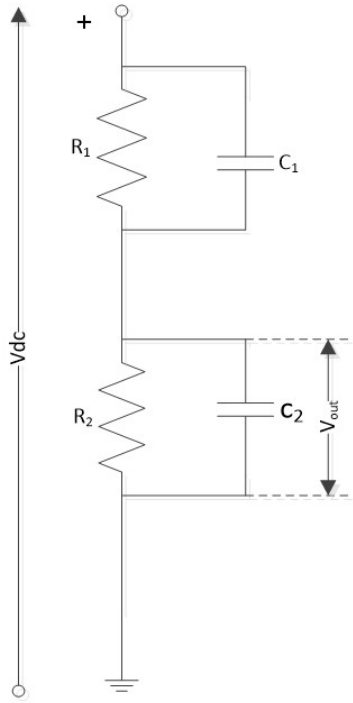

Figure 2.14: RC voltage divider.

In essence, the divider is designed such that $R_1C_1 = R_2C_2$, thereby maintaining frequency-independent voltage scaling, while the associated time constant determines the transient response of the system [17].

Voltage Measurement Using the Pockels Effect

Voltage measurement based on the Pockels effect provides a high-bandwidth, non-intrusive optical technique suitable for both AC and DC power systems. The principle relies on the electro-optic behaviour of certain crystals, such as bismuth germanate (BGO) and lithium niobate ($LiNbO_3$), whose refractive index changes when subjected to an external electric field [17].

When linearly polarised light propagates through such a crystal, the applied electric field induces birefringence, producing a phase retardation between two orthogonal polarisation components aligned with the crystal axes. When the modulated light is subsequently analysed using an optical polariser, the phase difference is converted into a measurable intensity variation. This intensity modulation is directly related to the applied electric field and can therefore be used to reconstruct the voltage waveform over a wide frequency range.

2.6 Comparison of Current Measurement Technologies for HVDC Applications

To assess the suitability of existing current sensing technologies for HVDC monitoring, the principal sensing approaches are compared against key performance criteria, including measurement accuracy, bandwidth, power requirement, galvanic isolation, and suitability for distributed deployment. Table 2.1 summarises the relative characteristics of the major current sensing technologies used in HVDC applications.

Table 2.1: Comparison of current sensing technologies for HVDC applications

Technology	**Measurement Principle**	**DC Capability**	**Accuracy**	**Power Requirement**	**Suitability for Distributed HVDC Monitoring**
Shunt Resistor [21], [22], [24]	Ohm's law (voltage drop)	Excellent	Very High	Very Low	Moderate suitability; limited by lack of isolation and thermal constraints
Hall Effect [32], [38]	Lorentz force / Hall voltage	Good	Moderate	Moderate	Limited scalability due to power requirement and susceptibility to interference
Fluxgate [32], [38]	Magnetic core saturation detection	Excellent	Very High	High	Poor suitability for distributed systems due to high power consumption and complexity
Magnetoresistive	Resistance variation under magnetic field	Good	Moderate	Low–Moderate	Limited applicability due to temperature sensitivity and stability concerns
Optical (Faraday) [17], [39]	Magneto-optic rotation	Excellent	High	Very Low	Highly suitable for distributed monitoring due to isolation and multiplexing capability
Hybrid (Shunt + LVT)	Multi-stage transduction (electrical to optical)	Excellent	High	Very Low	Very high suitability for distributed HVDC monitoring with enhanced performance

From Table 2.1, it is evident that conventional magnetic-field-based sensors, such as Hall-effect and fluxgate devices, provide galvanic isolation and acceptable measurement performance, but their dependence on electrical power supply, limited multiplexing capability, and susceptibility to electromagnetic interference restrict their suitability for large-scale distributed HVDC monitoring. By contrast, optical sensing technologies offer intrinsic electrical isolation, immunity to electromagnetic interference, and the ability to support remote multiplexed interrogation over long distances. These characteristics make optical sensing particularly attractive for distributed HVDC monitoring and motivate the sensing approach developed in this research.

2.7 Limitations of Existing Current Sensing Technologies in HVDC Systems

Building on the comparative assessment presented earlier, this section highlights the practical limitations associated with currently available HVDC current-sensing methods. In contrast to conventional AC networks, HVDC protection requires significantly faster response times and often higher measurement fidelity. Fault detection and isolation in HVDC systems must typically be achieved within approximately 10 ms or less to minimise equipment damage and maintain system stability [40], [41]. Achieving reliable measurement over long transmission distances under such constraints remains challenging for conventional sensing technologies.

Over recent decades, several DC current sensing methods have been developed, including resistive shunts and magnetic-field-based sensors such as Hall-effect and fluxgate devices. While magnetic sensors are widely adopted because they provide galvanic isolation, shunt-based sensors generally offer superior linearity, wider bandwidth, and potentially higher measurement accuracy [37], [41].

Recent advances in Hall-effect technology have extended the operational temperature range and measurement capability of such devices, with some sensors operating over ranges such as $-40\,^{\circ}\mathrm{C}$ to $150\,^{\circ}\mathrm{C}$ while supporting substantial current levels [42], [43], [44]. However, these devices typically require a continuous electrical supply

current, making them unsuitable for low-power or self-powered distributed sensing applications. In addition, their reliance on electrical output wiring limits long-distance remote interrogation and prevents efficient multiplexing, thereby restricting scalability in distributed HVDC monitoring.

Fluxgate sensors provide high sensitivity and excellent accuracy, but they also present significant practical limitations in HVDC applications. These sensors require dedicated excitation circuitry to periodically drive the magnetic core into saturation, leading to increased power consumption and added circuit complexity [27], [45], [46]. Their comparatively bulky structure and dependence on local electronic conditioning further reduce their suitability for compact, embedded, or widely distributed measurement architectures. As with Hall-effect devices, they also lack inherent multiplexing capability and require dedicated wiring for each sensor.

Hybrid configurations, such as Rogowski coil–LVT or current transformer–LVT arrangements, can provide useful information during transient conditions. However, because these devices fundamentally respond to time-varying current, they are not well suited to accurate steady-state DC current measurement. Their use in HVDC systems is therefore largely confined to transient detection rather than continuous monitoring and control.

These limitations highlight the need for an alternative sensing technology capable of simultaneously providing high accuracy, low power consumption, galvanic isolation, and remote multiplexed interrogation over long distances. Addressing these requirements is essential for improving observability and enabling distributed monitoring in HVDC networks.

The advantages and limitations of the currently available DC current measurement technologies are summarised in Table 2.2, which provides a comparative overview of their operating principles, performance characteristics, and suitability for HVDC applications.

Table 2.2: Detailed comparison of current sensing technologies for HVDC applications

Sensor Type	**Principle**	**Current Type**	**Range**	**Bandwidth**	**Sensitivity**	**Merits**	**Limitations**
Shunt	Ohm's law	AC/DC	mA–kA	Up to several MHz	Depends on resistance	Simple, highly accurate, reliable for large current measurement [21], [22]	No galvanic isolation, power dissipation, parasitic inductance, limited high-frequency performance [28]
Hall Effect	Galvanomagnetic effect	AC/DC	A–kA	DC to hundreds of kHz	Low	Direct AC/DC measurement, fast response, easy integration [25], [26]	Temperature drift, low sensitivity to weak fields, limited precision, EMI susceptibility [38]
Fluxgate	Core saturation / harmonic detection	AC/DC	mA–kA	DC to few kHz	High	High accuracy, excellent sensitivity, low noise [30]	High power consumption, bulky structure, complex design, limited high-frequency capability [45]
Rogowski Coil	Faraday's law of induction	AC only	A–MA	Several MHz	High	Excellent for high-frequency measurement, no saturation, lightweight, flexible [24]	Cannot measure DC, low output signal, requires integration circuitry [17]
AMR	Magnetoresistance	AC/DC	mA–kA	DC to tens of MHz	Moderate	Low power consumption, compact, suitable for low to moderate fields [31]	Temperature sensitivity, nonlinearity at high field [33]
GMR	Magnetoresistance	AC/DC	mA–kA	DC to MHz	High	High sensitivity, suitable for weak fields, wide dynamic range [31], [32]	Complex fabrication, higher power consumption [33]
TMR	Tunnelling magnetoresistance	AC/DC	nT–mT	DC to few MHz	Very High	Extremely high sensitivity, high SNR, low power [34]	Temperature sensitivity, limited field range, higher cost [32]
Optical Fibre	Faraday effect	AC/DC	kA–MA	DC to MHz	High	EMI immunity, electrical isolation, wide bandwidth, long-distance interrogation [41], [47]	Temperature sensitivity, fragile optical components [39]

Table 2.2 shows that, although several technologies can measure DC current with reasonable performance, none of the conventional sensing methods simultaneously satisfy the principal requirements of modern HVDC monitoring systems, namely low power consumption, multiplexing capability, galvanic isolation, and suitability for distributed deployment over long cable distances. Magnetic-field-based sensors, such as Hall-effect and fluxgate devices, require continuous electrical power and dedicated wiring, which limits their scalability for wide-area monitoring. Shunt-based methods, although highly accurate, require direct electrical contact and introduce thermal dissipation and insulation challenges. These limitations motivate the investigation of alternative sensing approaches that can provide accurate, low-power, and distributed measurements for HVDC networks.

The sensing architecture proposed in this thesis addresses these limitations through the integration of optical sensing techniques, which provide immunity to electromagnetic interference and enable remote multiplexed interrogation.

2.8 Summary

This chapter has reviewed the principal technologies underpinning HVDC transmission systems, with particular emphasis on converter technologies, transmission media, protection requirements, and sensing approaches relevant to current and voltage measurement. The distinctive behaviour of HVDC systems, notably the absence of natural current zero-crossings and the rapid rise of fault current, has been highlighted to establish the stringent requirements placed on protection-oriented measurement systems.

A critical assessment of existing current sensing technologies has been presented, including resistive shunts, magnetic-field-based sensors such as Hall-effect and fluxgate devices, optical sensing methods based on the Faraday effect, and hybrid measurement architectures. Resistive shunts were shown to provide high linearity and wide bandwidth, but to require careful thermal management and electrical integration. Magnetic-field-based sensors provide galvanic isolation and mature industrial implementation, but remain constrained by temperature drift, excitation requirements, local

power dependency, and limited scalability for distributed deployment. Optical sensing approaches were identified as particularly promising for HVDC monitoring because of their immunity to electromagnetic interference, galvanic isolation, and suitability for remote multiplexed interrogation.

Overall, the analysis in this chapter demonstrates that no conventional sensing technology fully satisfies the combined requirements of high bandwidth, low power consumption, scalability, and distributed deployment in HVDC networks. This gap motivates the hybrid optical sensing approach developed in this thesis.

This chapter therefore establishes the technical foundation and justification for the sensing architecture presented in the subsequent chapters, where the limitations identified here are addressed through the integration of a resistive shunt, optical transduction, and low-power signal conditioning techniques.

Chapter 2 References

[1] M. Eremia, C. Liu, and A. Edris, *Advanced Solutions in Power Systems: HVDC, FACTS, and Artificial Intelligence*. IEEE-Wiley, 2016.

[2] A. Stan, S. Costinas, and G. Ion, "Overview and assessment of hvdc current applications and future trends," *Energies*, vol. 15, no. 3, 2022. DOI: 10.3390/en15031193.

[3] D. V. Hertem, O. Gomis-Bellmunt, and J. Liang, *HVDC Grids*. IEEE-Wiley, 2016.

[4] G. Mazzanti, "High voltage direct current transmission cables to help decarbonisation in europe," *IET High Voltage*, vol. 7, no. 4, 2022. DOI: 10.1049/hve2.12222.

[5] M. Rashwan, *Status and trends of hvdc*, CIGRE, 2016.

[6] Siemens Energy, *High voltage direct current transmission: Proven technology for power exchange*, [Online]. Available: https://www.siemens-energy.com, 2024.

[7] B. E. Nygaard, H. Agustsson, and L. A. Moen, "Monitoring and forecasting ice loads on transmission lines," in *CIGRE*, 2016.

[8] B. Thorsteinsson, K. Halsan, M. Abraha, and P. Hagen, "Design of a 525 kv hvdc line in norway," in *CIGRE*, 2016.

[9] M. Ardelean, *Hvdc submarine power cables state-of-the-art*, 2015. DOI: 10.2790/023689.

[10] Y. Zhang, X. Xiao, and X. Yan, "Measurement technologies of dc high voltage," *IEEE*, 2015.

[11] J. Laninga et al., "Monitoring technologies for hvdc transmission lines," *Energies*, vol. 16, no. 13, 2023. DOI: 10.3390/en16135085.

[12] Prysmian, *Extruded cables for hvdc power transmission*, 2024.

[13] J. V. Rossum et al., "Hpte insulation for mv cables," in *CIRED*, 2019.

[14] Prysmian, *Extruded cables for hvdc power transmission*, 2024.

[15] SSEN, *Hvdc technology capability*, 2018.

[16] W. Leterme and D. V. Hertem, "Classification of fault clearing strategies for hvdc grids," in *CIGRE*, 2015.

[17] D. Tzelepis et al., "Voltage and current measuring technologies for hvdc supergrids," *IEEE Access*, vol. 8, 2020. DOI: 10.1109/ACCESS.2020.3035905.

[18] IEC, *Iec 61869-9*, 2019.

[19] V. Csutar et al., *Hvdc architecture and protection*, 2021.

[20] ENTSO-E, *Hvdc grid code requirements*, 2016.

[21] D. W. Braudaway, "Behavior of resistors and shunts," *IEEE Transactions on Instrumentation and Measurement*, vol. 48, no. 5, 1999.

[22] P. Piekielny, "Current shunt measurement," *Sensors*, 2021.

[23] W. H. Hayt, *Engineering Electromagnetics*. McGraw-Hill, 2010.

[24] S. Ziegler, "Current sensing techniques," *IEEE Sensors Journal*, 2009.

[25] A. Karsenty, "Review of hall effects," *Sensors*, 2020. DOI: 10.3390/s20154163.

[26] M. Crescentini, "Hall-effect current sensors," *IEEE Sensors Journal*, 2022.

[27] Danisense, *Ds200id current transducer datasheet*, 2022.

[28] Texas Instruments, "Shunt resistor and hall-effect current-sensing solutions," *Application Report*, 2019.

[29] LEM, *Lem isolated current and voltage transducers*, Datasheet, pp. 28–31. [Online]. Available: https://www.lem.com, 2020.

[30] S. Wei, "Fluxgate sensors review," *Sensors*, 2021.

[31] L. Jogschies, "Magnetoresistive sensors," *Sensors*, 2015.

[32] Z. Yang, "Magnetoresistive sensors review," *Journal of Low Power Electronics*, 2024.

[33] M. Vopalensky et al., "Magnetoresistive current sensors," *Sensors*, 2013.

[34] C. Lei et al., "Tunnelling magnetoresistive sensors: Principles and applications," *Sensors*, 2022.

[35] B. A. van Tiggelen, "Manipulating light with magnetic field," *Physics Reports*, 2002.

[36] G. Rikken, "Optical energy flow in magnetic field," *Physical Review Letters*, 1997.

[37] A. Amiolemen, "Photonic current sensor for hvdc," in *Conference Proceedings*, 2024.

[38] M. Paun, "Hall effect sensor analysis," *Sensors*, 2013.

[39] M. O'Dwyer, "Thermal effects in fbg," *Measurement Science and Technology*, 2004.

[40] M. Muniappan, "Hvdc fault protection," *Springer*, 2021.

[41] A. Amiolemen, "Self-powered optical current sensor," *IEEE Sensors Letters*, 2023.

[42] Infineon Technologies, *Tle4906 hall-effect sensor datasheet*, [Online; accessed 02-Apr-2024], 2020. [Online]. Available: https://www.infineon.com.

[43] Allegro Microsystems, *Hall-effect current sensor ics*, [Online; accessed 02-Apr-2024], 2022. [Online]. Available: https://www.allegromicro.com.

[44] Texas Instruments, *Tmag5124 linear hall-effect sensor datasheet*, [Online; accessed 02-Apr-2024], 2023. [Online]. Available: https://www.ti.com.

[45] S. Tang, "Fluxgate sensor excitation," *Sensors and Actuators A*, 2004.

[46] P. Ripka, "Advances in fluxgate sensors," *Sensors and Actuators A: Physical*, vol. 106, no. 1–3, pp. 8–14, 2003. DOI: 10.1016/S0924-4247(03)00258-9.

[47] Y. Zhang et al., "Optical fibre dc sensor for hvdc," *Measurement and Control*, 2016. DOI: 10.1177/0142331215575420.

Chapter 3

HVDC Transmission and Fault Characteristics

3.1 HVDC Transmission

This chapter examines the fundamental characteristics of HVDC transmission systems, with particular emphasis on fault behaviour, detection, and protection requirements. The discussion begins with an overview of HVDC technology and its advantages over conventional AC systems, followed by an analysis of the operational challenges introduced by DC fault dynamics, which underpin the need for fast and reliable protection mechanisms.

High-Voltage Direct Current (HVDC) transmission has emerged as a critical technology in modern power systems due to its superior technical and operational performance relative to conventional alternating current (AC) transmission. Key advantages include higher power transfer capability per conductor, reduced transmission losses over long distances, elimination of reactive power flow, absence of steady-state skin effect, and the ability to interconnect asynchronous networks. In addition, HVDC systems provide precise, independent control of power flow, thereby improving system stability and operational flexibility. These characteristics make HVDC particularly suitable for long-distance bulk power transmission, cross-border interconnections, and large-scale

integration of renewable energy resources, thereby supporting global decarbonisation and Net Zero objectives.

Electric power generation is inherently AC-based; therefore, HVDC transmission requires power conversion at both terminals of the link. This conversion is achieved using converter stations comprising power electronic converters, either line-commutated converters (LCCs) or voltage source converters (VSCs), along with associated control, protection, and auxiliary systems. Depending on environmental and geographical constraints, HVDC transmission can be implemented using overhead lines or underground/subsea cables. Underground and subsea cables are particularly preferred in densely populated regions and offshore wind applications where overhead lines are impractical.

Figure 3.1: German HVDC transmission projects supporting large-scale renewable energy integration [1].

The deployment of HVDC cable systems has increased significantly in recent years, particularly for connecting remote renewable generation sites to load centres. A notable example is the German HVDC transmission programme, which includes major projects such as A-Nord (300 km), SuedLink (580 km), and SuedostLink (270 km), with a combined transmission capacity of approximately 5 GW. These developments form part of a broader strategy to expand renewable generation capacity towards approximately 70 GW by 2050.

Despite these advantages, HVDC systems introduce distinct operational and protection challenges. In contrast to AC systems, HVDC networks lack natural current zero crossings, leading to rapid fault-current rise and sustained fault conditions. Consequently, protection systems must operate within stringent time constraints to prevent equipment damage and ensure system stability.

3.2 Rationale for HVDC Transmission

Although AC transmission systems, particularly ultra-high-voltage (UHV) AC systems ($\geq$1000 kV), remain widely deployed, several inherent limitations limit their effectiveness for long-distance and cable-based transmission.

HVDC transmission exhibits lower losses over long distances because it is not affected by skin and proximity effects, which increase the effective resistance in AC conductors. Furthermore, AC cable systems are constrained by capacitive charging currents, which increase with cable length and significantly reduce usable transmission capacity. In contrast, HVDC cables do not suffer from charging current limitations, making them more suitable for long-distance underground and subsea applications [2].

AC systems also require continuous reactive power compensation to account for line inductance and capacitance. This necessitates additional infrastructure such as shunt reactors, series capacitors, and FACTS devices, increasing system complexity and cost. HVDC transmission eliminates reactive power flow along the line, enabling more efficient utilisation of transmission corridors.

Additionally, HVDC systems provide direct control of active power, thereby im-

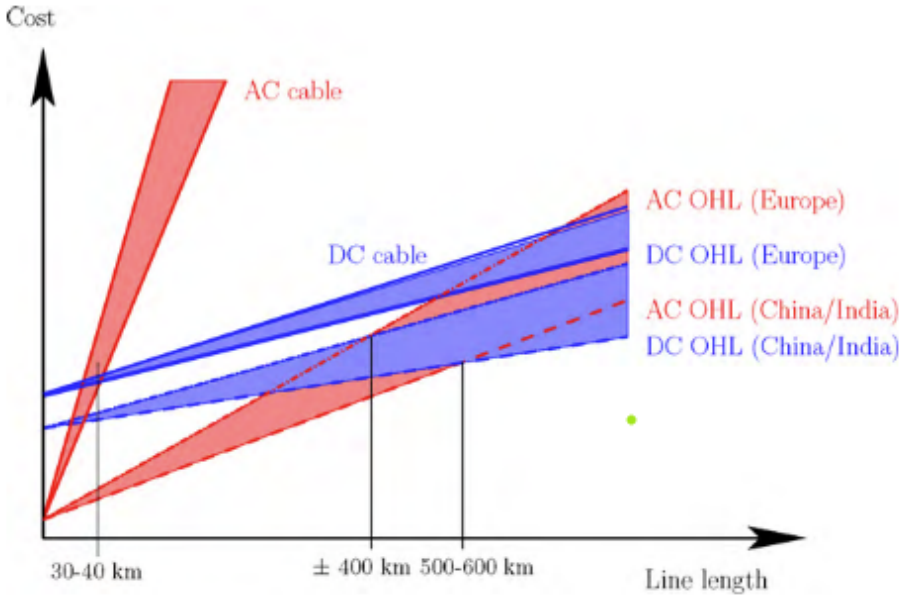

Figure 3.2: Comparative cost and distance characteristics of AC and DC transmission systems [3], [4].

proving stability, enhancing controllability, and enabling seamless interconnection of asynchronous grids [5]. These capabilities are particularly important for integrating variable renewable energy sources such as offshore wind.

From a non-technical perspective, HVDC cables offer reduced visual impact and lower electromagnetic emissions, facilitating deployment in environmentally sensitive and densely populated regions.

The economic viability of HVDC relative to AC depends on transmission distance. Typically, the break-even distance is approximately 50–100 km for cable systems and 400–600 km for overhead lines. Beyond these distances, HVDC becomes more cost-effective.

Future power systems are therefore expected to adopt hybrid AC/DC architectures, leveraging the advantages of both technologies as required.

3.3 Fault Characteristics in HVDC Systems

Fault currents in HVDC systems rise extremely rapidly following fault inception, typically reaching several kiloamperes within a few milliseconds and, in some cases, exceeding 20 kA within 10–20 ms [6], [7]. Unlike AC systems, DC fault currents are non-periodic and do not exhibit natural zero crossings, resulting in sustained fault conditions unless actively interrupted.

The rapid rise and sustained nature of fault current impose severe electrical and thermal stress on converters, cables, and associated equipment. Consequently, fault detection and isolation must be achieved within approximately 5–10 ms to prevent equipment damage.

Although DC current distribution is uniform under steady-state conditions, transient fault behaviour is influenced by network inductance, resistance, and distributed capacitance. The total fault energy, contributed by DC-link capacitors and cable capacitance, can be substantial, further increasing system vulnerability [8], [9].

These characteristics necessitate high-speed, high-resolution sensing and measurement systems to enable rapid fault detection, accurate localisation, and effective protection.

3.4 Fault Evolution in HVDC Systems

Faults in HVDC systems can originate from either the AC side or the DC side of the converter. AC-side faults resemble conventional AC disturbances and may lead to commutation failure in LCC systems. In contrast, DC-side faults are more severe, particularly in VSC systems.

The evolution of a pole-to-pole DC fault is typically described in three stages:

3.4.1 Capacitor Discharge Stage

Immediately following fault inception, energy stored in the DC-link capacitor and cable capacitance is rapidly discharged into the fault. Due to the low impedance path [10],

the rate of rise of current (di/dt) can reach several kA/ms. This stage produces the highest peak current and represents the most critical period for converter protection.

3.4.2 Diode Freewheeling Stage

Following voltage collapse, current continues to flow through anti-parallel diodes within the converter. The current is sustained by inductive energy stored in the network and decays gradually depending on the system resistance and inductance [11]. This stage prolongs fault current flow and increases thermal stress on system components.

3.4.3 Grid Feeding Stage

In this stage, the AC grid contributes to the fault current while converter switching devices are blocked. The converter behaves as an uncontrolled rectifier [12], sustaining fault current at a quasi-steady-state level. Without prompt intervention, this stage can result in severe damage to equipment [12], [13], [14].

3.5 Fault Detection Strategies

Due to the rapid evolution of DC faults, detection systems must operate within 1–3 ms, with full fault interruption achieved within 5–10 ms. Although advancements in converter technologies, such as modular multilevel converters (MMCs), have improved fault response through mechanisms including converter blocking, capacitor isolation, and suppression of diode conduction [15], these measures do not eliminate the requirement for detection systems capable of operating within sub-millisecond to a few millisecond time scales

Several fault detection techniques have been proposed:

3.5.1 Voltage Derivative Methods

These methods detect faults based on rapid changes in voltage and current:As the fault-induced signal travels along the line, the initially elevated current signal gradually attenuates, while the decayed voltage signal begins to recover proportionally. To

quantify this behaviour, the DC voltages are measured, and their magnitude are computed. A weighted sum of these derivatives is then evaluated against a predefined variance threshold. If the calculated variance exceeds the threshold, the protection mechanism is triggered [16].

$$w = C_1 \frac{dv}{dt} + C_2 \frac{di}{dt} \tag{3.1}$$

Although simple, these methods are sensitive to noise and variations in system parameters, which can compromise detection accuracy. These factors may lead to false positives or erroneous protection system operations, thereby reducing its reliability under fault conditions.

3.5.2 Travelling Wave Methods

The occurrence of transient traveling waves, originating from fault inception points or other locations along DC transmission lines, induces voltage spikes at sections of the HVDC network that are inductively terminated. These spikes cause deviations from the nominal system voltage [16]. Travelling wave-based methods utilise electromagnetic wave propagation along the line:

$$v(x,t) = f_f(t - x/c) + f_r(t + x/c) \tag{3.2}$$

$$i(x,t) = \frac{1}{Z_0} \left[f_f(t - x/c) + f_r(t + x/c) \right] \tag{3.3}$$

The high frequency oscillations generated by system perturbations are inherently attenuated over time and eventually decay [12], [17], [18]. Utilization of the traveling wave method entails observing the voltage at the inductively terminated sections of the line, which becomes a function of the line impedance and current at that specific location. However, this method exhibits several vulnerabilities. Signal-detection accuracy can be compromised by variations in system impedance, and it is less effective at detecting close-in faults. Additionally, the method is susceptible to external noise, which

further impacts its reliability in fault detection and protection within HVDC networks. While travelling-wave-based fault detection offers potential benefits for identifying disturbances over long transmission distances, its sensitivity to impedance variations and inherent noise susceptibility limit its application [12], [16], particularly in scenarios where precise and rapid fault location is critical. These limitations underscore the need for more robust techniques or complementary protection strategies to ensure the reliability and safety of HVDC systems.

3.5.3 Current Differential Protection

This method compares current measurements at both ends of the transmission line. This approach is conceptually straightforward and demonstrates effectiveness in detecting both internal and external faults by analysing the signal polarity. However, a major limitation is its reliance on sensors installed at the cable's terminal ends. This dependency introduces a time lag due to the propagation of travelling-wave signals through the cable, thereby delaying fault detection and subsequent mitigation.

3.5.4 Natural Frequency Methods

Faults introduce frequency components into an otherwise DC signal. Detection is based on identifying deviations from steady-state behaviour. This technique offers a more direct method of fault detection. It provides a potentially efficient means of fault detection in HVDC systems by focusing on the presence of unintended frequency components [19], [20]. However, its sensitivity to these components can make it susceptible to noise, which could be misinterpreted as a fault.

3.6 Fault Mitigation Strategies

Fault clearing strategies in HVDC systems are classified into three categories according to CIGRE WG B4/B5.59:

- Fully selective

- Partially selective
- Non-selective

3.6.1 Fully Selective Protection

Fully selective protection isolates only the faulted section of the network, allowing the remainder of the system to continue operating. This approach is particularly suitable for multi-terminal DC (MTDC) systems, where maintaining system availability is critical. The strategy is further segmented into different categories based on system topology and the components employed, as summarised in Table 3.1 [15], [21]. This approach is particularly suited to multi-terminal HVDC (MTDC) networks, where multiple lines and interconnections enable selective isolation while maintaining continuity of supply in healthy sections.

Table 3.1: Fully Selective Fault Clearing Strategies [21]

Fault Clearing Strategy	**Limiting Device**	**Breaking Device**
Fully selective fault clearing with power electronic breakers	Inductor / None	Power electronic breakers
Fully selective fault clearing with hybrid DC circuit breakers	Inductor	HDCCB
Fully selective fault clearing with unidirectional DC circuit breakers	Inductor	HDCCB
Fully selective fault clearing with mechanical DC circuit breakers	Inductor	MDCCB
Fully selective fault clearing with SFCL and mechanical circuit breakers	SCFCL	MDCCB

3.6.2 Non-Selective Protection

In a non-selective fault-clearing strategy, the entire HVDC grid is treated as a single protection zone. Upon fault detection, all converters and associated AC-side circuit breakers are tripped, resulting in a complete system shutdown. Consequently, both

healthy and faulty sections of the network are disconnected simultaneously.

This approach is typically implemented using AC circuit breakers located on the AC side of converter stations. While the strategy is relatively simple and does not require complex coordination, it is unsuitable for multi-terminal HVDC (MTDC) systems, as it results in a total loss of power transfer and poor system availability. Furthermore, it does not provide fault localisation capability.

The classification of non-selective strategies based on system configuration and component arrangement is summarised in Table 3.2 [21].

Table 3.2: Non-Selective Fault Clearing Strategies [21]

Fault Clearing Strategy	**Limiting Device**	**Breaking Device**
Non-selective fault clearing with AC circuit breakers	None	AC circuit breaker and HSS
Open grid configuration	Inductor	HDCCB
Non-selective with full-bridge MMC	None	MMC FB and HSS
Non-selective with DCCB at converter terminals	Inductor / None	MDCCB / HDCCB
Non-selective fault clearing with SFCL at converter terminals	SCFCL	MDCCB

3.6.3 Partially Selective Protection

Partially selective protection divides the HVDC grid into a limited number of protection zones. When a fault occurs, only the affected zone is isolated, while the remaining sections of the network continue operation.

This approach improves system availability relative to non-selective strategies by confining the fault impact to a specific region. However, it does not achieve full selectivity at the individual line or bus level. The segmentation of protection zones is determined by system topology and economic considerations, particularly the cost of DC circuit breakers (DCCBs) and associated infrastructure [21], [22].

Table 3.3: Partially Selective Fault Clearing Strategies [21]

Fault Clearing Strategy	**Limiting Device**	**Breaking Device**
Grid splitting with DC/DC converters	None	DC/DC converter and HSS
Grid splitting with hybrid DCCB and HSS	Inductor	HDCCB and HSS

The classification of partially selective strategies is presented in Table 3.3 [21].

3.6.4 Limitations of Existing Protection Strategies

The selection of fault detection and isolation strategies in HVDC systems is strongly influenced by system configuration and economic constraints. Although grid-level or zonal protection reduces implementation cost, it compromises selectivity and may result in unnecessary disconnection of healthy sections.

A fundamental limitation of existing HVDC protection schemes, whether fully selective, partially selective, or non-selective, is their reliance on measurements obtained at converter terminals. As a result, fault detection is inherently dependent on the time required for disturbance signals to propagate along the transmission line.

This dependency is governed by the distributed inductance–capacitance (LC) parameters of the line, which define the propagation velocity of electromagnetic waves. In long-distance HVDC cable systems, particularly subsea cables with high capacitance, this propagation delay becomes significant.

Conventional detection techniques, including voltage-derivative methods, travelling-wave analysis, frequency-domain approaches, and current differential protection, share a common constraint: fault identification is possible only after the disturbance reaches the measurement location. Consequently, detection speed is fundamentally limited by line propagation characteristics.

In addition to propagation delay, signal attenuation and distortion further degrade measurement fidelity, reducing the reliability of fault detection. These limitations are particularly critical in HVDC systems, where protection must operate within a time

frame of approximately 1–10 ms.

To address these challenges, there is a need for alternative sensing strategies that provide localised measurements and operate independently of line propagation effects. Such approaches have the potential to significantly reduce detection latency, enhance fault localisation accuracy, and improve overall system reliability.

A comparative summary of the principal HVDC fault detection techniques and their associated limitations is presented in Table 3.4. The comparison highlights that most conventional approaches are fundamentally constrained by their dependence on signal propagation and terminal-based measurements, which introduce inherent detection delays.

To further quantify the impact of propagation delay on fault detection performance, Table 3.5 presents typical signal travel times for HVDC transmission lines of varying lengths.

Using the distributed-parameter line values of $L = 1.35$ mH/km and $C = 0.16$ μF/km, the propagation velocity in the HVDC cable is approximately 6.80×10^7 m/s, which is substantially lower than the propagation velocity in optical fibre, taken here as approximately 2.00×10^8 m/s. Table 3.5 compares the corresponding signal travel times over representative transmission distances.

The results presented in Table 3.5 demonstrate that fault-induced disturbances require several milliseconds to propagate along long HVDC transmission lines before reaching terminal measurement points. For example, in a 500 km HVDC link, the propagation delay alone can reach approximately 2.5 ms, which represents a significant proportion of the total allowable protection response time (typically 5–10 ms).

This inherent delay places a fundamental limitation on terminal-based protection schemes, as fault detection cannot occur until the disturbance signal arrives at the sensing location. Furthermore, additional delays associated with signal processing, filtering, and decision-making further increase the overall response time.

Consequently, the reliance on propagation-based detection methods constrains the achievable speed of HVDC protection systems. This limitation becomes more pronounced in long-distance cable systems, where higher capacitance further influences

Table 3.4: Comparison of HVDC fault detection methods and their limitations

Method	**Operating Principle**	**Typical Detection Time**	**Key Limitations**
Voltage Derivative Method	Detects rapid changes in dv/dt and di/dt during fault inception	∼1–3 ms	Highly sensitive to noise and system parameter variations; threshold selection is non-trivial; limited robustness under varying operating conditions [12], [23]
Travelling Wave Method	Detects fault-generated wavefronts propagating along the transmission line	$<$ 1 ms (signal level) but decision delayed by propagation	Dependent on line propagation velocity; requires high sampling rate; sensitive to attenuation, reflections, and noise; reduced accuracy for close-in faults [23], [24]
Current Differential Protection	Compares current measurements at both ends of the line via communication links	∼2–5 ms	Requires reliable high-speed communication; susceptible to latency and data loss; high implementation cost; limited scalability for MTDC systems [7], [25]
Frequency-Domain / Signal Processing (WT, ST, EMD)	Analyses transient frequency components introduced by faults	∼3–10 ms	Computationally intensive; requires signal windowing and decomposition; sensitive to noise; performance depends on signal quality and parameter tuning [26], [27], [28]
Natural Frequency Method	Detects abnormal frequency components in DC signal	∼2–5 ms	Susceptible to noise; may misinterpret switching harmonics; limited reliability in complex network conditions [19], [29]
Distributed Sensing (Proposed)	Localised measurement of electrical quantities along the cable infrastructure	$<$ 1 **ms (local detection)**	Requires deployment of distributed sensors; integration and synchronisation complexity; however, eliminates propagation delay limitation [13]

Table 3.5: Comparison of propagation delay in HVDC cable and optical fibre

Length (km)	**HVDC Velocity (10^7 m/s)**	**HVDC Delay (ms)**	**Fibre Velocity (10^8 m/s)**	**Fibre Delay (ms)**
50	6.80	0.735	2.00	0.250
100	6.80	1.470	2.00	0.500
200	6.80	2.939	2.00	1.000
300	6.80	4.409	2.00	1.500
500	6.80	7.348	2.00	2.500
1000	6.80	14.697	2.00	5.000

signal propagation characteristics.

These observations reinforce the need for localised sensing approaches that are capable of detecting faults independently of line propagation effects. By enabling measurements closer to the point of fault inception, distributed sensing can significantly reduce detection latency and improve the overall responsiveness of HVDC protection systems.

3.7 DC Circuit Breakers and Fault Interruption

HVDC circuit breakers (DCCBs) are essential components for interrupting fault currents in DC networks. Unlike AC systems, where natural current zero crossings facilitate interruption, DC fault interruption requires the active generation of a counteracting voltage.

A DCCB typically consists of three functional branches:

- Continuous current branch (normal operation)
- Commutation branch (current transfer during interruption)
- Energy absorption branch (dissipation of stored energy)

The operational structure of a DCCB is illustrated in Fig. 3.3, while a typical circuit configuration is shown in Fig. 3.4 [30].

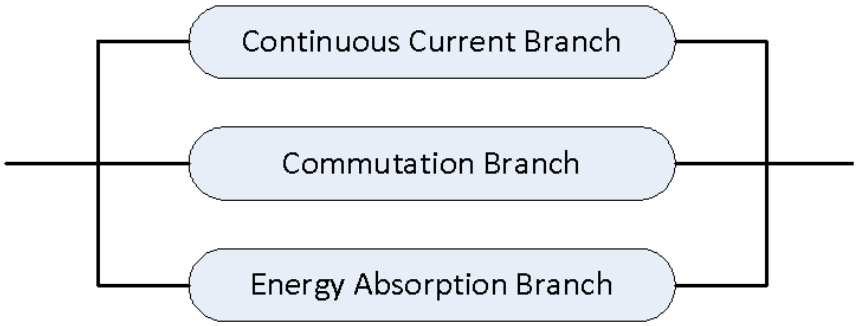

Figure 3.3: Functional branches of a DC circuit breaker illustrating the current conduction, commutation, and energy absorption paths [30].

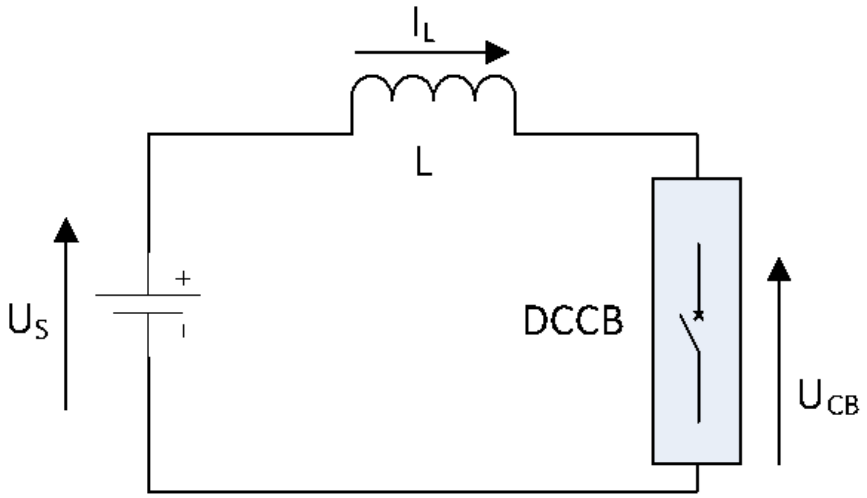

Figure 3.4: Typical circuit configuration of a DC circuit breaker showing the main current path, commutation branch, and energy absorption branch [30].

3.7.1 Transient Interruption Principle

The interruption process is governed by the relationship between the source voltage, breaker voltage, and current dynamics [30]:

$$U_s = L\frac{di}{dt} + U_{CB} \tag{3.4}$$

$$\frac{di}{dt} = \frac{U_s - U_{CB}}{L} \tag{3.5}$$

where U_s is the source voltage, U_{CB} is the breaker voltage, and L is the equivalent inductance of the fault current path.

For successful interruption, the breaker must generate a voltage such that:

$$U_{CB} > U_s \tag{3.6}$$

This condition ensures a negative current derivative, forcing the current toward zero. The generated voltage is referred to as the *transient interrupting voltage* (TIV).

The effectiveness of interruption is therefore dependent on both the magnitude and the rate of TIV development. Early fault detection is critical, as it enables timely activation of the breaker before the fault current reaches damaging levels.

3.7.2 Types of DC Circuit Breakers

DC circuit breakers are broadly classified into three categories [30]:

Mechanical DC Breakers

Mechanical breakers utilise physical contacts and auxiliary commutation circuits to create artificial current zero crossings. They exhibit low conduction losses and high current capability but have relatively slow interruption times (typically tens of milliseconds).

Solid-State DC Breakers

Solid-state breakers employ semiconductor devices such as IGBTs to interrupt current electronically. They offer extremely fast operation (on the order of a few milliseconds) but incur high conduction losses under normal operating conditions.

Hybrid DC Breakers

Hybrid breakers combine mechanical and semiconductor elements. Under normal conditions, current flows through a low-loss mechanical path. During a fault, current is rapidly commutated to a semiconductor branch for interruption. This configuration achieves both low losses and fast interruption, typically within 2–5 ms, making it highly suitable for MTDC applications.

3.8 Implications for Protection and Sensing

The preceding analysis highlights that a major challenge in HVDC protection is the limited observability of the DC network. Conventional protection schemes rely predominantly on terminal-based measurements, which introduce detection delays associated with signal propagation along the transmission line.

In long HVDC cable systems, this delay becomes increasingly significant and may compromise the ability of protection systems to operate within required time constraints.

Improving the spatial resolution of measurements within the network is therefore essential. Distributed sensing approaches that enable direct measurement of electrical quantities along the cable, particularly at intermediate points such as joints, offer a pathway to enhanced observability.

By capturing disturbances closer to their point of origin, distributed sensing can reduce detection latency, improve fault-localisation accuracy, and enable faster and more selective protection strategies.

The sensing methodology proposed in this thesis addresses these limitations by enabling localised current measurement within HVDC cable infrastructure, thereby

enhancing detection speed and providing improved visibility of system conditions.

3.9 Conclusion

This chapter has presented an overview of HVDC transmission systems and their role in modern power networks. The advantages of HVDC—including high power transfer capability, reduced losses, controllability, and asynchronous interconnection—make it a key enabler for long-distance transmission and renewable energy integration.

However, HVDC systems introduce significant protection challenges due to the rapid rise and sustained nature of fault currents. Unlike AC systems, the absence of natural current zero crossings necessitates ultra-fast detection and interruption, typically within 1–10 ms.

The chapter has examined fault evolution mechanisms and reviewed existing detection techniques, including derivative-based, travelling-wave, differential, and frequency-domain methods. While effective in certain applications, these approaches are fundamentally constrained by their reliance on terminal measurements and signal propagation.

The analysis demonstrates that enhancing measurement capability through distributed sensing represents a critical pathway for improving HVDC protection performance. By enabling faster, localised fault detection, such approaches can significantly improve system reliability, responsiveness, and selectivity in future HVDC networks.

Chapter 3 References

[1] NicoElNino, *German hvdc cable projects: At the core of the european energy transition*, pp. 2–8, 2016.

[2] Siemens, *Answers for energy: High voltage direct current transmission—proven technology for power exchange*, pp. 39–43. [Online]. Available: `http://www.siemens.com/energy/hvdc`. Accessed: Apr. 2, 2024.

[3] D. V. Hertem and M. Ghandhari, "Multi-terminal vsc hvdc for the european supergrid: Obstacles," *Renewable and Sustainable Energy Reviews*, 2010, pp. 2–6. DOI: 10.1016/j.rser.2010.07.068.

[4] D. V. Hertem, O. Gomis-Bellmunt, and J. Liang, *HVDC Grids*. IEEE-Wiley, 2016, pp. 88–95.

[5] D. Naidoo and N. M. Ijumba, "Hvdc line protection for the proposed future hvdc systems," in *IEEE Conference Proceedings*, 2004, pp. 2–4.

[6] CIGRE, "Protection and control of hvdc grid," CIGRE, Tech. Rep., pp. 17–24.

[7] CIGRE, "Protection and local control of hvdc grids," CIGRE, Tech. Rep. B4/B5.59 N739, 2018, pp. 14–30.

[8] W. Liu, J. Yu, G. Li, J. Liang, and C. E. Ugalde-Loo, *Analysis and protection of converter-side ac faults in a cascaded converter-based mvdc link: Angle-dc project*, pp. 3–8.

[9] A. Pragati, M. Mishra, P. K. Rout, et al., "A comprehensive survey of hvdc protection system fault analysis methodology, issues, challenges, and future perspective," *MDPI*, 2023, pp. 3–6.

[10] J. C. Das, *Short-Circuits in AC and DC Systems*. New York: CRC Press, 2018, vol. 1, pp. 542–552.

[11] J. Yang, J. E. Fletcher, and J. O'Reilly, "Short-circuit and ground fault analyses and location in vsc-based dc network cables," in *IEEE Conference Proceedings*, pp. 1–6.

[12] M. Muniappan, "A comprehensive review of dc fault protection methods in hvdc transmission systems," *Protection and Control of Modern Power Systems*, vol. 6, no. 1, 2021, pp. 2–11. DOI: 10.1186/s41601-020-00173-9.

[13] D. Tzelepis et al., "Single-ended differential protection in mtdc networks using optical sensors," *IEEE Transactions on Power Delivery*, vol. 32, no. 3, pp. 1605–1615, Jun. 2017. DOI: 10.1109/TPWRD.2016.2645231.

[14] S. Ademi, D. Tzelepis, D. Adam, S. Subramanian, and H. Ha, "Fault current characterisation in vsc-based hvdc systems," in *IET Conference Proceedings*, 2016, pp. 2–6.

[15] F. Page, S. Finney, and L. Xu, *An alternative protection strategy for multi-terminal hvdc*, pp. 3–7. [Online]. Available: `http://www.epsrc.ac.uk`. Accessed: Apr. 3, 2024.

[16] D. Naidoo and N. M. Ijumba, "Hvdc line protection for the proposed future of hvdc system," in *IEEE Conference Proceedings*, Nov. 2004, pp. 2–5.

[17] M. Eremia, C.-C. Lu, and A.-A. Edris, *Advanced Solutions in Power Systems: HVDC, FACTS, and Artificial Intelligence*. IEEE-Wiley, 2016, pp. 224–228.

[18] Hitachi Energy, "High voltage direct current (HVDC) transmission: Enabling the energy transition," Hitachi Energy, Tech. Rep., 2024, Enguerrand Ducene, Regional Sales Manager MEA, pp. 15–22.

[19] S. F. Huang, *A fault location scheme based on spectrum characteristic of fault-generated high frequency transient signals*, pp. 4–6, 2009.

[20] E. Styvaktakis, M. H. J. Bollen, and I. Y. H. Gu, "A fault location technique using high frequency fault clearing transients," *IEEE PES Review*, pp. 1–3.

[21] PROMOTioN, *D4.2—broad comparison of fault clearing strategies for dc grids*, pp. 30–167. [Online]. Available: `http://www.promotion-offshore.net`. Accessed: Apr. 2, 2024.

[22] Y. Han et al., "Fault detection and zonal protection strategy of multi-voltage level dc grid based on fault traveling wave characteristic extraction," *Electronics*, vol. 12, no. 8, Apr. 2023. DOI: `10.3390/electronics12081764`.

[23] J. Sneath and A. D. Rajapakse, "Fault detection and interruption in an earthed hvdc grid using rocov and hybrid dc breakers," *IEEE Transactions on Power Delivery*, vol. 31, no. 3, pp. 973–981, Jun. 2016. DOI: `10.1109/TPWRD.2014.2364547`.

[24] X. Liu, A. H. Osman, and O. P. Malik, "Hybrid traveling wave-boundary protection for monopolar hvdc systems," *IEEE Transactions on Power Delivery*, vol. 24, no. 2, pp. 569–578, Apr. 2009.

[25] R. G. Arrabé, C. A. Platero, F. Á. Gómez, and E. R. López, "New differential protection method for multiterminal hvdc cable networks," *Energies*, vol. 11, no. 12, Dec. 2018, pp. 3–8. DOI: 10.3390/en11123387.

[26] D. Li, A. Ukil, K. Satpathi, and Y. M. Yeap, "Improved s transform-based fault detection method in voltage source converter interfaced dc system," *IEEE Transactions on Industrial Electronics*, vol. 68, no. 6, pp. 5024–5035, Jun. 2021. DOI: 10.1109/TIE.2020.2988193.

[27] Y. M. Yeap, N. Geddada, and A. Ukil, "Analysis and validation of wavelet transform based dc fault detection in hvdc system," *Applied Soft Computing*, vol. 61, pp. 17–29, Dec. 2017. DOI: 10.1016/j.asoc.2017.07.039.

[28] L. Sabug, A. Musa, F. Costa, and A. Monti, "Real-time boundary wavelet transform-based dc fault protection system for mtdc grids," *International Journal of Electrical Power and Energy Systems*, vol. 115, Feb. 2020, pp. 2–6. DOI: 10.1016/j.ijepes.2019.105475.

[29] A. Imani, Z. Moravej, and M. Pazoki, "A novel time-domain method for fault detection and classification in vsc-hvdc transmission lines," *International Journal of Electrical Power and Energy Systems*, vol. 140, Sep. 2022, pp. 3–6. DOI: 10.1016/j.ijepes.2022.108056.

[30] R. P. P. Smeets and N. A. Belda, "Hvdc fault current interruption technology," in *IET Conference Proceedings*, 2019, pp. 2–6.

Chapter 4

Distributed Photonic Sensing

4.1 Introduction

This chapter establishes the theoretical foundation for the sensing methodology adopted in this research by introducing the concept of distributed photonic sensing and its relevance to modern power transmission systems. It highlights the limitations of conventional electrical measurement techniques in high-voltage direct current (HVDC) environments, particularly with respect to insulation constraints, electromagnetic interference, and the difficulty of achieving wide-area system observability. In response to these limitations, the chapter motivates the need for distributed, electrically isolated sensing solutions capable of supporting high-resolution and spatially distributed measurements across transmission infrastructure.

The chapter then presents fibre Bragg grating (FBG)-based photonic sensing as a suitable approach and outlines its fundamental operating principles, fabrication techniques, and interrogation methods. Building on this foundation, a hybrid low-voltage transducer (LVT) architecture is introduced that combines a piezoelectric transducer (PZT) with an FBG sensor to enable electromechanical-to-optical signal conversion for current measurement. This integrated sensing approach forms the core focus of the chapter and provides the theoretical basis for the modelling, calibration, and experimental validation presented in the subsequent chapters.

4.2 Photonic Current Sensors

Photonic sensors exploit the interaction between light and external physical quantities to detect variations in a measurand. These sensors operate by modulating one or more optical parameters of the propagating light field, including amplitude, phase, wavelength, polarisation, or scattering characteristics. Changes in these optical properties can then be analysed to determine the magnitude of the physical parameter being measured [1]. Depending on the sensing mechanism employed, photonic sensors may be broadly classified as wave-modulated, phase-modulated, scattering-based, or polarisation-modulated devices. The interaction between the optical field and the measurand alters the propagation characteristics of the light signal, resulting in measurable effects such as phase shifts, polarisation rotation, or wavelength variations, as illustrated in Figure 4.1. In fibre Bragg grating (FBG) sensors, this interaction manifests primarily as a shift in the reflected wavelength that satisfies the Bragg condition.

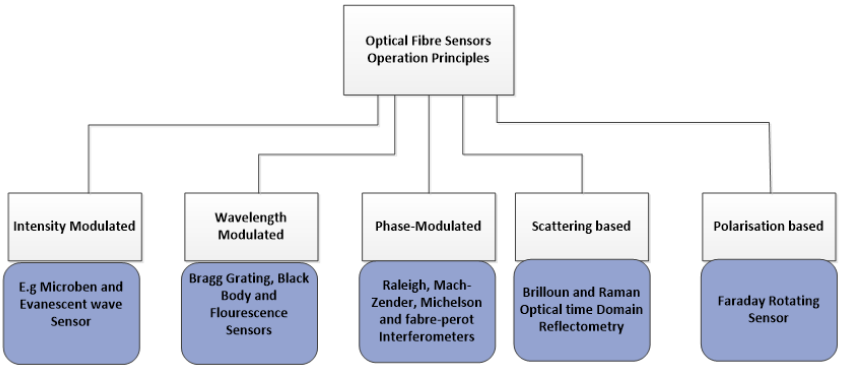

Figure 4.1: Fibre sensor types with respect to their operating principles.

The advantages of photonic sensors make them well-suited for monitoring in high-voltage environments. Optical fibre sensors are electrically passive and immune to electromagnetic interference, enabling reliable operation in environments characterised by strong electric and magnetic fields. In addition, optical fibres support multiplexed sensing architectures in which multiple sensing elements can be deployed along a single fibre, thereby enabling distributed measurement over large distances. In HVAC systems, photonic sensing technologies have been successfully integrated into hybrid

monitoring architectures that combine conventional current and voltage transformers with optical transducers. These systems have demonstrated reliable performance and have been implemented for distributed monitoring of electrical networks [2], [3].

However, comparable photonic sensing approaches have not yet been extensively applied to HVDC networks, where the requirements for rapid fault detection and distributed system observability remain significant. This research therefore investigates the application of photonic sensing technologies for current measurement in HVDC transmission systems using a hybrid LVT-based sensing approach.

4.3 Hybrid LVT Photonic Sensor Configuration

The LVT utilised in this work comprises a hybrid configuration integrating a multilayer piezoelectric transducer (PZT) and an FBG sensor. The PZT is a PICMA® stack 882.11 [4]. It serves as the electromechanical interface, converting the applied electrical signal into a corresponding mechanical strain. This strain is subsequently transduced into the optical domain by the FBG element, which is inscribed within a single-mode optical fibre and mechanically suspended across the active surface of the PZT, as shown in Figure 4.2.

When an external voltage is applied across the PZT terminals via hermetically sealed Kovar pins, the resulting electric field induces deformation in the PZT material. This deformation imposes axial strain on the FBG region, thereby altering both the grating period and the effective refractive index. As broadband light propagates through the optical fibre, the spatial discontinuity introduced by the strained FBG modulates the reflected spectrum. Specifically, the FBG reflects a narrowband component of the incident light whose wavelength satisfies the Bragg condition.

The entire assembly is housed in a robust butterfly package that provides thermal stability and environmental protection, thereby improving the device's operational robustness. This electromechanical-to-optical conversion mechanism enables the LVT to function as a compact and electrically isolated voltage-sensing unit suitable for harsh environments and capable of high-fidelity signal acquisition within its uncertainty limits

in HVDC applications [4].

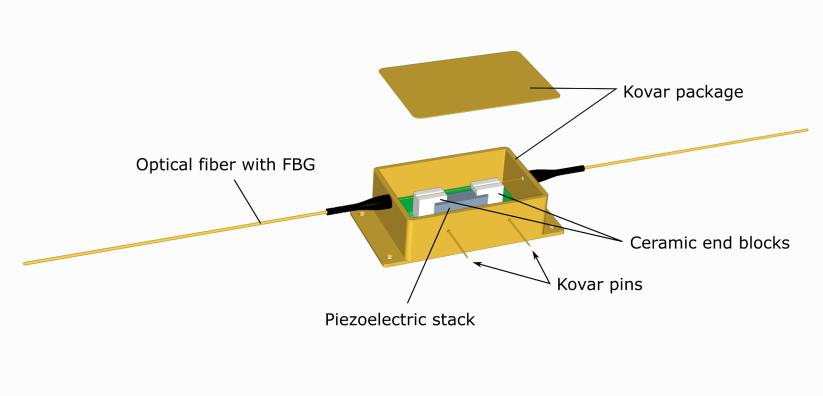

Figure 4.2: Hybrid LVT sensor configuration.

The FBG is a key component of the hybrid LVT and represents a mature sensing technology, with well-established fabrication and interrogation techniques. A brief overview of the relevant fabrication and interrogation methods is presented in the following sections.

4.4 Principle of Fibre Bragg Grating Sensors

Fundamentally, fibre Bragg grating (FBG) sensors operate on the principle of wavelength-selective reflection induced by periodic perturbations in the refractive index and grating pitch along the core of an optical fibre [5]. The essential sensing element, the Bragg grating, is inscribed by exposing a photosensitive fibre section to a spatially modulated ultraviolet light pattern, resulting in a permanent periodic modulation of the core refractive index. This engineered structure renders the fibre responsive to physical parameters such as strain, temperature, and pressure by altering the grating period and effective refractive index in response to external stimuli. These perturbations modulate the Bragg wavelength, thereby encoding the magnitude and nature of the applied measurand into the reflected optical signal [6].

In operation, a broadband light source is launched into the optical fibre core. As the light propagates through the fibre, it encounters the grating section, which acts as a wavelength-selective reflector. A specific wavelength component is reflected, while

the remaining wavelengths continue to propagate through the fibre. This reflection occurs only for the wavelength that satisfies the Bragg condition, which depends on the effective refractive index of the fibre core and the periodicity of the grating. The Bragg wavelength, λ_B, is expressed as

$$\lambda_B = 2n_{\text{eff}}\Lambda \tag{4.1}$$

where n_{eff} is the effective refractive index and Λ is the grating pitch.

Variations in environmental or operating conditions, such as temperature, mechanical strain, or applied pressure, alter the effective refractive index and/or the grating period of the FBG. These perturbations produce a corresponding shift in the Bragg wavelength, which constitutes the device's fundamental sensing mechanism. Since the wavelength shift is directly related to the magnitude of the applied stimulus, it provides a reliable and quantifiable means of measuring the influencing physical parameter.

The wavelength-selective reflective property of the FBG enables precise detection of these shifts, making it an effective sensing element for monitoring applications. The reflected optical signal is processed by an interrogation system, which converts the measured wavelength variation into electrical or digital data proportional to the measurand. This enables accurate real-time quantification of physical phenomena and supports high-resolution monitoring in demanding operating environments.

4.5 FBG Fabrication

FBGs can be fabricated using several techniques, the most widely adopted being the interferometric and phase mask methods. Each approach offers distinct advantages and limitations depending on the application requirements. For example, the interferometric method provides greater flexibility for fabricating chirped FBGs, whereas the phase mask method is particularly suitable for standard FBG production. The interferometric method employs two coherent ultraviolet (UV) beams to generate an interference pattern within the photosensitive fibre core, enabling flexible control of grating period and pitch. However, the technique requires high optical stability and is sensitive to en-

vironmental disturbances such as vibration and thermal fluctuations. In contrast, the phase mask method uses a diffractive optical element to directly imprint a periodic index modulation onto the fibre during UV exposure [5]. This technique is simpler, highly reproducible, and widely adopted in commercial manufacturing, although it offers less flexibility in tailoring grating profiles than interferometric arrangements.

4.5.1 Interferometric Method of FBG Fabrication

The interferometric method of FBG fabrication involves diffusing hydrogen molecules (H_2) into a photosensitive section of the fibre to enhance its photosensitivity. When the hydrogen-treated section is exposed to UV light, photochemical reactions occur within the fibre core, modifying the refractive index of the exposed region. This method can be applied to both germanium-doped and non-germanium-doped fibres.

The interferometric approach may be implemented using holographic or source-tunable techniques. Both methods rely on creating an interference pattern within the fibre core, either by adjusting the angle between the writing beams, as in the holographic method, or by tuning the source wavelength, as in the source-tunable method. In the holographic approach, the varying wavelength pattern is achieved by precise adjustment of the mirror angles, as illustrated in Figure 4.3. In the source-tunable method, the central wavelength of the inscription is controlled by tuning the source wavelength [5], [6].

The grating pitch, or period of index modulation, is determined by

$$\Lambda = \frac{\lambda_{uv}}{\theta} \tag{4.2}$$

where Λ is the grating pitch, λ_{uv} is the wavelength of the UV light, and θ is the angle between the writing beam and the normal axis to the fibre.

4.5.2 Phase Mask Method

The phase mask method involves exposing a fibre section to a UV beam through a diffractive element to generate an interference pattern within the fibre core. This

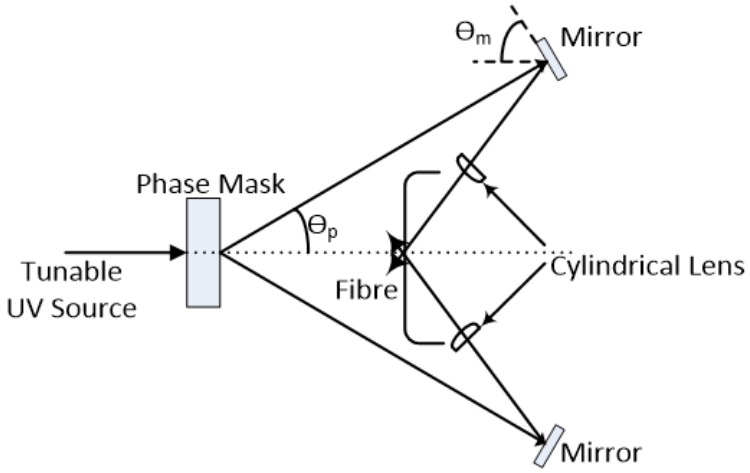

Figure 4.3: Schematic of the interferometric method for FBG fabrication [5].

technique produces a periodic pattern corresponding to the geometry of the phase mask, as shown in Figure 4.4. The periodic pattern alters the refractive index distribution and grating pitch of the exposed section of the optical fibre.

Unlike the interferometric technique, the phase mask method does not require tuning of the source wavelength or precise adjustment of mirror angles during inscription. The required grating pattern can be achieved either using a fixed phase mask or by moving the fibre relative to the mask. In the fixed phase mask technique, the UV beam passes through the diffractive element to directly create the interference pattern. In the moving fibre scanning method, the fibre is translated relative to the mask during inscription [5].

4.6 FBG Grating Structure

The structural composition of an FBG can be modified to achieve different spectral and sensing characteristics. The principal grating forms considered in this work are [6], [7]:

- uniform FBG,
- apodized FBG,

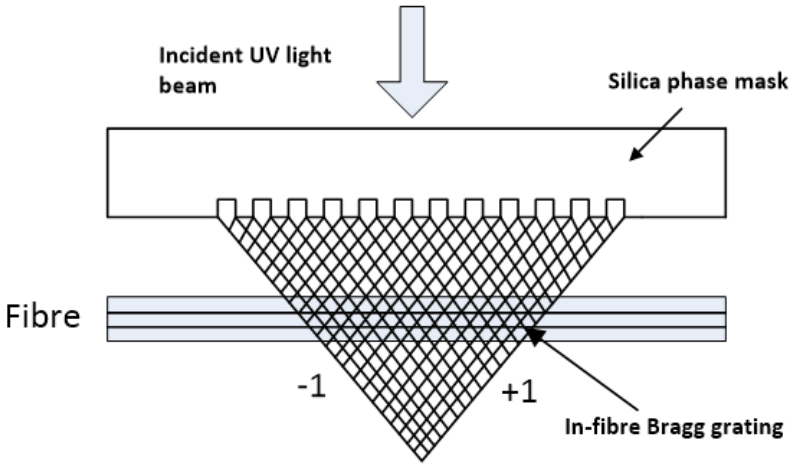

Figure 4.4: Schematic diagram of the phase mask writing method [5].

- chirped FBG,
- phase-shifted FBG.

4.6.1 Uniform FBG

In a uniform grating, as illustrated in Figure 4.5, the periodic sections are equally spaced and have equal refractive index modulation strength. When forward-propagating light encounters the grating region, a portion of the light satisfying the Bragg condition is reflected, while the remaining optical power is transmitted through the fibre. The reflected wave, therefore, exhibits a spectral peak at the Bragg wavelength [5], [8], [9].

The Bragg relationship governs the wavelength of the reflected light.

$$\lambda_B = 2n_{\text{eff}}\Lambda \tag{4.3}$$

where n_{eff} is the effective refractive index and Λ is the grating pitch.

4.6.2 Apodized FBG

An apodized grating has a constant grating period but a varying modulation strength along the grating length, so that the refractive index profile follows a bell-shaped profile. This characteristic is achieved through controlled exposure of the grating region during

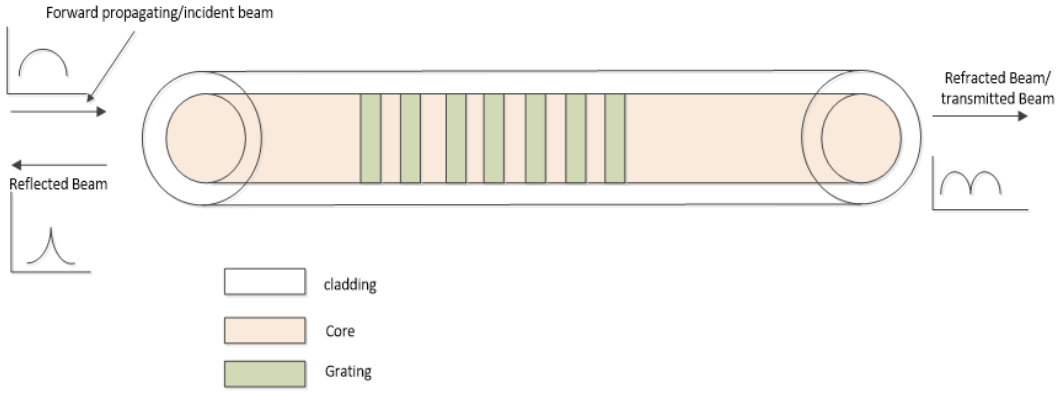

Figure 4.5: Uniform FBG inscription.

fabrication. The resulting non-uniform modulation strength produces a reflectivity profile that is stronger at the centre of the grating than at the edges, as illustrated in Figure 4.6 and Figure 4.7 [6], [10].

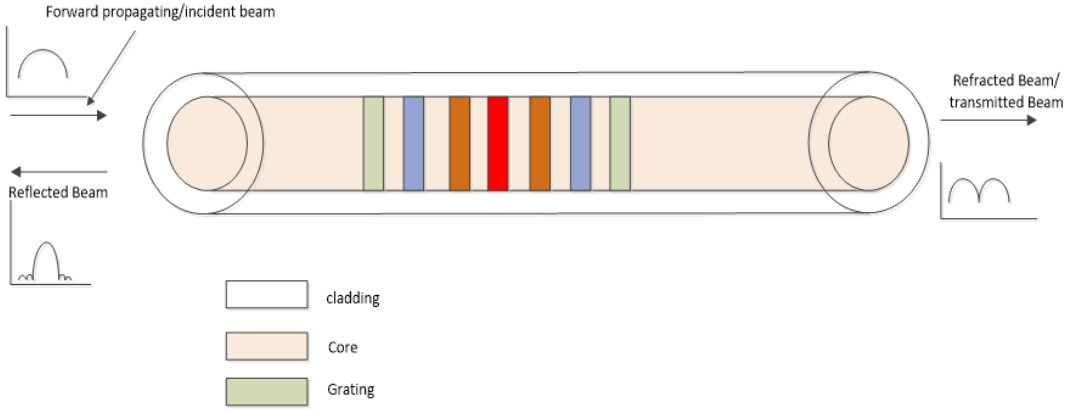

Figure 4.6: Apodized FBG inscription.

This grating form suppresses side lobes in the reflected spectrum and therefore offers an advantage over uniform gratings, which are more susceptible to side-lobe effects [11].

4.6.3 Chirped FBG

A chirped FBG consists of a grating structure with spatially non-uniform periodicity, resulting in a grating period that varies along the fibre length [9]. This non-uniformity

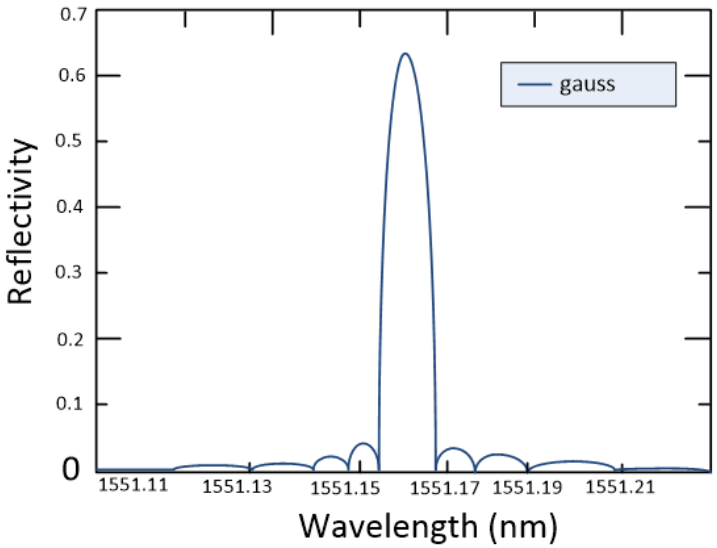

Figure 4.7: Gaussian reflectivity profile of an apodized FBG [7].

gives rise to multiple local reflection conditions, such that different wavelength components are reflected at different axial positions along the grating [8], [12]. Consequently, the overall spectral response becomes a function of the refractive index and grating period variation along the propagation axis.

To account for the spatial dependence of the grating characteristics, the Bragg relationship may be expressed as

$$\lambda_B(z) = 2n_{\text{eff}}(z)\Lambda(z) \tag{4.4}$$

where both the effective refractive index and the grating pitch vary as functions of the axial position, z.

Figure 4.8 shows a chirped FBG with a spatially varying grating period. This spatial variation produces reflected components that satisfy multiple local Bragg conditions, such that the overall reflected beam is a superposition of multiple reflected components. This leads to a broader spectral bandwidth. The wavelength range of the reflected beam is also a function of the total grating length [8], [9], [11], [12].

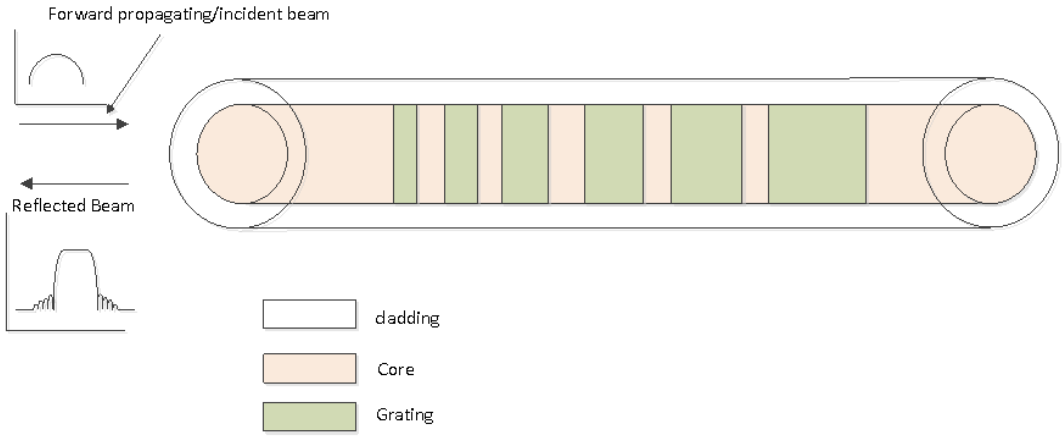

Figure 4.8: Chirped FBG.

4.6.4 Phase-Shifted FBG

A phase-shifted FBG consists of spatially separated adjacent grating sections, thereby forming a Fabry–Pérot-like structure.

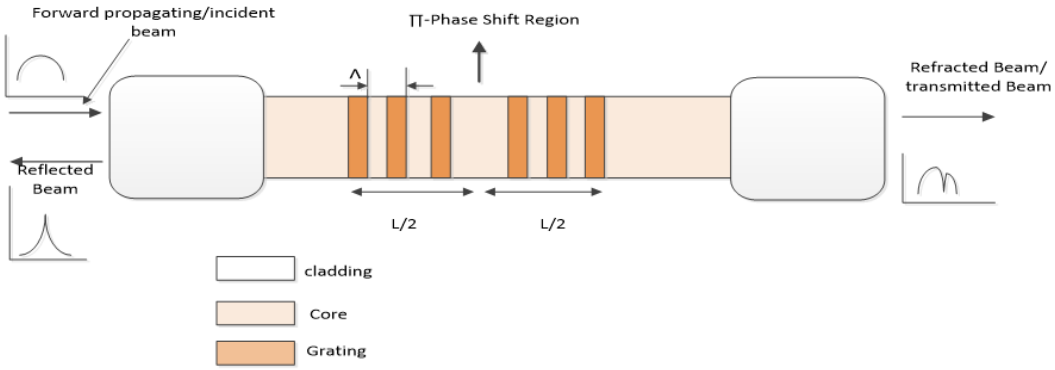

Figure 4.9: π-phase-shifted FBG **ref52**, [13].

Figure 4.9 shows an FBG structure with a distinct discontinuity that separates the grating into two sections, forming an evenly spaced pair around the π-phase region. The phase shift introduces a narrow spectral transmission resonance at the centre of the transmission spectrum of the grating, as shown in Figure 4.10.

Although phase-shifted FBGs offer high sensitivity and can be deployed for a range of measurement applications, interrogation of the backwards-propagating signal can

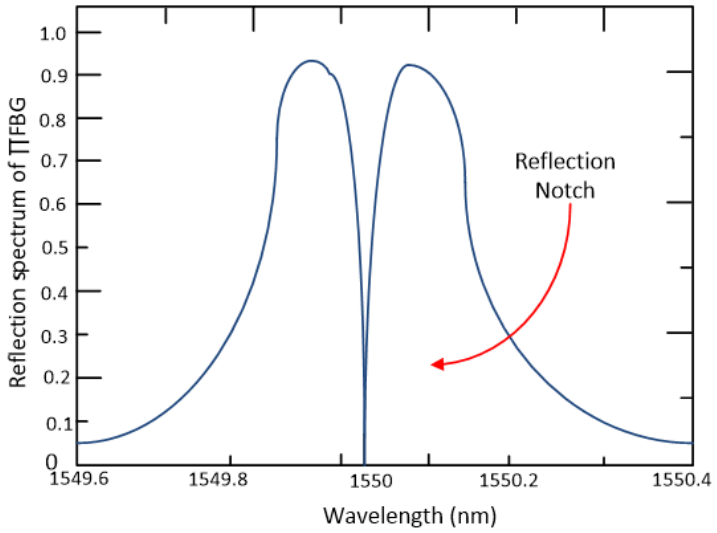

Figure 4.10: Reflection spectrum of a π-phase-shifted FBG [14].

be challenging because the narrow spectral trough is close to the error floor of many interrogation systems. The width of the reflected band is approximately 1 pm. Most commercially available analysers require a minimum spectral bandwidth greater than 0.15 nm [14]. One of the most effective approaches for interrogating the backwards-propagating wave in a π-phase-shifted FBG is the Pound–Drever–Hall (PDH) method, which has demonstrated measurement sensitivity down to the picostrain ($p\varepsilon$) level. However, this improved detection capability is accompanied by increased experimental complexity **ref53**, [15].

Generally, for a uniform FBG of grating length L, the reflectivity spectrum of the grating section of the optical fibre, together with the reflected amplitude and power, may be expressed by [6], [11]

$$\rho = \frac{-k \sinh\left(\sqrt{k^2 - \hat{\sigma}^2}\, L\right)}{\hat{\sigma} \sinh\left(\sqrt{k^2 - \hat{\sigma}^2}\, L\right) + i\sqrt{k^2 - \hat{\sigma}^2} \cosh\left(\sqrt{k^2 - \hat{\sigma}^2}\, L\right)} \tag{4.5}$$

The reflected power is given by

$$r = |\rho|^2 = \frac{\sinh^2\left(\sqrt{k^2 - \hat{\sigma}^2}\, L\right)}{\cosh^2\left(\sqrt{k^2 - \hat{\sigma}^2}\, L\right) - (\hat{\sigma}^2/k^2)} \tag{4.6}$$

The bandwidth, or full width at half maximum (FWHM), is given by

$$\mathrm{FWHM}_\lambda = \lambda_B S \left[\left(\frac{\Delta n}{2n_{co}}\right)^2 + \left(\frac{1}{N}\right)^2\right]^{1/2} \tag{4.7}$$

where k is the AC coupling coefficient, $\hat{\sigma}$ is the DC self-coupling coefficient, L is the grating length, S is a grating parameter that is approximately 1 for highly reflective gratings and 0.5 for weak gratings, and N is the number of grating periods.

4.7 Different Types of Commercially Available FBGs

Commercially available FBGs exhibit diverse structural and spectral characteristics, which are primarily dictated by their intended application and the fabrication methodology employed. The manufacturing process significantly influences key performance parameters, including reflectivity, bandwidth, thermal stability, and mechanical robustness. FBGs can be broadly classified into three categories based on fabrication technique.

The first category comprises standard FBGs, fabricated using the interferometric or phase mask technique, in which a periodic refractive index modulation is induced in the fibre core by ultraviolet (UV) laser exposure. This method offers high precision and repeatability and is therefore widely adopted for telecommunications and sensing applications, as shown in Table 4.1.

The second category comprises Draw Tower Gratings (DTGs), in which the grating structure is inscribed *in situ* during the fibre drawing process. This approach enables the production of long, continuous gratings with enhanced mechanical durability. It is particularly advantageous for applications requiring high strain tolerance, such as structural health monitoring and aerospace sensing.

The third category uses femtosecond (fs) laser inscription, in which the grating is directly inscribed into the fibre core, including through the protective coating where

required. This method relies on nonlinear multiphoton absorption to induce permanent refractive index changes, enabling the fabrication of highly resilient FBGs capable of operating under extreme environmental conditions, including high temperatures and radiation-prone environments.

Table 4.1: Different types of commercially available FBGs [16].

Type of FBG	**Geometry (Cladding, Length, Coating)**	**FWHM (pm)**	**SLSR (dB)**	**Reflectivity (%)**
Standard FBG (Phase Mask)	(80 μm, 10 mm, Polyamide)	100	17–20	60–80
	(125 μm, 10 mm, Polyamide)	100	12–15	40–50
Drawn Tower Grating (DTG)	(80 μm, 8 mm, Ormocer)	100	8–12	20–25
	(125 μm, 8 mm, Ormocer)	100	8–12	20–25
Femtosecond Inscribed FBG	(80 μm, 4.6 mm, Acrylate)	290–300	20–23	30–50
	(125 μm, 5.2 mm, Carbon-PI)	240–300	12–22	8–50

FWHM: Full width at half maximum
SLSR: Side-lobe suppression ratio

Each of these fabrication techniques presents distinct advantages and trade-offs, making them suitable for specific operational environments and application domains, including optical communication, structural monitoring, and advanced photonic sensing.

4.8 FBG Interrogation

When a physical phenomenon perturbs an FBG, the periodic grating structure and the effective refractive index experience a state change. This change in the grating region produces a backwards-propagating wave from the incident forward-propagating beam whose wavelength satisfies the Bragg condition. The reflected spectrum is then analysed to obtain information about the physical phenomenon interacting with the FBG. In practice, nanometre- to picometre-level resolution is required for useful information to be extracted from the optical signal. The general requirements for an ideal interrogation system include [5]:

- high resolution, typically from nanometre to picometre level,
- good accuracy and adequate measurement bandwidth,
- compatibility with multiplexing topologies to support distributed measurements.

FBG interrogation techniques can be classified into five broad categories. For the purpose of this research, tunable filtering, interferometric techniques, and optical spectrum analysis are introduced. Other interrogation methods are discussed extensively in the literature [1], [6], [17]. The main interrogation classes are illustrated in Figure 4.11.

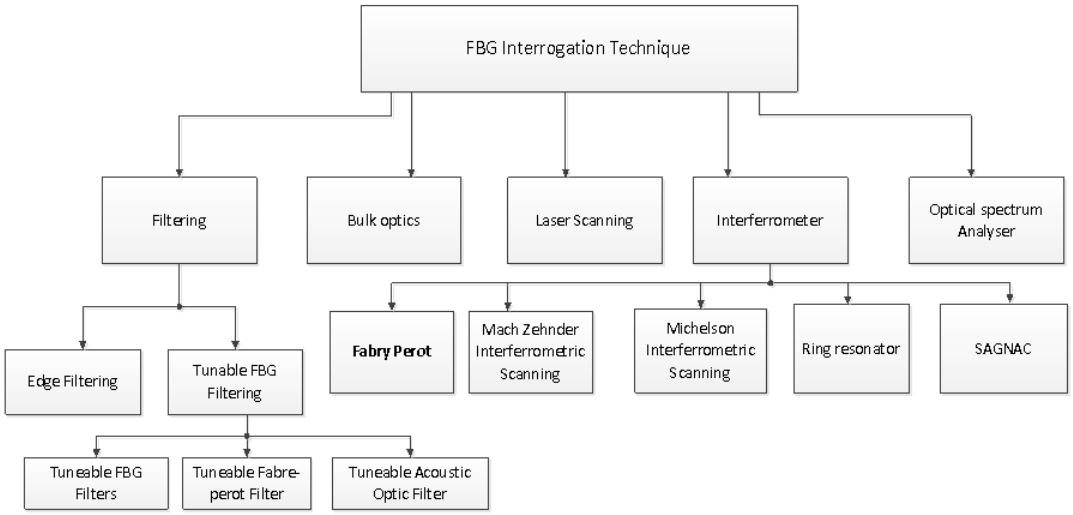

Figure 4.11: Classification of FBG interrogation techniques.

4.8.1 Tunable FBG Filtering

Tunable FBG interrogation operates by sweeping the passband of a tunable optical filter across the wavelength range of interest. As the filter scans, its transfer function overlaps with the reflected spectrum of the sensing FBG, producing an output intensity profile corresponding to the convolution-like interaction between the filter response and the FBG spectrum. A peak occurs when the filter passband aligns with the Bragg wavelength of the sensing FBG, thereby allowing wavelength shifts to be tracked. However, this method is sensitive to intensity fluctuations and limited by the finite scanning speed of the tunable filter, making it less suitable for applications requiring high-speed or real-time dynamic measurements [5], [17].

4.8.2 Interferometric Scanning

An interferometric scanner analyses the wavelength shift associated with changes in the Bragg properties and converts it into a phase variation at the output. It utilises the optical path difference created by two travelling arms of the reflected optical signal, as illustrated in Figure 4.12. One of the optical paths is modulated by a piezoelectrically perturbed element driven by a ramp generator, while the other path remains unmodified. The difference in optical path length between the two arms results in a change in optical path difference (OPD), depending on both the magnitude of the measurand and the modulation introduced by the piezoelectric element.

The normalised interference signal from the scanned interferometer is given by

$$I_{\text{intf}} = I_0 \left(1 + B \cos \left[\Delta\Phi_B + \phi(t)\right]\right) \tag{4.8}$$

where I_0 is the intensity of the incident light, B is the visibility of the interference signal, $\phi(t)$ is the thermally induced phase shift, and $\Delta\Phi_B$ is the change in optical phase.

The change in optical phase can be expressed as

$$\Delta\Phi_B = \left(\frac{2\pi\Delta L_{SI}}{\lambda_B^2}\right)\Delta\lambda_B = \left(\frac{2\pi\Delta L_{SI}}{\lambda_B}\right)\xi_g \Delta Y \tag{4.9}$$

where ΔY is the variation in strain or temperature applied to the FBG, ΔL_{SI} is the optical path difference of the interferometric scanner, and ξ_g is the normalised sensitivity for strain or temperature.

The above relationship summarises the optical phase change as a function of optical path difference. These OPD changes arise from the extent to which the perturbed piezoelectric element in the reflection path and the sensing FBG influence the propagating signal.

The normalised sensitivity for strain and temperature is given by

$$\xi_g = \frac{1}{\lambda_B}\frac{\partial\lambda_B}{\partial Y} \tag{4.10}$$

and hence

$$\frac{\Delta\Phi_B}{\Delta Y} = \left(\frac{2\pi\Delta L_{SI}}{\lambda_B}\right)\xi_g \tag{4.11}$$

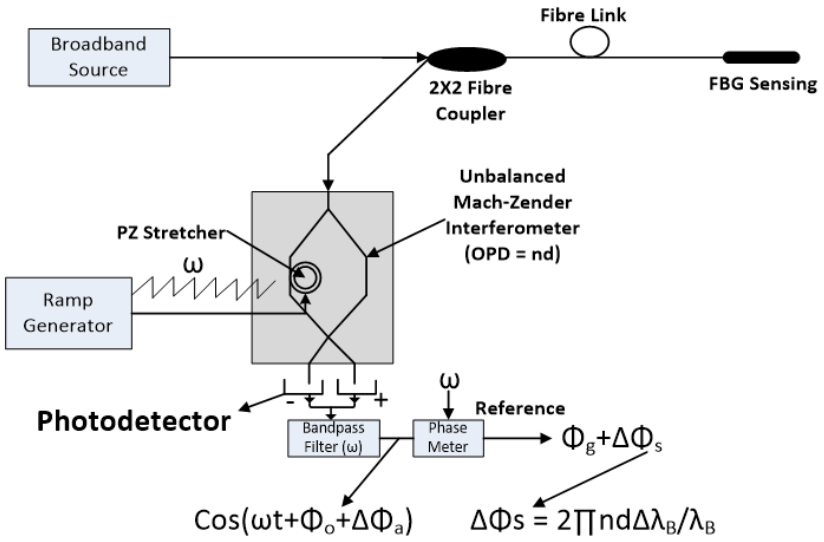

Figure 4.12: Interferometric scanning scheme [5].

4.8.3 Optical Spectrum Analyser

In Fibre Bragg Grating (FBG) sensor systems, the optical spectrum analyser (OSA) serves as a high-resolution diagnostic tool for monitoring the spectral characteristics of the reflected Bragg signal. When the FBG is subjected to external perturbations, such as strain or temperature, the associated changes in grating condition produce a measurable shift in the Bragg wavelength. The OSA captures these shifts by analysing the reflected spectrum, thereby enabling the quantification of the physical phenomena that influence the grating structure. This spectral interrogation approach is important for extracting high-quality data from FBG-based transducers in real-time sensing applications. The device is widely used in optical metrology, communications, laser systems, instrumentation, vibration analysis, temperature measurement, pressure monitoring, and strain measurement.

Most optical spectrum analysers employ a base interrogation technology, such as

tunable filtering or interferometric interrogation, together with reflected- or transmitted-grating techniques and associated electronic and computer-on-board systems for optical signal acquisition and processing. The base interrogation technology may take several forms, including laser tunable filtering, as in FAZT interrogators [18], Fabry–Pérot tunable filtering, as in Micron Optics interrogators [19], interferometric scanning, as in APEX optical spectrum analysers [20], and transmission grating technology, as in IBSEN photonic interrogators [21].

For interrogators or spectrum analysers that use tunable filters, the system continually scans between the sensing FBG and the receiving stage. The filter continuously tunes to align the receiving FBG with the reflected signal from the sensing FBG. This interrogation technique can be limited in speed when very fast dynamic measurements are required **ref51**, [5], [6]. Nevertheless, it provides precise and reliable measurement approximation. Interferometric scanning offers very high detection speed and resolution and is suitable for applications requiring high sensitivity and fast measurement; however, its principal limitation is its susceptibility to environmental, thermal, and vibration fluctuations [17]. Transmission grating-based interrogators provide acceptable speed, although accuracy and precision may present some challenges [21].

4.9 FBG Sensor Applications for Measurement

The widespread adoption of FBG sensors across various sectors has been driven by their ability to perform reliably in harsh environments and under demanding operating conditions. These attributes, together with their passive nature and chemical inertness, further enhance their suitability for a wide range of sensing applications. The inherent resilience of FBG sensors allows them to operate in environments where conventional electrical sensors may fail due to thermal, electromagnetic, or chemical stress.

In the area of current and voltage measurement, FBG sensors have been successfully integrated into AC networks as important measurement devices [2], [22]. These systems often combine FBG sensors with additional transducers to form comprehensive measurement solutions for electrical quantities such as current and voltage. In AC power

networks, where the signal characteristics are sinusoidal, FBG-based measurement systems have demonstrated good accuracy, stability, and durability. Despite this success in AC systems, FBG sensors have not yet been extensively trialled in HVDC systems, where there remains a strong need for innovation in wide-area electrical measurement technologies.

4.10 Current Measurement Using Hybrid (PZT and FBG) LVT

The application of fibre Bragg grating (FBG) sensors for measuring electrical quantities such as current remains an active area of research. Conventional approaches typically rely on magnetic-field interaction, in which a current-induced magnetic field induces strain in a magnetostrictive material. This strain modifies the FBG grating period, resulting in a measurable shift in the reflected Bragg wavelength, from which the current magnitude can be inferred.

In the hybrid sensing configuration adopted in this work, a different transduction pathway is employed. A piezoelectric transducer (PZT), capable of generating mechanical strain in response to an applied electric field, is mechanically coupled to an FBG element to form a multi-stage sensing structure within the low-voltage transducer (LVT). In this arrangement, the PZT serves as the primary sensing element, while the FBG functions as the secondary optical transducer. Electrical signals originating from the shunt are first converted into a proportional voltage, which is subsequently transformed into mechanical strain by the PZT. This strain is then transferred to the FBG, resulting in a shift in the Bragg wavelength. This electromechanical-to-optical conversion process enables accurate and electrically isolated current measurement, making the proposed hybrid sensor suitable for distributed sensing applications in HVDC systems. The detailed transduction mechanism is described in Section 4.11.

4.11 Strain and Temperature Sensing

The basic physics governing the operation of the LVT, from voltage-to-strain conversion through to wavelength shift, is illustrated in Figure 4.13.

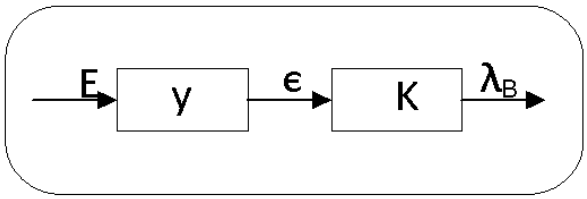

Figure 4.13: LVT functional process flow.

E: voltage; y: voltage-to-strain transduction; ε: strain; K: strain-to-wavelength transduction; λ_B: FBG centre wavelength.
E represents the external electric field, y is the PZT transfer function with ε as its output (strain), while K represents the FBG transfer function with λ_B (Bragg wavelength) as its output [23].

$$y = M \cdot d_{xy} \tag{4.12}$$

$$\varepsilon = M \cdot d_{xy} \cdot E \tag{4.13}$$

$$\frac{\Delta l}{l} = \frac{M \cdot d_{xy} \cdot V}{l} \tag{4.14}$$

$$\Delta l = M \cdot d_{xy} \cdot V \tag{4.15}$$

where d_{xy} is the PZT strain coefficient, Δl is the change in length, V is the applied voltage, and M is the strain amplification coefficient.

$$\lambda_B = \varepsilon \cdot K \tag{4.16}$$

For a single-mode fibre (SMF-28), the wavelength shift ratio can be expressed as [6]:

$$\frac{\Delta\lambda}{\lambda} = 0.79\varepsilon \tag{4.17}$$

$$K = 2n_{\text{eff}}\Lambda \tag{4.18}$$

$$\lambda_B = M \cdot d_{xy} \cdot E \cdot (2n_{\text{eff}}\Lambda) \tag{4.19}$$

The coefficient 0.79 represents the photo-elastic constant linking strain to wavelength variation in a single-mode fibre.

As illustrated in Figure 4.13, under the influence of an external electric field, the PZT element undergoes deformation, producing strain. This strain is transferred to the FBG, resulting in a shift in Bragg wavelength. The interrogation system subsequently evaluates the wavelength shift. The LVT, therefore, quantifies voltage in terms of wavelength shift (pm).

—

4.12 Strain and Temperature Effects

The wavelength response under strain can be expressed as:

$$\Delta\lambda_{bs} = 2\left[\Lambda\frac{\partial n_{\text{eff}}}{\partial l} + n_{\text{eff}}\frac{\partial\Lambda}{\partial l}\right]\Delta l \tag{4.20}$$

$$\Delta\lambda_{bs} = \lambda_B(1-\rho_\sigma)\varepsilon \tag{4.21}$$

where ρ_σ is the photo-elastic coefficient of the fibre.

The temperature dependence of the Bragg wavelength is given by:

$$\Delta\lambda_{bT} = 2\left[\Lambda\frac{\partial n_{\text{eff}}}{\partial T} + n_{\text{eff}}\frac{\partial\Lambda}{\partial T}\right]\Delta T \tag{4.22}$$

$$\Delta\lambda_{bT} = \lambda_B(1+\alpha)\Delta T \tag{4.23}$$

where α represents the thermo-optic and thermal expansion contribution.

—

4.12.1 Pressure Measurement

When pressure is applied to the grating structure, it alters both the refractive index and the grating pitch. These changes result in a shift in the reflected Bragg wavelength, enabling pressure measurement.

$$\frac{\Delta\lambda_{bP}}{\lambda_B} = \left(\frac{1}{\Lambda}\frac{\partial\Lambda}{\partial P} + \frac{1}{n}\frac{\partial n}{\partial P}\right)\Delta P \tag{4.24}$$

The dominant contribution typically arises from refractive index variation.

The strain induced by pressure is given by:

$$\frac{\Delta l}{l} = -\frac{(1-2\nu)P}{E} \tag{4.25}$$

$$\frac{\Delta n}{n} = \frac{n^2 P}{2E}(1-2\nu)(2\rho_{12}+\rho_{11}) \tag{4.26}$$

where E is Young's modulus, ν is Poisson's ratio, and ρ_{11}, ρ_{12} are strain-optic coefficients.

$$\frac{\Delta\Lambda}{\Lambda\partial P} = -\frac{(1-2\nu)}{E} \tag{4.27}$$

$$\frac{1}{n}\frac{\partial n}{\partial P} = \frac{n^2}{2E}(1-2\nu)(2\rho_{12}+\rho_{11}) \tag{4.28}$$

$$\frac{\Delta\lambda_B}{\lambda_B} = \left(\frac{1}{\Lambda}\frac{\partial\Lambda}{\partial P} + \frac{1}{n}\frac{\partial n}{\partial P}\right)\Delta P \tag{4.29}$$

$$\Delta\lambda_{BP} = \lambda_B \left[-\frac{(1-2\nu)}{E} + \frac{n^2}{2E}(1-2\nu)(2\rho_{12}+\rho_{11}) \right] \Delta P \tag{4.30}$$

Although pressure sensing is not the primary focus of this work, it is included to demonstrate the broader sensing capability and versatility of FBG-based systems.

—

4.13 Conclusion

This chapter has presented the fundamental principles underlying distributed photonic sensing and its relevance to modern power transmission systems. As power networks scale and complexity increase, particularly with the growing deployment of HVDC transmission infrastructure, the need for sensing technologies capable of supporting wide-area monitoring and fast protection becomes increasingly critical.

Distributed sensing architectures offer significant advantages by enabling measurements across spatially distributed locations, thereby improving system observability and enhancing protection and control strategies. Photonic sensing technologies are particularly well suited to such applications due to their passive operation, electrical isolation, and immunity to electromagnetic interference.

The chapter has introduced fibre Bragg grating (FBG) sensors, including their operating principles, fabrication techniques, structural configurations, and interrogation methods. The sensing mechanism was described by wavelength-selective reflection arising from periodic refractive-index modulation within the fibre core, in which external perturbations, such as strain, temperature, and pressure, induce measurable wavelength shifts.

Building on these principles, the hybrid low-voltage transducer (LVT) architecture was presented. This configuration integrates a piezoelectric transducer with an FBG sensor to establish an electromechanical-to-optical transduction pathway. Electrical signals are first converted into mechanical strain via the piezoelectric effect, and subsequently encoded as wavelength shifts in the FBG. This approach enables indirect measurement of electrical quantities in the optical domain while maintaining electrical

isolation.

Although photonic sensing has demonstrated successful deployment in HVAC systems, its application to HVDC networks remains limited. HVDC systems impose additional challenges due to the absence of natural current zero-crossings and the rapid propagation of fault transients. Consequently, sensing technologies capable of delivering high-fidelity, distributed measurements are of considerable importance.

The theoretical framework developed in this chapter forms the basis for the sensing methodology proposed in this work. Subsequent chapters present the modelling, calibration, and experimental validation of the hybrid LVT-based photonic sensing system for HVDC current monitoring and protection applications.

Chapter 4 References

[1] C. Pendão and I. Silva, "Optical fiber sensors and sensing networks: Overview of the main principles and applications," *Sensors*, Oct. 2022, pp. 2–6. DOI: 10.3390/s22197554.

[2] G. Fusiek and P. Niewczas, "Photonic voltage transducer with lightning impulse protection for distributed monitoring of mv networks," *Sensors*, vol. 20, no. 17, pp. 1–23, Sep. 2020. DOI: 10.3390/s20174830.

[3] P. Niewczas, A. Dyśko, C. Booth, and P. Orr, *Fbg-based fibre-optic current sensors for power systems protection: Laboratory evaluation*, pp. 3–7, 2009. Accessed: Apr. 4, 2024. [Online]. Available: http://strathprints.strath.ac.uk/.

[4] G. Fusiek and P. Niewczas, "Preliminary characterisation of an optical current sensor for hvdc networks," in *Proc. IEEE I2MTC*, Piscataway, NJ, 2018, pp. 1–3.

[5] Y.-J. Rao, "In-fibre bragg grating sensors," *Measurement Science and Technology*, vol. 8, pp. 1–4, 1997.

[6] C. E. Campanella, A. Cuccovillo, C. Campanella, A. Yurt, and V. M. N. Passaro, "Fibre bragg grating based strain sensors: Review of technology and applications," *Sensors*, Sep. 2018, pp. 3–9. DOI: 10.3390/s18093115.

[7] S. S. A. Khan and M. S. Islam, "Determination of the best apodization function and grating length of linearly chirped fiber bragg grating for dispersion compensation," *Journal of Communications*, vol. 7, no. 11, pp. 840–846, 2012. DOI: 10.4304/jcm.7.11.840-846.

[8] K. O. H. et al., "Chirped in-fiber bragg gratings for compensation of optical-fiber dispersion," 1994, pp. 3–5.

[9] D. Tosi, "Review of chirped fiber bragg grating (cfbg) fiber-optic sensors and their applications," *Sensors*, Jul. 2018, pp. 4–8. DOI: 10.3390/s18072147.

[10] S. Maiti and V. Singh, *Performance Analysis of Apodized Fiber Bragg Gratings for Sensing Applications*. Springer, 2020. DOI: 10.1007/s12633-020-00852-0.

[11] T. Erdogan, "Fiber grating spectra," *IEEE Journal of Lightwave Technology*, 1997, pp. 2–6. DOI: 10.1109/50.618322.

[12] T. Imai, T. Komukai, and M. Nakazawa, "Dispersion tuning of a linearly chirped fiber bragg grating without a center wavelength shift by applying a strain gradient," *IEEE Photonics Technology Letters*, 1998, pp. 2–4.

[13] L. Wei and J. W. Y. Lit, "Phase-shifted bragg grating filters with symmetrical structures," *IEEE*, vol. 15, no. 8, pp. 2–4, 1997.

[14] M. D. Nadeem, S. K. Raghuwanshi, and S. Kumar, "Recent advancement of phase shifted fiber bragg grating sensor for ultrasonic wave application: A review," *IEEE Sensors Journal*, vol. 22, no. 8, pp. 4–7, 2022. DOI: 10.1109/JSEN.2022.3158090.

[15] B. Das, D. Srivastava, U. K. Tiwari, and B. C. Choudhary, "Dynamic strain response of a π-phase-shifted fbg sensor with phase-sensitive detection," *OSA Continuum*, vol. 1, no. 4, pp. 3–4, 2018. DOI: 10.1364/osac.1.001172.

[16] S. K. I. et al., "Optimization of fiber bragg grating parameters for sensing applications," in *SPIE Fiber Optic Sensors and Applications XIV*, pp. 3–5, 2017. DOI: 10.1117/12.2262103.

[17] J. Chen, B. Liu, and H. Zhang, "Review of fiber bragg grating sensor technology," *Frontiers of Optoelectronics*, 2011, pp. 3–4. DOI: 10.1007/s12200-011-0130-4.

[18] S. K. I. et al., "Enabling technologies for fiber optic sensing," in *SPIE Optical Sensing and Detection IV*, pp. 2–11, 2016. DOI: 10.1117/12.2234975.

[19] M. Optics, *Optical sensing interrogator sm130*, pp. 2–4, 2020. Accessed: Apr. 15, 2024. [Online]. Available: http://www.micronoptics.com/product_designation.php.

[20] A. OSA, *Apex osa for interrogating fiber bragg grating sensors*, pp. 1–3.

[21] I. Photonics, *I-mon usb interrogation monitor specifications*, pp. 1–4, 2022. Accessed: Jun. 20, 2022. [Online]. Available: http://www.ibsen.com.

[22] D. R. et al., "A fiber-bragg-grating-based sensor for simultaneous ac current and temperature measurement," *IEEE Sensors Journal*, vol. 6, no. 6, pp. 1539–1542, 2006.

[23] R. Pallás-Areny and J. G. Webster, *Sensors and Signal Conditioning*, 2nd. Wiley, 2001, pp. 351–354.

Chapter 5

Photonic Current Sensor Design and Components Evaluation

5.1 Introduction

This chapter presents the design methodology, analytical modelling, and experimental evaluation of the proposed optical current sensing (OCS) system for HVDC current monitoring. The sensor architecture integrates a resistive shunt current transducer, an ultra-low-voltage energy harvesting circuit, a nonlinear signal conditioning stage, and a low-voltage transducer (LVT), which converts the conditioned electrical signal into an optical response using a piezoelectric–fibre Bragg grating (FBG) structure. The objective of this chapter is to evaluate the behaviour and performance of these subsystems and to demonstrate how their integration enables reliable current measurement in HVDC environments.

The chapter begins by introducing the sensor concept and the measurement requirements imposed by HVDC systems, particularly the need for accurate current measurement over a wide dynamic range while maintaining sensitivity to low-level signals. The overall sensing architecture is then described, highlighting the function and interaction of each subsystem within the measurement chain.

A detailed analytical investigation of the individual sensor building blocks is sub-

sequently presented. The resistive shunt is examined as the primary current-to-voltage transducer, including the derivation of its electrical characteristics, thermal behaviour, and geometric design considerations. The ultra-low-voltage energy harvesting circuit is then analysed to demonstrate its capability to extract usable power from the millivolt-level voltage developed across the shunt, thereby enabling autonomous operation of the sensor electronics.

The nonlinear signal conditioning stage is further investigated, with emphasis on the diode-controlled feedback mechanism that enables adaptive gain behaviour. This approach provides high gain for low-level signals while compressing higher-amplitude inputs. Analytical derivation of the amplifier transfer characteristics and switching thresholds is presented to explain the observed nonlinear behaviour.

Finally, the operation of the low-voltage transducer (LVT) is analysed. The electromechanical response of the piezoelectric actuator and its interaction with the fibre Bragg grating sensing element are examined to characterise the voltage-to-strain conversion and the dynamic response of the sensing system. Experimental results are presented to validate the performance of the complete sensing chain and to demonstrate its capability to capture both steady-state currents and fast transient fault signals.

Overall, the analytical and experimental investigations presented in this chapter establish the performance limits, operational characteristics, and practical constraints of the proposed optical current sensor, forming a foundation for its application in HVDC monitoring, protection, and control systems.

5.2 Sensor Concept

The proposed sensor architecture is illustrated in Fig. 5.1. A low-resistance shunt is employed as the primary current-to-voltage transducer, designed to produce a nominal output of approximately 50 mV at a rated line current of 1 kA. The voltage developed across the shunt serves a dual function: it provides the measurement signal and simultaneously acts as the input source for an ultra-low-voltage energy harvester.

The energy harvester constitutes a key innovation in the system, enabling extraction

and conversion of millivolt-level electrical energy into a usable supply for the sensor electronics. However, the shunt output alone is insufficient to directly drive the low-voltage transducer (LVT), which is a hybrid piezoelectric–photonic device requiring an operating voltage of approximately 1 V. Consequently, a signal amplification stage is required.

This amplification is realised using a dedicated low-power precision operational amplifier, powered entirely by the harvested energy. The amplifier boosts the shunt voltage to a level suitable for driving the LVT, thereby enabling the complete sensing system to operate in a self-sustained and passive manner without reliance on an external power supply.

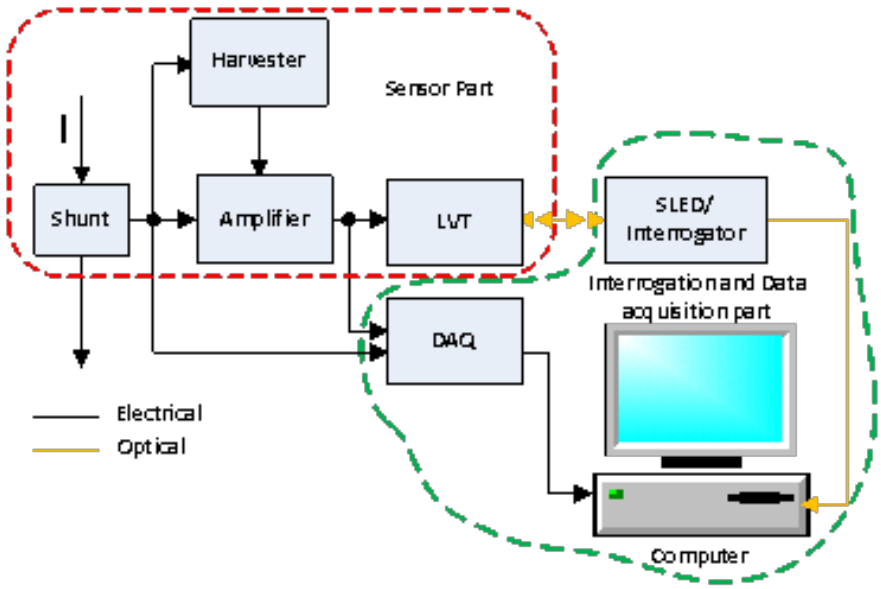

Figure 5.1: HVDC sensor concept

Due to the stringent power constraints imposed by the energy harvesting mechanism, all system components were carefully selected to operate within an ultra-low-power budget. The design and performance of these individual components are analysed in detail in the subsequent sections.

5.3 Measurement Requirements

The rated current of high-voltage direct current (HVDC) transmission systems typically lies in the range of 1 kA to several kiloamperes, depending on transmission capacity and converter station design [1], [2]. During normal operation, the line current may deviate from its nominal value due to variations in power transfer, converter operating conditions, and system control actions. Under abnormal conditions such as short circuits or insulation failures, the current can rise to several times its nominal value within a very short time interval.

Consequently, a current measurement device for HVDC applications must accurately resolve both low-level currents under steady-state conditions and high-magnitude current excursions during transient fault events.

5.4 Design Justification of Shunt Resistance and Power Dissipation

The selection of shunt resistance and its corresponding power dissipation is governed by two competing requirements: thermal constraints within the HVDC cable environment and measurement sensitivity. These impose conflicting design conditions, requiring a balanced optimisation.

For HVDC transmission systems, a nominal current of 1 kA is adopted as the design reference. The power dissipated in the shunt due to Joule heating is given by

$$P = I^2 R \tag{5.1}$$

Even small resistance values can result in significant heat generation at high current levels. In this work, a maximum allowable power dissipation of 50 W is selected based on the thermal limitations of the cable splice joint environment, particularly the presence of XLPE insulation, which typically has a continuous operating temperature limit of approximately 70°C.

The temperature rise of the shunt can be approximated as

$$\Delta T = P \cdot R_{\text{th}} \tag{5.2}$$

where R_{th} is the effective thermal resistance between the shunt and its surroundings. Due to the confined geometry of the splice joint and limited heat dissipation paths, excessive power dissipation may lead to:

- Degradation of insulation materials
- Drift in shunt resistance due to temperature dependence
- Reduced long-term reliability of the sensing system

By constraining power dissipation to approximately 50 W, the resulting temperature rise remains within acceptable limits of XLPE insulation, ensuring safe operation.

Substituting this constraint into (5.1) gives the required shunt resistance:

$$R = \frac{P}{I^2} = \frac{50}{(1000)^2} = 50\ \mu\Omega \tag{5.3}$$

This produces a corresponding voltage drop of

$$V = IR = 1000 \times 50\ \mu\Omega = 50\ \text{mV} \tag{5.4}$$

This voltage level is sufficient for signal conditioning while remaining compatible with ultra-low-voltage energy harvesting.

The selected value of 50 $\mu\Omega$ therefore represents an optimal trade-off between thermal constraints and measurement sensitivity. Lower resistance values would reduce power dissipation but result in reduced signal amplitude and increased susceptibility to noise, particularly at low current levels. Conversely, higher resistance values would improve signal magnitude but lead to excessive heat generation.

Furthermore, IEC 61869-14 requires accurate current measurement down to 5% of nominal current. For a 1 kA system, this corresponds to 50 A, yielding a minimum shunt voltage of

$$V = IR = 50 \times 50\ \mu\Omega = 2.5\ \text{mV} \tag{5.5}$$

This defines the lower bound of the measurable signal and directly influences the design of subsequent amplification and energy harvesting stages.

In summary, the combined selection of 50 W power dissipation and 50 $\mu\Omega$ resistance ensures thermal safety while maintaining adequate signal detectability across the required operating range.

5.5 Measurement Range Requirement

According to IEC 61869-14, DC current measurement devices must maintain specified accuracy over an extended range, typically from 5% to 300% of nominal current for an accuracy limit factor (KALF) of 3.

For a nominal current of 1 kA:

$$I_{\text{min}} = 0.05 \times 1000 = 50\ \text{A} \tag{5.6}$$

$$I_{\text{max}} = 3 \times 1000 = 3000\ \text{A} \tag{5.7}$$

These values define the minimum and maximum current levels that the sensing system must measure while maintaining acceptable accuracy.

5.6 Justification for the Energy Harvester Operating Range

The proposed optical current sensor operates as a self-powered system, with energy harvested directly from the shunt voltage. However, commercially available ultra-low-voltage energy harvesting circuits impose minimum input voltage constraints.

The LTC3108 energy harvesting converter is capable of operating with input voltages as low as 20 mV when used with a suitable step-up transformer. Consequently, the harvester operates within an input range of approximately 20 mV to 400 mV.

The lower limit (20 mV) exceeds the 2.5 mV produced at 5% nominal current, implying that the harvester becomes active only when:

$$I = \frac{20 \text{ mV}}{50 \ \mu\Omega} = 400 \text{ A} \tag{5.8}$$

This corresponds to approximately 40% of nominal current.

However, the inclusion of an energy storage capacitor allows the system to sustain operation once initial start-up has been achieved, even if the input voltage subsequently drops below the start-up threshold. This ensures continuous operation during transient current variations.

The upper limit of 400 mV corresponds to fault conditions where current levels may significantly exceed nominal values. Designing for this range ensures sufficient energy availability without exceeding device limitations.

Based on these considerations, the sensing system must satisfy the following requirements:

- Accurate measurement from 5% to 300% of nominal current in accordance with IEC standards
- Reliable amplification of signals ranging from 2.5 mV to several hundred millivolts
- Controlled thermal dissipation within the cable joint structure
- Autonomous operation through energy harvesting

The resulting optical current sensor (OCS) system specification is summarised in Table 5.1.

5.6.1 Amplification Need and Measurement Standard

The voltage developed across the shunt is on the order of a few millivolts and is therefore insufficient to directly power auxiliary system components. Consequently, an energy harvesting stage is required to extract this low-level voltage and convert it into usable electrical power for the supporting circuitry.

Table 5.1: System specification

Parameter	**Specification (Range)**
Current (A)	1000
Voltage (V)	0.05
Resistance (Ω)	50 $\mu\Omega$
Harvester Input (V)	0.020 – 0.400
Harvester Output (V)	1 – 5
Amplifier Gain (V/V)	$\sim$13 to $\geq$100
LVT Input (V)	1
Power Dissipation (W)	$\sim$50
Temperature Limit (°C)	$\sim$70

In parallel, the low-amplitude nature of the shunt signal necessitates high-gain amplification to enable reliable detection at the lower operating boundaries, specifically 5% and 20% of nominal current, corresponding to approximately 2.5 mV and 10 mV, respectively. At the same time, the signal conditioning architecture must accommodate higher-amplitude operating conditions (up to 120% and 300% of nominal current) by compressing the output to remain within the measurable range of the acquisition system.

This dual requirement of high sensitivity at low signal levels and controlled response at high amplitudes is achieved without compromising measurement accuracy. Compliance with IEC 61869-14 requires that the sensor maintains specified accuracy limits up to a multiple of the nominal current defined by the accuracy limit factor (KALF).

The required current amplitude (ratio) error limits defined by IEC 61869-14 for DC current transformers (DCCTs) are summarised in Table 5.2. In this standard, K_{pcr} and K_{ALF} represent the rated extended primary current factor and the accuracy limit factor, respectively. Typical values of K_{ALF} include 3, 6, 10, and 20 [3].

For this investigation, a K_{ALF} value of 3 is selected. Consequently, the proposed sensing system is required to maintain compliant measurement performance over a current range spanning 5% to 300% of the nominal value.

Table 5.2: Limits of ratio error for DCCT as per IEC 61869-14

Accuracy Class	**Ratio Error (%) at Current (% of Rated)**				
	5	20	100	K_{pcr}	K_{ALF}
0.1	1	0.25	0.1	0.1	1
0.2	2	0.5	0.2	0.2	2
0.5	3.5	1	0.5	0.5	5
1	5	2	1	1	10

5.6.2 Transient Detection Requirement

With respect to fault detection, the sensor must exhibit sufficient bandwidth and sensitivity to capture fast transient signatures associated with short circuits, insulation failures, and other fault events. In HVDC networks, fault-induced travelling waves propagate along transmission lines at velocities determined by line parameters, typically on the order of 10^6–10^8 m/s.

Consequently, the sensor must be capable of detecting the onset of a fault and resolving the arrival of associated transient wavefronts within millisecond time scales. For practical protection applications, the relevant detection window lies within approximately 2 ms to 10 ms, corresponding to the time required for fault identification and initiation of protective actions such as converter blocking and DC breaker operation.

Accurate capture of transient behaviour within this time frame is essential to ensure rapid fault isolation, limit fault current escalation, prevent equipment damage, and maintain system stability. The performance of the proposed sensor with respect to these requirements is evaluated through a combination of simulation studies and experimental measurements, providing a quantitative assessment of its dynamic response and bandwidth capability.

5.6.3 Software Tools Utilised in Sensor Design and Analysis

A suite of advanced software tools supported the analysis and validation of the sensor, each contributing to different aspects of modelling, simulation, and experimental validation.

LabVIEW

National Instruments LabVIEW was used for data acquisition, sensor control, and signal processing [2], [4], [5]. Its graphical programming environment enabled seamless integration with measurement hardware, facilitating real-time monitoring and control. It was particularly effective for handling time-sensitive datasets associated with fault detection and thermal response, while automation improved repeatability and reduced human error.

COMSOL Multiphysics

COMSOL Multiphysics was employed for thermal and electromagnetic simulations using finite element analysis (FEA) [6], [7], [8]. Thermal simulations provided insight into heat distribution and hotspot formation due to Joule heating, while electrostatic modelling enabled evaluation of electric field interactions within the HVDC environment. These simulations supported design validation prior to prototype development.

AutoCAD and Autodesk Fusion 360

AutoCAD was used for precise 2D drafting [9], [10], while Autodesk Fusion 360 enabled 3D modelling and realistic visualisation of the sensor structure [11], [12]. Together, they ensured mechanical compatibility, spatial optimisation, and accurate representation of the sensor assembly within the splice joint environment.

MATLAB and Simulink

MATLAB and Simulink were used for analytical modelling, signal processing, and system-level simulation [13], [14], [15], [16], [17]. MATLAB facilitated data analysis and post-processing, while Simulink enabled dynamic modelling of the sensor within an HVDC network, particularly for fault detection and transient response evaluation.

KiCAD and LTSpice

KiCAD was used for schematic capture and PCB design [18], while LTSpice was used for circuit-level simulations [19], [20]. These tools enabled optimisation of amplifier circuits, power management modules, and signal conditioning stages prior to hardware implementation.

I-MON Evaluation Software

The I-MON evaluation software developed by IBSEN Photonics was used for interrogating fibre Bragg grating (FBG) responses within the LVT. It enables real-time monitoring of wavelength shifts based on the Bragg condition, providing high-resolution detection of strain-induced optical changes. Its transmission grating technology ensures high-precision wavelength measurement, making it essential for optical sensing applications.

5.6.4 Sensor Building Blocks

The sensor is composed of interconnected subsystems designed to operate cohesively under HVDC conditions. The modular architecture ensures that each subsystem complements the others while maintaining efficiency in challenging environments. The main components are:

- Shunt
- Energy Harvester
- Amplifier
- Low Voltage Transducer (LVT)

The complete sensing system is embedded within a cable splice joint, as illustrated in Fig. **??**.

5.6.5 Shunt

The primary sensing element is the shunt, implemented as a butt splice joint connector serving a dual purpose: electrical continuity between cable sections and current measurement. It provides a low-resistance path for current flow while generating a measurable voltage drop.

The selected shunt resistance is in the micro-ohm range (50 $\mu\Omega$), ensuring minimal power dissipation while maintaining measurable signal levels. The material chosen is manganin, an alloy composed of approximately 84% copper, 12% manganese, and 4% nickel, with a temperature coefficient of resistance (TCR) of approximately ± 10 ppm/°C. This low TCR ensures resistance stability under thermal variation, which is critical for accurate current measurement.

5.6.6 Electrical, Thermal and Material Design of the Shunt

Electrical, thermal, and material considerations govern the design of the shunt. From an electrical perspective, the voltage-current relationship is given by

$$V = IR \tag{5.9}$$

Thermally, the resistance must be low enough to limit Joule heating, ensuring operation within the thermal constraints of the splice joint. Material selection further ensures stability under temperature variation, with manganin providing significantly lower TCR compared to copper.

5.6.7 Shunt Geometry and Dimensional Design

The resistance of the shunt is defined by

$$R = \rho \frac{L}{A} \tag{5.10}$$

or equivalently,

$$R = \rho \frac{L}{\pi r^2} \tag{5.11}$$

Rearranging gives the required shunt length:

$$L = \frac{\pi V r^2}{\rho I} \tag{5.12}$$

Using a conductor cross-sectional area of 800 mm^2, the corresponding radius is 15.86 mm, and the calculated shunt length is approximately 90 mm. This ensures compatibility with HVDC cable systems while maintaining acceptable current density and thermal performance.

Cable specifications from the ABB submarine cable catalogue are summarised in Table 5.3.

Table 5.3: ABB submarine cable datasheet (Table 36)

Cross Section (mm^2)	**Wide Spacing (A)**	**Close Spacing (A)**
185	580	445
240	670	505
300	750	560
400	845	620
500	950	690
630	1065	760
800	1180	830
1000	1290	895

Also, cable specifications from the ABB submarine cable catalogue (Table 40) [21], presented in Table 5.4, provide detailed information on cable structural dimensions, insulation thickness, capacitance, and inductance per unit length. These parameters are essential for sensor sizing and for estimating signal propagation velocity based on line characteristics.

In summary, the shunt geometry and design parameters are defined as follows:

- Current, $I = 1000$ A
- Resistivity, $\rho = 45 \times 10^{-8}\ \Omega \cdot \mathrm{m}$

- Shunt length, $L = 0.09$ m
- Voltage drop, $V = 50$ mV
- Radius, $r = 15.86$ mm

The inner radius was neglected and filled with material in the final design, as simulation results indicated negligible impact on the voltage distribution. The resulting shunt geometry and dimensions are illustrated in Fig. 5.2 to Fig. 5.6. The conceptual configuration and internal layout of the shunt are further shown in Fig. 5.7 to Fig. 5.9.

Table 5.4: Cable cross section and conductor diameter

Cross-section (mm^2)	**Conductor Diameter (mm)**	**Insulation Thickness (mm)**	**Diameter over Insulation (mm)**	**Lead Sheath Thickness (mm)**	**Outer Diameter (mm)**	**Weight (Al) (kg/m)**	**Weight (Cu) (kg/m)**	**Capacitance (μF/km)**	**Charging Current (A/km)**	**Inductance (mH/km)**
630	29.8	28.0	89.2	3.1	123.4	23.3	35.2	0.14	8.8	1.40
800	33.7	27.0	91.1	3.1	125.9	24.3	37.5	0.15	9.7	1.37
1000	37.9	26.0	93.3	3.1	128.1	25.3	39.9	0.17	10.7	1.35
1200	41.2	25.0	94.6	3.1	129.4	26.1	42.0	0.18	11.1	1.33
1400	44.4	25.0	97.8	3.1	132.8	27.4	44.9	0.19	11.6	1.32
1600	47.4	25.0	100.8	3.1	135.8	28.7	47.7	0.20	12.1	1.31

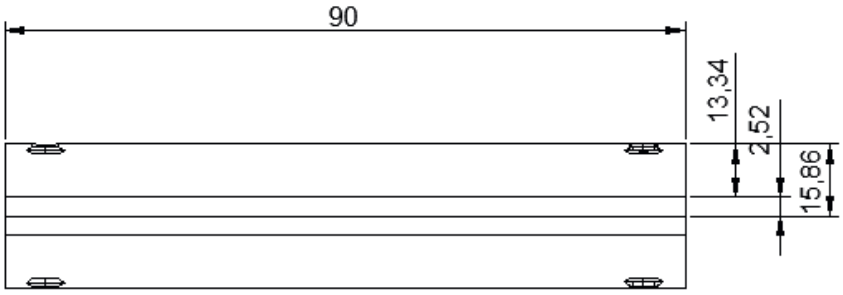

Figure 5.2: Shunt design dimension

Figure 5.3: Realistic view of the shunt design

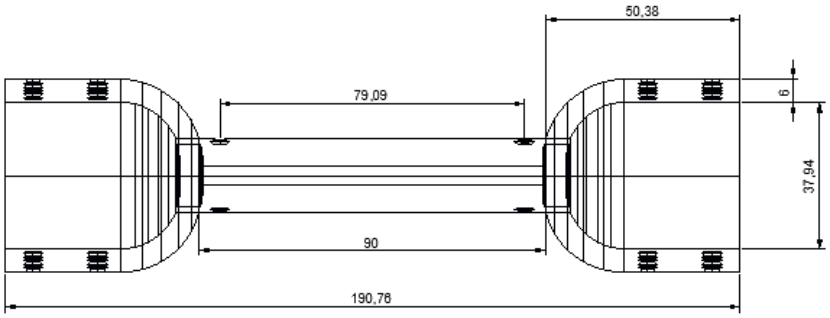

Figure 5.4: Shunt butt wireframe assembly

Figure 5.5: Shunt realistic butt assembly

Figure 5.6: Isometric view of shunt assembly

Figure 5.7: Conceptual shunt (front view)

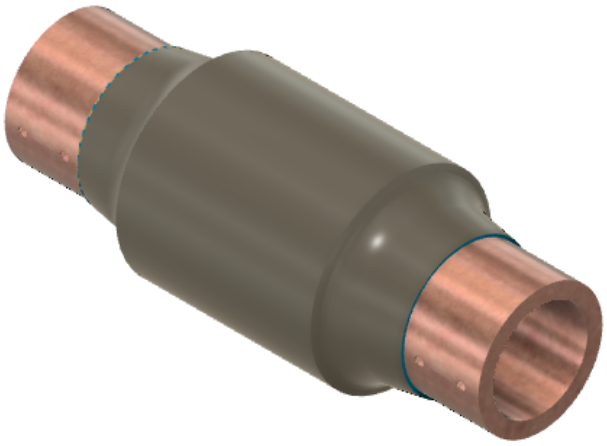

Figure 5.8: Conceptual shunt for splice joint connection (isometric view)

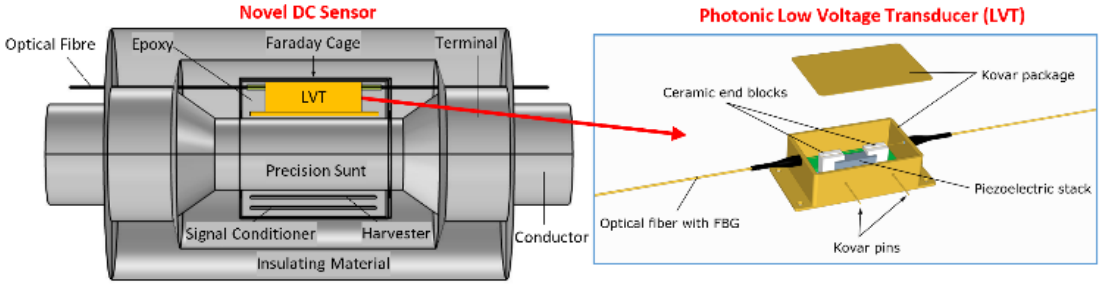

Figure 5.9: Internal view of the shunt

5.6.8 Voltage Drop Across the Shunt

The cable crimping joint has an inner diameter of 37.94 mm and an outer diameter of 43.94 mm, corresponding to a wall thickness of 6 mm. This provides the required mechanical strength for crimping while ensuring structural integrity. The crimping joint section is manufactured from copper to maintain material homogeneity with the incoming and outgoing cable conductors, thereby minimising contact resistance and ensuring uniform current distribution.

The conceptual design of the full sensor assembly is illustrated in Fig. 5.7 to Fig. 5.9. The voltage developed across the shunt can be analytically modelled. The shunt inherently provides proportional current-to-voltage transduction under both DC and AC excitation, provided it operates within its ohmic region. This makes it a reliable sensing element despite practical challenges associated with galvanic contact.

For AC excitation, the voltage drop across the shunt is given by:

$$V_{\text{drop}} = L\frac{di}{dt} + Ri \tag{5.13}$$

For DC conditions, this reduces to:

$$V_{\text{drop}} = IR \tag{5.14}$$

Thermal Behaviour of the Shunt

The resistance variation due to thermal effects (self-heating and ambient temperature) can be expressed as:

$$R_T = R_A\left(1 + \alpha_{TK}(T - T_A)\right) \tag{5.15}$$

or equivalently,

$$R_T = R_A\left(1 + \alpha_{TK}\Delta T\right) \tag{5.16}$$

where the temperature rise is given by:

$$\Delta T = T_{\text{self}} + T_{\text{ambient}} \tag{5.17}$$

The self-heating component arises from Joule heating:

$$P_{\text{loss}} = R(T)I^2 \tag{5.18}$$

$$T_{\text{self}} = R_{\text{th,total}} \cdot P_{\text{loss}} = R_{\text{th,total}} \cdot R(T)I^2 \tag{5.19}$$

Substituting the thermal relationships into the resistance model yields:

$$R(I, \Delta T_{\text{amb}}) = R_A \left(1 + \alpha_{TK}\Delta T_{\text{amb}} + \alpha_{TK} R_{\text{th,total}} R_A I^2\right) \tag{5.20}$$

The resulting voltage drop under thermal conditions is:

$$U_{\text{shunt}} = R(I, \Delta T_{\text{amb}})I \tag{5.21}$$

$$U_{\text{shunt}} = R_A \left(1 + \alpha_{TK}\Delta T_{\text{amb}}\right) I + \left(\alpha_{TK} R_{\text{th,total}} R_A^2\right) I^3 \tag{5.22}$$

This expression demonstrates that the shunt's voltage response exhibits a third-order polynomial characteristic under thermal stress. The linear term represents ideal ohmic behaviour, whereas the higher-order term captures nonlinear deviations arising from temperature-dependent changes in resistance.

These nonlinearities are primarily driven by the temperature coefficient of resistance (TCR) and Joule heating. As the current increases, power dissipation elevates the shunt temperature, modifying its effective resistance and causing deviation from the nominal voltage output. Consequently, even under constant current, the voltage may exceed the designed 50 mV value as thermal equilibrium shifts.

The voltage produced by the shunt serves a dual function: it serves as the input to both the energy harvester and the signal-conditioning circuitry within the embedded joint.

Embedding the sensor within the cable splice joint ensures direct electrical coupling to the conductor while eliminating air gaps, mechanical tolerances, and positional uncertainties associated with external sensors. This improves measurement repeatability, enhances signal-to-noise ratio under high di/dt conditions, and enables deployment in subsea or spatially constrained environments.

The shunt is expected to exhibit strong thermal stability due to the use of manganin, which has a low TCR. At a nominal current of 1 kA, the design maintains minimal temperature rise while producing a voltage drop of approximately 50 mV.

The material properties of the shunt and associated components are summarised in Table 5.5.

Table 5.5: Material properties of shunt splice section

Material	ϵ_r	**E (Pa)**	ν	**CTE (1/K)**	**k (W/mK)**	C_p **(J/kgK)**	σ **(S/m)**	ρ **(kg/m^3)**
Manganin	2.00	1.30×10^{11}	0.350	2.50×10^{-5}	30.0	406	2.07×10^{6}	8400
Epoxy	2.30	3.35×10^{9}	0.300	6.00×10^{-7}	0.20	800	1.00×10^{-8}	1110
XLPE	2.50	2.00×10^{8}	0.320	3.20×10^{-4}	0.33	2174	2.00×10^{-13}	930

Note: E is the Young's modulus, ν is the Poisson ratio, CTE is the coefficient of thermal expansion, k is the thermal conductivity, C_p is the specific heat capacity, σ is the electrical conductivity, ρ is the material density, and ϵ_r is the relative permittivity of the material.

5.6.9 Non-Ideal Effects in the Shunt

Although the shunt resistor offers advantages such as direct current measurement, high linearity, and wide bandwidth, it is subject to non-ideal effects that may influence measurement accuracy, particularly under high-current and transient conditions. These include contact resistance at material interfaces and parasitic inductance arising from the conductor geometry.

Contact Resistance Between Shunt and Conductors

The electrical contact resistance between the copper conductor and the manganin shunt arises because current transfer occurs through a finite number of microscopic asperities rather than across the full apparent contact area. The interface resistance can therefore be represented as the sum of the constriction and film resistances.

For a circular contact spot of radius a, the constriction resistance based on Holm's theory is approximated as:

$$R_{\text{constriction}} \approx \frac{\rho_{\text{Cu}} + \rho_{\text{Mn}}}{4a} \tag{5.23}$$

where ρ_{Cu} and ρ_{Mn} are the resistivities of copper and manganin, respectively.

If the real contact area is related to the applied force F and material hardness H, such that $A_{\text{real}} \approx \frac{F}{H}$, then the effective contact radius is:

$$a = \sqrt{\frac{F}{\pi H}} \tag{5.24}$$

Substituting into (5.23) gives:

$$R_{\text{contact}} \approx \frac{\rho_{\text{Cu}} + \rho_{\text{Mn}}}{4} \sqrt{\frac{\pi H}{F}} + R_{\text{film}} \tag{5.25}$$

This expression shows that contact resistance decreases with increasing contact force and increases with higher resistivity or oxide film formation [22], [23]. In practice, accurate determination of contact resistance requires experimental validation, typically using a four-terminal Kelvin measurement.

Parasitic Inductance of the Shunt

Although the shunt behaves predominantly as a resistive element under steady-state conditions, its physical geometry introduces a parasitic inductance that becomes relevant during fast current transients.

For a cylindrical conductor, the self-inductance is approximated as [24]:

$$L = \frac{\mu_0 l}{2\pi}\left[\ln\left(\frac{2l}{r}\right) - 1\right] \tag{5.26}$$

where l is the conductor length, r is the radius, and μ_0 is the permeability of free space.

Using the designed shunt parameters:

- $l = 0.09$ m
- $r = 0.01586$ m
- $\mu_0 = 4\pi \times 10^{-7}$ H/m

The inductance is approximately:

$$L \approx 30 \text{ nH} \tag{5.27}$$

Inductive Voltage Contribution During Faults

The voltage contribution from the shunt parasitic inductance becomes relevant during fast transient events, particularly under HVDC fault conditions, where the current exhibits a very high rate of change. To establish a realistic upper bound for this transient behaviour, the rate of rise of current is derived based on HVDC protection constraints and DC circuit breaker (DCCB) performance.

Hybrid DCCBs are typically required to operate within a response time of 2–5 ms [25], [26], [27]. Adopting the faster response of 2 ms, together with an additional 1 ms processing interval for fault detection and decision-making, and accounting for propagation delay between the fault location and the protection device, results in a

total delay of approximately 3.5 ms when optical fibre communication is employed, and 4.5 ms when propagation is considered through the XLPE cable.

For a DCCB with a maximum interrupting capability of 9 kA, the corresponding maximum rate of rise of current can be estimated as

$$\frac{dI}{dt} \approx \frac{9 \text{ kA}}{3.5 \text{ ms}} = 2.56 \text{ kA/ms} \tag{5.28}$$

for the optical-fibre-assisted case, and

$$\frac{dI}{dt} \approx \frac{9 \text{ kA}}{4.5 \text{ ms}} = 2.0 \text{ kA/ms} \tag{5.29}$$

for the XLPE propagation case.

These values represent realistic upper bounds for the transient current slope in HVDC fault scenarios. For a 500 kV DC system, the corresponding current-limiting inductance required to constrain the fault current is obtained from

$$V = L\frac{dI}{dt} \qquad \Rightarrow \qquad L = \frac{V}{dI/dt} \tag{5.30}$$

Substituting the faster transient case,

$$L = \frac{500 \times 10^3}{2.56 \times 10^6} \approx 0.195 \text{ H} = 195 \text{ mH} \tag{5.31}$$

which is consistent with typical current-limiting inductance values reported for HVDC protection systems [27].

Using the derived value of $\frac{dI}{dt}$ as a conservative estimate of the transient current slope, the voltage contribution arising from the parasitic inductance of the shunt can be expressed as

$$V_L = L_p\frac{dI}{dt} \tag{5.32}$$

where L_p is the parasitic inductance of the shunt. From the geometrical analysis of the shunt conductor, the parasitic inductance was previously estimated as

$$L_p \approx 30 \text{ nH} \tag{5.33}$$

The current rate-of-rise during the fault is estimated as

$$\frac{dI}{dt} = 2.56 \text{ kA/ms}$$

which is equivalent to

$$\frac{dI}{dt} = 2.56 \times 10^6 \text{ A/s}$$

for consistency with SI units in (5.32). Therefore,

$$V_L = L_p \frac{dI}{dt} = 30 \times 10^{-9} \times 2.56 \times 10^6 \approx 76.8 \text{ mV}.$$

That is by substituting into (5.32) using the upper-bound current slope,

$$V_L = 30 \times 10^{-9} \times 2.56 \times 10^6 \approx 76.8 \text{ mV} \tag{5.34}$$

Similarly, for the XLPE-based propagation case,

$$V_L \approx 30 \times 10^{-9} \times 2.0 \times 10^6 = 60 \text{ mV} \tag{5.35}$$

Although the fault develops and is interrupted within a millisecond timescale, the inductive voltage contribution is still evaluated using SI units for dimensional consistency. Thus, the value of 76.8 mV does not imply a seconds-scale response; rather, it represents the instantaneous voltage developed across the parasitic inductance of the shunt during the short transient interval in which the current rise rate is approximately 2.56 kA/ms. Therefore, this voltage should be interpreted as a transient component superimposed on the resistive shunt voltage during fault initiation, rather than as a sustained steady-state voltage.

These results indicate that the inductive voltage contribution during fast transient conditions is of the same order of magnitude as the nominal resistive voltage drop of the shunt (50 mV at 1 kA). Consequently, the instantaneous voltage measured across

the shunt during fault conditions consists of both resistive and inductive components.

While the resistive term dominates under steady-state conditions, the inductive component becomes significant during high $\frac{dI}{dt}$ events. This behaviour introduces additional dynamic features into the measurement signal, which may enhance sensitivity to fast transient phenomena such as travelling waves. However, it also implies that the shunt cannot be treated as a purely ohmic element under transient conditions, and appropriate consideration must be given during signal interpretation and calibration of the sensing system.

5.6.10 Energy Harvester

Energy harvesting is particularly valuable in isolated environments where conventional power sources are impractical. Established techniques include vibration, thermoelectric, RF, and photovoltaic energy harvesting [28].

In this work, energy is harvested from the voltage drop across the shunt, ranging from 20 mV to 500 mV. This enables the extraction of energy from otherwise negligible voltage levels, which is then used to power the signal conditioning circuitry.

The schematic of the harvester is shown in Fig. 5.10. The system is based on the LTC3108 integrated circuit, a specialised ultra-low-voltage step-up converter. It incorporates a resonant oscillator, a step-up transformer, synchronous rectifiers, voltage-regulation stages, and energy-storage functionality.

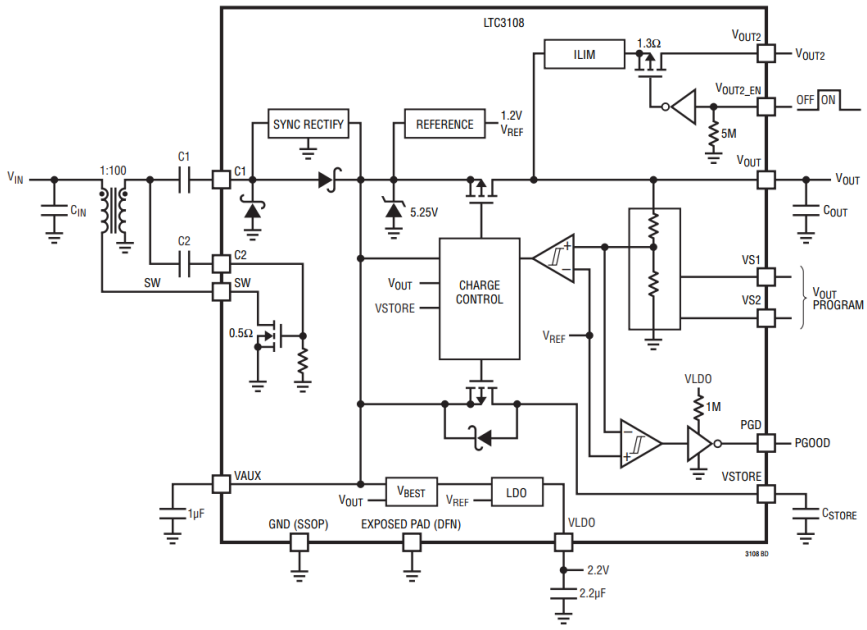

Figure 5.10: Harvester (LTC3108) circuit

The device operates by accumulating charge at an auxiliary node (VAUX), enabling stable power delivery even under intermittent input conditions. A 1:100 transformer was selected to allow operation at input voltages as low as 20 mV, with a corresponding output current of approximately 700 μA [29], [30], [31], [32].

5.6.11 Harvester Characterisation

The harvester was experimentally characterised under two output configurations: 3.3 V and 5 V. The input voltage ranged from 2.5 mV (5% nominal current) to 250 mV (500% nominal current). The corresponding op-amp response was also monitored.

The results are shown in Fig. 5.11.

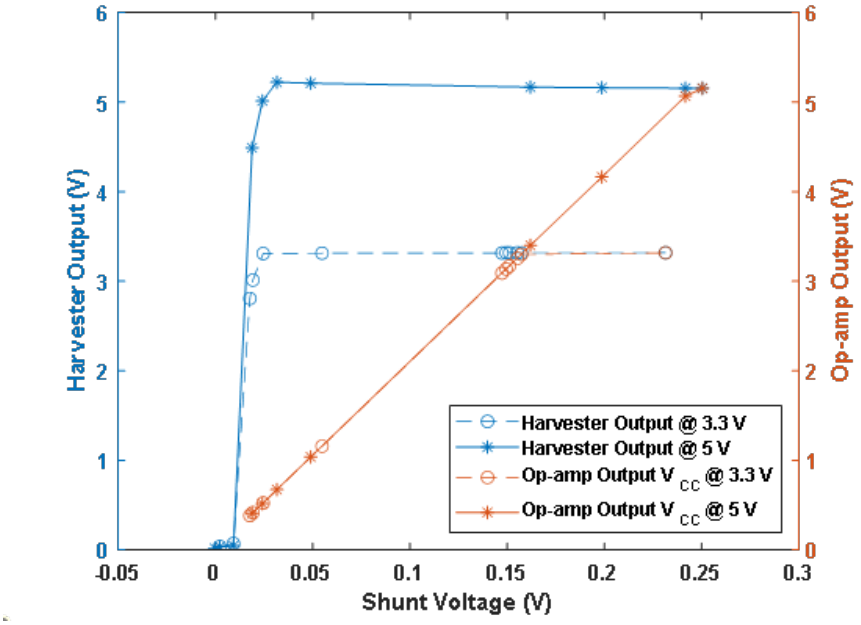

Figure 5.11: Harvester and op-amp operation characteristics

The harvester successfully generated sufficient voltage to drive the op-amp and LVT once the input reached approximately 20 mV. The op-amp exhibited a linear amplification profile up to saturation, confirming stable operation under varying conditions.

The charging and discharging behaviour of the system, governed by the storage capacitors, is illustrated in Fig. 5.12.

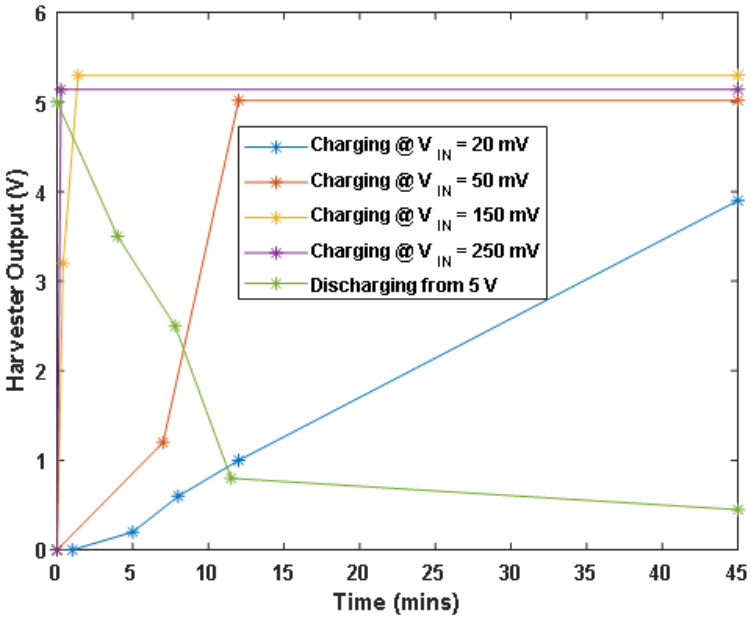

Figure 5.12: Harvester charging versus time response

Under worst-case black-start conditions, the system required approximately 12 minutes to reach full charge at a 50 mV input. The stored energy allowed the system to remain operational for up to 11 minutes during discharge, demonstrating resilience to temporary voltage drops and ensuring continued operation within defined limits.

5.6.12 Signal Conditioning

The selection of a low-voltage transducer (LVT) with a nominal operating voltage of 1 V introduces a key challenge, as the voltage developed across the shunt is on the order of a few millivolts and is therefore insufficient to directly drive the transducer. Consequently, signal amplification is required.

An initial approach employed a linear non-inverting operational amplifier configuration to scale the shunt voltage to the required level. While this provided basic functionality, it was insufficient in addressing the inherent limitations of the sensing system. In particular, the amplified signal at low input levels remained below the detection threshold of the optical interrogation system, making it difficult to distinguish between noise and valid signal.

This limitation is further compounded by the interrogation system's characteristics, which exhibit repeatability of approximately 3 pm and linearity of 5 pm [33]. At low input voltages, the signal-to-noise ratio (SNR) falls below acceptable levels, reducing measurement accuracy and sensitivity.

Limitations of Linear Amplification

A fixed-gain amplifier presents a fundamental trade-off. Increasing gain improves sensitivity to low-level signals but reduces dynamic range and leads to saturation at higher input levels. Conversely, reducing gain preserves dynamic range but limits the detectability of weak signals. This trade-off renders a linear amplification strategy unsuitable for the wide dynamic range required in HVDC current sensing.

5.6.13 Proposed Nonlinear Amplification Strategy

To overcome the limitations of linear amplification in low-signal sensing applications, a nonlinear signal conditioning approach is adopted. The amplifier is implemented in a non-inverting configuration with a segmented feedback network comprising multiple resistors and diode-controlled branches. This architecture enables the effective gain of the amplifier to vary as a function of the signal amplitude, thereby enhancing sensitivity at low input levels while preventing saturation at higher amplitudes.

Under DC steady-state conditions, the feedback capacitor behaves as an open circuit, and the circuit behaviour is governed solely by the resistive feedback network and the conduction states of the diodes.

The schematic diagram of the nonlinear op-amp circuit is shown in Fig. 5.13.

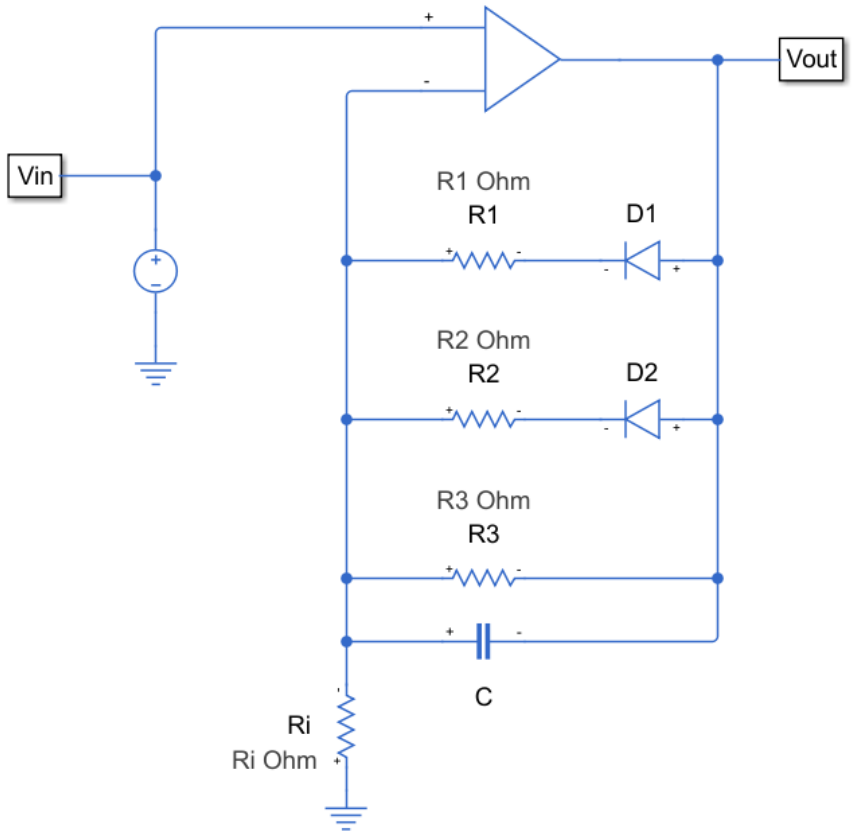

Figure 5.13: Non-linear op-amp circuit configuration

5.6.14 Piecewise Analytical Derivation of the Nonlinear Amplifier

The nonlinear amplifier operates in distinct regions determined by the conduction states of the diodes. A rigorous analysis therefore requires a piecewise formulation. The derivation is carried out by applying Kirchhoff's Current Law (KCL) at the inverting input node, assuming ideal op-amp behaviour such that

$$v^- \approx v^+ = v_{in} \tag{5.36}$$

—

Region 1: No Diode Conduction

At low input levels, both diodes are reverse biased. Only R_3 contributes to the feedback path. Applying KCL gives

$$\frac{v_o - v_{in}}{R_3} = \frac{v_{in}}{R_i} \tag{5.37}$$

Solving,

$$v_o = \left(1 + \frac{R_3}{R_i}\right) v_{in} \tag{5.38}$$

and the corresponding gain is

$$G_1 = 1 + \frac{R_3}{R_i} \tag{5.39}$$

The first switching event occurs when diode D_2 becomes forward biased:

$$v_o - v_{in} = V_{D2} \tag{5.40}$$

Substituting gives

$$V_{\text{in,th1}} = R_i \left(\frac{V_{D2}}{R_3}\right) \tag{5.41}$$

—

Region 2: Diode D_2 Conducting

When D_2 conducts, R_2 is introduced into the feedback network. Applying KCL,

$$\frac{v_o - v_{in}}{R_3} + \frac{v_o - v_{in} - V_{D2}}{R_2} = \frac{v_{in}}{R_i} \tag{5.42}$$

Define

$$\frac{1}{R_{\text{eq23}}} = \frac{1}{R_2} + \frac{1}{R_3} \tag{5.43}$$

Then

$$v_o = \left(1 + \frac{R_{\text{eq23}}}{R_i}\right) v_{in} + \frac{V_{D2} R_{\text{eq23}}}{R_2} \tag{5.44}$$

with gain

$$G_2 = 1 + \frac{R_{\text{eq23}}}{R_i} \tag{5.45}$$

The second switching event occurs when diode D_1 conducts:

$$v_o - v_{in} = V_{D1} \tag{5.46}$$

Substituting gives

$$V_{\text{in,th2}} = R_i \left(\frac{V_{D1} - V_{D2}}{R_2} + \frac{V_{D1}}{R_3}\right) \tag{5.47}$$

—

Region 3: Both Diodes Conducting

When both diodes conduct, all feedback branches are active:

$$\frac{v_o - v_{in}}{R_3} + \frac{v_o - v_{in} - V_{D2}}{R_2} + \frac{v_o - v_{in} - V_{D1}}{R_1} = \frac{v_{in}}{R_i} \tag{5.48}$$

Define

$$\frac{1}{R_{\text{eq123}}} = \frac{1}{R_1} + \frac{1}{R_2} + \frac{1}{R_3} \tag{5.49}$$

Then

$$v_o = \left(1 + \frac{R_{\text{eq123}}}{R_i}\right) v_{in} + \frac{V_{D1} R_{\text{eq123}}}{R_1} + \frac{V_{D2} R_{\text{eq123}}}{R_2} \tag{5.50}$$

and

$$G_3 = 1 + \frac{R_{\text{eq123}}}{R_i} \tag{5.51}$$

—

5.6.15 Design Methodology of the Nonlinear Amplifier

Three key constraints govern the amplifier design:

- Limited power availability from the energy harvester (approximately 700 μA),
- Requirement for high gain at low signal levels,
- Need for gain compression to avoid saturation.

To minimise current consumption, mega-ohm range resistors are selected. High initial gain is achieved using $R_3 \gg R_i$, while diode-controlled branches progressively reduce the effective feedback resistance, enabling dynamic range extension.

—

5.6.16 Numerical Evaluation of the Switching Thresholds

Using

$$R_i = 50\ \text{k}\Omega, \quad R_3 = 15\ \text{M}\Omega, \quad R_2 = 2\ \text{M}\Omega, \quad R_1 = 1\ \text{M}\Omega \tag{5.52}$$

and

$$V_{D2} \approx 0.2\ \text{V}, \quad V_{D1} \approx 0.3\ \text{V} \tag{5.53}$$

the Region 1 gain is

$$G_1 = 301 \tag{5.54}$$

The first threshold becomes

$$V_{\text{in,th1}} \approx 0.667 \text{ mV} \tag{5.55}$$

The equivalent resistance in Region 2 is

$$R_{\text{eq23}} \approx 1.765 \text{ M}\Omega \tag{5.56}$$

with

$$G_2 \approx 36.3 \tag{5.57}$$

The second threshold becomes

$$V_{\text{in,th2}} \approx 3.50 \text{ mV} \tag{5.58}$$

The Region 3 resistance is

$$R_{\text{eq123}} \approx 0.638 \text{ M}\Omega \tag{5.59}$$

and

$$G_3 \approx 13.8 \tag{5.60}$$

—

5.6.17 Summary of Amplifier Behaviour

The nonlinear amplifier, therefore, operates in three regions:

- Region 1: $V_{in} < 0.667$ mV (high gain)
- Region 2: $0.667 \text{ mV} \leq V_{in} < 3.50$ mV (moderate gain)
- Region 3: $V_{in} \geq 3.50$ mV (compressed gain)

This confirms that the amplifier provides high sensitivity at low signal levels and

progressive gain compression at higher amplitudes, thereby extending the effective dynamic range while remaining compatible with the constraints of self-powered operation.

5.6.18 Determination of the Circuit Time Constant

Under steady-state DC operation, the capacitor behaves as an open circuit because the excitation frequency approaches zero and its impedance

$$Z_c = \frac{1}{2\pi f C} \tag{5.61}$$

tends to infinity. Under transient conditions, however, the capacitor influences the dynamic response of the circuit.

The transient response is governed by the time constant

$$\tau = R_{\text{th}} C \tag{5.62}$$

where R_{th} is the Thevenin equivalent resistance seen by the capacitor with independent sources set to zero.

To determine R_{th}, the capacitor is removed conceptually and the resistance seen at its terminals is evaluated. Because the amplifier contains diode-controlled feedback branches, the equivalent resistance must be determined piecewise.

Region 1: No diode conduction

At low output voltages, all diodes are reverse biased, and only R_{f1} is active. Thus,

$$R_{\text{th1}} = R_3 \tag{5.63}$$

and the corresponding time constant is

$$\tau_1 = R_3 C \tag{5.64}$$

Region 2: First diode conduction

When the output voltage exceeds V_{f1}, the first diode becomes forward biased and R_{f2} is introduced in parallel with R_{f1}. Therefore,

$$R_{\text{th2}} = R_3 \parallel R_2 \tag{5.65}$$

and

$$\tau_2 = (R_3 \parallel R_2)C \tag{5.66}$$

Region 3: Both diodes conducting

When the output voltage exceeds V_{f2}, both diode-controlled branches are active, giving

$$R_{\text{th3}} = R_3 \parallel R_2 \parallel R_1 \tag{5.67}$$

and

$$\tau_3 = (R_3 \parallel R_2 \parallel R_1)C \tag{5.68}$$

This analysis assumes that:

- the diodes behave as ideal switches when forward biased,
- their dynamic resistance is negligible compared with the feedback resistors, and
- the operational amplifier bandwidth is sufficiently high such that the RC network governs the dominant dynamics.

Under these assumptions, the circuit behaves as a first-order system. The time constant is not fixed, but varies with the operating region. At low signal levels, the time constant is largest because R_{f1} dominates, resulting in slower response. As the signal amplitude increases and additional feedback paths are activated, the effective resistance decreases, producing a reduced time constant and faster response. This behaviour is consistent with the intended operation of the nonlinear amplifier, where

high sensitivity is preserved at low signal levels and faster response with reduced gain is achieved at higher signal amplitudes.

5.6.19 Amplifier Characterisation

To assess the nonlinear amplifier response over its intended operating range, experimental characterisation was carried out for supply voltages ranging from 1.5 V to 5 V. The input voltage was generated using the data acquisition system and incremented in steps of 2.5 mV.

Operation of the Nonlinear Feedback Network Figure 5.13 illustrates the nonlinear feedback configuration of the proposed amplifier. The circuit consists of a non-inverting operational amplifier with a segmented feedback network formed by resistors R_1, R_2, and R_3, and two diode-controlled branches (D_1 and D_2). The resistor R_i defines the gain-setting path to ground.

At low output voltage levels, both diodes are reverse-biased, and the feedback path is established solely through R_3. In this region, the amplifier behaves as a conventional non-inverting amplifier with high gain determined by R_3 and R_i.

As the output voltage increases, the voltage difference $(v_o - v_{in})$ reaches the forward voltage threshold of diode D_2. At this point, D_2 becomes forward-biased, introducing R_2 into the feedback network. This reduces the effective feedback resistance and consequently reduces the amplifier gain.

At higher output levels, when $(v_o - v_{in})$ exceeds the forward voltage threshold of diode D_1, the second diode becomes forward biased, activating an additional feedback branch through R_1. This further reduces the effective feedback resistance, thereby producing additional gain compression.

The circuit therefore operates in a piecewise manner, where the effective gain is determined by the number of active feedback branches. This staged activation mechanism enables high amplification of low-level signals while preventing saturation at higher input amplitudes.

Figure 5.14 shows the characterisation of the nonlinear amplifier under different

supply rail voltages. Figure 5.15 presents the calculated, simulated, and experimentally measured input–output response of the nonlinear amplifier on a log–log scale. Figure 5.16 compares the gain characteristics of the linear and nonlinear circuit configurations.

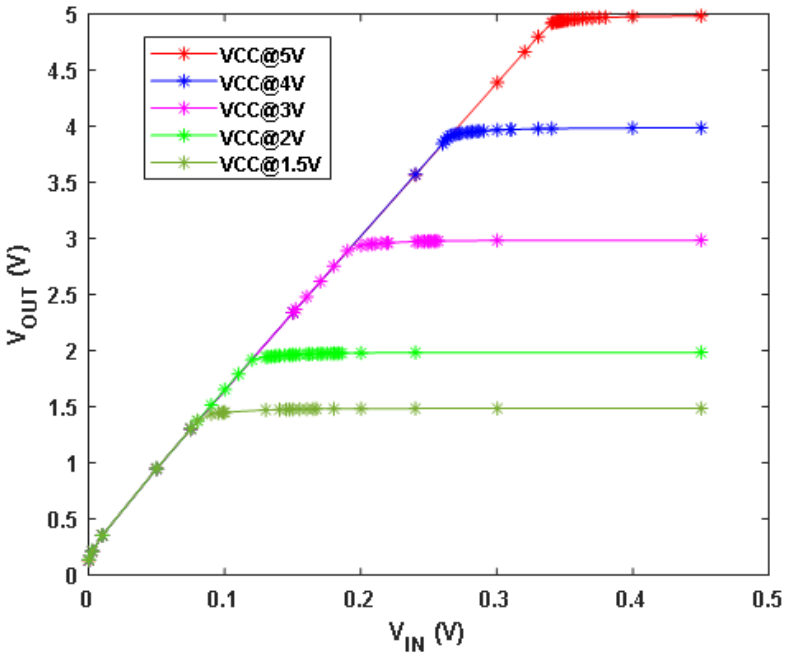

Figure 5.14: Characterisation of the nonlinear amplifier across supply rail voltages

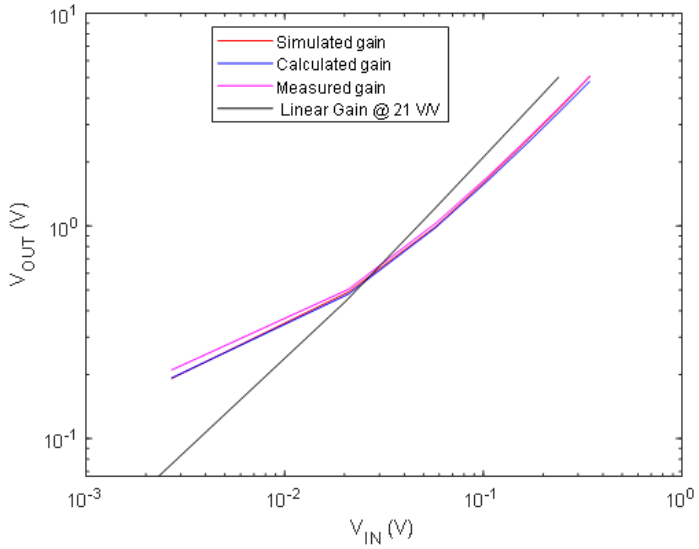

Figure 5.15: Calculated, simulated, and experimental nonlinear amplifier response on a log–log scale

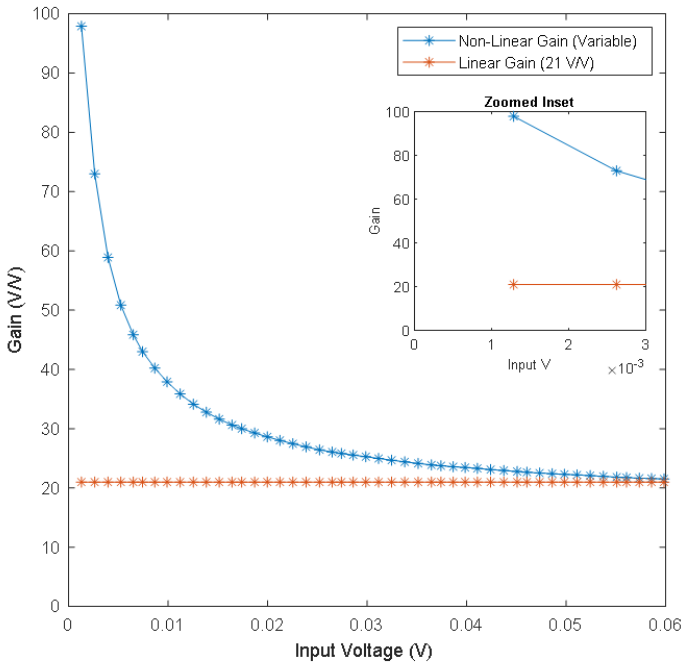

Figure 5.16: Gain profile of linear and nonlinear circuit configurations

Interpretation of Input–Output Characteristics Figure 5.15 presents the relationship between the output voltage and input voltage for the nonlinear amplifier, including calculated, simulated, and measured results, together with the response of an equivalent linear amplifier.

It is important to note that this figure represents the absolute input–output characteristic of the amplifier, rather than the gain directly. As a result, the apparent increase in slope at higher input voltages should not be interpreted as an increase in gain. The true gain of the amplifier is defined as

$$G = \frac{V_{\text{out}}}{V_{\text{in}}} \tag{5.69}$$

and must therefore be evaluated by normalising the output with respect to the input.

At low input voltages, the amplifier operates in Region 1, where only R_3 is active, resulting in a high gain. As the input increases beyond the first switching threshold, diode D_2 becomes forward biased, introducing R_2 into the feedback path and reducing the gain. At higher input levels, diode D_1 conducts, further reducing the effective feedback resistance and producing additional gain compression.

Although the absolute output voltage continues to increase with increasing input, the ratio $V_{\text{out}}/V_{\text{in}}$ decreases, confirming that the amplifier exhibits gain compression rather than gain expansion. This behaviour is consistent with the intended design objective.

To clearly demonstrate this effect, the gain profile is presented separately in Fig. 5.16, where it is observed that the gain decreases with increasing input amplitude.

The gain behaviour is more clearly illustrated in Fig. 5.16, where the nonlinear configuration is compared directly with the equivalent linear amplifier. The nonlinear circuit provides substantially higher gain at low input levels, followed by progressive gain reduction as additional feedback branches become active. This confirms that the proposed design achieves the intended trade-off between low-signal sensitivity and high-signal accommodation.

The numerical calculation of the nonlinear amplifier output voltage is based on the piecewise analytical expressions derived for each operating region, namely (5.38), (5.44), and (5.50), and is summarised in Table 5.6.

Table 5.6: Numerical calculation of nonlinear op-amp output voltage

V_{in} **(V)**	V_{out} **(V)**
0.0025	0.289734
0.0050	0.324148
0.0075	0.358563
0.0100	0.392978
0.0125	0.427393
0.0200	0.530638
0.0500	0.943617
0.0600	1.081276
0.0750	1.287765
0.1500	2.320212
0.2200	3.283829
0.3500	5.073404

Adjustment of the nonlinear amplifier parameters enables the measurement range to be tailored to a specified nominal current or voltage, subject to the operational limits of the circuit. The true gain is defined as

$$G = \frac{V_{\text{out}}}{V_{\text{in}}} \tag{5.70}$$

and must be evaluated by normalising the output with respect to the input.

At low input voltages, the amplifier operates in its highest-gain region, where only R_{f1} is active. In this region, very small input signals are strongly amplified, enabling them to exceed the interrogation system's detection threshold. As the input increases, diode conduction progressively activates additional feedback branches, reducing the effective feedback resistance and compressing the gain.

Thus, although V_{out} increases with V_{in}, the ratio $V_{\text{out}}/V_{\text{in}}$ decreases, indicating gain compression. The curvature observed in Fig. 5.15 is therefore consistent with the intended nonlinear behaviour.

This behaviour is further illustrated in Fig. 5.16, where the gain is explicitly plotted

as a function of input voltage, clearly demonstrating the transition from high-gain operation at low input levels to gain compression at higher input amplitudes.

Experimental results show that the linear amplifier reaches saturation at approximately 5.02 V for a maximum input of 240 mV, while producing approximately 3.15 V at 150 mV input. In contrast, the nonlinear configuration produces approximately 3.4 V at 240 mV and 2.25 V at 150 mV (KALF condition). This controlled compression of high-level signals significantly extends the measurement range and reduces the effective hysteresis width, as further discussed in the LVT analysis section.

5.6.20 Comparison of Amplifier Architectures for Ultra-Low Voltage Sensing

Several amplification strategies were evaluated, including linear, gain-selecting, logarithmic, and the proposed nonlinear segmented feedback amplifier.

A linear amplifier provides constant gain but cannot simultaneously achieve high sensitivity and wide dynamic range. A gain-selecting amplifier improves range but introduces switching transients and increased power consumption. Logarithmic amplifiers offer wide dynamic range but suffer from temperature sensitivity and reduced accuracy at low signal levels.

The proposed nonlinear amplifier overcomes these limitations by employing diode-controlled feedback paths that enable continuous gain adaptation without switching transients. This makes it particularly suitable for ultra-low-power sensing applications.

Table 5.7: Proposed amplifier comparison to other amplifiers

Feature	**Proposed Nonlinear Amplifier**	**Logarithmic Amplifier**	**Gain-Selecting Amplifier**
Principle of Operation	Piecewise gain adaptation using diode-controlled feedback paths	Exponential I–V characteristics of semiconductor devices	Discrete switching between gain stages
Transfer Function	Piecewise linear with controlled transitions	Continuous logarithmic compression	Discrete step changes
Gain Behaviour	High gain at low signals, progressive compression	Continuously decreasing gain	Fixed gain per stage
Dynamic Range Handling	Extended range via adaptive compression	Very wide range but nonlinear response	Extended via switching
Implementation Complexity	Moderate, passive components only	Moderate to high, temperature compensation required	High, requires control logic
Temperature Sensitivity	Low	High	Moderate

Feature	**Proposed Nonlinear Amplifier**	**Logarithmic Amplifier**	**Gain-Selecting Amplifier**
Calibration Requirements	Region-based, predictable	Complex nonlinear calibration	Stage-wise calibration
Signal Linearity	Linear within regions	Inherently nonlinear	Linear per stage
Suitability for Precision Measurement	High	Moderate	High
Typical Applications	Sensor conditioning, adaptive instrumentation	RF measurement, radar	ADC front-end, instrumentation

5.6.21 LVT Analysis

The piezoelectric (PZT) actuator, which forms a key component of the hybrid low-voltage transducer (LVT), is examined in this section. The operating principles and sensing characteristics of the fibre Bragg grating (FBG) have been presented in Chapter 4 and are not repeated here. Instead, this section focuses on the electromechanical behaviour of the PZT actuator and its role in voltage-to-strain transduction within the hybrid PZT–FBG architecture.

Piezoelectric Crystal

The piezoelectric effect is strongly dependent on crystal symmetry. Materials with lower symmetry exhibit higher sensitivity, producing greater polarisation or strain when subjected to an external electric field [34]. This makes low-symmetry crystals particularly suitable for low-voltage sensing applications.

The converse piezoelectric effect is illustrated in Fig. 5.17, where an applied electric field produces mechanical strain.

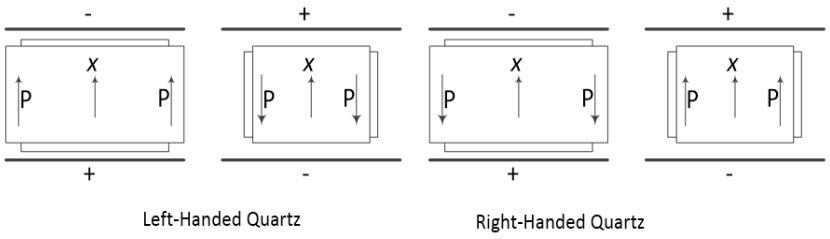

Figure 5.17: Converse piezoelectric effect

The strain generated in the material is given by:

$$S_{xx} = d_{xxx}E \tag{5.71}$$

where d_{xxx} is the piezoelectric coefficient and E is the applied electric field.

Piezoelectric Crystal Analysis

The equivalent electrical model of the piezoelectric crystal is shown in Fig. 5.18 and Fig. 5.19.

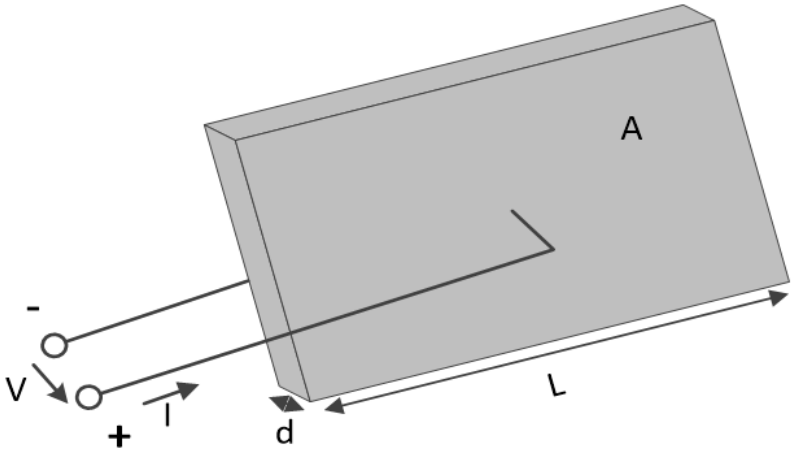

Figure 5.18: Piezoelectric crystal

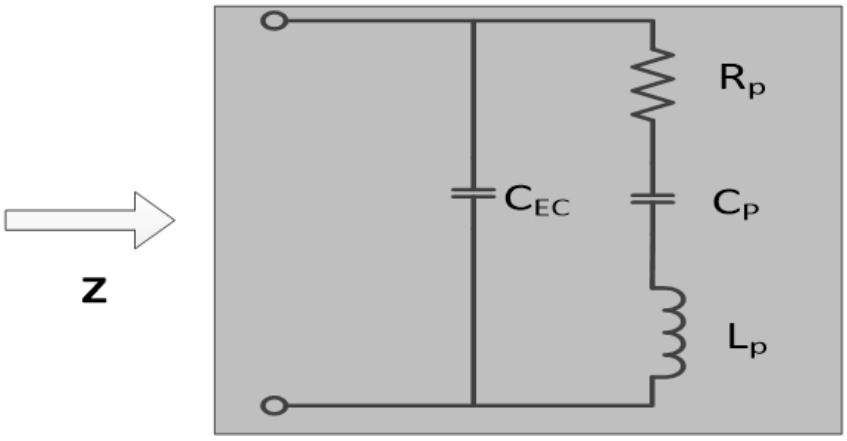

Figure 5.19: Van Dyke equivalent circuit of PZT

The impedance components are defined as:

$$X_{Lp} = j2\pi f L_p, \quad X_{Cp} = \frac{1}{j2\pi f C_p}, \quad X_{EC} = \frac{1}{j2\pi f C_{EC}} \tag{5.72}$$

$$X_s = \sqrt{R^2 + (X_{Lp} - X_{Cp})^2} \tag{5.73}$$

$$Z_p = \frac{X_s \cdot X_{EC}}{X_s + X_{EC}} \tag{5.74}$$

The resonant frequency is given by:

$$f = \frac{1}{2\pi\sqrt{LC}} \tag{5.75}$$

Using datasheet parameters, the inductance is estimated as:

$$L \approx 9.2\ \mu\text{H} \tag{5.76}$$

Electromechanical Model

The piezoelectric actuator converts electrical input into mechanical displacement. For static conditions:

$$x = d_{33} \cdot n \cdot V \tag{5.77}$$

For dynamic conditions:

$$F(t) = n \cdot d_{33} \cdot V(t) \cdot Y \tag{5.78}$$

$$F(t) = m\ddot{x}(t) + c\dot{x}(t) + kx(t) \tag{5.79}$$

Taking Laplace transform:

$$H(s) = \frac{X(s)}{V(s)} = \frac{nd_{33}Y}{ms^2 + cs + k} \tag{5.80}$$

Natural frequency and damping ratio are defined as:

$$\omega_n = \sqrt{\frac{k}{m}}, \quad \zeta = \frac{c}{2\sqrt{km}} \tag{5.81}$$

For sinusoidal steady-state:

$$\left|\frac{X(j\omega)}{V(j\omega)}\right| = \frac{nd_{33}Y}{\sqrt{(k - m\omega^2)^2 + (c\omega)^2}} \tag{5.82}$$

Due to unavailable stiffness and damping parameters, full analytical evaluation is not pursued. Instead, dynamic behaviour is assessed through simulation.

PZT Linear (Static) Response

A Simulink model was developed to evaluate the displacement response of the PZT under DC excitation, as shown in Fig. 5.20.

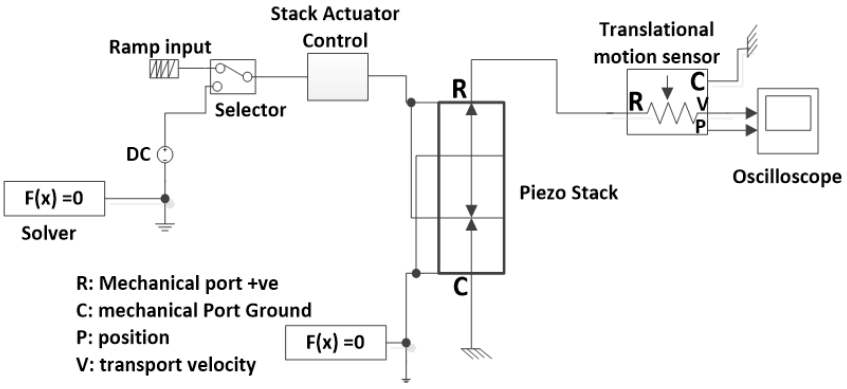

Figure 5.20: Piezo actuator motion simulation

The simulation parameters were obtained from the PICMA 882.11 datasheet [35] and are summarised in Table 5.9.

PZT Static Response

The simulation was performed using parameters obtained from the PZT datasheet. The no-load displacement was estimated from the manufacturer's trajectory curve, as it was not explicitly provided. A ramp input voltage in the range of 0–5 V was applied,

Table 5.9: Piezo stack parameters (PICMA 882.11)

Parameter	**Value**	**Unit**
Stack Area	27	mm^2
Stack Length	9	mm
No-load displacement (0V)	0.00021	μm
Blocking Force	190	N
d_{33}	300×10^{-12}	m/V
Test Voltage	5	V
Capacitance	0.15	μF
Frequency	135	kHz

and the resulting displacement was measured using a translational motion sensor.

The simulated response was consistent with the analytical strain-voltage relationship in (5.77), confirming the linear dependence of displacement on the applied voltage and the piezoelectric coefficient.

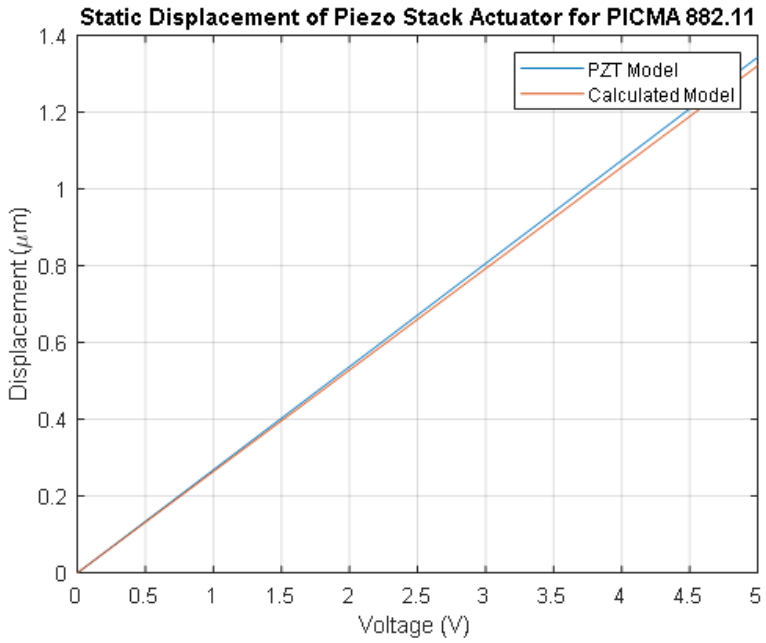

Figure 5.21: Static displacement of PZT stack actuator (PICMA 882.11)

The displacement exhibits a linear relationship with applied voltage under static conditions. It should be noted that hysteresis effects were not included in this model; their inclusion would introduce nonlinearity and require alternative modelling approaches.

PZT Resonance Behaviour

The frequency response of the PZT was analysed using the impedance relationships in (5.73)–(5.74). The results show:

- Series resonance at approximately 70.3 kHz
- Parallel resonance at approximately 134 kHz

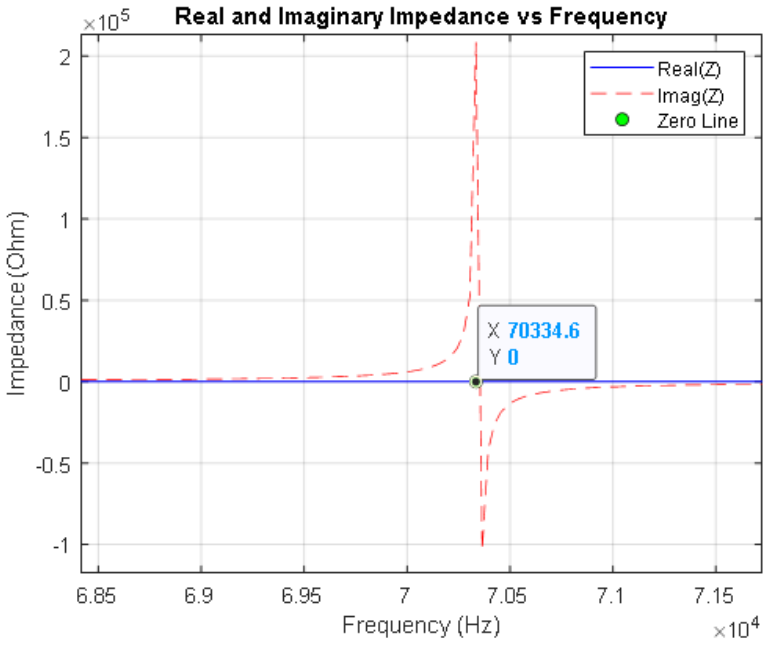

Figure 5.22: Series resonant frequency of PZT

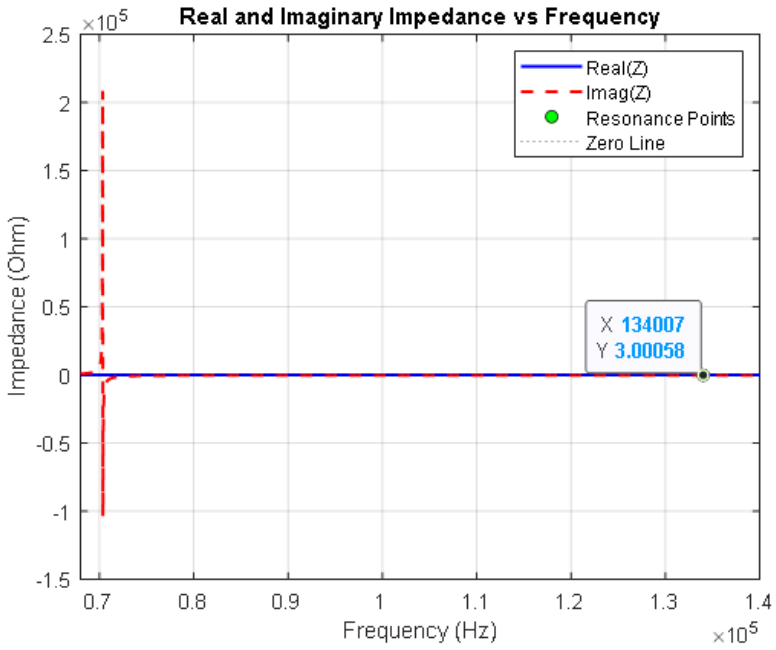

Figure 5.23: Parallel resonant frequency of PZT

These results imply:

- For current-driven operation (inductive behaviour), the series resonance (70.3 kHz) should not be exceeded.
- For voltage-driven operation (capacitive behaviour), the parallel resonance (134 kHz) defines the upper operating limit.

The parallel resonance closely matches the datasheet value (135 kHz), validating the modelling approach.

Although this bandwidth may limit high-frequency transient capture, advanced PZT devices with resonant frequencies up to 2 MHz have been reported [36], offering potential for enhanced high-speed sensing applications.

LVT Dynamic Response

The LVT integrates a PZT actuator with an FBG sensor to enable electrical-to-optical signal conversion. To evaluate its dynamic performance, a fault waveform obtained from the HVDC simulation environment was applied to the PZT model.

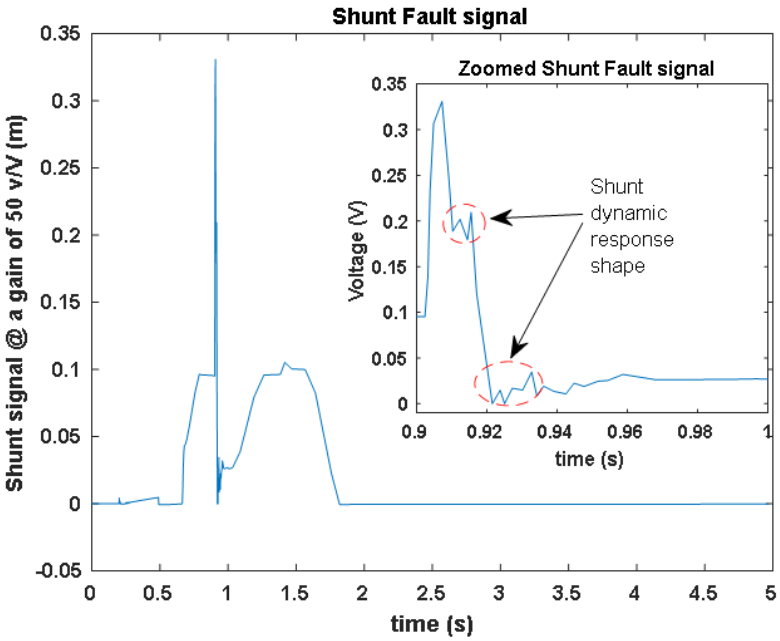

Figure 5.24: Shunt response to fault signal

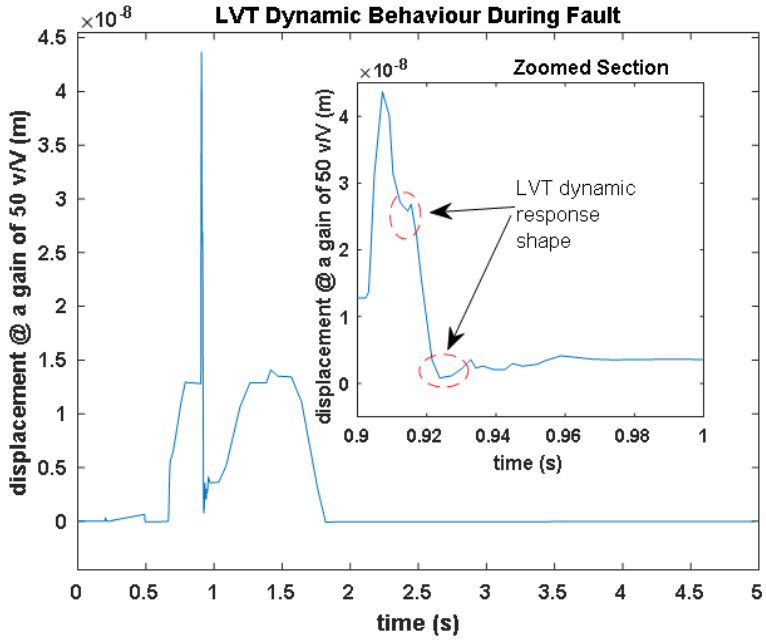

Figure 5.25: LVT dynamic response to fault signal

The LVT output closely follows the injected fault waveform, preserving key features such as rise time, polarity, and oscillatory behaviour. Minor attenuation is observed due to the second-order dynamics of the PZT.

FFT analysis of the signal is shown in Fig. 5.26.

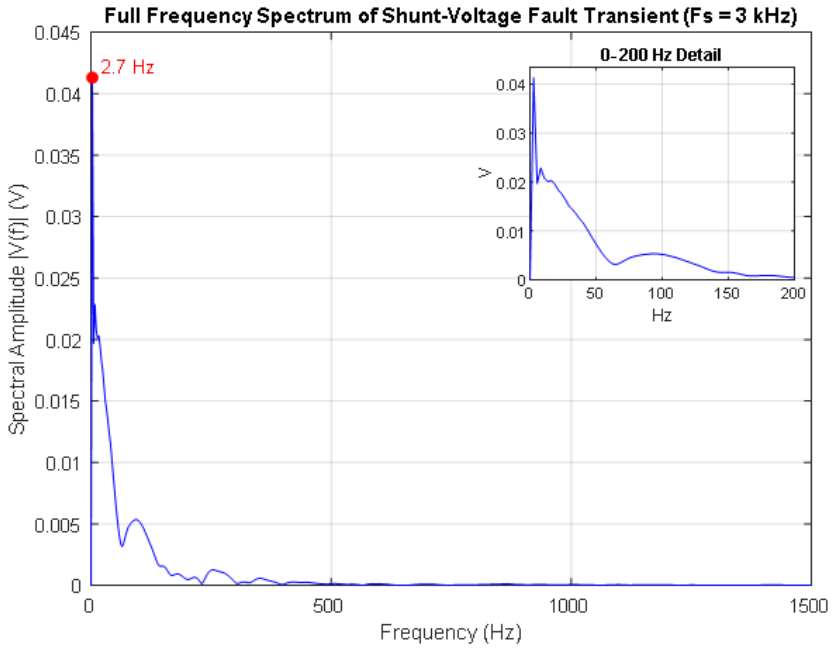

Figure 5.26: Frequency component extraction from fault signal

The dominant spectral content lies below 50 Hz, with components extending up to approximately 1 kHz. This confirms that the LVT bandwidth is sufficient to capture the dominant characteristics of HVDC fault transients.

The observed differences between the shunt and LVT responses arise from their dynamic behaviour:

- The shunt behaves as a near-instantaneous (first-order) system
- The PZT-based LVT exhibits second-order dynamics (mass–spring–damper)

Despite this, the LVT successfully captures the magnitude and trend of the fault signal.

FBG Transduction Mechanism

Mechanical deformation of the PZT induces strain in the FBG, altering its grating period and shifting the reflected wavelength. This wavelength shift is measured by an optical interrogator, enabling reconstruction of the applied voltage. Through calibration, this voltage can be mapped to current, allowing the LVT to function as a current sensor.

5.6.22 LVT Characterisation

The LVT was characterised under both linear and nonlinear excitation conditions to evaluate its performance across different operating regimes.

Linear Characterisation

The LVT was tested using an NI USB-6003 DAQ and an IBSEN I-MON interrogator. Input voltage was ramped cyclically, and the corresponding optical response was recorded.

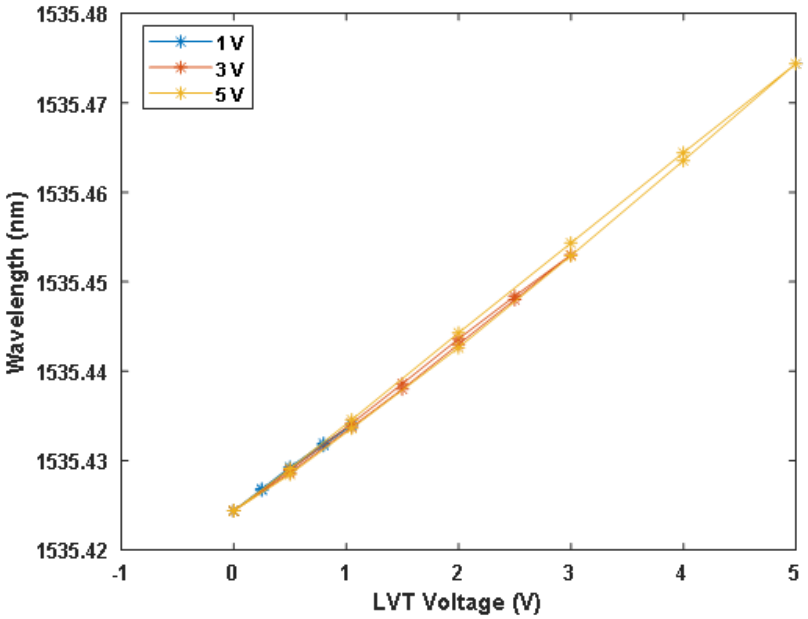

Figure 5.27: LVT linear characteristic

The results exhibit hysteresis loops due to PZT polarisation dynamics. The loop width increases with applied voltage, reflecting increased nonlinear behaviour at higher excitation levels.

Nonlinear Characterisation

Under nonlinear amplification, the LVT exhibits improved performance:

- High gain ($\sim$100 V/V) at low input levels
- Gain compression ($<$14 V/V) at higher amplitudes

This behaviour enhances low-signal detectability while preventing saturation.

The nonlinear amplification also reduces hysteresis width, improving measurement accuracy and energy efficiency. This enables operation over a wider dynamic range without increasing supply voltage.

Curve fitting using second-order regression was applied to model the electro-optic relationship, enabling accurate calibration and compensation for residual nonlinearity.

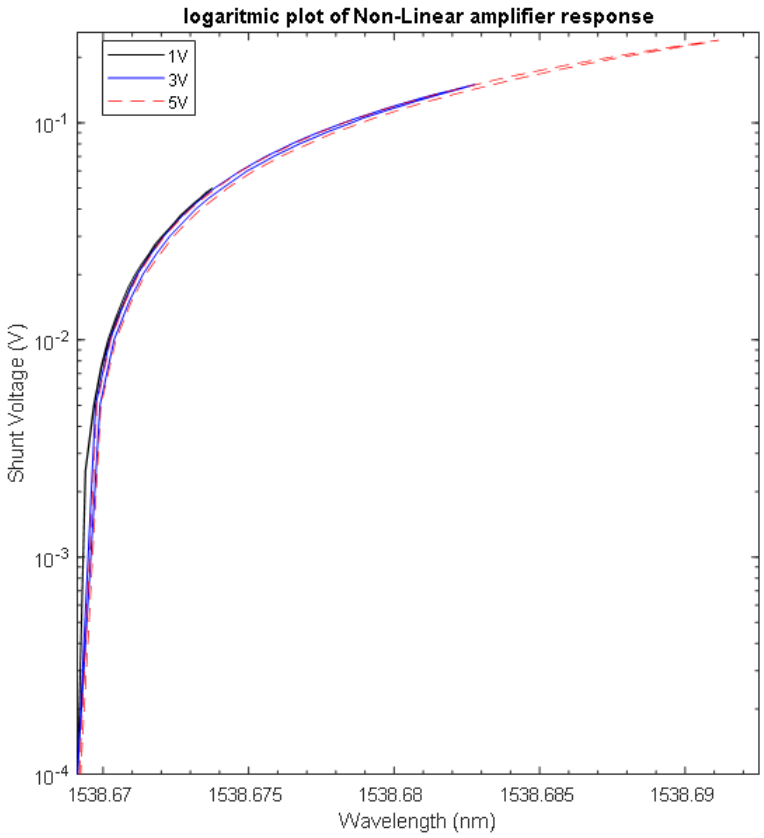

Figure 5.28: Inverse logarithmic characterisation of LVT/shunt relationship

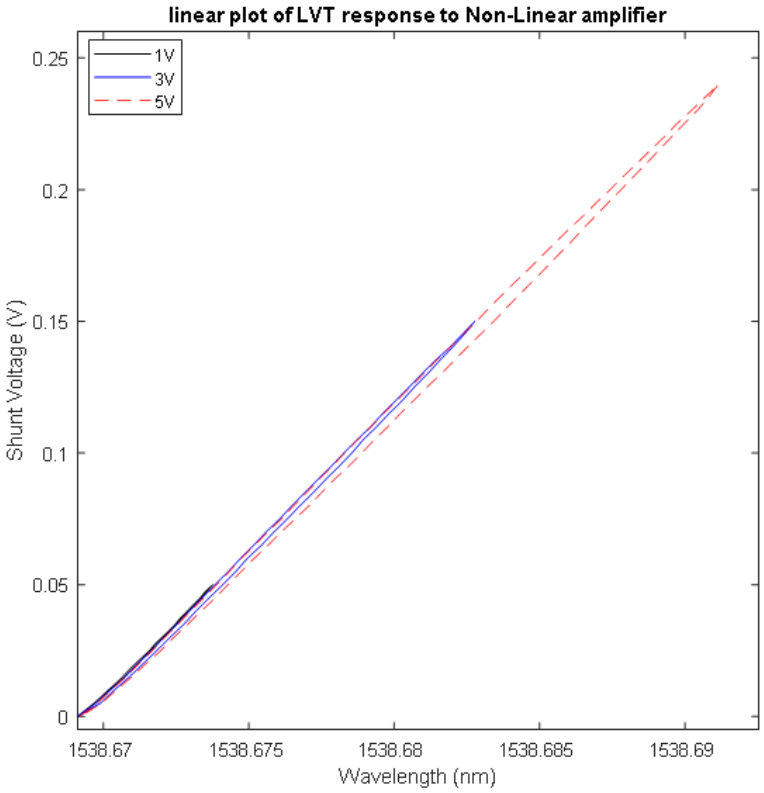

Figure 5.29: Inverse linear characterisation of LVT/shunt relationship

5.6.23 Conclusion

This chapter presented the design, analytical modelling, and experimental validation of the proposed optical current sensing (OCS) system for HVDC applications.

The resistive shunt demonstrated stable current-to-voltage transduction with predictable thermal behaviour, while highlighting the influence of temperature-dependent resistance and parasitic inductance under transient conditions.

The energy harvesting subsystem successfully enabled self-powered operation, extracting usable energy from millivolt-level signals and sustaining operation under dynamic conditions.

The nonlinear signal conditioning stage was shown to significantly enhance system performance by improving low-signal detectability while preventing saturation at higher amplitudes. The piecewise gain compression mechanism provides a practical solution for extending dynamic range within the constraints of low-power operation.

The LVT exhibited reliable electro-mechanical-to-optical transduction, with hysteresis behaviour that can be mitigated through nonlinear amplification and calibration techniques. The dynamic response analysis confirmed that the sensor is capable of capturing the dominant spectral components of HVDC fault signals.

Overall, the integration of resistive sensing, nonlinear amplification, energy harvesting, and photonic interrogation establishes a robust sensing architecture capable of autonomous operation with high sensitivity and wide dynamic range. These characteristics make the proposed OCS system well suited for distributed sensing applications in HVDC networks, enabling improved fault detection, enhanced system observability, and advanced protection and control strategies.

Chapter 5 References

[1] D. V. Hertem, O. Gomis-Bellmunt, and J. Liang, *HVDC Grids*. IEEE Press, 2018, pp. 88–95.

[2] National Instruments, *Labview signalexpress: Getting started with labview*, pp. 10–18, 2007.

[3] *Instrument transformers – part 14: Additional requirements for current transformers for dc applications*, pp. 23–24, IEC, 2019.

[4] National Instruments, *Labview tutorials*, pp. 4–25.

[5] National Instruments, *Dynamic signal acquisition*, pp. 10–15.

[6] COMSOL, *Comsol multiphysics reference manual*, pp. 851–875. [Online]. Available: www.comsol.com/blogs. Accessed: 3 June 2024, 1998.

[7] COMSOL, *Introduction to comsol multiphysics*, pp. 59–176.

[8] COMSOL, *Modeling cables in comsol multiphysics: 8-part tutorial series*, pp. 1–6.

[9] Autodesk, *AutoCAD 2015 and AutoCAD LT 2015 Bible*, pp. 55–140.

[10] G. Omura and B. C. Benton, *Mastering AutoCAD and AutoCAD LT*. John Wiley & Sons, 2017, pp. 30–70.

[11] L. S. Cline, *Part i: Understanding fusion 360*, pp. 10–15.

[12] G. Verma and S. Malik, *Autodesk Fusion 360 Black Book*. CADCAMCAE Works, 2018, pp. 30–45.

[13] MathWorks, *Matlab programming fundamentals r2017a*, [Online]. Available: www.mathworks.con pp. 10–21. Accessed: 23 May 2024, 1984.

[14] S. Nagar, *Introduction to MATLAB for Engineers and Scientists: Solutions for Numerical Computation and Modeling*. Apress, 2017, pp. 13–28. DOI: 10.1007/978-1-4842-3189-0.

[15] B. Hahn and D. T. Valentine, *Essential MATLAB for Engineers and Scientists*, pp. 86–290.

[16] M. Kalechman, *Practical MATLAB Applications for Engineers*, pp. 101–138, 457–538.

[17] W. Bobber, C. T. Sai, and O. Massory, *Numerical and analytical methods with matlab*, pp. 45–76, 141–186.

[18] D. Jahshan, *Kicad step by step tutorial*, pp. 1–32. [Online]. Available: http://iut-tice.ujf-grenoble.fr/cao/. Accessed: 30 May 2024, 2006.

[19] G. Kraus and E. Tettnang, *Spice-simulation using ltspice iv: Tutorial for successful simulation of electronic circuits with the free full version of ltspice iv*, pp. 52–75. [Online]. Available: www.linear.com. Accessed: 30 May 2024, 2010.

[20] Analog Devices and B. Dobkin, *Analog Circuit Design: A Tutorial Guide to Applications and Solutions*. Elsevier, 2011, pp. 17–38.

[21] ABB, *Xlpe submarine cable systems: Attachment to xlpe land cable systems – user's guide, rev. 5*, pp. 3–12. [Online]. Available: www.abb.com/cables. Accessed: 3 June 2024.

[22] K. E. Pitney, *Electrical Contacts for Low Energy Uses*, 1st. Bloomfield, Connecticut: Deringer-Ney Inc., 2022, pp. 13–17. [Online]. Available: http://www.deringerney.com/. Accessed: 11 March 2026.

[23] F. L. S. and G. D. A., *Heat Transfer Between Surfaces in Contact*. NASA, 1971, pp. 30–37.

[24] F. W. Grover, *Inductance Calculations*. New York: D. Van Nostrand Company, Inc., 1946, pp. 34–36.

[25] R. P. P. Smeets and N. A. Belda, "High-voltage direct current fault current interruption: A technology review," *High Voltage*, 2021. DOI: 10.1049/hve2.12063.

[26] S. Khalid et al., "Technical assessment of hybrid hvdc circuit breaker components under mtdc faults," *Energies*, vol. 14, no. 23, pp. 4–8, 2021. DOI: 10.3390/en14238148.

[27] D. Tzelepis et al., "Single-ended differential protection in mtdc networks using optical sensors," *IEEE Transactions on Power Delivery*, vol. 32, no. 3, pp. 1605–1615, Jun. 2017. DOI: 10.1109/TPWRD.2016.2645231.

[28] R. J. M. Vullers, R. van Schaijk, H. J. Visser, J. Penders, and C. V. Hoof, "Energy harvesting for autonomous wireless sensor networks," *IEEE Solid-State Circuits Magazine*, pp. 2–8, 2021.

[29] Analog Devices, *Ltc3108 (rev. d)*, [Online]. Available: www.analog.com. pp. 2–6. Accessed: 3 Nov. 2021.

[30] A. Amiolemen, G. Fusiek, and P. Niewczas, "Self-powered signal conditioning circuit for an hvdc optical current sensor," *IEEE Sensors Letters*, vol. 7, no. 11, pp. 2–5, Nov. 2023. DOI: 10.1109/LSENS.2023.3311676.

[31] A. Amiolemen, G. Fusiek, and P. Niewczas, "Towards the development of a photonic current sensor for hvdc networks," in *2024 IEEE International Instrumentation and Measurement Technology Conference (I2MTC)*, IEEE, May 2024, pp. 2–5. DOI: 10.1109/I2MTC60896.2024.10560732.

[32] *Coupled inductors – lpr6235*, pp. 1–2.

[33] Ibsen Photonics, *I-mon usb interrogation monitors specifications: I-mon software operating principle*, pp. 1–2. [Online]. Available: www.ibsen.com. Accessed: 10 Oct. 2021.

[34] J. Tichý, J. Erhart, E. Kittinger, and J. Přívratská, *Fundamentals of Piezoelectric Sensorics: Mechanical, Dielectric, and Thermodynamical Properties of Piezoelectric Materials*. Springer Berlin Heidelberg, 2010, pp. 10–138. DOI: 10.1007/978-3-540-68427-5.

[35] PI, *Ceramic-insulated high-power actuators picma stack multilayer piezo actuators with high reliability*, pp. 2–7.

[36] Thorlabs, *Thorlabs pn5fc1 pzt actuator*, pp. 1–4. [Online]. Available: www.thorlabs.com/contact. Accessed: 13 June 2023, 2020.

Chapter 6

Simulation and Experimental Results

6.1 Introduction

This chapter presents numerical and experimental validation of the proposed photonic current-sensing architecture for high-voltage direct current (HVDC) cable systems. The primary objective is to evaluate the electro-thermal behaviour of the instrumented splice joint, the performance of the signal-conditioning circuitry, and the dynamic response of the electro-optical sensing mechanism under representative operating conditions.

The sensing system integrates three principal subsystems: a manganin shunt element for current measurement, an ultra-low-power signal-conditioning circuit powered via energy harvesting, and a piezoelectric-based optical voltage transducer (LVT) that converts the electrical signal into an optical response. Given that the sensing electronics are embedded within an HVDC cable splice joint, the design must maintain reliable operation under high electric field stress, elevated current loading, and fast transient disturbances associated with network faults.

To assess these constraints, a combined numerical and experimental approach is adopted. First, the electro-thermal behaviour of the shunt and surrounding cable structure is investigated using COMSOL Multiphysics. These simulations quantify Joule

heating, thermal gradients, and electric-field distributions within the instrumented splice assembly, with particular emphasis on the effectiveness of electrostatic shielding provided by a Faraday cage.

Second, the performance of the signal-conditioning circuitry is evaluated through circuit simulation and experimental validation. Both linear and nonlinear amplification architectures are analysed to assess their ability to resolve low-amplitude shunt signals while remaining compatible with the limited power budget imposed by the energy-harvesting stage.

Finally, the end-to-end sensing system is experimentally validated on a laboratory platform that reproduces steady-state and transient electrical conditions representative of HVDC operation. Electrical signals are acquired using a data acquisition system, while the corresponding optical responses are measured using a fibre Bragg grating interrogator. Additional validation is performed using fault-transient waveforms derived from HVDC network simulations to assess the sensor's ability to capture high-frequency disturbance signatures.

The results presented in this chapter provide a comprehensive evaluation of the proposed sensing architecture, demonstrating the feasibility of integrating distributed electro-optical current sensing within HVDC cable infrastructure while maintaining thermal stability, electromagnetic compatibility, and adequate dynamic response.

6.2 Electro-Thermal Behaviour of the Instrumented Splice

The proposed sensor is designed for integration within HVDC cable splice joints, serving a dual function as both a mechanical butt-joint connector and an embedded sensing unit. In addition to ensuring electrical continuity, the system provides real-time monitoring of current flow, thermal loading, and fault conditions.

To ensure operational reliability, the sensor performance is evaluated over a wide range of thermal, electrical, and fault-induced stress conditions. This multi-physics assessment defines the operational envelope of the sensing system and establishes its suitability for deployment in HVDC environments.

From a thermal perspective, Joule heating is a dominant factor due to the high current levels present in HVDC systems. Resistive losses within the shunt element result in localised temperature rise, which must be carefully managed to prevent degradation of surrounding insulation materials and embedded electronics.

From an electrical perspective, the sensor is exposed to high electric-field intensities due to HVDC operating voltages. These fields can influence dielectric materials and induce unwanted coupling effects if not adequately controlled. Therefore, the electric field distribution within the splice assembly is analysed to inform the design of appropriate shielding mechanisms, ensuring electromagnetic compatibility and long-term reliability.

6.2.1 Joule Heating and Analysis of the Shunt

The design specifications developed in Chapter 5 were used to construct a detailed geometrical model of the shunt. The initial geometry was created in AutoCAD and subsequently refined in Fusion 360 to approximate the physical assembly. However, for Multiphysics simulation, the model was reconstructed directly within COMSOL using its native geometry tools.

This approach was necessary because imported geometries in `.STL` and `.PLY` formats are treated as surface meshes, which do not preserve internal material domains. Such representations are unsuitable for electro-thermal simulations of composite structures, where accurate definition of internal material boundaries is essential.

The reconstructed geometry enables coupled electro-thermal simulations, allowing the evaluation of Joule heating and the resulting temperature distribution within the shunt under electrical excitation. As established in Chapter 5, manganin is selected as the shunt material due to its low temperature coefficient of resistance and stable electrical characteristics. The thermo-electrical and mechanical properties used in the COMSOL model are summarised in Table 6.1.

The general energy conservation equation governs the heat transfer in solids within COMSOL:

Table 6.1: Thermo-electrical and mechanical properties of manganin utilised in the shunt design for coupled electro-thermal modelling

Property	**Value**	**Unit**
Heat capacity at constant pressure	406	J/(kg·K)
Relative permeability	1	–
Resistivity	4.50×10^{-7}	Ω·m
Thermal conductivity	30	W/(m·K)
Young's modulus	1.30×10^{11}	Pa
Density	8400	kg/m^3
Coefficient of thermal expansion	1.70×10^{-5}	1/K
Electrical conductivity	2.07×10^{6}	S/m
Relative permittivity	1	–

$$\rho C_p \left(\frac{\partial T}{\partial t} + \mathbf{u} \cdot \nabla T \right) + \nabla \cdot (\mathbf{q} + \mathbf{q}_r) = \alpha T \frac{dS}{dT} + Q \tag{6.1}$$

For steady-state conditions, the temporal variation of temperature is negligible, such that:

$$\nabla \cdot (\mathbf{q} + \mathbf{q}_r) = \alpha T \frac{dS}{dT} + Q \tag{6.2}$$

The thermoelastic damping term, which accounts for coupling between thermal and mechanical fields in solids, is expressed as:

$$Q_{\text{ted}} = \alpha T \frac{dS}{dT} \tag{6.3}$$

The dominant volumetric heat source in the present study arises from Joule heating:

$$Q = \mathbf{J} \cdot \mathbf{E} \tag{6.4}$$

where:

- ρ — material density (kg/m^3)
- C_p — specific heat capacity at constant pressure (J/kg·K)
- T — absolute temperature (K)

- $\mathbf{u}$ — velocity vector (m/s)
- $\mathbf{q}$ — conductive heat flux (W/m^2)
- $\mathbf{q}_r$ — radiative heat flux (W/m^2)
- α — coefficient of thermal expansion (1/K)
- S — second Piola–Kirchhoff stress tensor (Pa)
- Q — volumetric heat source (W/m^3)

According to Fourier's law of heat conduction, the conductive heat flux is given by:

$$\mathbf{q} = -k\nabla T \tag{6.5}$$

where k is the thermal conductivity of the material and ∇T represents the temperature gradient.

Substituting (6.5) into (6.2) yields the governing steady-state heat conduction equation used in the COMSOL model:

$$\nabla \cdot (-k\nabla T) = Q + Q_{\text{ted}} \tag{6.6}$$

The coupled electro-thermal problem is solved across all material domains with appropriate boundary conditions, ensuring convergence of temperature and electric field distributions within the sensor assembly.

Electro-thermal response of the shunt under Joule heating To evaluate the thermal and electrical behaviour of the shunt, a nominal current of 1 kA was applied at the conductor terminal. The material properties and geometric definitions of the model were specified according to Tables 6.2–6.7.

The simulation was conducted within a fully coupled three-dimensional COMSOL environment, where each material domain was explicitly defined. Joule heating physics was employed under steady-state conditions, while electric field distribution was eval-

Table 6.2: Thermo-electrical properties and geometrical configuration of manganin used in the COMSOL model

Property	**Value**	**Unit**	**Geometry (mm)**
Heat capacity at constant pressure	406	J/(kg·K)	Radius: 15.86
Thermal conductivity	30	W/(m·K)	Length: 90
Relative permittivity	1	–	Position: (0,0,0)
Relative permeability	1	–	–
Resistivity	4.50×10^{-7}	Ω·m	–
Young's modulus	1.30×10^{11}	Pa	–
Density	8400	kg/m^3	–
Coefficient of thermal expansion	2.50×10^{-5}	1/K	–
Electrical conductivity	2.237×10^{6}	S/m	–

uated using electrostatics under a stationary solver. Particular attention was given to geometric continuity to eliminate boundary overlap and ensure numerical stability.

The simulation results indicate a temperature gradient of approximately 12°C across the shunt under nominal operating conditions, demonstrating acceptable thermal performance within the design constraints. The spatial distributions of temperature resulting from Joule heating are shown in Fig. 6.3a and Fig. 6.3b.

The detailed material properties, geometry, and spatial configuration of the sensor assembly used in the simulation are summarised in Tables 6.2–6.7.

The material properties and geometrical definitions of the remaining domains in the simulation, including the copper conductor, epoxy encapsulation, XLPE insulation, Faraday cage, and the LVT enclosure, are summarised in Tables 6.3–6.7.

The coupled Joule heating and electrostatic simulations presented in Fig. 6.3(a–b) and Fig. 6.5–Fig. 6.8 illustrate both the thermal response of the sensor assembly and the influence of electrostatic shielding on electric field distribution.

The results demonstrate that the inclusion of the Faraday cage effectively suppresses electric field penetration into the sensor cavity, resulting in a near-uniform potential region within the enclosed electronics. In contrast, removing the Faraday cage leads to significant intensification of the electric field within the sensor region, which may compromise measurement integrity and long-term reliability. This observation validates the necessity of electrostatic shielding in the proposed embedded sensing architecture.

Table 6.3: Material properties and geometrical configuration of the copper conductor used in the COMSOL model

Property	**Value**	**Unit**	**Segment**	**xw**	**yw**	**Additional**
Heat capacity	385	J/(kg·K)	1	-50 to -20	30 to 30	
Relative permittivity	1	–	2	-20 to 0	30 to 15.86	
Thermal conductivity	400	W/(m·K)	3	0 to 0	15.86 to 10	
Relative permeability	1	–	4	0 to -20	10 to 24	
Electrical conductivity	6.0×10^7	S/m	5	-20 to -50	24 to 24	
Coefficient of thermal expansion	1.65×10^{-5}	1/K	6	-50 to -50	24 to 30	
Density	8960	kg/m^3	Revolve	0		
Young's modulus	1.1×10^{11}	Pa				
Poisson ratio	0.35	–				
Reference resistivity	1.72×10^{-8}	Ωm				
Temperature coefficient	0.0039	1/K				
Reference temperature	298	K				

Table 6.4: Material properties and geometrical configuration of epoxy fill used for sensor encapsulation

Property	**Value**	**Unit**	**Segments**	**xw**	**yw**
Thermal conductivity	10	W/(m·K)	1–9	Various	Various
Relative permittivity	2.3	–			
Heat capacity	800	J/(kg·K)			
Density	1600	kg/m^3			
Young's modulus	3.35×10^9	Pa			
Poisson ratio	0.3	–			
Thermal expansion	6.0×10^{-7}	1/K			
Electrical conductivity	1.0×10^{-8}	S/m			

Table 6.5: Material properties and geometrical configuration of XLPE insulation

Property	**Value**	**Unit**	**Segments**	**xw**	**yw**
Relative permittivity	2.5	–	Multiple	Various	Various
Thermal conductivity	0.33	W/(m·K)			
Heat capacity	2174	J/(kg·K)			
Density	930	kg/m^3			
Poisson ratio	0.32	–			
Thermal expansion	3.2×10^{-4}	1/K			
Electrical conductivity	2.0×10^{-13}	S/m			
Bulk modulus	2.0×10^8	Pa			

Table 6.6: Material properties and geometrical configuration of the aluminium foil Faraday cage

Property	**Value**	**Unit**	**Segments**	**xw**	**yw**
Heat capacity	385	J/(kg·K)	Multiple	Various	Various
Relative permittivity	1	–			
Thermal conductivity	237	W/(m·K)			
Electrical conductivity	6.0×10^7	S/m			
Thermal expansion	1.7×10^{-5}	1/K			
Density	8960	kg/m^3			
Young's modulus	1.1×10^{11}	Pa			
Poisson ratio	0.35	–			

Table 6.7: Material properties and geometrical configuration of the LVT enclosure

Property	**Value**	**Unit**	**Geometry**
Relative permittivity	1	–	Width = 14 mm
Heat capacity	$C_p(T)$	J/(kg·K)	Depth = 30 mm
Thermal conductivity	$k(T)$	W/(m·K)	Height = 45 mm
Thermal expansion	α	1/K	Position = (24.5, -15, 33.86)
Density	$\rho(p, T)$	kg/m^3	
Speed of sound	$c_s(T)$	m/s	
Refractive index	1	–	

Fig. 6.1 shows the solved mesh of the instrumented splice, while Fig. 6.2 presents the transparent view of the sensor assembly.

Figure 6.1: Solved mesh of the instrumented splice

Fig. 6.3(a) and (b) illustrate the Joule heating distribution within the shunt and the corresponding thermal response obtained from a parametric current sweep ranging from 200 A to 3000 A. The results demonstrate a clear nonlinear increase in temperature with increasing current magnitude, consistent with the quadratic dependence of resistive losses on current. The parameter sweep further highlights the sensor's thermal behaviour under both nominal and extreme operating conditions, providing insight into its thermal stability and operational limits.

Figure 6.2: Sensor transparent frame

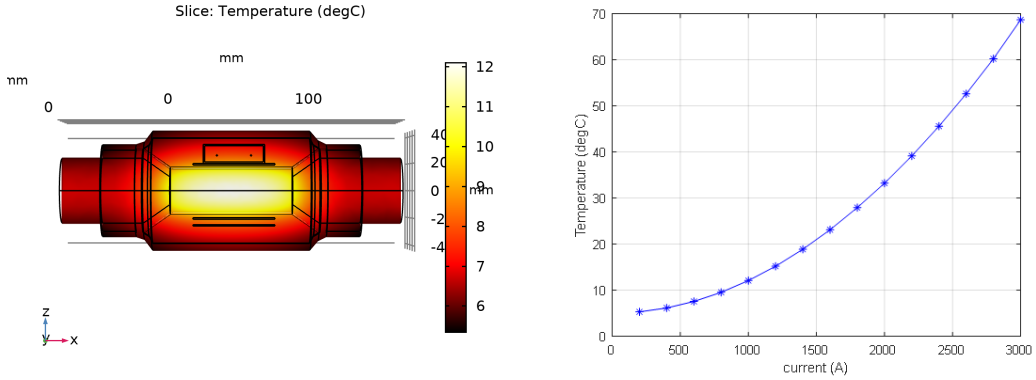

Figure 6.3: (a) Joule heating distribution, (b) Joule heating parameter sweep

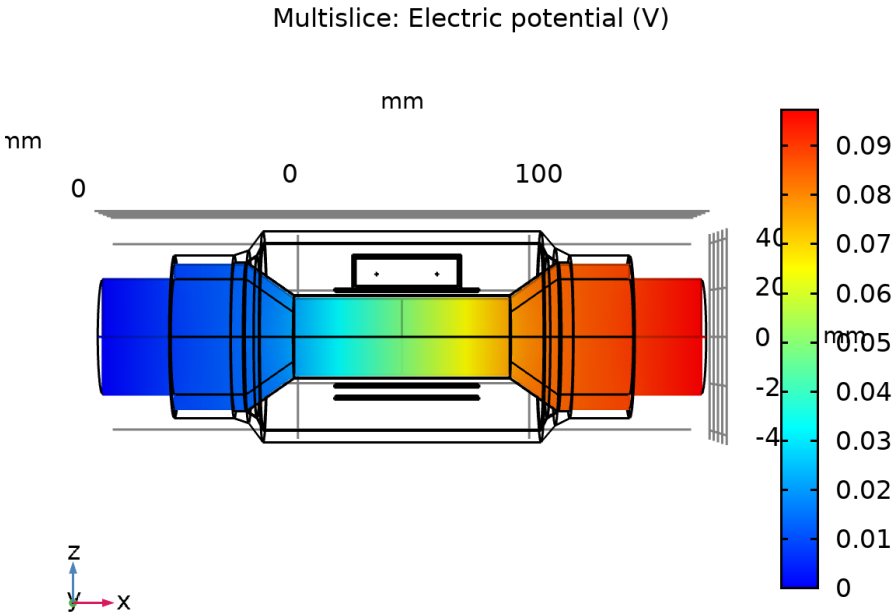

Figure 6.4: Voltage drop from current flow

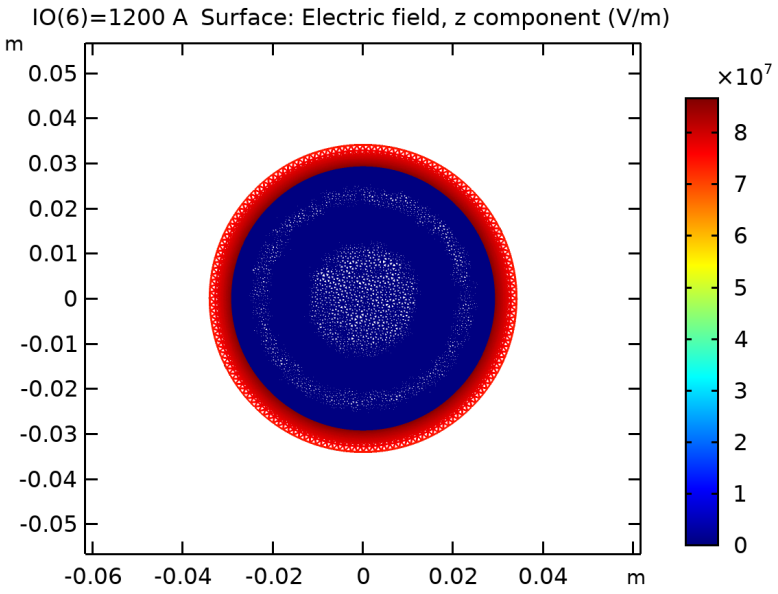

Figure 6.5: Electric field distribution with Faraday cage

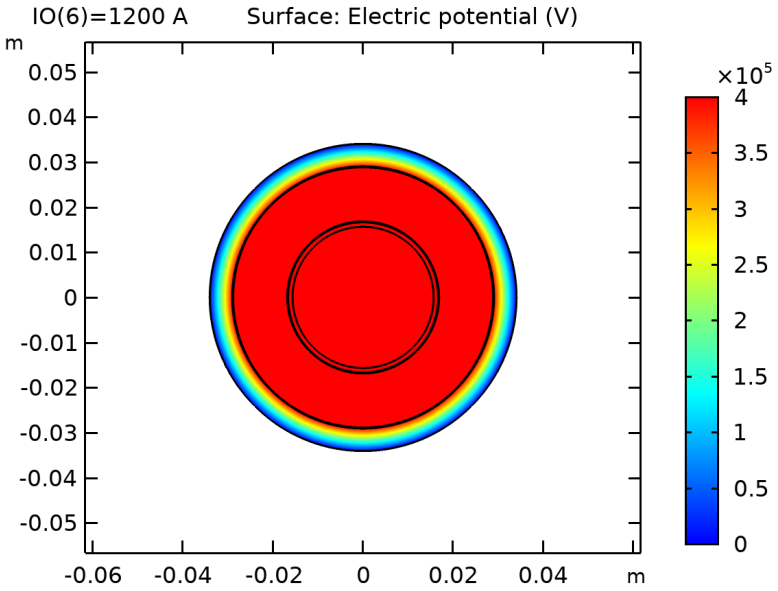

Figure 6.6: Electric potential distribution with Faraday cage

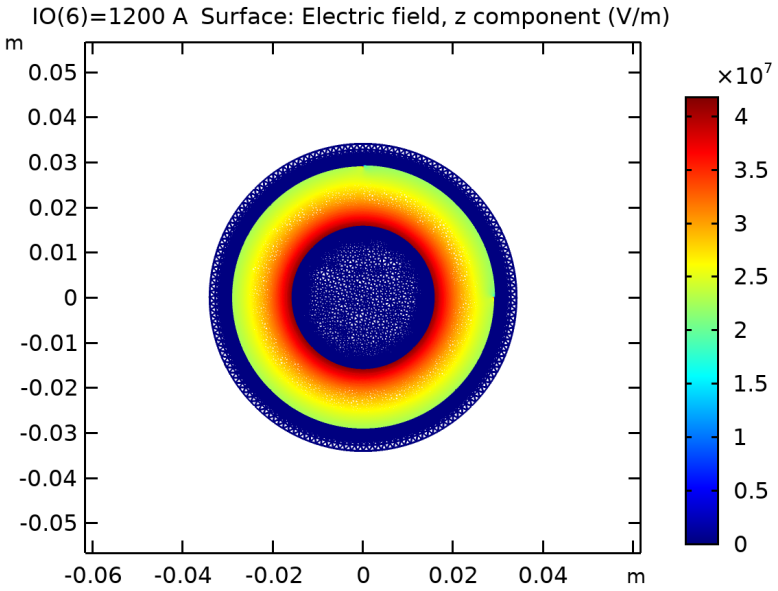

Figure 6.7: Electric field distribution without Faraday cage

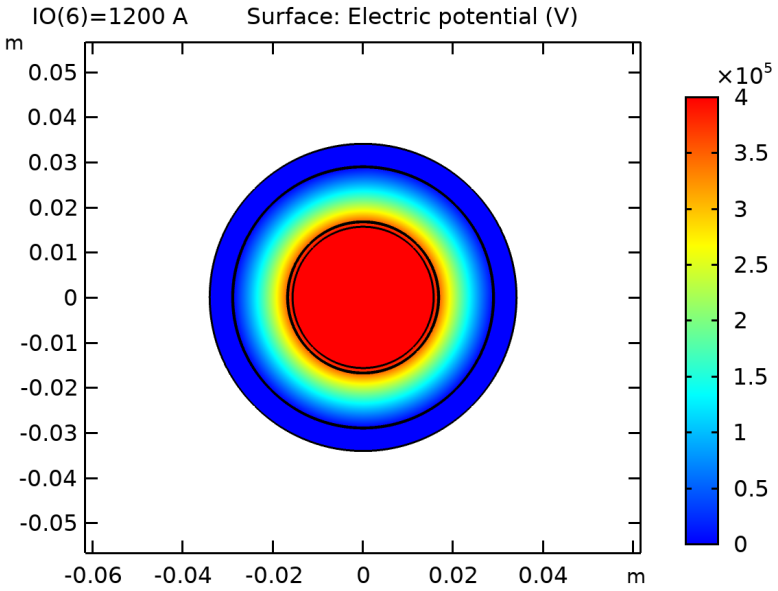

Figure 6.8: Electric potential distribution without Faraday cage

The simulation results indicate a temperature rise of approximately 12°C across the shunt structure under the applied current, confirming that the thermal design remains within acceptable operational limits.

Thermal Dissipation Paths in the Splice Joint

Heat generated within the shunt is dissipated through two principal pathways: radial conduction through the surrounding cable insulation layers and axial conduction along the conductor. The concentric layered structure of the XLPE cable is illustrated in Fig. 6.9.

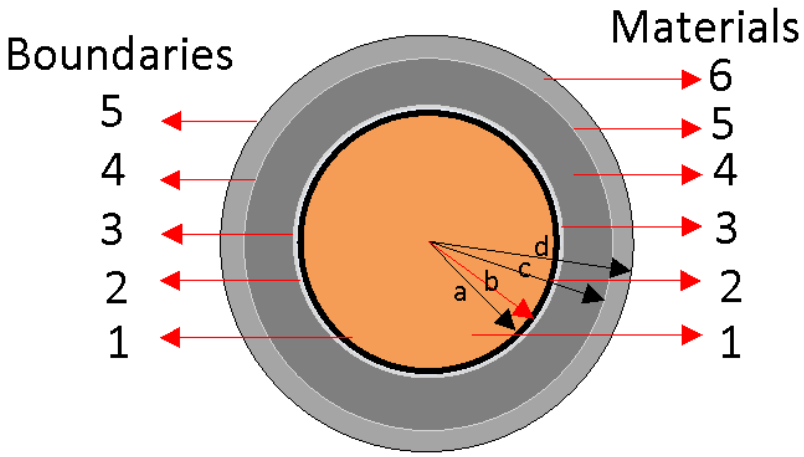

Figure 6.9: Cable concentric layers

In this representation, a, b, c, and d denote the inner and outer radii of the concentric cable insulation layers.

The equivalent thermal circuit representing the heat dissipation pathways is shown in Fig. 6.10, where each insulation layer is represented by a thermal resistance and each material interface is treated as a thermal junction.

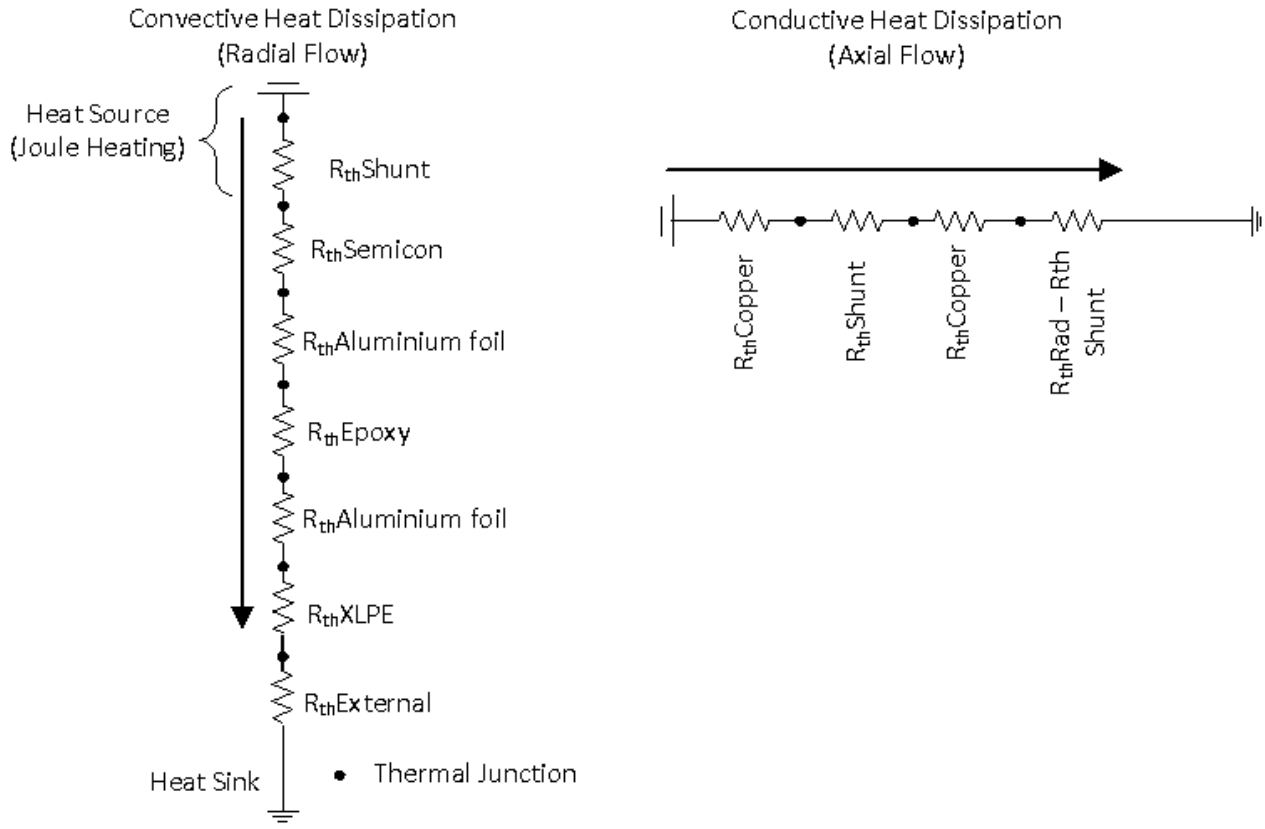

Figure 6.10: Equivalent circuit of conductor thermal resistance

The Joule-heating distribution and the parametric thermal response are shown in Fig. 6.3(a) and Fig. 6.3(b), respectively. The corresponding voltage drop across the shunt under current excitation is presented in Fig. 6.4. The electric field and electric potential distributions, with and without the Faraday cage (FC), are shown in Fig. 6.5 to Fig. 6.8.

The simulation results indicate a temperature rise of approximately 12°C across the shunt structure under the applied current, confirming that the thermal design remains within acceptable operational limits.

Thermal Dissipation Paths in the Splice Joint

Heat generated within the shunt is dissipated through two principal pathways: radial conduction through the surrounding cable insulation layers and axial conduction along the conductor. The concentric layered structure of the XLPE cable is illustrated in Fig. 6.9.

In this representation, a, b, c, and d denote the inner and outer radii of the concentric cable insulation layers.

The equivalent thermal circuit representing the heat dissipation pathways is shown in Fig. 6.10, where each insulation layer is represented by a thermal resistance and each material interface is treated as a thermal junction.

Table 6.8: Cable boundary interfaces and corresponding material layers in the instrumented splice assembly

Parameter/Label	**1**	**2**	**3**	**4**	**5**
Boundary	Conductor–Semicon	Semicon–Foil	Foil–Epoxy	Epoxy–Foil	Foil–XLPE
Material	Manganin	Semiconducting Screen	Thin Foil	Epoxy	XLPE
Thickness (mm)	15.89	1	0.2	13	5

Radial Heat Dissipation In the COMSOL model, heat generated within the shunt is conducted radially outward through the surrounding cable layers, while heat exchange with the external environment (seawater) occurs via convection at the outer boundary. Under subsea operating conditions, convective heat transfer at the cable surface constitutes the dominant mechanism for heat rejection to the surrounding medium.

The conductive heat transfer within the cable structure is governed by radial conduction through concentric cylindrical layers, extending from the manganin shunt through the semiconducting screen, metallic foil, epoxy encapsulation, and XLPE insulation. At the outer surface, heat is dissipated into the seawater through convective heat transfer.

The total radial thermal resistance of the system is therefore expressed as:

$$R_{\text{th,total}} = \sum_{i=1}^{n} \frac{\ln\left(r_{i+1}/r_i\right)}{2\pi k_i L} + R_{\text{conv}} \tag{6.7}$$

$$R_{\text{conv}} = \frac{1}{h\, 2\pi r_{\text{out}} L} \tag{6.8}$$

where:

- r_i and r_{i+1} are the inner and outer radii of each cylindrical layer
- k_i is the thermal conductivity of layer i ($\mathrm{W\,m^{-1}\,K^{-1}}$)
- L is the axial length of the section (m)
- r_{out} is the outer radius of the cable
- h is the convective heat transfer coefficient ($\mathrm{W\,m^{-2}\,K^{-1}}$)

For subsea conditions, the convective heat transfer coefficient typically ranges from 50 to 400 $\mathrm{W\,m^{-2}\,K^{-1}}$, depending on water movement and local thermal conditions.

Accordingly, the total thermal resistance may be written as:

$$R_{\text{th,total}} = R_{\text{manganin}} + R_{\text{semicon}} + R_{\text{foil}} + R_{\text{epoxy}} + R_{\text{XLPE}} + R_{\text{conv}} \tag{6.9}$$

The individual layer resistances are calculated as:

$$R_{\text{manganin}} = \frac{\ln(15.86 \times 10^{-3}/15.86 \times 10^{-3})}{2\pi \cdot 30 \cdot 90 \times 10^{-3}} = 0 \text{ K/W} \tag{6.10}$$

$$R_{\text{semicon}} = \frac{\ln(16.86 \times 10^{-3}/15.86 \times 10^{-3})}{2\pi \cdot 1.5 \cdot 90 \times 10^{-3}} = 7.21 \times 10^{-2} \text{ K/W} \tag{6.11}$$

$$R_{\text{foil}} = \frac{\ln(17.06 \times 10^{-3}/16.86 \times 10^{-3})}{2\pi \cdot 237 \cdot 90 \times 10^{-3}} = 8.8 \times 10^{-5} \text{ K/W} \tag{6.12}$$

Due to variations in material properties across layers, thermal conductivity varies at each interface, thereby affecting the overall thermal resistance network. A complete summary of the thermal resistance contributions for radial heat dissipation is provided in Table **??**.

If external convective heat exchange is considered, its contribution to the overall thermal resistance remains relatively small. This is due to the relatively high convective heat transfer coefficient for still seawater, which can reach values up to 400 $\text{W m}^{-2} \text{K}^{-1}$.

The total thermal resistance of the system is therefore expressed as:

$$R_{\text{th,total}} = \sum_{i=1}^{n} \frac{\ln(r_{i+1}/r_i)}{2\pi k_i L} + R_{\text{conv}} \tag{6.13}$$

The convective thermal resistance at the outer boundary is given by:

$$R_{\text{conv}} = \frac{1}{h\, 2\pi r_{\text{out}} L} \tag{6.14}$$

Substituting $h = 400 \text{ W m}^{-2} \text{K}^{-1}$, $r_{\text{out}} = 3.53 \times 10^{-2}$ m, and $L = 90 \times 10^{-3}$ m:

$$R_{\text{conv}} = \frac{1}{400 \cdot 2\pi \cdot 3.53 \times 10^{-2} \cdot 90 \times 10^{-3}} = 0.125 \text{ K/W} \tag{6.15}$$

Hence, the total thermal resistance becomes:

$$R_{\text{th,total}} = 9.92 \times 10^{-1} + 0.125 = 1.117 \text{ K/W} \tag{6.16}$$

Conductive Heat Dissipation In addition to radial heat dissipation, axial conductive heat transfer along the conductor provides an additional pathway for thermal energy dissipation. These pathways can be considered parallel thermal-resistance networks.

For axial conduction, the dominant contribution arises from the copper conductor due to its significantly higher thermal conductivity compared to the surrounding materials. The contribution of the manganin shunt to axial conduction is therefore neglected in this analysis.

The thermal resistance for conductive heat transfer along the conductor is given by:

$$R_{\text{th,conductor}} = \frac{L}{Ak} \tag{6.17}$$

where A is the cross-sectional area of the conductor and k is its thermal conductivity.

Assuming a unit length of 1 m, the conductive heat-dissipation pathway is evaluated using the material properties and geometry of the cable layers. The corresponding thermal resistance contributions are summarised in Table 6.9.

Table 6.9: Thermal conductivity and axial thermal resistance of cable materials

Material	k (W/m·K)	r_i (m)	r_o (m)	L (m)	R_{th} (K/W)
Manganin (Shunt)	30	1.59×10^{-2}	1.59×10^{-2}	1.00	0.00×10^{0}
Semiconducting Screen	1.5	1.59×10^{-2}	1.69×10^{-2}	1.00	6.49×10^{-3}
Aluminium Foil	237	1.69×10^{-2}	1.71×10^{-2}	1.00	7.92×10^{-6}
Thermally Enhanced Epoxy	10	1.71×10^{-2}	3.01×10^{-2}	1.00	9.02×10^{-3}
Aluminium Foil	237	3.01×10^{-2}	3.03×10^{-2}	1.00	4.45×10^{-6}
XLPE	0.33	3.03×10^{-2}	3.53×10^{-2}	1.00	7.38×10^{-2}
Total					8.93×10^{-2}

The total resistance from the conductor-side pathway includes the convective component for heat dissipation to the external environment:

$$R_{\text{conv}} = \frac{1}{400 \cdot 2\pi \cdot 3.53 \times 10^{-2} \cdot 1} = 0.01127 \text{ K/W} \tag{6.18}$$

$$R_{\text{th,conductor}} = 0.0210 + 8.93 \times 10^{-2} + 0.01127 = 0.12127 \text{ K/W} \tag{6.19}$$

The total thermal resistance is obtained from the parallel combination of radial (convective-dominated) and axial (conductive) dissipation pathways:

$$R_{\text{th,combined}} = \frac{R_{\text{th,total}} \cdot R_{\text{th,conductor}}}{R_{\text{th,total}} + R_{\text{th,conductor}}} \tag{6.20}$$

$$R_{\text{th,combined}} = \frac{0.12127 \cdot 1.117}{0.12127 + 1.117} = 0.1094 \text{ K/W} \tag{6.21}$$

The temperature rise of the shunt is therefore given by:

$$\Delta T = (I^2 R) \cdot R_{\text{th,combined}} \tag{6.22}$$

$$\Delta T = (1000^2 \cdot 50 \times 10^{-6}) \cdot 0.1094 = 5.47^\circ\text{C} \tag{6.23}$$

$$T_{\text{shunt}} = \Delta T + T_{\text{ext}} = 5.47 + 4 = 9.47^\circ\text{C} = 282.62 \text{ K} \tag{6.24}$$

The manganin shunt was selected due to its low temperature coefficient of resistance (approximately 10 ppm/K), making it suitable for high-precision, low-drift applications.

Standalone Thermal Estimation If the shunt is treated as an isolated component, its thermal resistance can be estimated from:

$$R_{\text{th}} = \frac{L}{Ak} \tag{6.25}$$

For a cylindrical geometry:

$$A = 2\pi r(r + h) \tag{6.26}$$

Given:

- $r = 15.86$ mm
- $L = 90$ mm
- $k = 30$ W/(m·K)

$$A = 10.54 \times 10^{-3} \text{ m}^2 \tag{6.27}$$

$$R_{\text{th}} = \frac{0.09}{30 \cdot 10.54 \times 10^{-3}} = 0.2846 \text{ K/W} \tag{6.28}$$

Power dissipation:

$$P = I^2 R = 1000^2 \cdot 50 \times 10^{-6} = 50 \text{ W} \tag{6.29}$$

$$\Delta T = R_{\text{th}} \cdot P = 0.2846 \cdot 50 = 14.23^\circ\text{C} \tag{6.30}$$

The analytical estimate (14.23°C), junction-based thermal model (9.47°C), and COMSOL simulation result (12°C) exhibit close agreement, thereby validating the modelling approach.

IEC Thermal Consideration

$$\Delta\theta = W_c(T_1 + nT_2 + n(T_3 + T_4)) \tag{6.31}$$

The permissible insulation temperature margin is:

$$\Delta\Theta = \Theta_{\max} - \Theta_a \tag{6.32}$$

$$\Delta\Theta = 70 - 4 = 66^\circ\text{C} \tag{6.33}$$

The calculated and simulated temperature rises are significantly below this threshold.

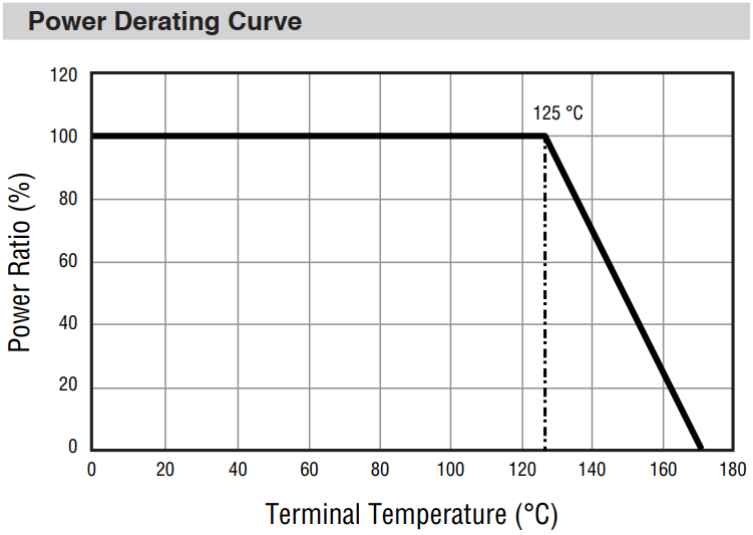

Figure 6.11: Power derating curve of shunt sensor

Electric Field Distribution and Shielding Effectiveness The sensor operates in a high electric-field environment inherent to HVDC systems. Without shielding, embedding the electronics directly within epoxy exposes the circuitry to field penetration, as illustrated in Fig. 6.7 and Fig. 6.8.

The incorporation of a Faraday cage effectively suppresses the internal electric field, producing a near-zero field region within the sensor enclosure, as demonstrated in Fig. 6.5 and Fig. 6.6.

Signal Conditioning Circuit Validation

Linear Amplification Configuration

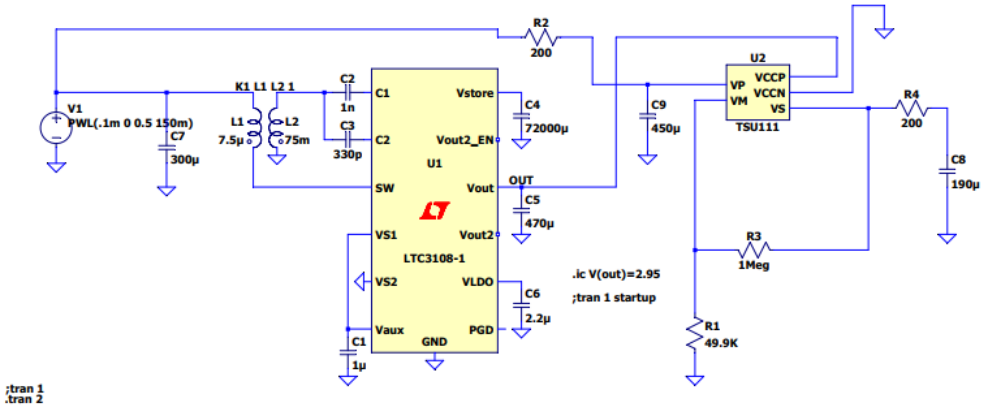

Figure 6.12: Sensor circuit in linear operation mode (LTSpice)

The linear amplifier was configured in a non-inverting mode with a gain of 21 V/V. However, this configuration exhibited limited sensitivity at low signal levels.

Non-linear Amplification Configuration

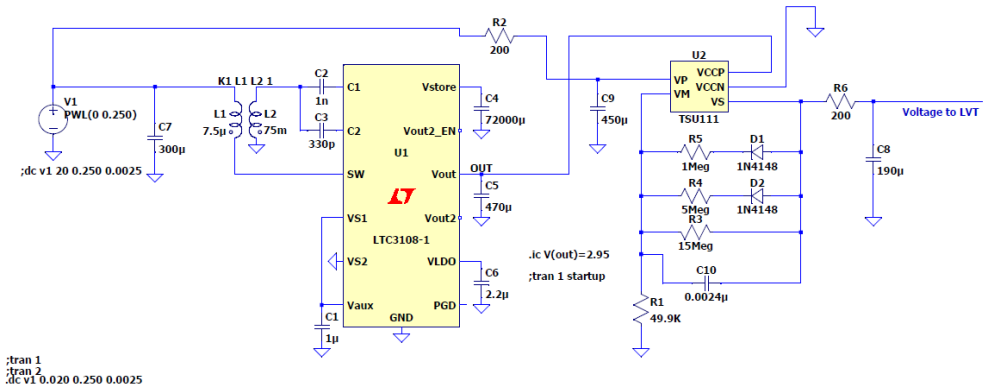

Figure 6.13: Sensor circuit in non-linear operation mode (LTSpice)

The non-linear amplifier was introduced to enhance sensitivity in the low-signal regime.

Simulation Results

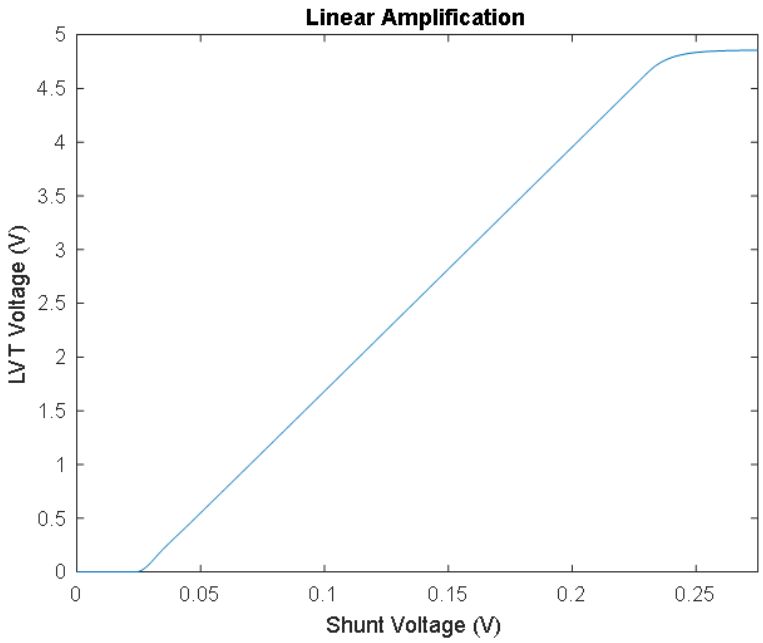

Figure 6.14: Simulated response of linear amplification

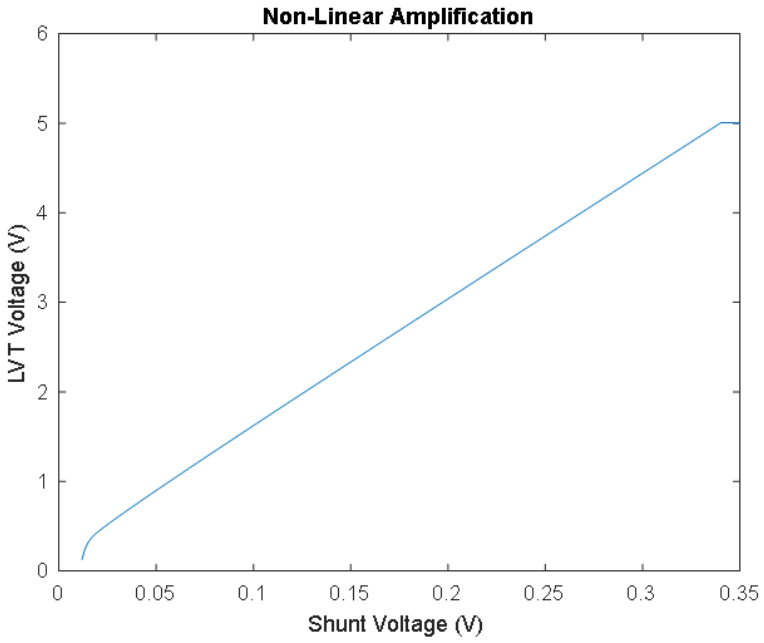

Figure 6.15: Simulated response of non-linear amplification

The non-linear amplification approach demonstrates improved sensitivity at low input levels by introducing a higher effective gain in the low-amplitude region.

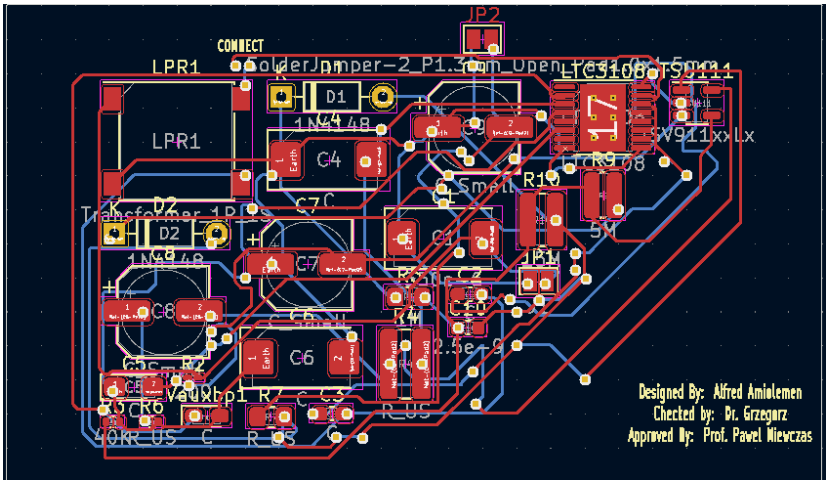

Figure 6.16: Footprint routing and PCB development in KiCAD

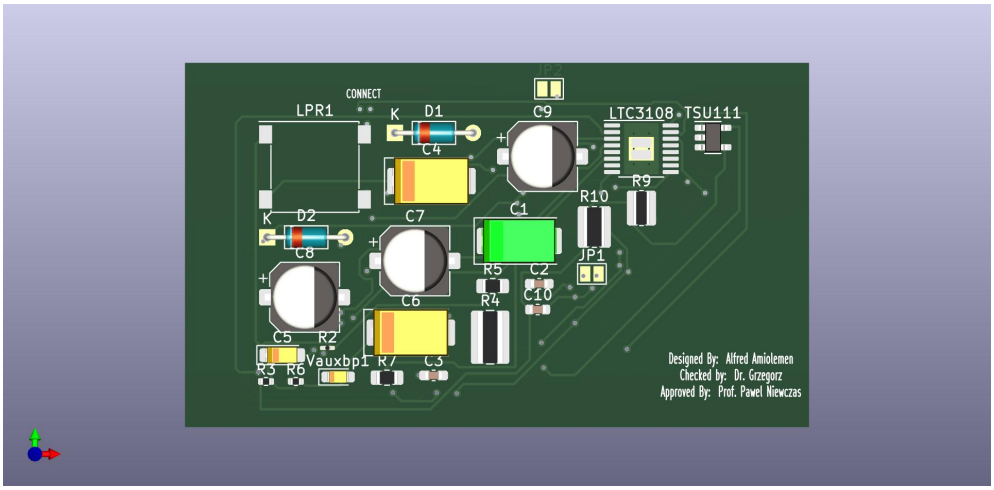

Figure 6.17: PCB component layout in KiCAD

PCB Development in KiCAD The LTSpice design was implemented in KiCAD, where schematic capture, footprint integration, and PCB routing were performed.

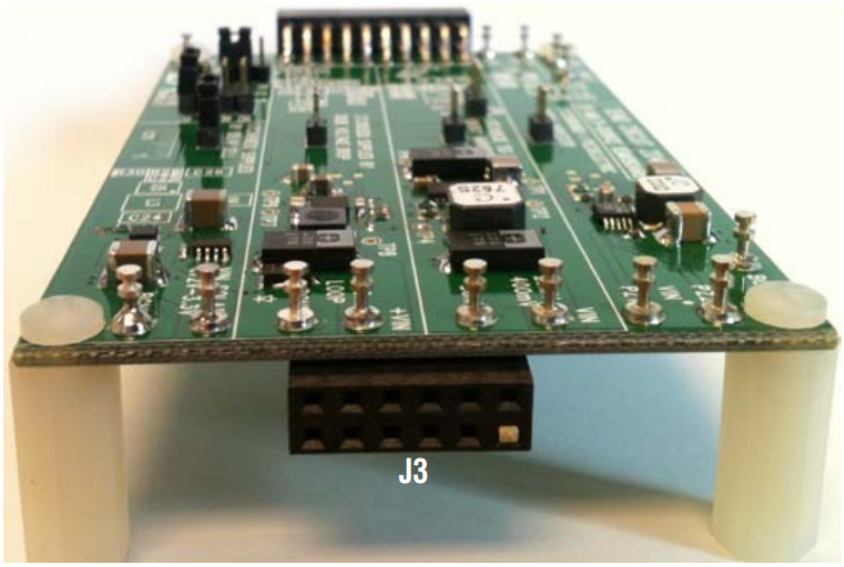

Figure 6.18: LTC3108 energy harvesting demonstration board

Due to fabrication constraints, a commercial demonstration board (DC2042A) incorporating the LTC3108 energy harvester was utilised for experimental validation.

While the demonstration board provided the energy harvesting functionality, other critical subsystems, including the operational amplifier circuitry and the LVT, were implemented on a prototyping board. This modular approach enabled independent validation of each subsystem while maintaining flexibility during circuit optimisation.

The remaining experimental investigations, including performance evaluation and circuit refinement, were conducted in a laboratory environment using the assembled prototype. Despite manufacturing constraints, the adopted approach enabled successful validation of the system, with experimental measurements confirming the expected performance.

6.3 Experimental Setup

The circuit presented in Fig. 6.13 was implemented on a prototyping board, with power supplied by the LTC3108 energy harvester and its associated circuitry. Ultra-low-power operational amplifiers (TSU111) and their gain-setting components were integrated into

the design.

Input excitation signals were generated using the analogue output channels of a National Instruments USB-6003 data acquisition (DAQ) device, while the corresponding output signals were acquired via its analogue input channels. For each input amplitude, 3000 samples were recorded at a sampling frequency of 3 kHz.

The experimental configuration was designed to emulate the voltage drop across the shunt under HVDC operating conditions. A programmable DC voltage source was used to reproduce this behaviour, enabling controlled excitation of the sensor system.

The experiments were conducted at the Technology and Innovation Centre (TIC), University of Strathclyde, under controlled laboratory conditions. The setup was configured to evaluate the performance of the LVT and associated signal-conditioning circuitry for HVDC splice-joint applications.

6.3.1 List of Equipment and Tools

To ensure measurement accuracy and repeatability, a range of precision instruments and data acquisition tools were employed:

Measuring Equipment

- Keysight 34410A Digital Multimeter — precision measurement of voltage, current, and resistance
- Temma 726202 Digital Multimeter — secondary instrument for cross-validation
- TeckniK Oscilloscope — real-time waveform monitoring
- LabVIEW Software Scope — virtual oscilloscope for signal visualisation and acquisition

Power Supply Equipment

- Aplab LVED 30/2 DC Power Supply — controlled DC excitation source

Software Tools

- LabVIEW 2018 — data acquisition, control, and analysis
- IMON Evaluation Software — IBSEN interrogator interface for FBG sensing

Prototyping Platform

- Breadboard — flexible circuit prototyping and rapid iteration

Components

- Low Voltage Transducer (LVT) — electro-optical sensing element
- Passive components (resistors, capacitors) — implemented according to KiCAD-generated bill of materials

Optical Interrogation System

- Super-luminescent LED (SLED) — broadband optical source
- IBSEN IMON 512 USB Interrogator — FBG interrogation with 3 pm repeatability and 5 pm linearity [1]

Data Acquisition System

- National Instruments USB-6003 — 16-bit DAQ with 100 kS/s sampling capability and 6 mV absolute accuracy [2]

6.3.2 Signal Conditioning Circuit

The signal conditioning circuit was designed to amplify the shunt voltage to a level compatible with the LVT input requirements. The selected components prioritised ultra-low power consumption to ensure compatibility with the energy harvesting system.

The key components used in the sensor construction are summarised in Table 6.10.

Table 6.10: Components used for sensor construction

ID	Designator	Package	Quantity	Description
1	C9, C8, C7	CP_Elec_6.3x3	3	Capacitors
2	C10	C_0603	1	2.5×10^{-9} F
3	C3, C2	C_0603	2	Capacitors
4	Vauxbp1	CP_EIA-2012	1	Capacitor
5	C5	CP_EIA-3216	1	Capacitor
6	C1	CP_EIA-7343	1	350 μF
7	C6, C4	CP_EIA-7343	2	Capacitors
8	D1, D2	DO-35	2	1N4148 Diodes
9	JP1	Solder Jumper	1	Jumper
10	LTC3108	HTSSOP-16	1	Energy Harvester IC
11	TSU111	SOT-23-5	1	Ultra-low power Op-Amp
12	R2	0201	1	200 Ω
13	R6	0402	1	Resistor
14	R3	0402	1	40 kΩ
15	R9	0612	1	5 MΩ
16	R7	0805	1	Resistor
17	R5	0805	1	1 MΩ
18	R10	0815	1	15 MΩ
19	R4	1020	1	Resistor
20	LPR1	Transformer	1	Coilcraft LPS 6235-682

Experimental Procedure

The electro-optical interaction between the shunt-derived electrical signal and the corresponding optical response generated by the LVT was verified using the experimental arrangement shown in Fig. 6.19. This setup was developed to reproduce representative HVDC steady-state and transient operating conditions while enabling the simultaneous acquisition of electrical and optical waveforms. By injecting the conditioned shunt signal into the LVT input stage and monitoring the resulting optical modulation, the arrangement provides a controlled framework for assessing the fidelity, responsiveness, and dynamic coupling behaviour of the electro-optical conversion mechanism.

The circuit was assembled on a breadboard. The DC voltage source was connected to a voltage divider comprising a 100 Ω series resistor and a 2 Ω burden resistor. This arrangement was designed to emulate the voltage drop across a 50 $\mu\Omega$ shunt resistor,

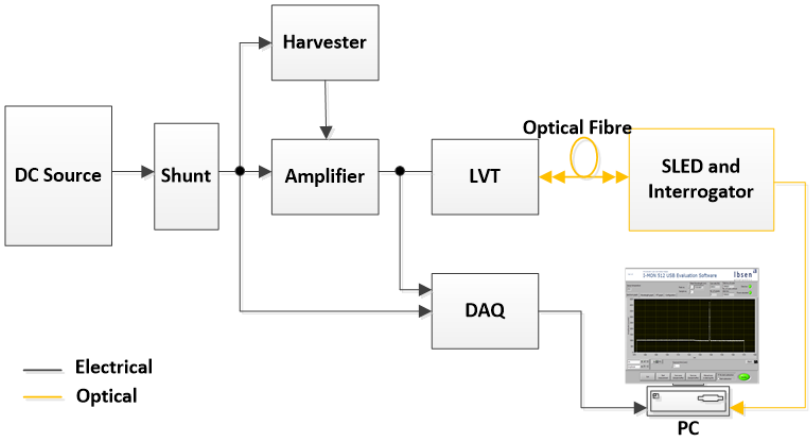

Figure 6.19: Block diagram of experimental setup

which, at a nominal current of 1 kA, corresponds to a 50 mV signal. The voltage developed across the 2 Ω burden resistor was used as the input to the energy harvester and, under normal operating conditions, also served as the excitation signal for the operational amplifier stage.

However, in this experimental evaluation, a controlled step input generated by the DAQ card was applied to the signal-conditioning circuit, with increments of 2.5 mV. The DC voltage source was additionally equipped with a rotary control interface, enabling fine adjustment of the supply voltage magnitude and, therefore, control of the simulated shunt current. These adjustments were performed to evaluate the ability of the energy harvester to supply sufficient power to the circuit over a wide operating range, extending from 40% of the nominal supply voltage, corresponding to 20 mV and representing near-threshold input conditions for the harvester, to 300% of the nominal supply voltage, corresponding to 150 mV and representing extreme overdrive conditions. This assessment was necessary to verify both the lower-bound sensitivity and the upper-bound robustness of the harvester under practical operating conditions.

As shown in Fig. 6.20, the input of the LVT was connected via Kovar pins to the output of the operational amplifier. The fibre-optic pigtail from the LVT was connected to a fibre coupler through a female connector. The fibre coupler split the optical signal

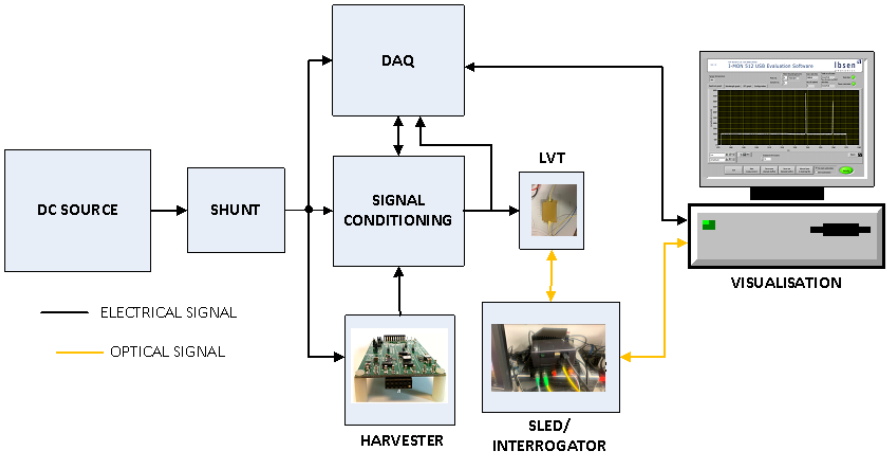

Figure 6.20: Block diagram of experimental setup with equipment visualisation

into transmitted and reflected components. The transmitted broadband light, originating from the SLED source, propagated through the fibre, while the reflected wave was directed to the IBSEN IMON 512 USB photonic interrogator. The interrogator analysed the reflected wavelength, which corresponds to the strain experienced by the fibre Bragg grating embedded within the LVT. The strain-induced wavelength shift was then correlated with the magnitude of the voltage drop across the shunt, thereby providing a reliable optical representation of the electrical signal under test.

Electrical Signal Acquisition To enable precise and repeatable measurements in the prototyping setup, data were acquired from both the shunt-voltage and the LVT-output voltages. The LVT voltage corresponds to the output of the operational amplifier and provides essential information for evaluating the response of the signal-conditioning stage. Together, the shunt voltage and LVT voltage provide the basis for assessing the overall functionality of the sensing system.

The acquisition of these voltages was performed using a National Instruments USB-6003 DAQ module. This DAQ module supports multiple analogue input configurations and integrates directly with LabVIEW for real-time monitoring and control. In the present experiment, the necessary connections were made to the single-ended analogue input channels of the DAQ, namely channels `ai0` to `ai7`. The DAQ module was con-

nected directly to the host computer through a standard USB interface, which simultaneously provided power and data transfer. This simplified the hardware arrangement and enabled straightforward integration with the LabVIEW environment.

LabVIEW, a graphical programming environment, was used to configure the data acquisition system. The software's block-diagram environment enabled the development of a robust acquisition routine for measurement, processing, and data logging. A DAQ Express block was employed for real-time voltage acquisition, providing efficient hardware configuration while reducing the need for extensive low-level coding.

The DAQ system was configured to acquire 3000 samples per measurement at a sampling frequency of 3 kHz. These settings were selected to ensure sufficient temporal resolution and measurement fidelity for capturing the signal variations associated with the emulated transient conditions. The chosen sampling frequency was adequate to represent the sensor's dynamic behaviour and enable reliable post-processing and interpretation.

A key feature of the LabVIEW program was its ability to continuously log data across multiple runs within a single measurement cycle. This automated logging strategy ensured that the results from each run were appended to the output file without manual intervention, thereby improving the efficiency and repeatability of the measurement process. The program was designed to handle multiple measurement cycles, with each cycle comprising several runs executed automatically.

To achieve this automation, a double `for` loop structure was implemented in the LabVIEW program, as shown in Fig. 6.21. The first loop controlled the incremental steps within each measurement cycle, while the second loop governed the number of runs per cycle. This structure provided precise control over the acquisition sequence and enabled the measurement process to continue automatically until the predefined stopping criteria were reached.

To enhance control over the acquisition logic, a case structure was incorporated to monitor the DAQ state in real time and determine whether the preset threshold for a "go" condition had been reached. Once this condition was satisfied, the logic returned a true state, enabling the DAQ sequence to transition from the "go" condition to the

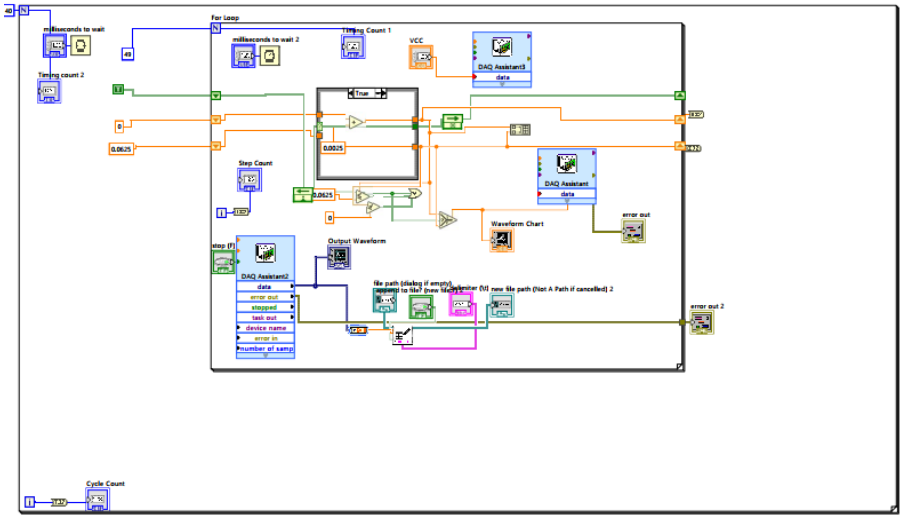

Figure 6.21: Automated data acquisition code in LabVIEW

"return" condition. This arrangement ensured automatic switching between measurement states according to predefined criteria, thereby reducing operator intervention and limiting the risk of experimental inconsistency.

In addition, two shift registers were employed to preserve the previous states of the "go" and "return" conditions between successive loop iterations. These stored states were used to perform arithmetic operations, including adding or subtracting fixed increments from the signal, thereby enabling controlled ramp-up and ramp-down sequences during the experiment. This functionality was essential for implementing the stepped excitation profile required for the measurement campaign.

The graphical programming environment in LabVIEW provided a visual representation of the complete acquisition architecture, facilitating real-time monitoring and debugging of the program. The block-diagram structure allowed rapid identification of issues in both program logic and hardware interfacing, thereby facilitating efficient refinement of the acquisition routine.

Figure 6.22 illustrates the front panel of the LabVIEW interface, which served as the primary dashboard for experiment control and signal monitoring. The front panel includes control elements, such as buttons and sliders, that enabled real-time adjustment of key experimental parameters. It also incorporated scope windows for real-time dis-

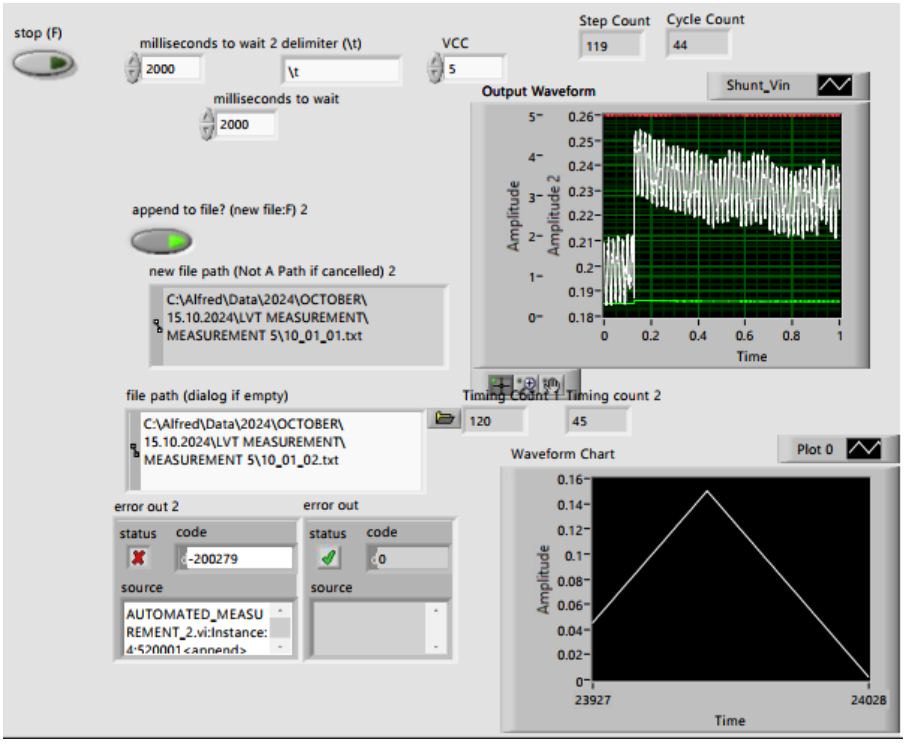

Figure 6.22: LabVIEW data acquisition panel

play of the acquired waveforms, providing immediate feedback on measurement quality and system performance.

The use of the NI USB-6003 DAQ module in conjunction with LabVIEW enabled automated acquisition and logging of measurement data under controlled laboratory conditions. The integration of automated loops, logical case structures, and shift registers ensured stable and efficient DAQ operation, while the graphical interface provided an intuitive and user-friendly means of controlling the experiment. This configuration enabled precise and repeatable measurements to support the study's overall objectives.

Optical Signal Acquisition To acquire the optical signal, the arrangement shown in Fig. 6.23 was implemented. The optical setup consisted of a dense optoelectronic superluminescent light-emitting diode (SLED) as the broadband light source, an IBSEN Photonics 256/512 interrogator, and optical fibre interconnections. These elements were coupled via a unit that connected the optical path to the LVT. The optical interrogator was connected to the computer using a dedicated communication interface, enabling

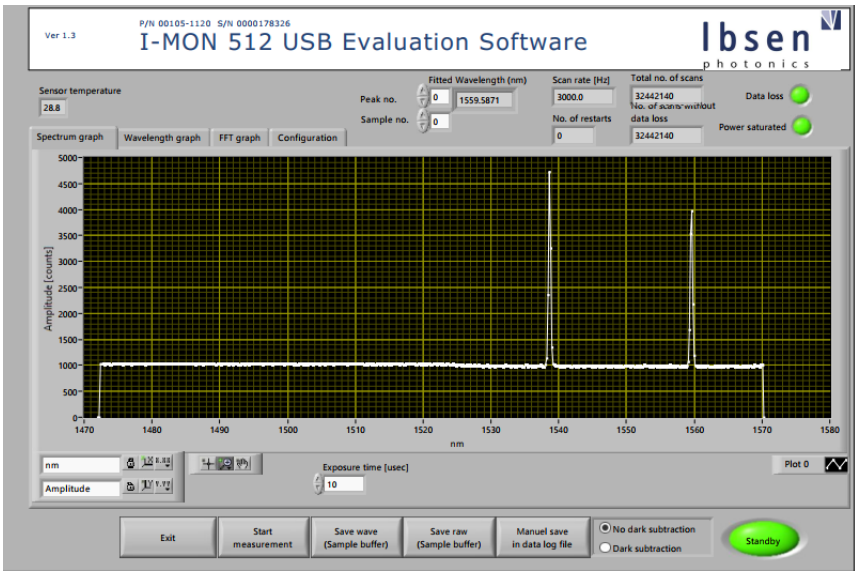

Figure 6.23: IBSEN I-MON wavelength monitoring window

both real-time data transfer and software-based instrument control.

Communication between the optical hardware and the visualisation interface was provided via the I-MON evaluation software, which offered a user-oriented front panel for configuring the principal acquisition parameters. These included the signal detection threshold, the number of samples collected per measurement, the exposure time, the number of FBGs to be interrogated, and the acquisition frequency. The I-MON software also provided visualisation functions, including spectral and wavelength graphs, enabling real-time monitoring of the optical response and adjustment of the acquisition settings as required.

6.4 Sensor Dynamic Response

As illustrated in Fig. 6.24 and Fig. 6.25, the dynamic correspondence between the electrical excitation and the resulting optical response confirms the electro-optical coupling within the sensing system. The wavelength spectra displayed in the I-MON interrogation software provide direct visualisation of the fibre Bragg grating response, enabling observation of wavelength shifts associated with strain variations in the sensing element. These measurements allow real-time monitoring of the optical signal behaviour and pro-

vide insight into the sensor's ability to resolve strain-induced changes occurring within the piezoelectric transducer. The observed wavelength variations therefore reflect the mechanical deformation induced by the applied electrical signal, thereby confirming the effectiveness of the optical interrogation process in capturing the electro-mechanical interaction within the sensor.

One limitation of the IBSEN photonic interrogator in this arrangement is the absence of direct synchronisation capability with the LabVIEW-based electrical acquisition system. Specifically, the interrogator cannot align its start and stop acquisition times with the DAQ-based measurement sequence, which poses a challenge for directly comparing the electrical and optical datasets on a sample-by-sample basis.

However, despite this lack of hardware-level synchronisation, the integrity and usefulness of the measurements remain unaffected. The optical system reliably captures the strain-induced FBG response, while LabVIEW reliably measures the corresponding electrical variations through the NI USB-6003 DAQ. Furthermore, the use of consistent sampling settings, including the number of samples per acquisition and the measurement frequency, enables reconciliation of the two datasets during post-processing. The I-MON software provides a robust interface for configuring and visualising the optical data, while careful processing in MATLAB enables consistent comparison between the electrical and optical responses.

6.4.1 Electrical and Optical Characteristic Response

Figures 6.24 and 6.27 present representative experimental results for the electrical and optical signals, respectively. During the test, the input signal was applied as a sequence of discrete voltage steps with an increment of 2.5 mV. These increments were accumulated through the LabVIEW shift-register implementation until 120% of the nominal threshold (60 mV) was reached. Each voltage level was maintained for 3 s to ensure a steady-state response before advancing to the next step.

Signal acquisition was performed using the NI USB-6003 DAQ for electrical measurements and the optical interrogator for wavelength measurements, both operating at a sampling frequency of 3 kHz. The recorded datasets were subsequently exported

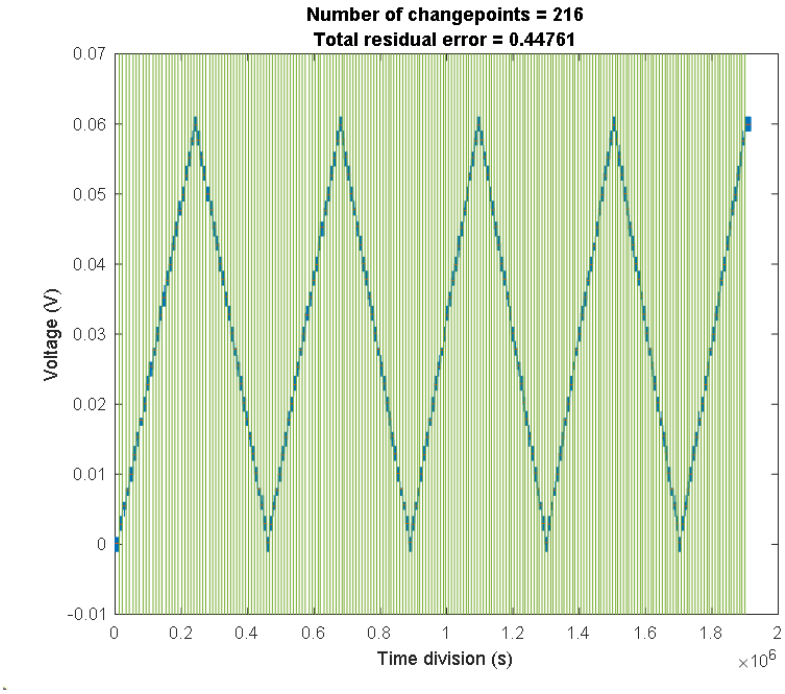

Figure 6.24: Measurement sliced into timeframe for electrical signal

to MATLAB for post-processing.

Due to the absence of hardware-level synchronisation between the electrical and optical acquisition systems, a post-processing alignment procedure was implemented. Each measurement run was divided into discrete time windows corresponding to the duration of each voltage step, as shown in Fig. 6.24 and Fig. 6.27. Within each time window, the acquired samples were averaged to obtain a single representative value for that measurement level. The resulting averaged data points are shown in Fig. 6.25 and Fig. 6.26.

This averaging approach enables consistent comparison between the electrical and optical measurements by ensuring that both datasets are evaluated over equivalent time intervals. In the resulting plots, the x-axis represents the discrete voltage steps (changepoints), while the y-axis corresponds to the measured signal amplitude. Each changepoint therefore corresponds to a stable operating point within the applied input sequence.

To ensure proper correlation between the two measurement systems, optical ac-

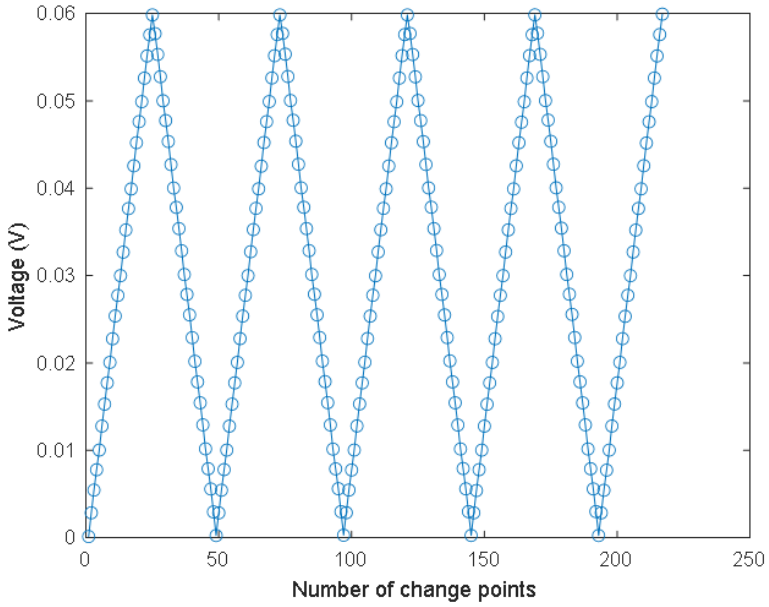

Figure 6.25: Averaged points for electrical signal

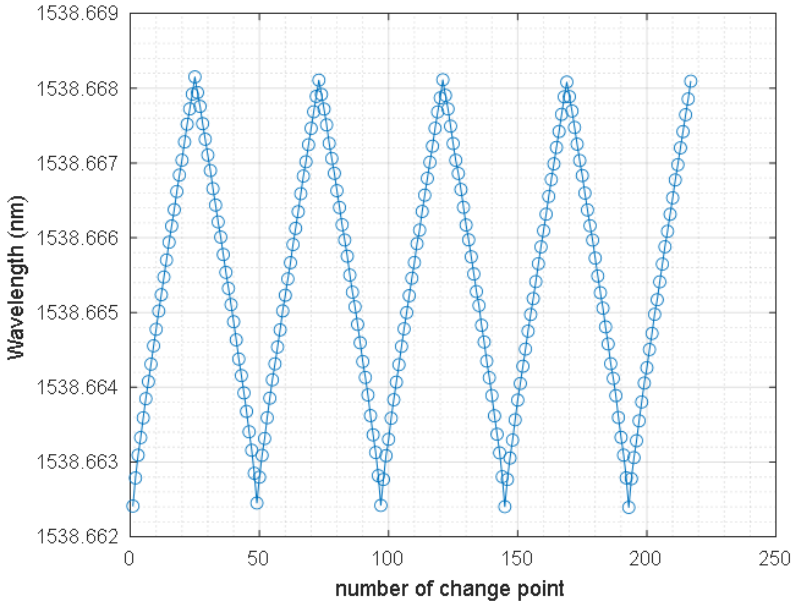

Figure 6.26: Averaged points for optical signal

quisition was initiated prior to the electrical excitation sequence. This ensured that the optical system was fully operational before the input signal began to vary, thereby

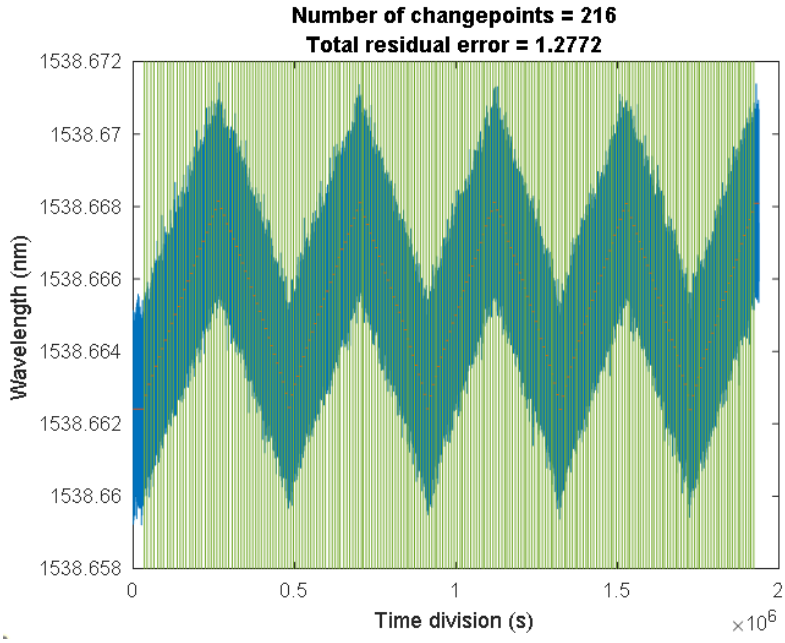

Figure 6.27: Optical measurement sliced into timeframe

allowing all subsequent electrical changes to be captured in the optical domain. Although the two systems were not synchronised in real time, this approach enabled effective alignment of the datasets during post-processing.

The input–output characteristics of the signal-conditioning circuit, obtained from multiple experimental runs, are presented in Fig. 6.28 and demonstrate good repeatability. The nonlinear behaviour of the amplifier is evident from the shape of the transfer curve, particularly in the enhanced response at low input amplitudes. This behaviour is essential for elevating weak signals above the resolution limit of the optical interrogator. Furthermore, the logarithmic representation shown in Fig. 6.31 improves the visibility of the nonlinear characteristics compared with the linear-scale plot.

LVT Hysteresis

The input–output relationship of the LVT exhibits a clear hysteresis loop, a characteristic commonly associated with energy-storing elements. While inductors store energy in magnetic fields and capacitors store energy in electric fields, piezoelectric materials, which are capacitive in nature, store and retain electrical charge during excitation.

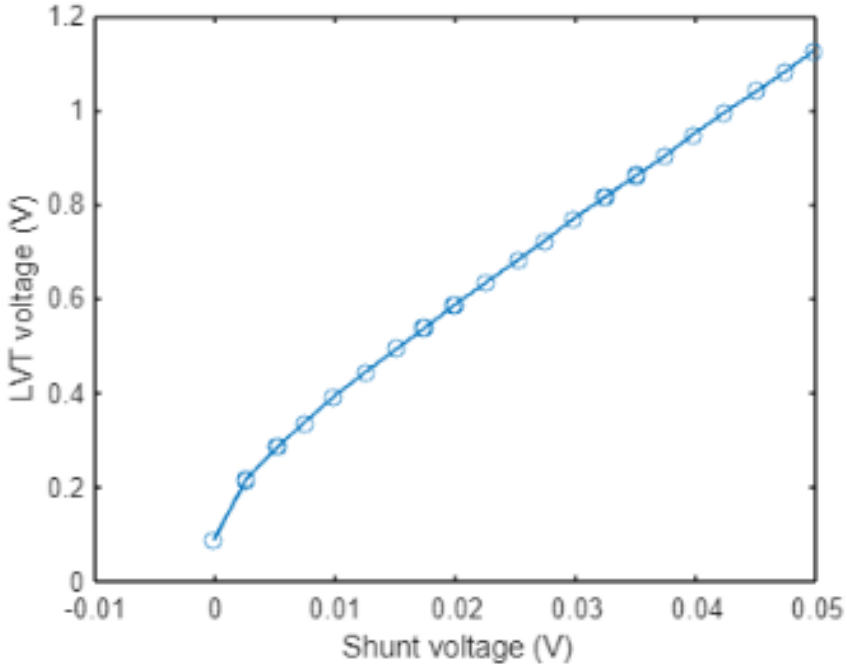

Figure 6.28: Input and output characteristic of the op-amp

In this case, hysteresis arises from the imbalance between polarisation and strain under the applied electric field. Owing to the counterbalance of polarisation at a given voltage level between the forward and reverse paths, displacement occurs, resulting in the hysteretic behaviour observed in Fig. 6.29 [3]. The hysteresis loop is narrower at lower voltages, consistent with established behaviour reported for piezoelectric transducers [3], [4], [5].

A comparative assessment of the hysteresis behaviour between the linear amplification configuration (see Fig. 5.27 in Chapter 5) and the nonlinear configuration (see Fig. 5.28 in Chapter 5 and Fig. 6.29 in this chapter) indicates that the linear amplifier exhibits a wider hysteresis loop. This is attributed to its approximately constant voltage gain of 21 V/V, which produces larger LVT output amplitudes at higher input levels and, consequently, a broader hysteresis width. In contrast, the nonlinear configuration, with a reduced effective gain of approximately 13 V/V at 240 mV input, generates a compressed output response and therefore produces a narrower hysteresis loop.

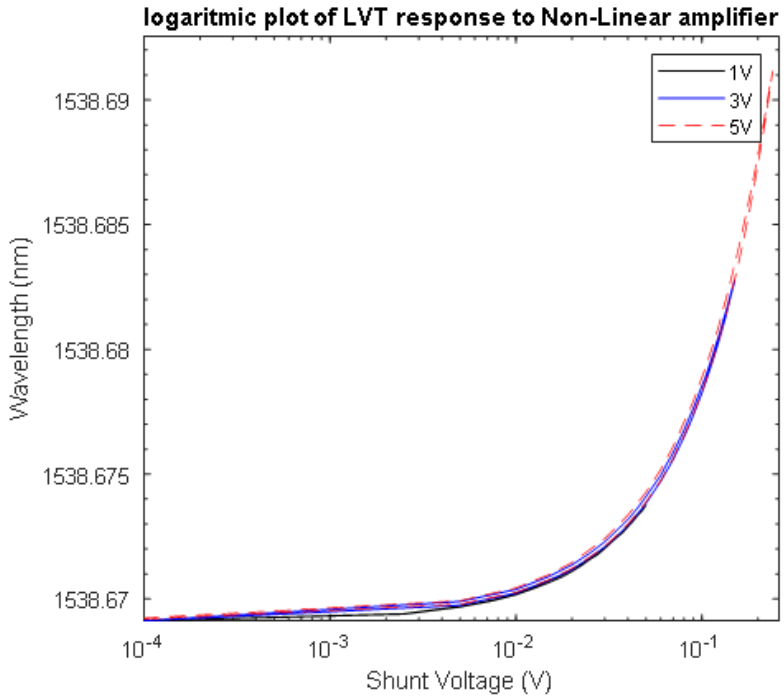

Figure 6.29: Hysteresis profile of the LVT

The nonlinear curve exhibits an asymmetric incremental progression relative to the response obtained using linear amplification. These results provide insight into the behaviour of the final optical current sensing solution.

Response to Transient Edge

The transient response of the circuit to variations in signal magnitude and rise time was evaluated to examine the behaviour of the LVT under fault-related operating conditions. A representative experiment was performed to emulate a 1 ms rising edge, corresponding to a fast current transient in a power network. The measured response, shown in Fig. 6.30, captures the principal characteristics of the transient behaviour.

During this event, the amplifier entered saturation, producing clipping at approximately 3.3 V. This saturation level corresponds both to the sensor's accuracy limit factor (KALF) and to the upper rail constraint imposed by the output stage of the energy-harvesting circuit. The results demonstrate strong agreement between the LVT electrical output and the corresponding optical signal, confirming the capability of the

proposed optical current sensor to capture critical transient events relevant to practical HVDC deployment.

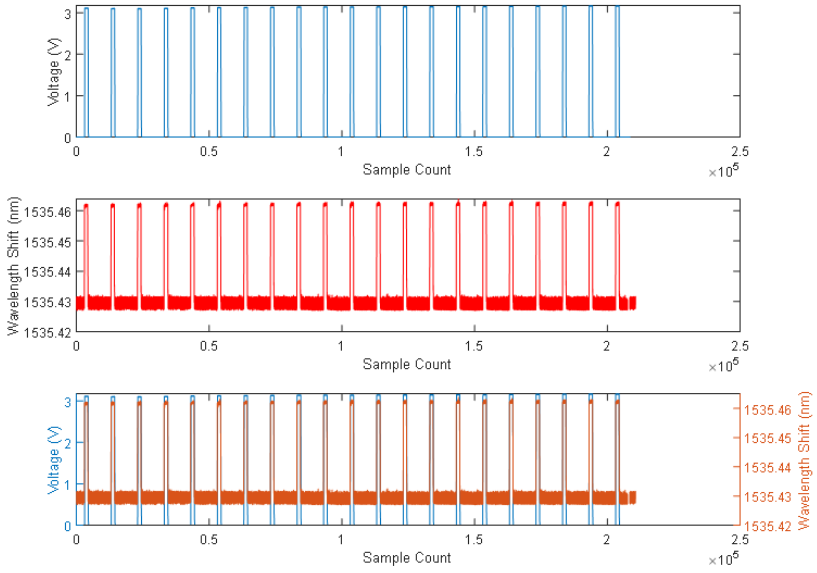

Figure 6.30: Circuit response to transient condition

Figures 6.32–6.35 illustrate the experimental arrangement from the prototyping stage to optical visualisation. Electrical variations occurring in the circuit are directly transduced by the LVT and observed as corresponding shifts in the reflected peak wavelength.

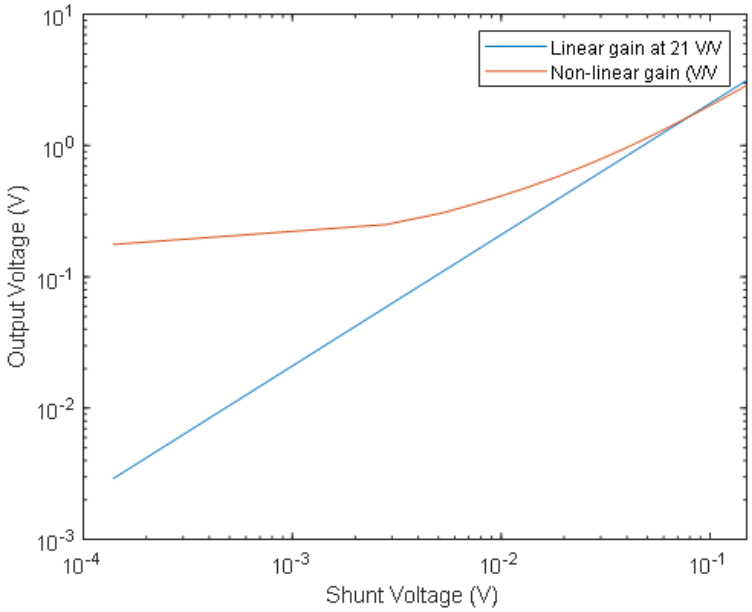

Figure 6.31: Logarithmic graph of shunt and LVT voltage

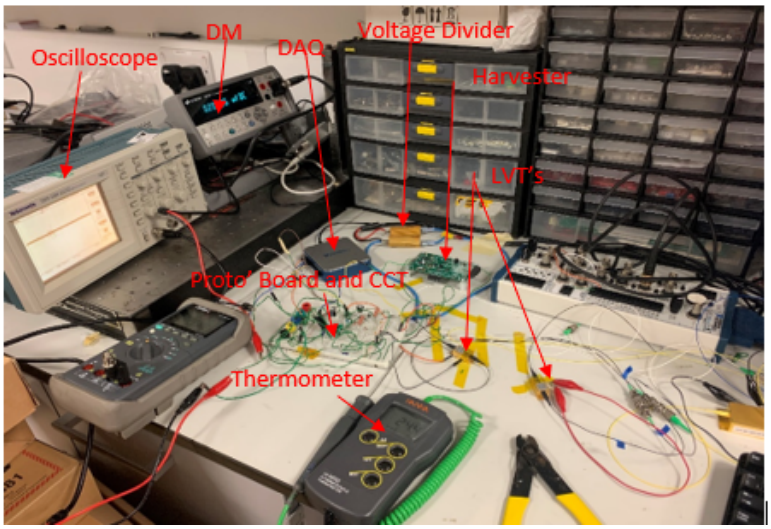

Figure 6.32: Experimental setup equipment

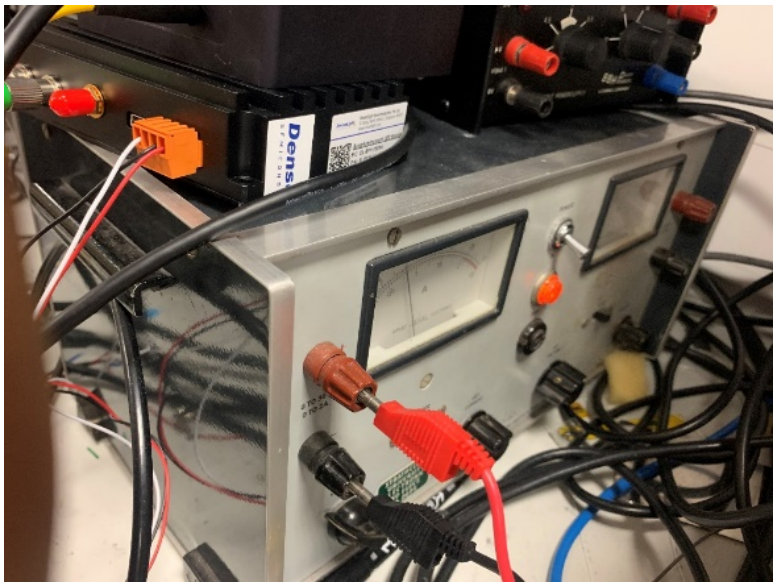

Figure 6.33: DC power source

Figure 6.34: Optical interrogator and light source

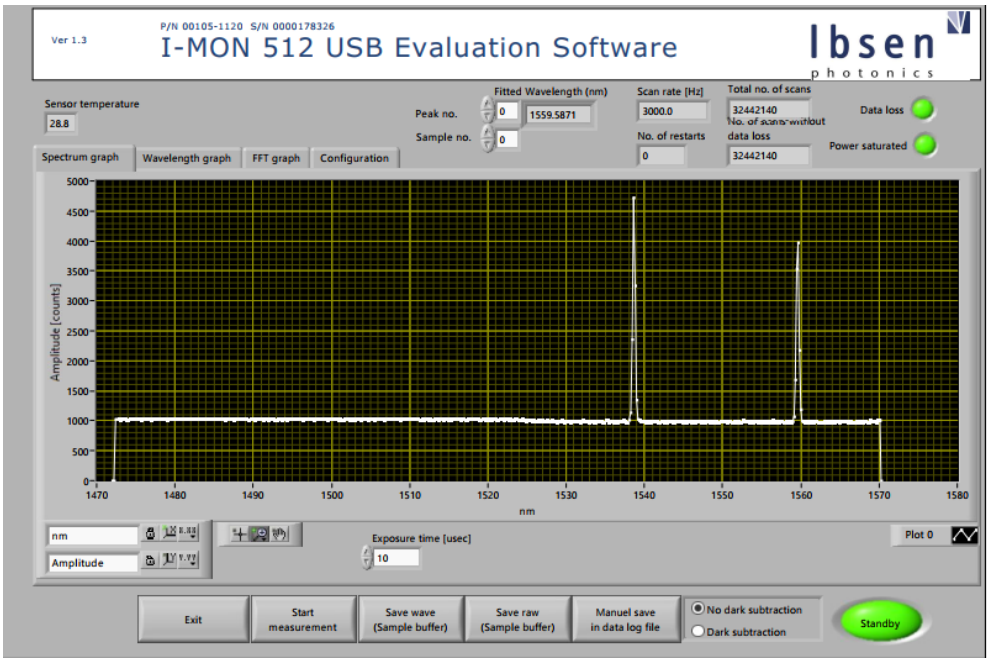

Figure 6.35: Electrical and optical data processing workflow

6.4.2 Experimental Setup

The objective of this validation stage is to assess the capability of the proposed sensing architecture to capture fast transient currents representative of HVDC fault conditions accurately.

To achieve this, fault-induced current waveforms were generated using the HVDC system model described in Chapter 8, as illustrated in Fig. 8.1. A pole-to-ground fault was applied at a distance of 110 km from Sensor 1 and 10 km from Sensor 2, with a fault resistance of 10 mΩ. This configuration produced transient responses characteristic of HVDC faults, with travelling-wave components.

The resulting fault current signals were exported from MATLAB and used as input stimuli in the experimental setup. These signals were replayed through the analogue-output channels of the NI USB-6003 DAQ system and injected into the signal-conditioning circuit. The conditioned electrical signal was then applied to the LVT, which converted the electrical input into a corresponding optical response via the embedded fibre Bragg grating.

This arrangement enabled direct comparison between the original electrical fault signal and the corresponding optical measurement obtained from the sensing system.

6.4.3 Signal Processing Methodology

The electrical signal at the output of the signal-conditioning circuit and the corresponding optical response from the LVT were acquired using the NI USB-6003 DAQ and the IMON optical interrogator, respectively. Both datasets were exported to MATLAB for post-processing and analysis.

The raw transient signals exhibited high-frequency oscillations and noise, obscuring key waveform features, including rise time, peak magnitude, and waveform shape. To enable meaningful comparison, a Savitzky-Golay filtering technique was applied to both the electrical and optical signals. This method provides local polynomial smoothing while preserving critical transient characteristics, including sharp transitions and peak values.

The use of this filtering approach ensured that the underlying physical behaviour of the transient signals was retained, thereby enabling accurate assessment of the sensor's dynamic response.

6.4.4 Validation Results

The results of the fault-transient validation are presented in Fig. 6.36–Fig. 6.41. The electrical signals represent the reference fault currents obtained from the HVDC simulation, while the optical signals correspond to the measured response of the proposed sensing system.

A direct comparison between the two sets of signals shows that the optical output reproduces the key features of the electrical transient, including:

1. the rapid rise in current following fault inception;
2. the peak magnitude and waveform envelope; and
3. the oscillatory behaviour associated with travelling-wave reflections.

Despite measurement noise in the raw signals, the processed trendlines show strong agreement between the electrical and optical responses. This confirms that the sensing system can track the temporal evolution of fast transient events.

These results validate the proposed electro-optical sensing architecture's ability to capture high-speed fault signatures in HVDC systems. In particular, the preservation of waveform features such as rise time and peak characteristics indicates that the sensor can support applications requiring rapid fault detection and transient analysis.

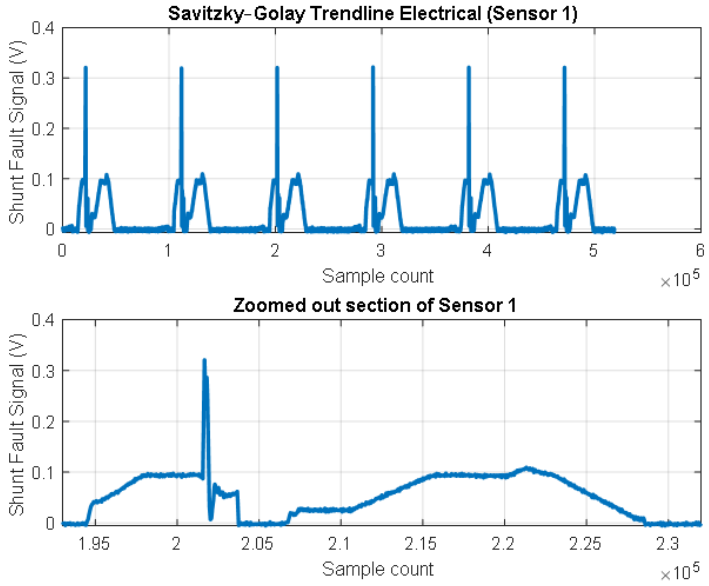

Figure 6.36: Sensor 1 electrical response to fault current

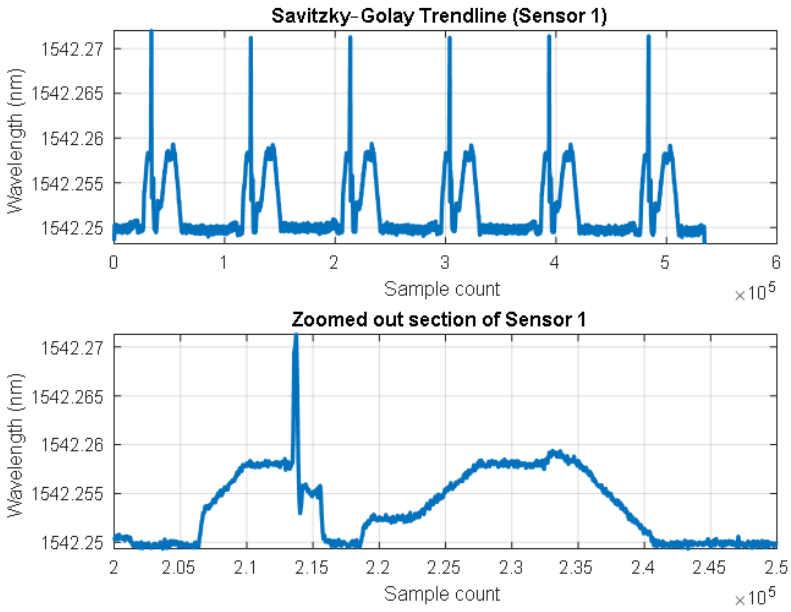

Figure 6.37: Sensor 1 optical response to fault transient

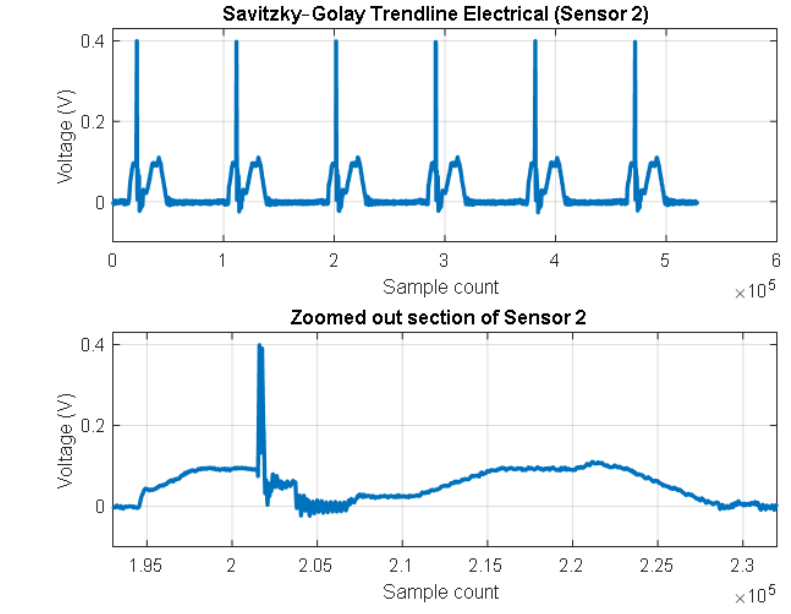

Figure 6.38: Sensor 2 electrical response to fault transient

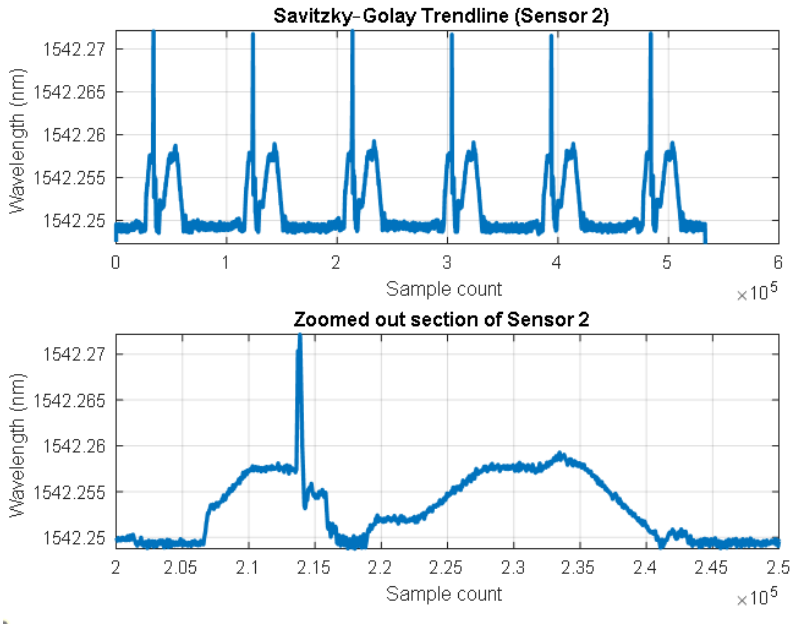

Figure 6.39: Sensor 2 optical response to fault transient

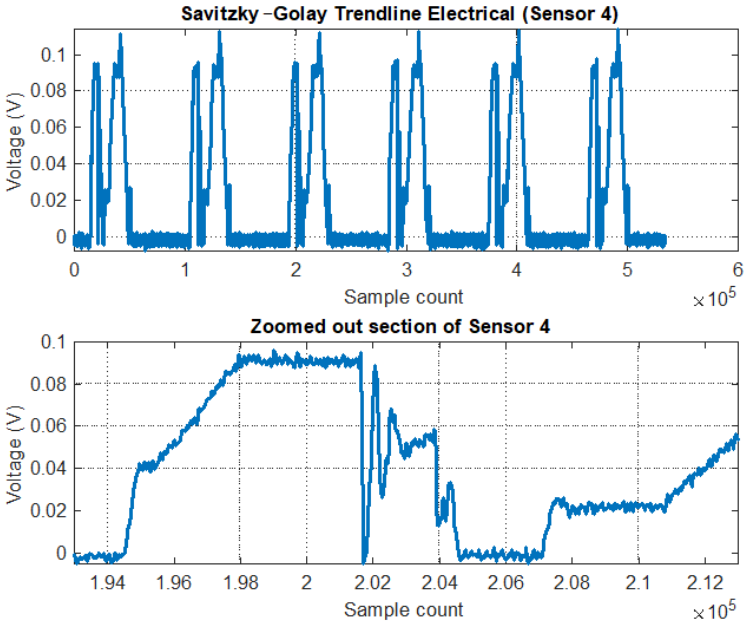

Figure 6.40: Sensor 4 electrical response to fault transient

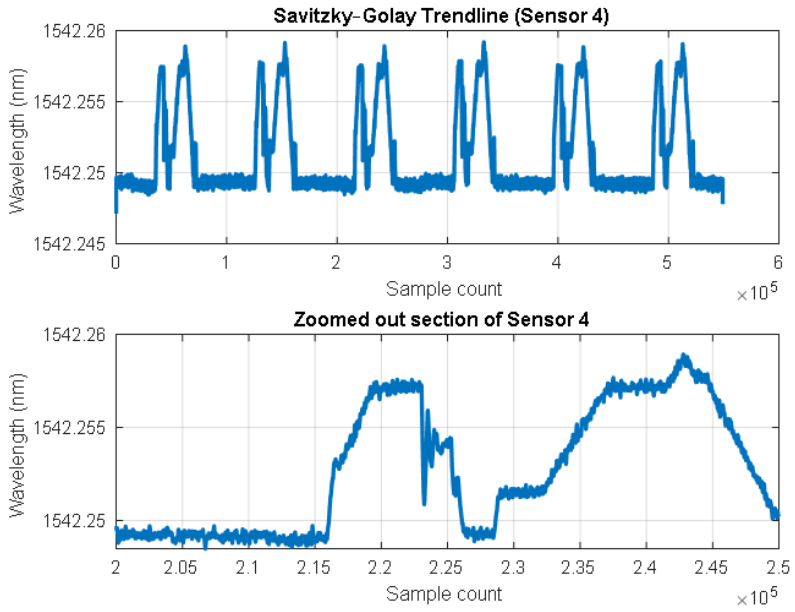

Figure 6.41: Sensor 4 optical response to fault transient

6.5 Results Discussion

The results presented in this chapter validate the proposed sensing architecture from three complementary perspectives: the thermal behaviour of the instrumented splice, the performance of the signal-conditioning circuitry, and the dynamic response of the electro-optical sensing mechanism.

The electro-thermal simulations show that the temperature rise in the manganin shunt remains within acceptable limits over the investigated current range. The predicted thermal gradients are consistent with analytical estimates based on the thermal resistance of the cable structure, indicating that integrating the sensing element does not introduce excessive thermal stress in the splice assembly.

The electric-field simulations demonstrate that the inclusion of the Faraday cage significantly reduces field penetration into the electronics enclosure. Without shielding, high electric-field gradients are observed in the epoxy region surrounding the electronics. With the Faraday cage present, the electric field inside the enclosure is effectively suppressed, thereby confirming the necessity of electrostatic shielding for reliable oper-

ation in HVDC environments.

The circuit simulations and experimental results confirm the advantages of the nonlinear amplification architecture. Whereas the linear amplifier exhibits limited sensitivity to weak input signals, the nonlinear configuration increases the effective gain in the low-signal region while avoiding premature saturation at higher signal levels. This behaviour is particularly beneficial when interfacing with the optical interrogation system, whose measurement accuracy imposes a minimum detectable signal threshold.

Experimental measurements further demonstrate consistent correspondence between the electrical and optical signals, confirming that the LVT successfully converts the amplified electrical signal into a measurable optical wavelength shift. The transient experiments also show that the sensing system can capture rapid changes in the input signal, which is essential for detecting disturbances in HVDC transmission systems.

Overall, the combined simulation and experimental results demonstrate that the proposed sensing approach can operate within the electrical, thermal, and dynamic constraints imposed by HVDC cable environments.

6.6 Conclusion

This chapter presents simulation and experimental validation of the proposed photonic current-sensing architecture for integration within HVDC cable splice joints. The investigations addressed three principal aspects of the system: the electro-thermal behaviour of the instrumented splice, the performance of the signal-conditioning circuitry, and the dynamic response of the electro-optical sensing mechanism.

Multiphysics simulations were first performed to analyse Joule heating and electric-field distribution within the splice assembly. The results indicate that the temperature rise in the manganin shunt remains within acceptable limits over the investigated current range, and the predicted thermal gradients are consistent with simplified analytical estimates. Thermal modelling further showed that the dominant heat-transfer mechanism is radial conduction through the cable insulation layers, while axial conduction along the conductor provides an additional dissipation pathway. Electric-field simula-

tions also demonstrated that the inclusion of an electrostatic shield significantly reduces field penetration into the sensor housing, thereby protecting the embedded electronics from high-field exposure.

Circuit-level investigations compared linear and nonlinear amplification strategies for conditioning the shunt voltage signal under ultra-low-power constraints. Both simulation and experiment confirmed that the nonlinear amplification approach improves sensitivity in the low-signal region while maintaining acceptable performance across the wider operating range. This characteristic is particularly important for resolving weak measurement signals close to the interrogator's accuracy threshold.

Experimental evaluation of the electro-optical sensing chain was performed on a laboratory test platform that simultaneously acquired electrical and optical signals. The results demonstrate good repeatability and consistent correspondence between electrical inputs and optical responses. The hysteresis behaviour observed in the LVT is consistent with the intrinsic characteristics of piezoelectric materials and remains within acceptable limits for the intended sensing application.

Additional validation using HVDC fault-transient waveforms demonstrated that the sensing system reproduces the key features of fast disturbance signals. After signal processing, the optical measurements closely followed the electrical trendlines, indicating that the proposed architecture can capture rapid current variations associated with fault events.

Overall, the combined simulation and experimental findings confirm the feasibility of the proposed sensing approach for distributed monitoring of HVDC cable systems. Although the experiments were conducted under controlled laboratory conditions, the results provide a strong foundation for further investigation into system-level deployment and integration within HVDC protection and monitoring frameworks. The following chapter extends this work by examining the impact of the proposed sensing architecture on HVDC network-level simulation and protection coordination.

Chapter 6 References

[1] IBSEN Photonics, *I-mon usb interrogation monitor specifications and operating principle*, [Online]. Available: `www.ibsen.com`. Accessed: 31-Oct-2021, 2021.

[2] National Instruments (Emerson), *Ni usb-6003 data acquisition device specifications*, pp. 2–8, 2021.

[3] H. Li, Y. Xu, M. Shao, L. Guo, and D. An, "Analysis for hysteresis of piezoelectric actuator based on microscopic mechanism," *IOP Conference Series*, pp. 1–6, 2018.

[4] J. Gan and X. Zhang, "A review of nonlinear hysteresis modeling and control of piezoelectric actuators," *AIP Advances*, pp. 1–5, 2019.

[5] A. Amiolemen, "Photonic current sensor for hvdc," in *Conference Proceedings*, 2024.

Chapter 7

Sensor Calibration and Measurement Error Analysis

7.1 Introduction

Accurate current measurement is a fundamental requirement for monitoring and protection in high-voltage direct current (HVDC) transmission systems. Optical current-sensing technologies offer significant advantages over conventional electromagnetic current transformers, particularly in high-voltage environments, where electrical isolation, immunity to electromagnetic interference, and distributed sensing are essential. However, practical deployment requires rigorous calibration and uncertainty evaluation to ensure that measured quantities reliably represent the true electrical parameters under varying operating conditions.

This chapter presents the calibration methodology, measurement error analysis, and uncertainty evaluation of the optical current sensor developed in this work. The analysis establishes a robust relationship between the electrical input quantity (shunt voltage corresponding to the measured current) and the optical response obtained from the fibre Bragg grating (FBG) sensing system. Particular attention is given to nonlinearities introduced by the signal-conditioning amplifier, measurement-instrumentation limitations, and temperature-induced drift inherent to FBG interrogation systems.

The chapter addresses three key aspects of sensor performance:

1. Sensor calibration methodology, including the development of a calibration model capable of accurately representing the nonlinear relationship between electrical excitation and optical response.

2. Measurement error and uncertainty analysis, identifying dominant contributors such as instrumentation limitations, quantisation effects, environmental influences, and signal acquisition constraints.

3. Error correction and drift compensation, where temperature-induced wavelength drift is mitigated using a differential FBG configuration.

A key contribution of this chapter is the development of a *segregated semi-piecewise calibration methodology*, specifically designed to address the nonlinear amplification behaviour required to detect low-amplitude signals near the measurement noise floor. Conventional polynomial calibration methods exhibit poor accuracy at low signal levels, whereas fully piecewise models require many calibration functions, thereby increasing implementation complexity. The proposed approach combines the advantages of both methods, enabling accurate calibration across the entire measurement range.

A second contribution is a temperature drift compensation technique based on differential FBG interrogation. Since FBG sensors are inherently sensitive to both strain and temperature, ambient variations introduce wavelength drift that can significantly affect measurement accuracy, particularly at low signal levels. To mitigate this effect, a reference FBG is deployed alongside the sensing FBG to isolate temperature-induced wavelength shifts from strain-induced signals. The differential response enables real-time compensation of both thermal drift and interrogator instability.

To establish metrological validity, the calibration and uncertainty analysis are evaluated against the requirements of IEC 61869-14, which specifies performance criteria for DC current transformers. The developed sensor is designed to meet Accuracy Class 1, requiring compliance with strict ratio error limits over a measurement range from 5% to 300% of nominal current.

The chapter is organised as follows. Section 7.2 introduces key metrological terminology. Section 7.3 presents conformity assessment principles and acceptance limits. Section 7.4 outlines the performance requirements of IEC 61869-14. Section 7.5 describes the experimental calibration setup. Section 7.6 presents the proposed calibration methodology. Sections 7.7 and 7.8 analyse measurement error and uncertainty. Section 7.9 introduces drift compensation techniques, and Section 7.10 evaluates measurement accuracy against IEC requirements.

Through this analysis, the measurement accuracy, uncertainty bounds, and reliability of the proposed optical current sensing system are established, demonstrating its suitability for HVDC network monitoring applications.

7.2 Terminology and Definitions

To ensure clarity and consistency, key terminologies related to calibration, error, and measurement uncertainty are defined in accordance with internationally recognised metrological standards.

7.2.1 Calibration

According to ISO/IEC Guide 99:2007, calibration is an operation that establishes a relationship between known quantity values provided by measurement standards and the corresponding measurement indications, including associated uncertainties. This relationship is subsequently used to determine measurement results from observed indications. The relationship may be expressed as a calibration function, curve, table, or diagram [1].

7.2.2 Metrological Traceability

Metrological traceability is the property of a measurement result whereby it can be related to a reference through an unbroken and documented chain of calibrations, each contributing to the overall measurement uncertainty [2].

7.2.3 Error

Error is defined as the difference between a measured value and its corresponding reference (true) value.

7.2.4 Measurement Repeatability

Measurement repeatability refers to the precision of measurements obtained under identical operating conditions [1].

7.2.5 Measurement Uncertainty

Measurement uncertainty is a parameter associated with a measurement result that characterises the dispersion of values that could reasonably be attributed to the measurand [1].

7.2.6 Measurement Accuracy

Accuracy is defined as the closeness of agreement between a measured value and the true value of the measurand. It reflects the combined influence of systematic and random errors within the measurement system [1], [2].

7.3 Tolerance and Acceptance Limits

The Joint Committee for Guides in Metrology (JCGM) [3] emphasises that conformity assessment should be based on acceptance and tolerance intervals applied to measured values, as illustrated in Fig. 7.1.

Tolerance limits define the permissible range within which the true value of the measurand is expected to lie, while acceptance limits define the range within which measured values are considered conforming. The selection of these intervals balances the risk of incorrect conformity decisions arising from measurement uncertainty.

In IEC 61869-14, explicit tolerance limits are not defined. Instead, conformity is determined solely by acceptance limits, which vary with the measurement current ratio. Any measurement exceeding these limits is classified as non-conforming.

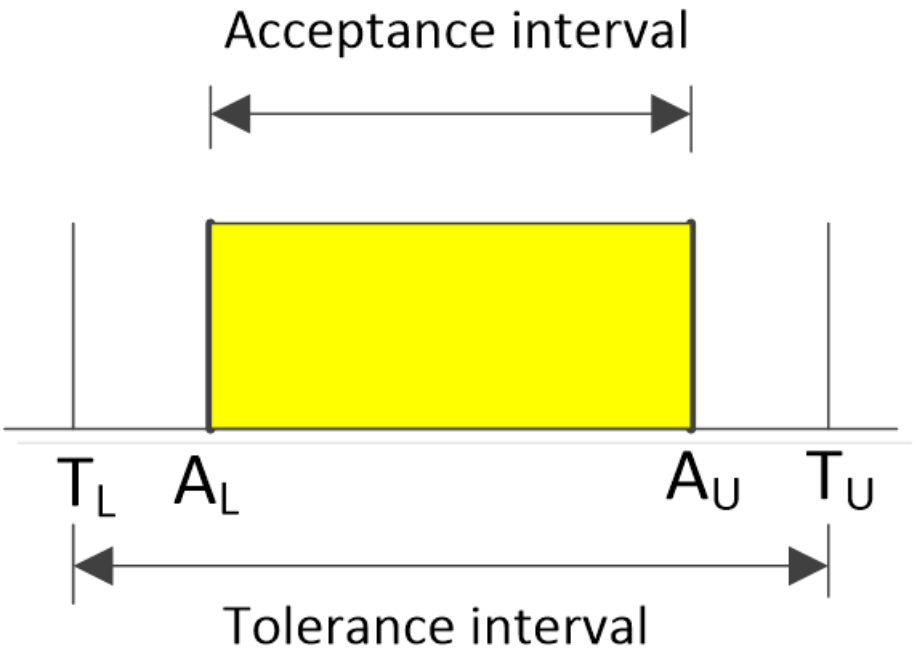

Figure 7.1: Conformity assessment interval

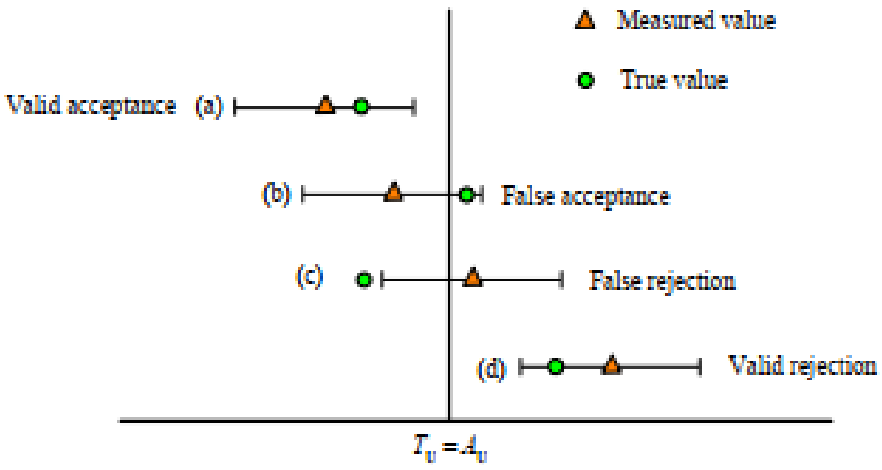

Figure 7.2: Acceptance decision rule

As shown in Fig. 7.2, reliance solely on acceptance limits introduces the possibility of misclassification. False acceptance occurs when a non-conforming item is incorrectly accepted, while false rejection occurs when a conforming item is rejected. To mitigate

Table 7.1: IEC 61869-14 accuracy class specification

Accuracy Class	**Ratio Error (±%) at Current (% of Rated)**			**Kpcr**	**KALF**
	5%	20%	100%		
0.1	1	0.25	0.1	0.1	1
0.2	2	0.5	0.2	0.2	2
0.5	3.5	1	0.5	0.5	5
1	5	2	1	1	10

this risk, a guard band may be introduced within the tolerance interval. However, IEC 61869-14 adopts strict acceptance criteria without tolerance margins, requiring high measurement accuracy to ensure compliance.

7.4 Sensor Requirements

The IEC 61869-14 standard defines the performance requirements and accuracy limits for DC current transformers, providing a benchmark for evaluating measurement reliability.

The proposed sensor is designed to meet Accuracy Class 1 over a measurement range from 5% to 300% of nominal current. The corresponding ratio error limits are:

- ±5% at 5% of nominal current
- ±2% at 20% of nominal current
- ±1% at nominal current
- ±1% at 120–150% (Kpcr)
- ±5% at 300% (KALF)

The performance boundaries for different accuracy classes are summarised in Table 7.1.

7.4.1 Extended Accuracy Factors

The parameter K_{pcr} is a dimensionless factor applied to the rated primary current (I_{pr}) to define an extended current level:

$$I_{epr} = K_{pcr} \cdot I_{pr} \tag{7.1}$$

over which the specified metering accuracy is maintained. For the proposed sensor, the extended operating range corresponds to 120–150% of the nominal current.

The accuracy limit factor, K_{ALF}, defines the upper current level beyond the extended range for which protection-class accuracy must be satisfied. Standard values of K_{ALF} include 3, 6, 10, and 20 [4]. In this work, a value of $K_{ALF} = 3$ is adopted.

7.5 Experimental Setup for Calibration and Measurement Uncertainty

The experimental configuration used for sensor calibration is illustrated in Fig. 6.19 and Fig. 6.20. A regulated DC supply, combined with a precision resistive voltage divider, was used to emulate the voltage developed across a shunt resistor in an HVDC system.

The resulting shunt voltage was used as the excitation input to both the energy-harvesting circuit and the signal-conditioning amplifier. The amplified output was subsequently fed into the low-voltage transducer (LVT), which was optically interrogated with an IBSEN super-luminescent LED (SLED) and an I-MON USB 256 spectrometer for wavelength demodulation.

Electrical measurements from both the amplifier output and the shunt reference were acquired simultaneously using a National Instruments NI USB-6003 data acquisition (DAQ) module. To ensure synchronisation between electrical and optical measurements, the DAQ sampling rate was configured to 3 kS/s, matching the 3 kHz interrogation rate of the optical system. All datasets were recorded for post-processing, calibration, and performance evaluation.

All instrumentation used in this study was traceable to the National Institute of

Standards and Technology (NIST) through calibration certificates [5], [6]. Although a dedicated reference instrument was not available for direct comparison with the device under test (DUT), traceability ensured confidence in the measurement results.

In conventional calibration procedures, the scale factor is determined by comparing the DUT output with that of a reference instrument under identical conditions. For n repeated measurements, the mean scale factor is given by:

$$F_g = \frac{1}{n} \sum_{i=1}^{n} F_{i,g} \tag{7.2}$$

The relative standard deviation is:

$$s_g = \frac{1}{F_g} \sqrt{\frac{1}{n-1} \sum_{i=1}^{n} (F_{i,g} - F_g)^2} \tag{7.3}$$

The relative standard uncertainty is:

$$U_g = \frac{s_g}{\sqrt{n}} \tag{7.4}$$

Typically, $n = 10$ measurements are sufficient for calibration purposes [7].

In this work, calibration is performed using a calibration curve rather than a scale factor. The input-output relationship of the measurement system is expressed as:

$$y[n] = f(x[n]) + m[n] \tag{7.5}$$

where $x[n]$ is the measurand, $y[n]$ is the measured output, and $m[n]$ represents the measurement uncertainty.

7.6 Sensor Calibration Curve

The measured shunt voltage and corresponding LVT wavelength response were plotted on a logarithmic scale, as shown in Fig. 7.3. The resulting characteristic reveals a nonlinear relationship between electrical input and optical output, primarily due to the

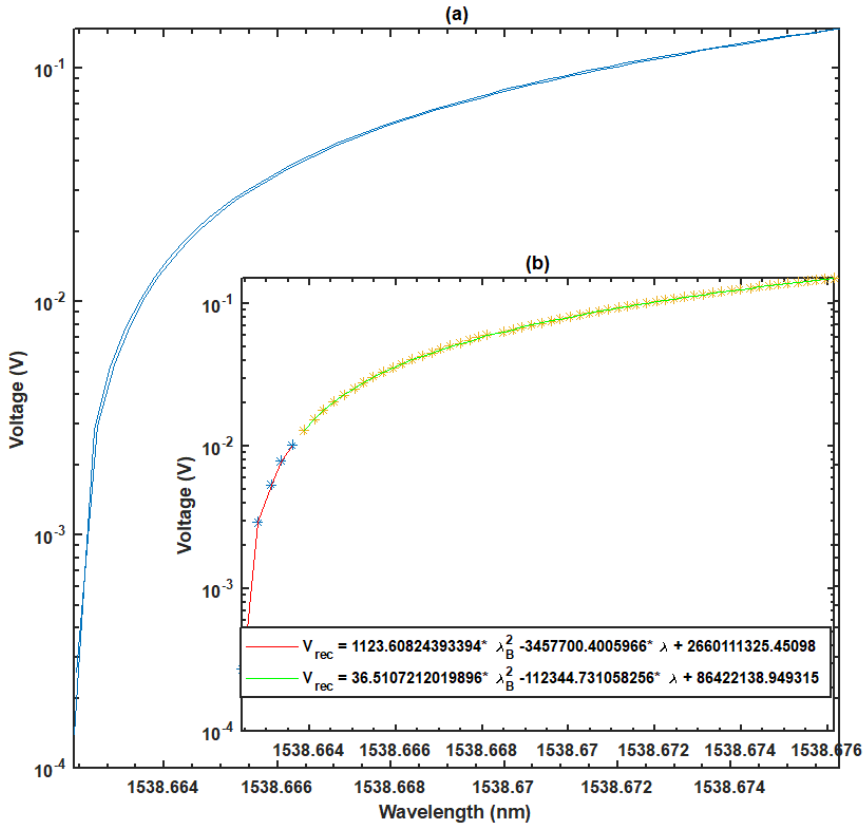

Figure 7.3: Calibration curve of the nonlinear amplifier: (a) hysteresis behaviour, (b) calibration curve

nonlinear gain profile of the signal-conditioning amplifier.

Initial calibration using higher-order polynomial models (2nd–6th order) yielded acceptable fitting at higher signal amplitudes but exhibited poor accuracy at low signal levels. To address this limitation, a segregated semi-piecewise second-order polynomial calibration method was developed.

The proposed approach divides the measurement range into two regions:

- 0–25% of nominal current (low-signal region)
- 25–300% of nominal current (high-signal region)

Each region is modelled using a second-order polynomial, enabling accurate representation of the nonlinear sensor response. The resulting coefficients of determination

Table 7.2: Accuracy class evaluation for reconstructed voltage (Class 1 DCCT)

Measurement	5%	20%	100%	120%	150%	300%
Limit	±5%	±2%	±1%	±1%	±1%	±5%
1	-4.40	-0.96	-0.16	0.11	0.36	-0.26
2	1.93	-0.36	0.07	0.12	0.07	0.15
3	3.98	1.70	0.35	1.02	0.95	0.51

(R^2) were 0.998772 and 0.999948 for the lower and upper regions, respectively, indicating excellent model fidelity.

7.7 Accuracy Test Results

The accuracy class results presented in Table 7.2 are derived from reconstructed voltage values obtained from measured wavelength shifts using the calibration model.

The reconstructed measurements satisfy the IEC 61869-14 accuracy requirements, demonstrating the effectiveness of the proposed calibration methodology.

Each fibre Bragg grating (FBG) sensor exhibits a unique Bragg wavelength determined during fabrication. While this enables multiplexing, it necessitates individual calibration for each sensor to account for wavelength-dependent sensitivity and interrogation characteristics [8].

7.8 Contribution of the Proposed Calibration Methodology

The calibration approach developed in this work represents a methodological advancement for nonlinear optical sensing systems operating near the measurement noise floor.

Conventional calibration approaches are typically based on either global polynomial fitting or fully segmented piecewise models. While global polynomial models offer simplicity, they fail to accurately represent low-amplitude behaviour in nonlinear systems. Conversely, fully piecewise models provide high accuracy but at the expense of increased computational complexity.

The proposed segregated semi-piecewise calibration method provides an effective compromise by dividing the measurement range into two regions corresponding to distinct amplifier operating regimes. Each region is modelled using a second-order polynomial, ensuring accurate representation while maintaining a compact analytical structure.

The lower region (0–25%) captures nonlinear amplification required for low-level signal detection, while the upper region (25–300%) represents stable amplifier operation. The resulting model achieves coefficients of determination exceeding 0.998, confirming high fidelity.

This approach enhances measurement accuracy across the full operating range while maintaining practical implementability for real-time systems. A comparison with conventional calibration approaches is presented in Table 7.3.

Table 7.3: Comparison of calibration approaches

Calibration Method	**Complexity**	**Low-Signal Accuracy**	**Suitability**
Global Polynomial	Low	Poor	Simple systems
Piecewise Calibration	High	Excellent	Complex systems
Proposed Semi-Piecewise Method	Moderate	Excellent	Moderate to complex nonlinear systems

7.9 Accuracy and Sources of Error

In this context, accuracy refers to the closeness of agreement between a measured value and the true value of the measurand [1], [2]. Deviations from the true value arise primarily from measurement errors, which in this investigation were primarily due to the accuracy limitations of the measurement instrumentation and circuit components. Although these error sources influenced the final results, the measured performance remained within the applicable standard limits.

Measurement errors can be broadly classified into two categories: systematic and random. Systematic errors arise from inherent characteristics of the measurement system and introduce a consistent bias in one direction, whereas random errors arise from unpredictable fluctuations within the system or its operating environment. In the present work, active and passive circuit components were used in the signal-conditioning stage, while digital acquisition hardware and optical interrogation systems were employed for electrical and optical measurements, respectively. Each subsystem contributed, to varying degrees, to the overall uncertainty and fidelity of the acquired data.

7.9.1 Influence of Equipment Limitations on Measurement

Equipment limitations constitute a fundamental source of measurement uncertainty, since instrument specifications define the achievable performance envelope of the measurement system. In practice, cost constraints and application-specific trade-offs often necessitate the use of instruments with finite accuracy, repeatability, and resolution. Consequently, all acquired data remain bounded by the inherent limitations of the instrumentation.

This consideration is particularly important in fibre Bragg grating (FBG)-based sensing systems, where overall performance is strongly influenced by interrogator resolution, repeatability, dynamic range, and wavelength accuracy. For example, SmartScan interrogators typically exhibit repeatability better than 1 pm, whereas IBSEN interrogators may exhibit repeatability up to 5 pm under comparable conditions [9],

[10]. These characteristics directly affect the achievable consistency and accuracy of wavelength-based measurements.

Environmental effects also influence measurement fidelity. Among these, temperature is particularly significant because FBG sensors are intrinsically sensitive to both strain and temperature. If the calibration conditions differ from the operating conditions, measurement bias may be introduced unless appropriate compensation is applied [8]. For this reason, temperature-induced drift was explicitly accounted for in the error analysis and the compensation methodology developed in this chapter.

7.9.2 Data Acquisition and Processing Error

One of the principal sources of error during experimental acquisition arose from the finite accuracy of the data acquisition system. The NI USB-6003 used in this study has a specified typical absolute accuracy of 6 mV at full scale, with a maximum deviation of 26 mV over the operating temperature range, and a system noise of approximately 0.4 mV_{rms} [11]. These limitations become particularly significant when measuring low-amplitude signals in the millivolt range.

In this work, signals as low as 2.5 mV were measured, placing them close to the lower boundary of the DAQ accuracy specification. This introduces a non-negligible source of uncertainty in the recorded data. Nevertheless, based on the measured results and subsequent analysis, the system performance remained within the expected specification limits at a confidence level corresponding to approximately 68% (1σ) [12].

7.9.3 Random Error

The elimination of systematic error does not, by itself, guarantee accurate measurement results, since random errors remain unavoidable. Random errors vary unpredictably and may be distributed on either side of the mean value. Their sources include ambient noise, electromagnetic interference, thermal fluctuations, and component tolerances within the measurement chain.

Unlike systematic errors, random errors do not accumulate in one direction over repeated measurements; instead, they tend to average out statistically [1]. Their distri-

bution is commonly approximated by a Gaussian centred on the mean. In the present study, random error was expected from passive component tolerances, environmental fluctuations, and measurement device noise. Although the contribution from circuit component tolerances was assessed to be small, the intrinsic noise floor of the measurement and acquisition equipment remained a limiting factor in low-signal operation. Where such noise becomes dominant, higher-performance instrumentation would be required to further suppress uncertainty contributions [12].

7.10 Measurement Error Analysis

Signals acquired from LabVIEW and the I-MON USB evaluation platform were exported to MATLAB for post-processing and extraction of representative data points. The sampling frequency was set to 3 kHz, and each excitation step was maintained for 3 s, yielding 9000 samples per step. The input excitation was incremented in steps of 2.5 mV.

To isolate the electrical and optical responses corresponding to each excitation level, the sampling frequency was converted into the corresponding time windows for each step transition. Since each second contains 3000 samples at 3 kHz, each 3 s measurement interval comprised 9000 data points. The time segmentation used for data extraction is illustrated in Fig. 7.4 and Fig. 7.5.

In one representative experiment, 4.5 measurement cycles were completed, with 48 step changes executed per cycle over the range 0–60 mV and 60–0 mV in 2.5 mV increments. This produced 216 transition points and approximately 1.9×10^6 samples over the entire experiment. Each transition was clearly identifiable in the sampled data, enabling the extraction of representative averaged values for subsequent analysis.

The best estimate of the measured variable is given by the arithmetic mean:

$$\bar{x} = \frac{1}{N} \sum_{i=1}^{N} x_i \tag{7.6}$$

where N is the total number of samples and x_i is the ith measurement.

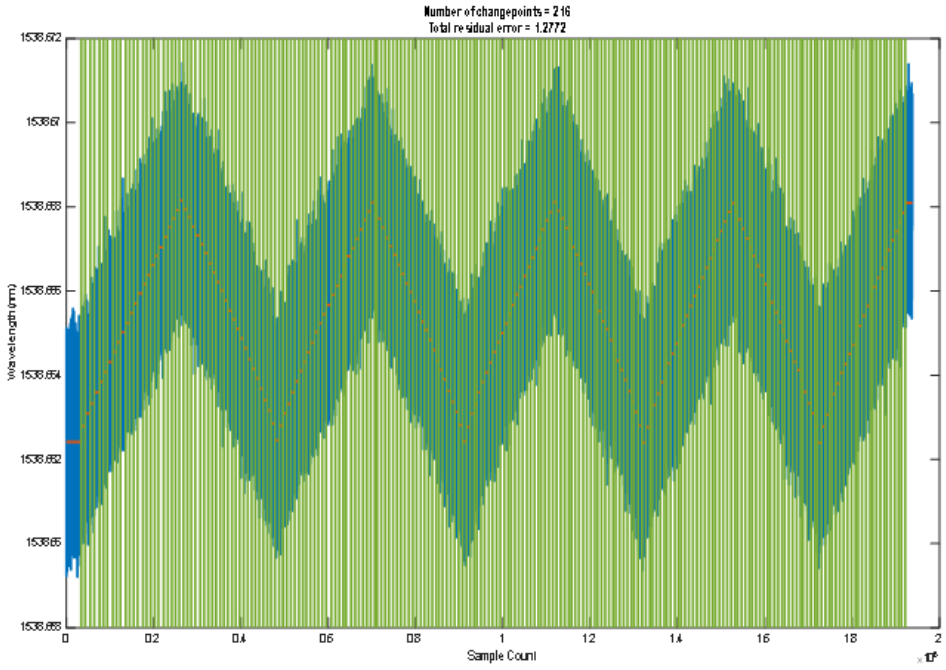

Figure 7.4: Time division of the optical measurement samples per transition point

Representative optical and electrical signals extracted at the 2.5 mV excitation level are shown in Fig. 7.6 and Fig. 7.7, respectively.

Figure 7.6 shows the optical response corresponding to a 2.5 mV electrical input. Although random fluctuations are visible, averaging reduces their influence and provides a stable estimate of the underlying signal. At this operating point, the optical signal exhibited approximately 3 pm peak-to-peak noise. A similar behaviour was observed in the corresponding electrical measurement shown in Fig. 7.7, where the measured values were distributed around the nominal input value. These results indicate that the random fluctuations are largely stochastic and tend to average out over repeated samples.

However, repeated measurements at the same excitation level revealed an additional drift in the optical response, attributable to uncompensated systematic effects, most notably temperature-induced drift and interrogator instability. As shown in Fig. 7.8, a drift of approximately 2 pm was observed over one measurement cycle. At low signal levels, such drift is particularly significant because a 1 pm wavelength shift corresponds

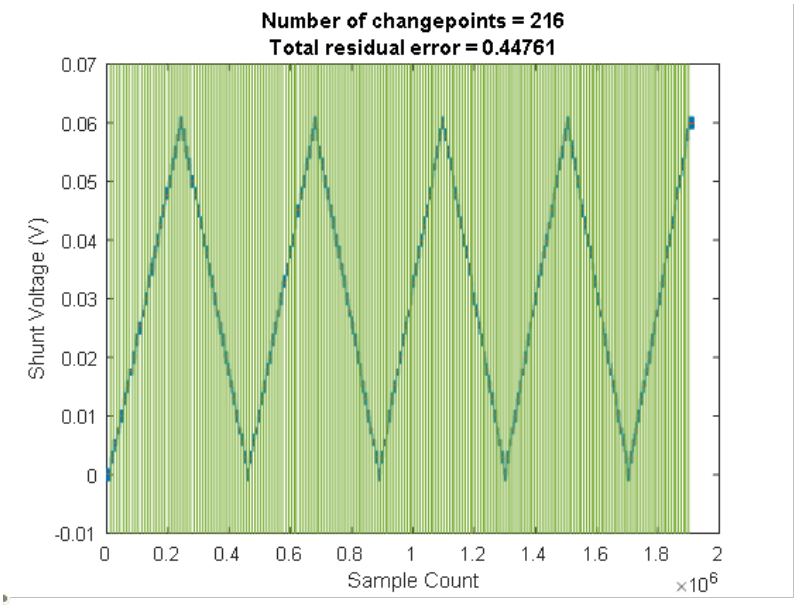

Figure 7.5: Time division of the electrical measurement samples per transition point

to an appreciable equivalent electrical variation. Consequently, low-amplitude signals, such as 2.5 mV or 10 mV, are disproportionately affected relative to higher-level signals, such as 50 mV or 60 mV. This effect motivates the use of a reference FBG for differential drift compensation, as discussed later in the chapter.

A comparison of Fig. 7.6 and Fig. 7.7 also shows that the optical data appear visually denser than the electrical data, despite identical nominal sampling rates and sample counts. This difference arises primarily from the distinct quantisation resolution, accuracy limits, and noise characteristics of the two acquisition systems.

According to the NI USB-6003 specification, the typical absolute accuracy is 6 mV at full scale. During the experiments, the DAQ was operated over a ±5 V input range. The corresponding relative full-scale error can be expressed as:

$$E_r = \frac{6 \text{ mV}}{10 \text{ V}} \times 100 = 0.06\% \tag{7.7}$$

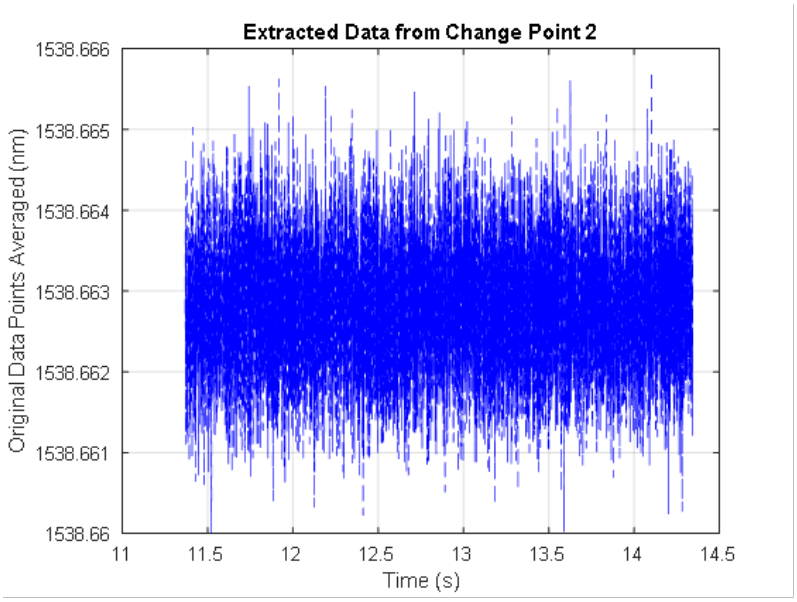

Figure 7.6: Extracted optical equivalent of 2.5 mV (5% of nominal)

For a 2.5 mV shunt signal, the gain-related equivalent error is therefore:

$$E_{r,\text{gain}} = 2.5 \text{ mV} \times 0.06\% = 1.5 \ \mu\text{V} \tag{7.8}$$

The more significant limitation, however, is the quantisation step size of the analogue-to-digital converter (ADC), which is determined by the least significant bit (LSB):

$$\text{ADC}_{\text{res}} = \frac{\text{Voltage Range}}{2^N} \tag{7.9}$$

where N is the number of effective bits.

Although the NI USB-6003 is nominally a 16-bit device, the specified system noise of approximately 0.4 mV_{rms} reduces its effective number of bits (ENOB). ENOB is estimated from the signal-to-noise-and-distortion ratio (SINAD) as [13], [14]:

$$\text{ENOB} = \frac{\text{SINAD} - 1.76}{6.02} \tag{7.10}$$

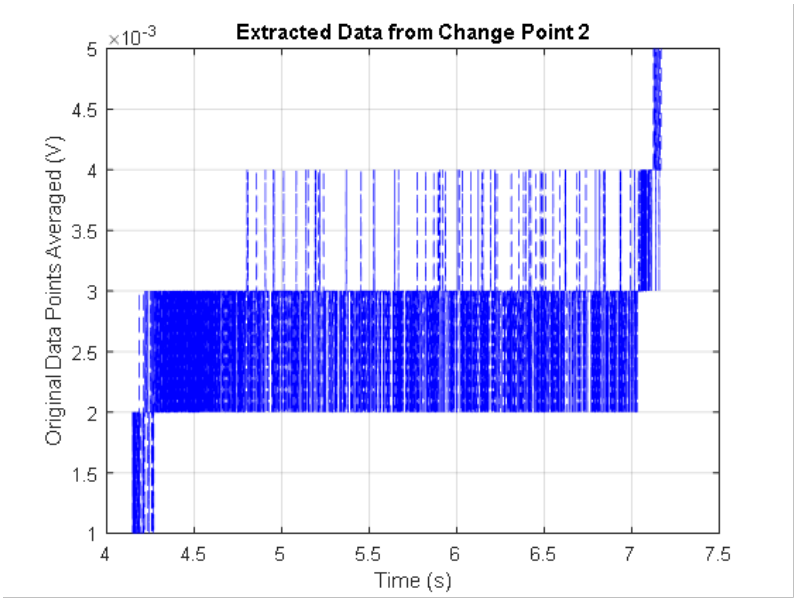

Figure 7.7: Extracted voltage signal (5% of nominal)

with

$$\text{SINAD} = 20\log_{10}\left(\frac{V_{\text{FS}}/(2\sqrt{2})}{V_{\text{noise,rms}}}\right) \tag{7.11}$$

For a ±10 V range and a noise level of 0.4 mV_{rms}, the calculated SINAD is approximately 84.9 dB, corresponding to an ENOB of about 14 bits. Since the actual measurements were acquired over a ±5 V range, the effective ADC resolution becomes:

$$\text{ADC}_{\text{res}} = \frac{10}{2^{14}} = 0.61 \text{ mV/LSB} \tag{7.12}$$

Thus, a 2.5 mV signal occupies only:

$$N_{\text{LSB}} = \frac{2.5 \text{ mV}}{0.61 \text{ mV}} \approx 4.1 \tag{7.13}$$

quantisation levels. When referenced to the amplified signal measured by the DAQ, this corresponds to approximately 393 LSBs. Because each quantisation step represents a

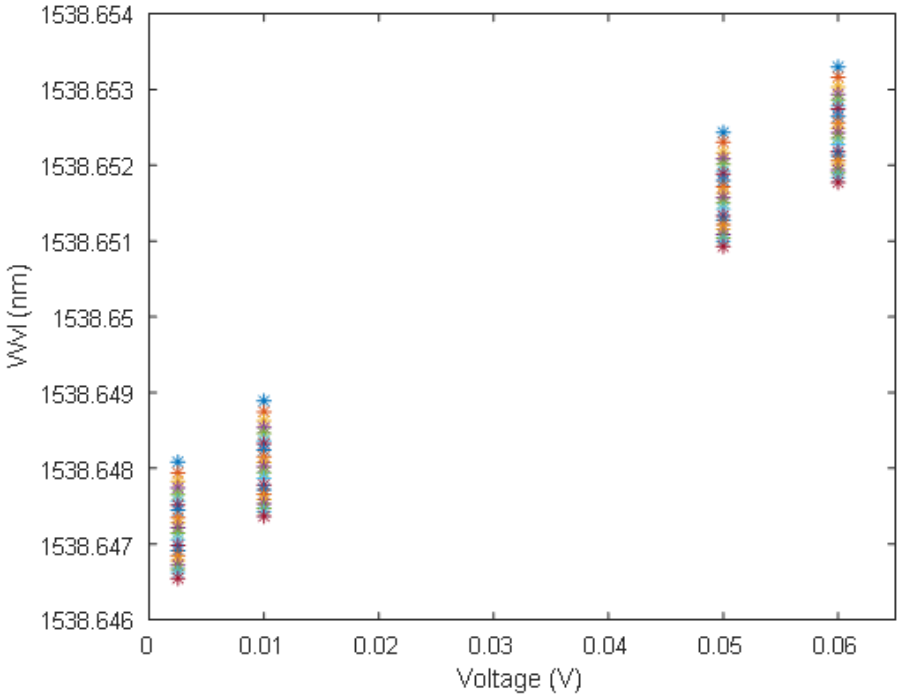

Figure 7.8: Measurement drift due to an uncompensated measurement cycle

significant fraction of the original low-level signal, the recorded waveform appears discretised rather than continuous. This explains the coarser appearance of the electrical data.

Furthermore, when the specified absolute accuracy is compared directly to the low-level input signal, the relative error becomes very large for millivolt-level measurements. For a 2.5 mV input, the potential relative error is substantially greater than for higher-level inputs, highlighting the limitation of directly measuring such low-level signals without amplification or suitable signal conditioning.

By contrast, although the exact ADC architecture of the IBSEN interrogator is not explicitly stated, its measurement domain operates in picometre wavelength shifts, implying much finer quantisation and a lower effective noise floor. This results in greater measurement granularity and explains the denser appearance of the optical data.

During measurement, drift may arise from environmental changes, self-heating within the sensing structure, or interrogator-related instability. Under identical PZT

polarisation and equivalent voltage excitation, the optical response exhibited a wavelength drift of approximately 2 pm over a measurement cycle, as shown in Fig. 7.8. This behaviour is characteristic of thermally induced drift in the absence of explicit compensation and may introduce a significant bias if left uncorrected.

7.11 Statistical Evaluation of Measurement Uncertainty

The uncertainty associated with the measurement system was evaluated using the statistical framework defined in the Guide to the Expression of Uncertainty in Measurement (GUM) [2]. Measurement uncertainty is generally classified as either Type A, obtained from statistical analysis of repeated observations, or Type B, derived from instrument specifications, calibration certificates, and manufacturer data.

In this study, repeated measurements were performed at each excitation level to quantify the statistical characteristics of the sensor response. For each step, 9000 samples were acquired over a 3 s interval at a sampling frequency of 3 kHz. The best estimate of the measured quantity was obtained from the arithmetic mean:

$$\bar{x} = \frac{1}{N} \sum_{i=1}^{N} x_i \tag{7.14}$$

where N is the total number of samples and x_i is the ith observation.

The dispersion of the measurements about the mean is characterised by the standard deviation:

$$\sigma = \sqrt{\frac{1}{N} \sum_{i=1}^{N} (x_i - \bar{x})^2} \tag{7.15}$$

The uncertainty associated with the estimated mean is given by the standard error:

$$SE = \frac{\sigma}{\sqrt{N}} \tag{7.16}$$

The standard error therefore quantifies the uncertainty in the estimated mean arising from random measurement noise. For systems dominated by random noise, the error distribution can be approximated by a Gaussian distribution centred on the mean.

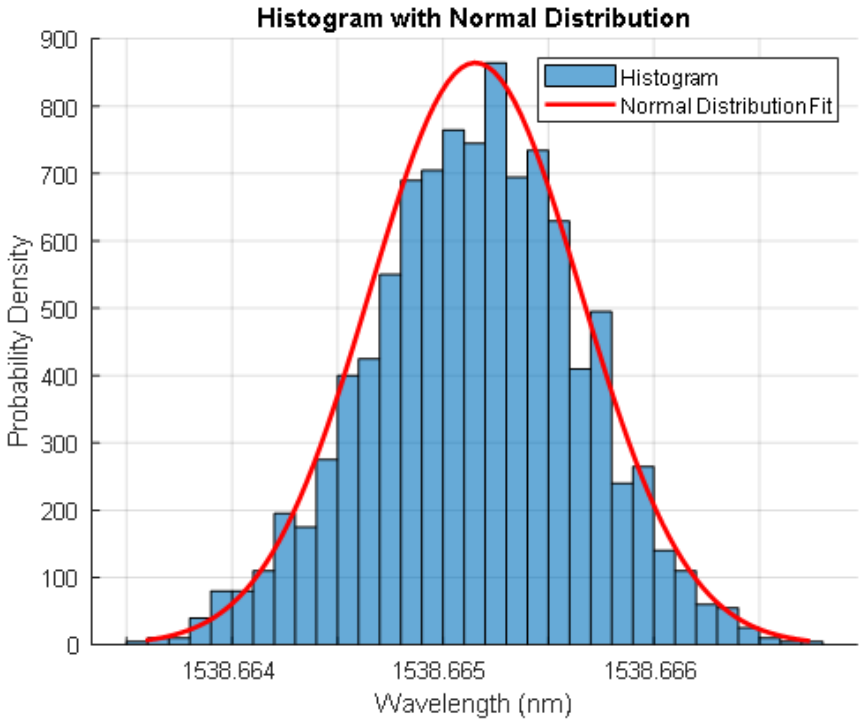

Figure 7.9: Probability distribution of the optical signal at 2.5 mV

Under this assumption, approximately 68% of measurements lie within $\pm 1\sigma$, while approximately 95% lie within $\pm 2\sigma$, corresponding to the commonly adopted expanded uncertainty with coverage factor $k = 2$.

The statistical parameters obtained from the measurements were used to evaluate repeatability and estimate the Type A uncertainty contribution. Representative distributions for the optical and electrical measurements at the lower operating range are shown in Fig. 7.9 and Fig. 7.10.

Figure 7.9 shows the probability distribution of the optical signal corresponding to a 2.5 mV excitation. For this measurement, using an FBG centred around 1538 nm, the mean value was 1538.665153 nm and the standard error was 0.000050 nm. The best estimate of the optical measurement is therefore:

$$m_{\text{est}} = 1538.66515 \pm 0.00005 \text{ nm} \tag{7.17}$$

Since the standard error corresponds to an approximate 68% confidence interval

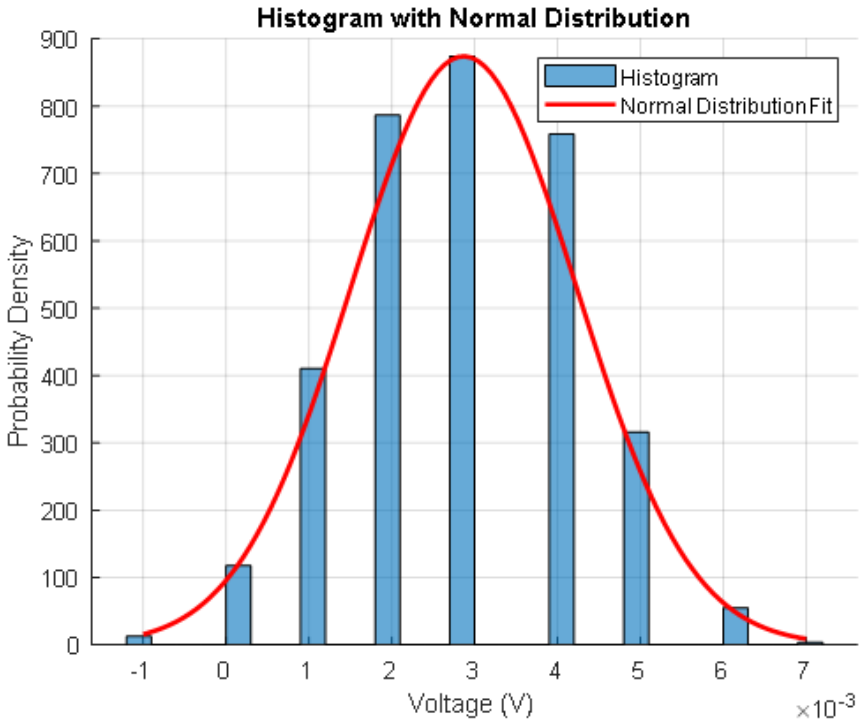

Figure 7.10: Probability distribution function of the 2.5 mV voltage signal

under the assumption of normality, the expanded uncertainty at approximately 95% confidence is obtained using a coverage factor of $k = 2$ [15], giving:

$$m_{\text{est}} = 1538.66515 \pm 0.00010 \text{ nm} \tag{7.18}$$

Similarly, Fig. 7.10 shows the probability distribution function of the 2.5 mV electrical measurement. The measured mean was 0.002611 V with a standard error of 0.0000451 V. The corresponding best estimate at approximately 95% confidence is therefore:

$$m_{\text{est}} = 0.002611 \pm 0.00009 \text{ V} \tag{7.19}$$

The probability density plots confirm the presence of random noise in both the electrical and optical measurements, which is expected due to intrinsic imperfections in electronic components, acquisition systems, and environmental conditions. In addition to this random contribution, a systematic drift of up to approximately 3 pm

was observed in the optical response over a full measurement cycle. This level of drift is particularly significant at low signal amplitudes, where the measurements approach the effective error floor of the acquisition system. The random contributions are classified as Type A uncertainty, while equipment accuracy, quantisation, and interrogator specifications contribute to the Type B uncertainty budget.

7.12 Electrical Equipment Uncertainty Contribution

The principal uncertainty contributions associated with the DAQ system are:

- absolute accuracy of the DAQ card,
- system noise,
- quantisation uncertainty associated with the ADC resolution.

According to the NI specification, the absolute accuracy includes the combined effects of gain error, offset error, and noise uncertainty, and may be expressed as:

$$\text{Absolute Accuracy} = \pm\left[(\text{Voltage Reading} \cdot \text{Gain Error}) + (\text{Voltage Range} \cdot \text{Offset Error}) + \text{Noise Unc}\right. \tag{7.20}$$

For the NI USB-6003, the manufacturer specifies an absolute accuracy of ±6.0 mV on the ±10 V range. Since no confidence level is stated in the datasheet, this specification was treated as a Type B contribution with a rectangular distribution. The corresponding standard uncertainty is therefore:

$$u_{\text{spec}} = \frac{6.0 \text{ mV}}{\sqrt{3}} = 3.464 \text{ mV} \tag{7.21}$$

The quantisation uncertainty of the USB-6003 was estimated from the least significant bit (LSB). For the ±5 V range used during measurement:

$$\text{LSB} = \frac{10}{2^{16}} = 152.6 \ \mu\text{V} \tag{7.22}$$

Assuming a rectangular distribution, the corresponding quantisation standard uncertainty is:

$$u_{\text{quant}} = \frac{\text{LSB}}{\sqrt{12}} = 0.044 \text{ mV} \tag{7.23}$$

7.13 Optical Equipment Uncertainty Contribution

7.13.1 Measurement Drift

Wavelength drift is defined as the wavelength shift per degree Celsius [16]. The IB-SEN interrogator specification indicates a wavelength drift of approximately 1 pm/°C (3 pm maximum), which was used in the uncertainty analysis. By taking 1 pm as the representative drift and modelling it as a Type B uncertainty with a rectangular distribution, the standard uncertainty becomes:

$$u_d = \frac{1 \text{ pm}}{\sqrt{3}} = 0.58 \text{ pm} \tag{7.24}$$

7.13.2 Measurement Repeatability

According to the I-MON specification, repeatability is defined as the peak-to-peak variation in measured wavelength under constant temperature and over a full 360° polarisation rotation [16]. The stated repeatability is 3 pm peak-to-peak (5 pm maximum). Treating this as a uniform Type B uncertainty, the standard uncertainty is:

$$u_{\text{rep}} = \frac{s/2}{\sqrt{3}} \tag{7.25}$$

Hence, for $s = 3$ pm:

$$u_{\text{rep}} = \frac{1.5}{\sqrt{3}} = 0.87 \text{ pm} \tag{7.26}$$

7.13.3 Wavelength Fit Resolution

The I-MON wavelength fit resolution is defined as the standard deviation obtained over a series of measurements under constant temperature and polarisation [16]. The specified wavelength fit resolution is < 0.5 pm (1σ), which is treated here as a Type B

uncertainty with normal distribution:

$$u_{\text{res}} = 0.5 \text{ pm} \tag{7.27}$$

7.13.4 Combined Optical Uncertainty

The combined standard uncertainty associated with the optical interrogator is obtained by root-sum-square combination of drift, repeatability, and wavelength fit resolution:

$$u_{\text{opc}} = \sqrt{u_d^2 + u_{\text{rep}}^2 + u_{\text{res}}^2} \tag{7.28}$$

Substituting the corresponding values:

$$u_{\text{opc}} = \sqrt{0.58^2 + 0.87^2 + 0.5^2} = 1.16 \text{ pm} \approx 1 \text{ pm} \tag{7.29}$$

From the established calibration relationship, a wavelength shift of approximately 1 pm corresponds to an electrical equivalent of about 10 mV, as summarised in Table 7.4. Consequently, the optical uncertainty contributes a significant equivalent electrical uncertainty, particularly in the low-amplitude region where the nonlinear calibration is steep.

The voltage equivalent of wavelength shift is obtained using the calibration relationship:

$$V_{\text{equivalent}} = a\lambda^2 + b\lambda + c \tag{7.30}$$

where a, b, and c are calibration constants, and λ is the wavelength.

For the range 0–25% of nominal current, the relationship is:

$$V_{\text{equivalent}} = 1123.60824393394\,\lambda^2 - 3457700.4005966\,\lambda + 2660111325.45098 \tag{7.31}$$

For the range 25–300% of nominal current, the relationship becomes:

$$V_{\text{equivalent}} = 36.5107212019896\,\lambda^2 - 112344.731058256\,\lambda + 86422138.949315 \tag{7.32}$$

Table 7.4: Voltage equivalent of wavelength shift

% of Nominal	Shunt Voltage (V)	Wavelength (nm)	Voltage Equivalent (V)
0–25%	0.00292	1538.662808	0.003037
		1 pm shift → 0.00915 V	
>25%	0.03006	1538.665475	0.030225
		1 pm shift → 0.01088 V	
High level	0.12010	1538.673544	0.120081
		1 pm shift → 0.01147 V	
		Average: 1 pm ≈ 0.0105 V	

Applying these relationships yields the voltage-equivalent shift associated with a 1 pm wavelength variation, as presented in Table 7.4.

This relatively large electrical equivalent arises from the sensitivity of the nonlinear calibration function, whereby small wavelength deviations are mapped to amplified voltage-equivalent variations.

The PZT-based low-voltage transducer was treated as thermally stable within the scope of this analysis. This assumption is supported by published literature indicating that PZT materials remain operational over wide temperature ranges, as well as by manufacturer specifications reporting minimal performance degradation over extended operating cycles [17], [18].

7.14 Combined Uncertainty

The overall combined standard uncertainty of the measurement system is obtained by combining the uncertainty contributions from the DAQ, amplifier, and optical interrogator:

$$u_c = \sqrt{u_{\text{DAQ}}^2 + u_{\text{amp}}^2 + u_{\text{opc}}^2} \tag{7.33}$$

where u_{DAQ} represents the DAQ uncertainty, u_{amp} represents the uncertainty associated with amplifier variation, and u_{opc} is the optical interrogator uncertainty expressed in voltage-equivalent form.

The amplifier contribution was treated as negligible because the specified offset drift is only 1.4 μV/°C and the input noise is 220 nV/$\sqrt{\text{Hz}}$ [19], both of which are small compared with the dominant DAQ and optical uncertainty contributions.

Substituting the dominant terms:

$$u_c = \sqrt{3.464^2 + 0.044^2 + 10^2} = 10.58 \text{ mV} \tag{7.34}$$

The expanded uncertainty for a coverage factor of $k = 2$ is:

$$U = ku_c = 2 \times 10.58 = 21.16 \text{ mV} \tag{7.35}$$

Accordingly, measurements from the sensor may be reported as:

$$x \pm 10.58 \text{ mV} \tag{7.36}$$

for standard uncertainty, or

$$x \pm 21.16 \text{ mV} \quad (k = 2) \tag{7.37}$$

for expanded uncertainty.

It should be noted that this uncertainty estimate is conservative, since it incorporates both DAQ and optical interrogation effects referred to the electrical domain. At low-amplitude operating points, the expanded uncertainty becomes significant relative to the IEC error limits, thereby highlighting the importance of calibration refinement and drift compensation.

The uncertainty budget used in this study is summarised in Table 7.5, while the relative uncertainty referred to representative shunt voltage levels is presented in Table 7.6.

Table 7.5: Measurement uncertainty budget (DAQ USB-6003 and IBSEN interrogator)

Source	**Symbol**	**Specification**	**Distribution**	**Std. Uncertainty**
DAQ accuracy	u_{acc}	6 mV	Rectangular	3.464 mV
Quantisation	u_{quant}	LSB/$\sqrt{12}$	Rectangular	0.044 mV
Interrogator drift	u_d	$\sim$1 pm	Rectangular	0.588 pm
Repeatability	u_{rep}	3 pm	Normal	0.87 pm
Resolution	u_{res}	$<$0.5 pm	Rectangular	0.5 pm
Combined (u_c)				**10.58 mV**
Expanded ($k = 2$)				**21.16 mV**

Table 7.6: Error contribution from DAQ and interrogator uncertainty

$V_{\mathbf{shunt}}$ **(V)**	**% Nom.**	**Rel. Unc. (%)**	$V_{\mathbf{out}}$ **(V)**	**Gain (%)**
0.002683	5%	4.40	0.240823	89.76
0.01075	20%	2.41	0.439273	40.86
0.050117	100%	0.96	1.10626	22.07
0.060121	120%	0.82	1.285672	21.38

Based on this analysis, the sensor exhibits relative standard uncertainties of approximately ±4.4%, ±2.41%, ±0.96%, and ±0.83% at the representative operating points considered. For a 95% confidence level, these standard uncertainties are multiplied by a coverage factor of $k = 2$.

These results indicate that the expected deviation from the true value remains bounded within the quantified uncertainty limits, while also showing that low-level signals are the most strongly affected by equipment-induced uncertainty. Overall, the uncertainty analysis confirms that the dominant contributors arise from the DAQ specification and the interrogator characteristics, and that these contributions must be explicitly considered when evaluating compliance with IEC 61869-14.

7.15 Error Correction and Compensation

Drift arising from interrogator accuracy limits, repeatability constraints, and environmental influence can cause measurement deviations that threaten compliance with the IEC-specified accuracy limits. If left uncompensated, these effects may introduce sig-

nificant bias, particularly at low signal amplitudes such as 2.5 mV, 5 mV, and 10 mV, where even a 1 pm wavelength drift may correspond to a substantial voltage-equivalent error. This effect is less pronounced at higher amplitudes, where the same wavelength deviation represents a smaller fraction of the measured signal.

To compensate for drift-related inaccuracies, a secondary fibre Bragg grating (FBG) was colocated within the same measurement environment as the sensing FBG. This reference FBG was exposed to the same environmental conditions but mechanically isolated from strain, thereby serving as a control channel. Its purpose was to capture drift arising from temperature variation and interrogator instability, enabling compensation of the sensing FBG output. Such correction is particularly important in FBG-based sensing systems, where measurement repeatability, thermal sensitivity, and interrogator limitations can otherwise degrade measurement accuracy [10].

The two FBG signals were multiplexed along a standard single-mode optical fibre and interrogated simultaneously, with each grating identified by its calibrated Bragg wavelength. This enables distributed sensing with simultaneous acquisition from multiple points.

The measured wavelength shift from the sensing FBG contains contributions from both strain and temperature. To isolate the strain-induced component, a differential compensation approach was adopted using the reference FBG. The compensated signal was obtained by subtracting the reference FBG response from the sensing FBG response and then referencing the result to the baseline no-load calibrated value. Since the induced strain is proportional to the voltage developed across the shunt resistor, this compensated optical signal can be used to reconstruct the electrical quantity of interest.

Mathematically, the extracted signal of interest is expressed as:

$$y = m - n + h \tag{7.38}$$

where m is the measured response of the sensing FBG (strain + temperature), n is the response of the reference FBG (temperature only), and h is the baseline FBG value obtained under no-load, controlled-temperature conditions.

In practice, however, the two FBGs may not exhibit identical thermal sensitivities. Under such conditions, direct subtraction does not completely eliminate temperature-induced effects, leaving a residual term of the form:

$$(K_{T1} - K_{T2})\Delta T \tag{7.39}$$

where K_{T1} and K_{T2} are the thermal sensitivity coefficients of the sensing and reference FBGs, respectively.

This residual term introduces bias in the inferred strain and, consequently, in the reconstructed current. To address this, a weighted differential compensation approach was adopted by calibrating the thermal sensitivities of both gratings. The corrected strain is then given by:

$$\varepsilon = \frac{\Delta m - \alpha \Delta n}{K_\varepsilon}, \qquad \alpha = \frac{K_{T1}}{K_{T2}} \tag{7.40}$$

where ε is the estimated strain, K_ε is the strain sensitivity coefficient of the sensing FBG, and α is the thermal compensation factor accounting for sensitivity mismatch.

This formulation improves suppression of temperature-induced drift and enhances the accuracy of the reconstructed electrical measurement, particularly under varying environmental conditions. The compensation is especially important at low signal levels, where small wavelength deviations can lead to large voltage-equivalent errors due to the sensing system's nonlinear calibration characteristics.

7.15.1 Extraction of the Signal of Interest

During measurement, the wavelength shift generated by the low-voltage transducer (LVT) in response to the applied electric field is influenced not only by strain but also by temperature and interrogator-related drift. To compensate for these effects, two LVT-FBG assemblies were used within the sensing setup, as illustrated in Fig. 7.11. The first, mechanically isolated from the applied voltage, served as the control FBG for temperature compensation, while the second, connected to the circuit, measured the combined effect of strain and temperature. The differential response between the two gratings provided the net strain-induced wavelength shift, as described by (7.38).

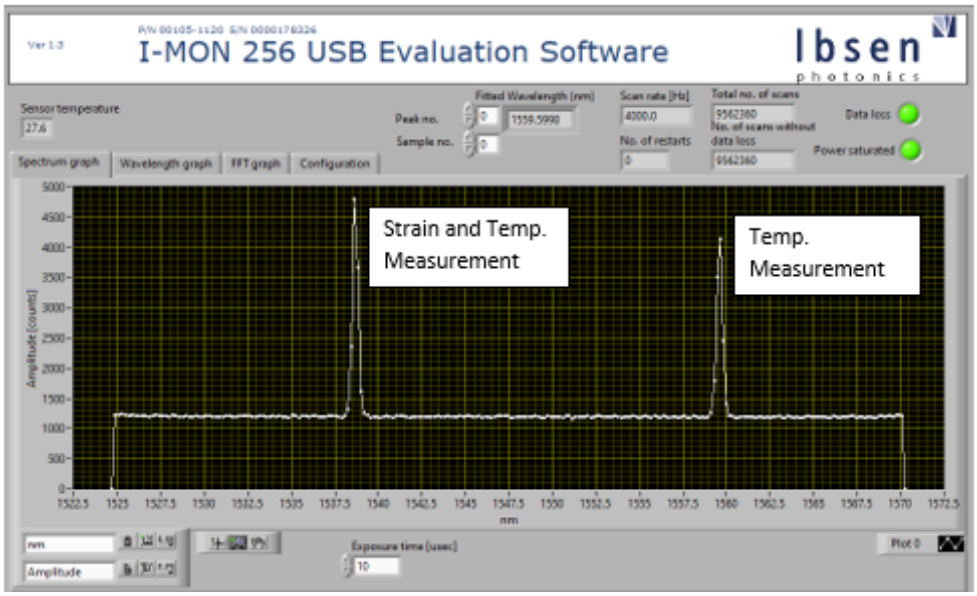

Figure 7.11: Interrogator output window

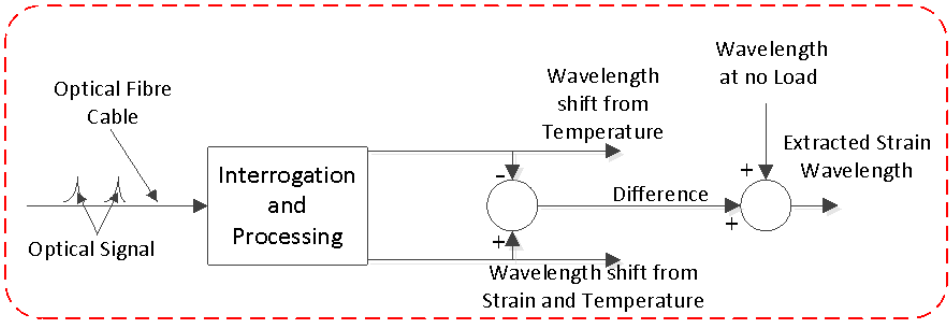

Figure 7.12: Differential interrogation process flow

The optical output of the LVT is proportional to the driving voltage applied to the PZT actuator, subject to some hysteresis. Since this driving voltage is derived from the shunt current, the measured optical response can be related back to the electrical excitation. Figure 7.12 illustrates the extraction of the signal of interest from the combined measurement signal.

Figure 7.13 summarises the measured voltages and their corresponding interrogated wavelength shifts. In this arrangement, the primary FBG centred at 1538 nm captured the strain-related signal superimposed with environmental and equipment-

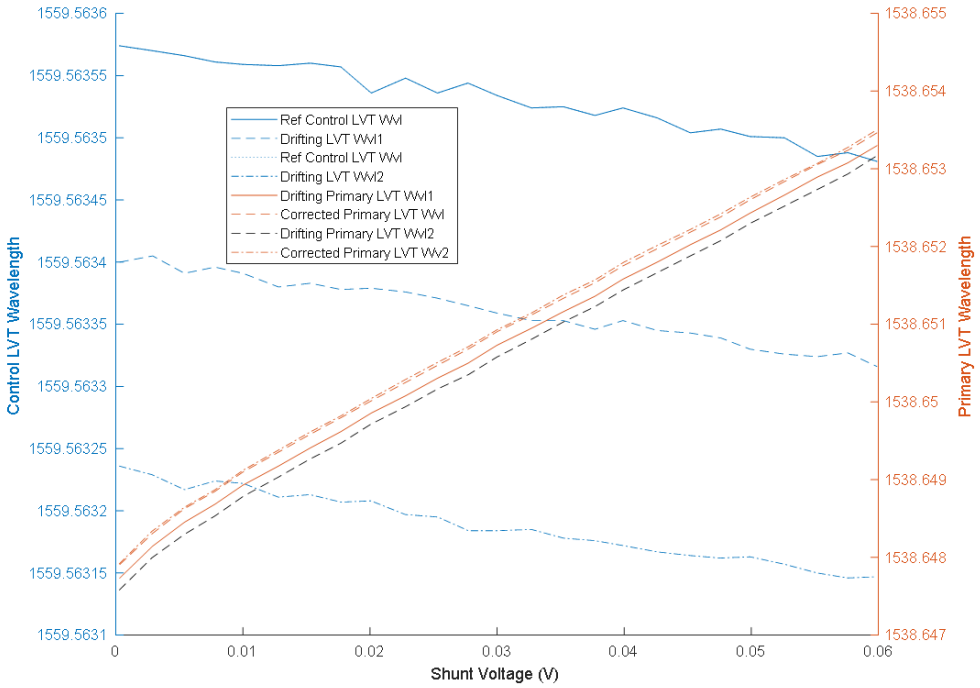

Figure 7.13: Error correction and wavelength drift trend

induced drift, while the secondary FBG centred at 1559 nm served as the reference grating. The true strain response was obtained by compensating the primary FBG output using the drift measured by the reference FBG.

In practice, one acquisition run from the reference FBG was taken as the baseline, and subsequent deviations were used to determine the drift correction factor. This correction factor was then applied to the primary FBG wavelength measurement. The compensation was implemented adaptively: when the operating temperature increased above ambient, a downward wavelength drift was observed, requiring addition of the correction factor; conversely, when the temperature fell below ambient, an upward drift was observed, requiring subtraction of the correction factor.

Figure 7.14 shows the thermally uncompensated optical measurement, while Fig. 7.15 shows the corrected response after compensation.

The results show that the application of drift compensation using a control FBG significantly improves measurement stability and accuracy. By isolating thermal and

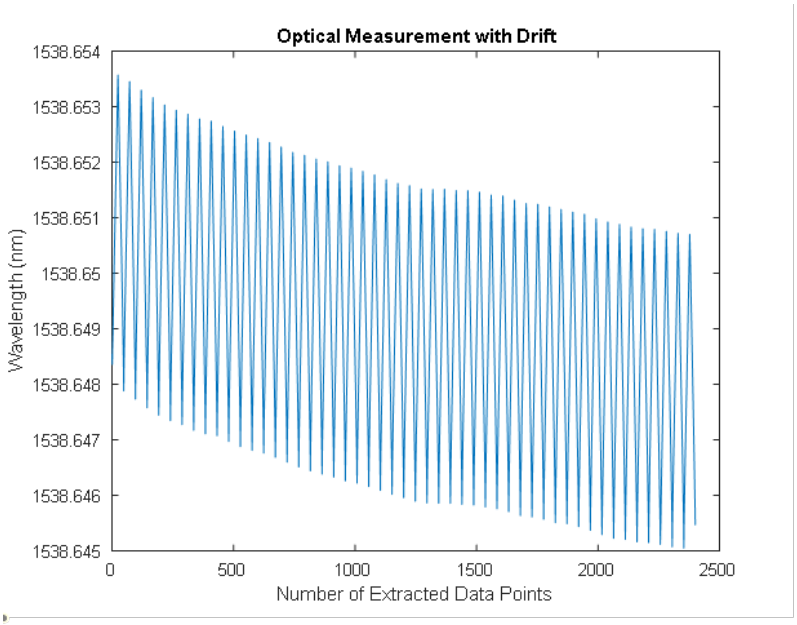

Figure 7.14: Measurement of thermally uncompensated optical signal

interrogator-induced variations, the corrected wavelength more faithfully represents the true measurand, thereby improving both accuracy and repeatability.

In addition to the empirical differential compensation method, the IBSEN I-MON interrogator provides a manufacturer-based analytical correction approach for wavelength drift. This method estimates the corrected wavelength directly from the measured optical response according to:

$$\lambda_{\text{corrected}}[\text{nm}] = \frac{\lambda_{\text{meas}}[\text{nm}] - \beta t_{\text{amb}}[^{\circ}\text{C}] - \beta_0}{1 + \alpha t_{\text{amb}}[^{\circ}\text{C}] + \alpha_0} \tag{7.41}$$

where the coefficients α, α_0, β, and β_0 are provided in the certificate of conformance [20]. This correction method provides an additional means of mitigating temperature-related drift in accordance with the manufacturer's specification.

Under thermally stable and compensated conditions, the optical response exhibited negligible drift, as shown in Fig. 7.16. The corresponding electrical and optical

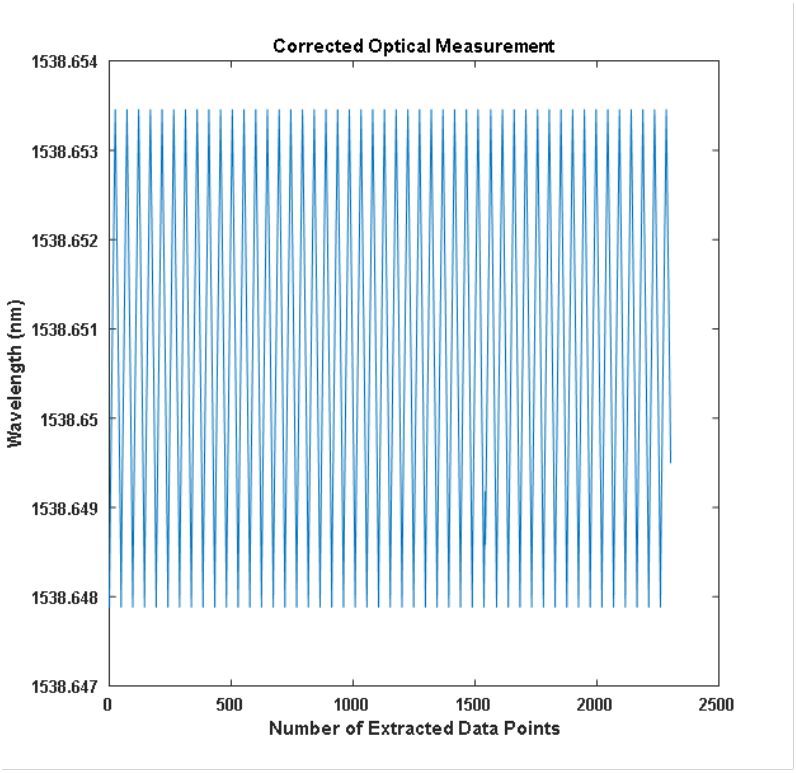

Figure 7.15: Corrected measurement

measurements over the full operating cycle further demonstrate the beneficial effect of thermal stabilisation on overall sensor performance.

7.15.2 Contribution of the Proposed Drift Compensation Method

A key contribution of this chapter is the development and implementation of a temperature drift compensation framework for FBG-based optical current sensing, specifically tailored for low-amplitude signal measurement in HVDC monitoring applications.

In FBG-based sensing systems, the measured wavelength shift is a superposition of strain-induced and temperature-induced effects. Conventional differential compensation methods commonly assume identical thermal sensitivities between sensing and

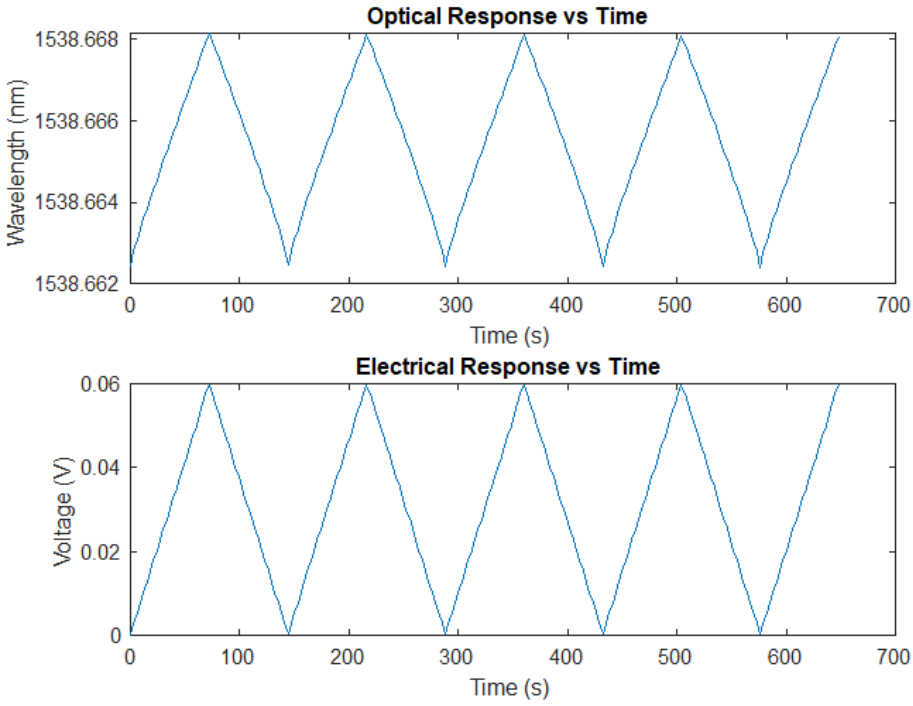

Figure 7.16: Measurement cycles of electrical signals and thermally compensated optical signal

reference gratings. In practice, however, this assumption is rarely exact due to fabrication tolerances, wavelength dependency, and material inconsistencies. As a result, direct subtraction leaves a residual thermal component that introduces bias into the inferred strain and degrades measurement accuracy.

To address this limitation, the proposed method incorporates a thermal-sensitivity-mismatch correction factor, thereby extending conventional differential compensation. By explicitly accounting for the ratio of thermal sensitivities between the sensing and reference FBGs, the method more effectively suppresses temperature-induced drift and reduces residual thermal error in the reconstructed electrical measurement.

This is particularly important at low signal amplitudes, where small wavelength deviations correspond to disproportionately large voltage-equivalent errors because of the nonlinear calibration characteristics of the sensing chain. The proposed method therefore improves both the robustness and the practical metrological performance of the sensor, supporting compliance with the requirements of IEC 61869-14.

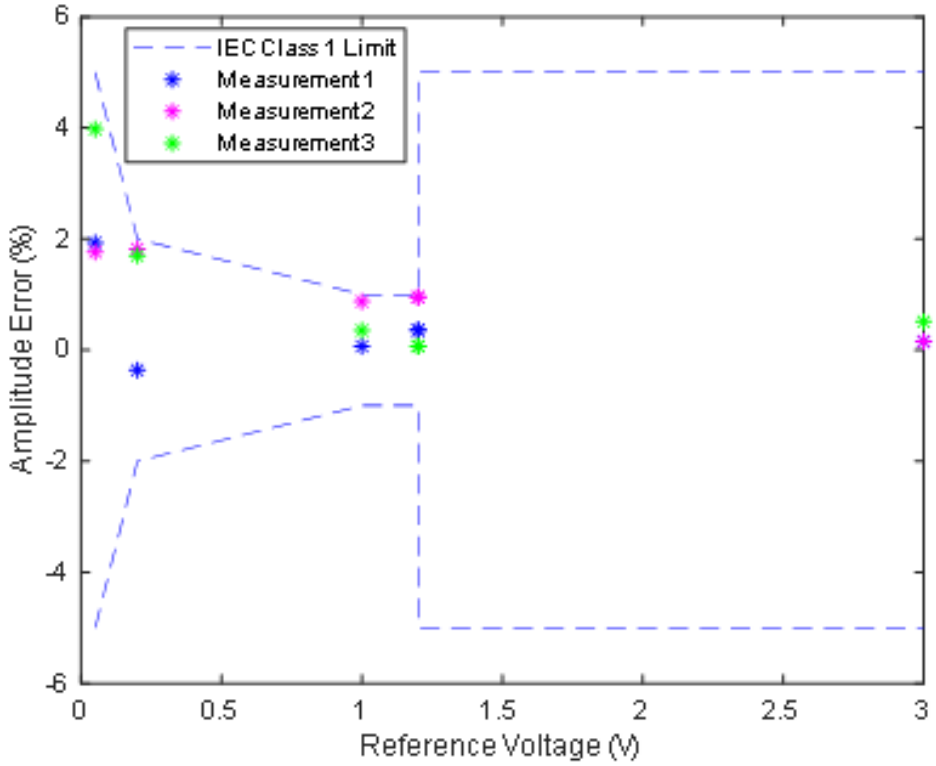

Figure 7.17: Error plot with IEC specification

7.16 Comparison of Results with IEC Standard Using Percentage Error

To evaluate the percentage error over the range from 5% to 300% of nominal current, the calibration curve was used to reconstruct voltage from the measured optical signal. The percentage error shown in Fig. 7.17 was calculated as:

$$\%\text{Error} = \frac{\text{Actual Input Voltage} - \text{Reconstructed Voltage}}{\text{Actual Input Voltage}} \times 100 \tag{7.42}$$

From the measurement error distribution in Fig. 7.17 and the uncertainty estimates summarised earlier in Table 7.6, it is evident that the measured error trend closely follows the overall uncertainty profile of the sensor system. This indicates that the dominant sources of deviation are consistent with the quantified contributors to uncertainty, namely DAQ accuracy, quantisation effects, noise, and interrogator-related

effects. The agreement between the measured error trend and the uncertainty model provides confidence that the principal sources of measurement deviation have been appropriately identified and quantified.

7.17 Conclusion

This chapter presented the calibration methodology, measurement-error analysis, uncertainty evaluation, and drift-compensation strategy for the proposed optical current sensor for HVDC monitoring applications. The objective was to establish a reliable relationship between the electrical input quantity and the optical response of the sensing system, and to quantify accuracy and identify the dominant contributors to measurement uncertainty.

A major challenge in calibrating the proposed sensing architecture arises from the nonlinear behaviour of the signal-conditioning amplifier. Although this nonlinear amplification stage was necessary to enhance sensitivity to very low-level shunt voltages, it produced a nonlinear relationship between electrical excitation and the optical response measured by the fibre Bragg grating interrogation system. To address this, a segregated semi-piecewise calibration approach was developed, in which the measurement range was divided into two operating regions, each represented by a second-order polynomial model. This approach provides a practical compromise between global polynomial fitting and fully piecewise modelling, enabling accurate calibration over the full range from 5% to 300% of nominal current. The resulting calibration curves showed coefficients of determination greater than 0.998, demonstrating excellent agreement with the experimental data.

Measurement uncertainty was evaluated using the GUM framework by considering both Type A and Type B contributions. Type A uncertainties were obtained from repeated measurements and statistical analysis, while Type B uncertainties were derived from instrument specifications and hardware limitations. The dominant contributors were identified as the absolute accuracy of the DAQ system, ADC quantisation effects, interrogator wavelength drift, and interrogator repeatability and resolution. The

combined standard uncertainty was obtained by propagating these contributions using the root-sum-square method, providing a quantitative basis for assessing the expected deviation of the measured result from the true value.

A further challenge in FBG-based sensing systems is their intrinsic sensitivity to temperature variation. Thermal fluctuations and interrogator instability introduce wavelength drift that can significantly affect measurement accuracy, particularly at low signal amplitudes. To mitigate this effect, a differential compensation method was implemented using a reference FBG colocated with the sensing FBG. The reference grating was mechanically isolated from strain but subjected to the same environmental conditions, enabling temperature-induced wavelength shifts to be identified and removed from the sensing signal. The proposed weighted compensation framework further accounted for mismatch in thermal sensitivity between the sensing and reference gratings, reducing residual thermal error and improving the fidelity of the reconstructed electrical measurement.

The experimental results demonstrated that the calibrated and compensated sensor system achieved measurement errors consistent with the accuracy limits specified in IEC 61869-14 for Class 1 DC current transformers. The uncertainty analysis further confirmed that the observed measurement deviations were consistent with the quantified uncertainty contributions from the acquisition and interrogation systems.

Overall, the results presented in this chapter establish the metrological validity and measurement reliability of the proposed optical current sensor. The combined use of nonlinear signal conditioning, segregated semi-piecewise calibration, and differential temperature compensation enables accurate current reconstruction over a wide dynamic range while maintaining compliance with IEC performance requirements. These findings demonstrate that the proposed sensing architecture provides a viable and robust solution for high-fidelity current monitoring in HVDC transmission networks, where accurate measurement and environmental resilience are essential for protection and operational reliability.

Chapter 7 References

[1] IEC, *IEC Guide 99:2007*, pp. 35–39, 2007.

[2] ISO/IEC, *Uncertainty of Measurement—Part 3: Guide to the Expression of Uncertainty in Measurement (GUM:1995), ISO/IEC Guide 98-3:2008(E)*, pp. 9–25, 2008.

[3] Joint Committee for Guides in Metrology, *Evaluation of Measurement Data—The Role of Measurement Uncertainty in Conformity Assessment*, pp. 4–25, 2012.

[4] IEC, *BS EN IEC 61869-14:2019*, pp. 23–24, 2019.

[5] NI Equipment, *Certificate of Calibration for USB-6003*, pp. 1–2.

[6] N. Chhabra, *Certificate of Conformance for NI USB-6003*, [Online], pp. 1–2. Accessed: Nov. 20, 2025. [Online]. Available: `https://sine.ni.com/apps/utf8/nical.main?action=CONF&serial_number=209E0E3`.

[7] IEC, *BS EN IEC 60060-2:2025*, pp. 6–17, 2025.

[8] Micron Optics, *Thermal Response of FBGs*, pp. 2–6.

[9] *SmartScan FBG Interrogator Product Manual*, pp. 2–5.

[10] Ibsen Photonics, *I-MON USB Interrogation Monitors Specifications: I-MON Software Operating Principle*, [Online], pp. 1–2. Accessed: Oct. 30, 2021. [Online]. Available: `http://www.ibsen.com`.

[11] NI (Emerson), *NI USB-6003*, pp. 1–3.

[12] I. Hughes and T. Hase, *Measurements and Their Uncertainties: A Practical Guide to Modern Error Analysis*. Oxford University Press, pp. 3–9.

[13] NI, *cDAQ Effective Number of Bits (ENOB): What Is the Effective Number of Bits (ENOB) for Various CompactDAQ Input Modules?* pp. 1–2.

[14] Texas Instruments, *Application Report*, [Online], pp. 3–8, 2011. Accessed: Jul. 10, 2025. [Online]. Available: `http://www.ti.com`.

[15] UKAS, *M3003: The Expression of Uncertainty and Confidence in Measurement*, [Online], pp. 17–32. Accessed: Jul. 10, 2025. [Online]. Available: http://www.ukas.com.

[16] Ibsen Photonics, *I-MON USB Product Specification*, pp. 1–3, 2014.

[17] J. Tichý, J. Erhart, E. Kittinger, and J. Přívratská, *Fundamentals of Piezoelectric Sensorics: Mechanical, Dielectric, and Thermodynamical Properties of Piezoelectric Materials*. Springer Berlin Heidelberg, 2010, pp. 10–207. DOI: 10.1007/978-3-540-68427-5.

[18] PI Ceramic / PICMA Technologies, *PZT Actuators*, pp. 4–7.

[19] STMicroelectronics, *TSU111, TSU112, TSU114*, [Online], pp. 2–6, 2019. Accessed: Dec. 6, 2021. [Online]. Available: http://www.st.com.

[20] I-MON, *I-MON USB Product Specification*, pp. 1–2, 2014.

Chapter 8

Use Case Application

8.1 Introduction

Reliable fault detection and localisation remain among the most critical challenges in high-voltage direct current (HVDC) transmission networks. In contrast to AC systems, HVDC networks lack inherent mechanisms that naturally limit fault currents, thereby placing stringent requirements on the speed of fault detection and mitigation to prevent rapid current escalation and equipment damage. As HVDC infrastructure expands to support long-distance bulk power transmission, offshore renewable integration, and emerging multi-terminal HVDC (MTDC) networks, the need for enhanced network observability and high-speed sensing technologies becomes increasingly critical.

This chapter investigates the application of a distributed optical current sensing architecture for rapid fault detection, localisation, and condition monitoring in HVDC cable systems. The sensing framework developed in this thesis integrates instrumented splice joints equipped with hybrid shunt–piezoelectric–fibre Bragg grating (FBG) sensing elements, enabling high-speed acquisition of current signatures along the transmission corridor. By utilising optical fibre as the signal transmission medium, the proposed sensing system achieves significantly faster propagation of measurement signals compared to conventional electrical sensing infrastructures, while simultaneously providing immunity to electromagnetic interference.

The principal contributions of this chapter are summarised as follows:

- **Fast Fault Signal Acquisition Using Optical Current Sensors:** The proposed sensing architecture enables rapid acquisition of fault-induced current transients through distributed optical sensing nodes, significantly reducing detection latency.
- **Fault Localisation Through Polarity Signature Analysis:** A novel localisation mechanism based on polarity inversion between adjacent sensors is used to identify the faulted segment.
- **Fault Distance Estimation Using Phase Information:** Phase shift information is utilised to estimate fault location under both homogeneous and inhomogeneous transmission conditions.
- **Insulation Condition Assessment Through LC Parameter Sensitivity:** Variations in inductance and capacitance are linked to insulation condition and dielectric ageing.

To validate these concepts, a MATLAB-based HVDC transmission model incorporating distributed sensors was developed, allowing interaction between sensing architecture and network dynamics under fault conditions.

8.2 Fault Detection in HVDC Network and Mitigation

Based on the experimental evaluation of sensor performance, a MATLAB/Simulink model of a thyristor-based HVDC transmission system was adapted to incorporate distributed sensing nodes, protection logic, and circuit breakers, as illustrated in Fig. 8.1.

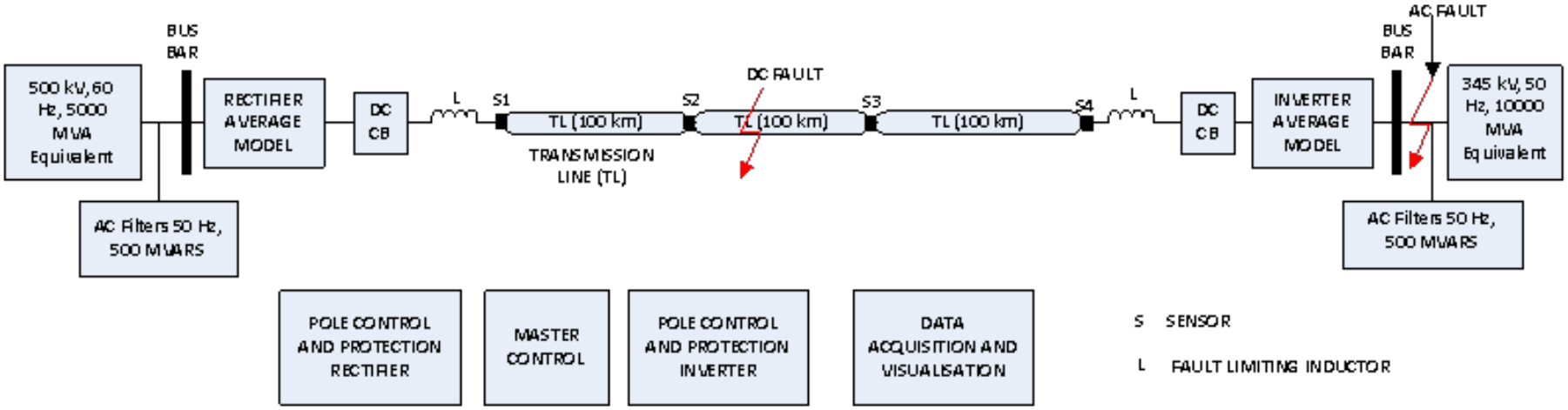

Figure 8.1: MATLAB Simulink model of HVDC with fault occurring at different sections of the cable

The base model employed is an average-value HVDC model, where switching dynamics are neglected and the converter is represented using averaged electrical quantities. This contrasts with full switching models, which explicitly simulate individual thyristor behaviour, commutation, and harmonic effects at the cost of increased computational complexity.

The original system represents a 1000 MW (500 kV, 2 kA) DC interconnection with a 300 km distributed parameter transmission line [1]. The line was segmented into three 100 km sections, with sensing nodes placed at the splice joints.

8.2.1 Fault Current Limitation Through Timely Acquisition of Fault Signals

Timely monitoring of current and rapid detection of transient fault signals are essential for preventing fault-current escalation [2], [3], [4]. Optical fibre links offer higher propagation speeds and immunity to electromagnetic interference compared to conventional copper-based systems.

8.2.2 Fault Detection Using Optical Fibre Versus XLPE Medium

The MATLAB simulation shown in Fig. 8.2 demonstrates the time advantage of optical fibre over XLPE propagation.

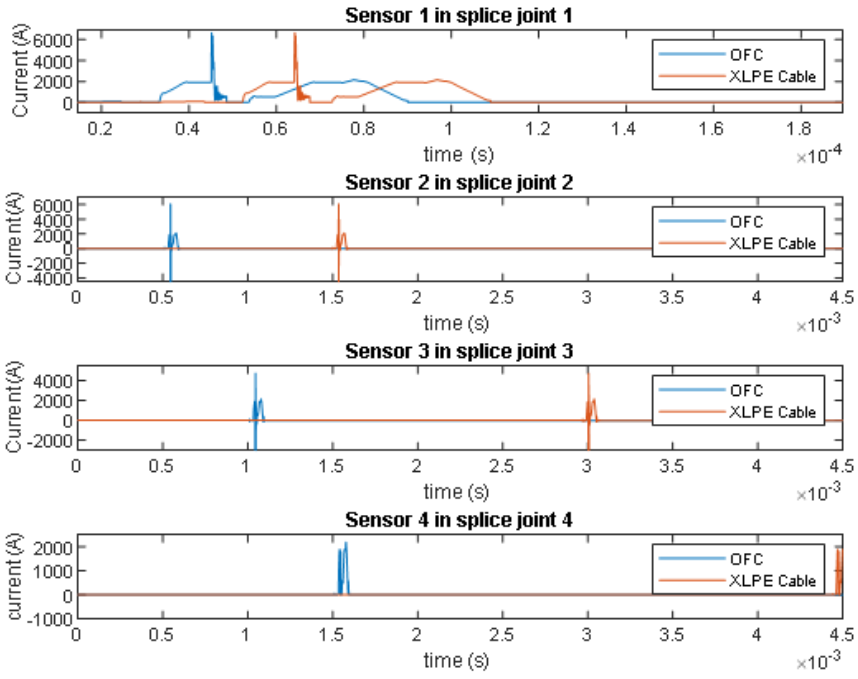

Figure 8.2: Fault wave propagation through different mediums

A pole-to-ground fault was simulated at 100 km and 200 km as shown in Fig. 8.3 and Fig. 8.4.

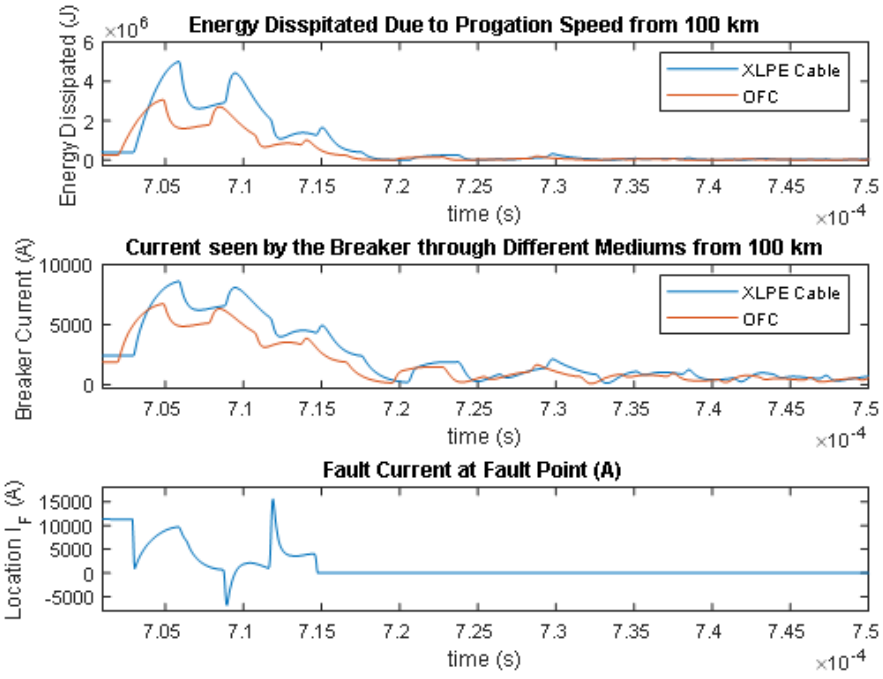

Figure 8.3: Current and energy dissipation at breaker for fault at 100 km

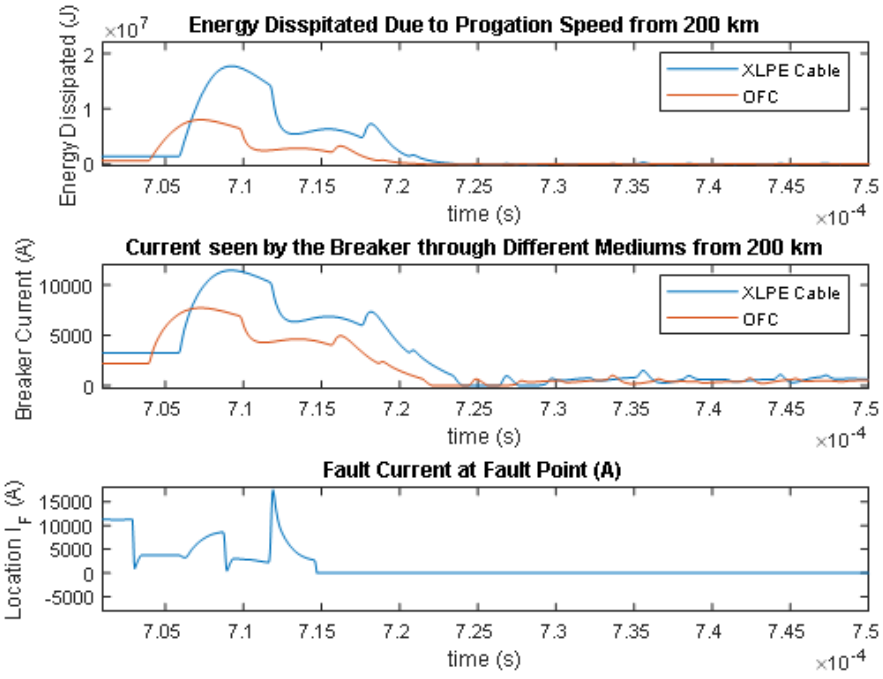

Figure 8.4: Current and energy dissipation at breaker for fault at 200 km

8.2.3 Propagation Speed Analysis

The propagation velocity of travelling waves in HVDC cables is given by:

$$V = \frac{1}{\sqrt{LC}} \tag{8.1}$$

Using ABB cable parameters ($L = 1.35$ mH/km, $C = 0.16\ \mu$F/km), the propagation speed in XLPE is approximately 6.8×10^7 m/s.

For a 100 km distance:

- Optical fibre: $t = 0.5$ ms
- XLPE cable: $t = 1.47$ ms

8.2.4 Dissipated Energy Reduction

The reduction in fault current and dissipated energy achieved through faster detection is summarised in Table 8.1.

Table 8.1: Signal propagation and cable parameter evaluation

Parameter	**Optical Fibre**	**XLPE Cable**
Propagation speed (m/s)	2.0×10^8	6.8×10^7
Cable length (km)	100	100
Inductance (mH/km)	–	1.35
Peak fault current (kA)	6.77	8.62
Time of arrival (ms)	0.5	1.47
Breaker operation time (ms)	2–5	2–5
Data processing time (ms)	1	1
Fault clearance time (ms)	3.5	4.5
$\mathrm{d}i/\mathrm{d}t$ (kA/ms)	2.56	2.0
Energy dissipation (MJ)	3.075	5.017

8.2.5 Fault Current Limitation and Inductor Sizing

The industry-standard response time for hybrid DC circuit breakers (DCCBs) is typically 2–5 ms [5], [6], [7]. Adopting a fast response of 2 ms [7], together with a 1 ms signal processing delay, results in a total response time of 3.5 ms for optical fibre-based detection and 4.5 ms for XLPE-based propagation.

To limit the rate of rise of fault current, a current-limiting inductor is required. The rate of change of current ($\mathrm{d}i/\mathrm{d}t$) is determined based on the maximum breaking capacity of the DCCB (9 kA). For propagation times of 3.5 ms and 4.5 ms, the corresponding $\mathrm{d}i/\mathrm{d}t$ values are 2.56 kA/ms and 2 kA/ms, respectively.

$$V = L\frac{\mathrm{d}i}{\mathrm{d}t}, \quad L = \frac{V}{\mathrm{d}i/\mathrm{d}t} \tag{8.2}$$

For a DC voltage of 500 kV, the required inductance values are:

- Optical fibre case: $L = 195$ mH
- XLPE case: $L = 250$ mH

This demonstrates that faster detection enabled by optical fibre allows the use of a smaller current-limiting inductor.

Using a 195 mH inductor, the corresponding $\mathrm{d}i/\mathrm{d}t$ is 2.56 kA/ms. The energy dissipated under fault conditions decreases by approximately 2.15 MJ (approximately 40%) when using distributed sensing compared to conventional travelling-wave detection. Depending on the formulation, the energy reduction may reach up to 3.56 MJ, highlighting the significant benefit of early fault detection.

8.3 Fault Localisation in HVDC Systems

Fault localisation plays a critical role in system restoration and network availability, particularly in multi-terminal HVDC (MTDC) systems.

Fault Localisation Through Polarity Signature

The polarity of the fault current provides a spatial indicator of fault location. As shown in Fig. 8.5, polarity inversion between adjacent sensors can be used to identify the faulted segment.

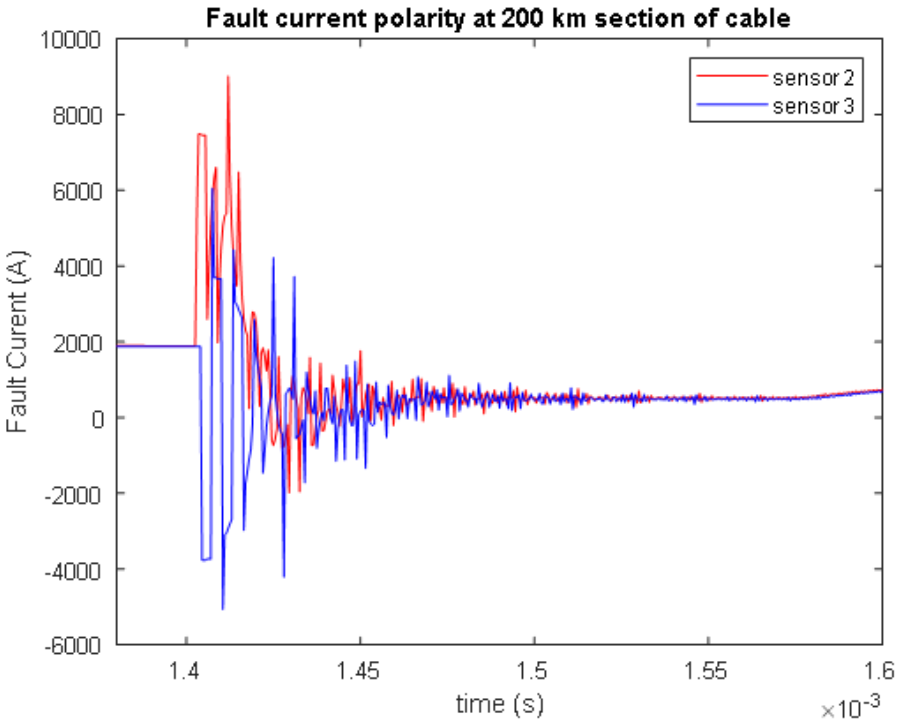

Figure 8.5: Polarity of the fault signals between sensors

Fault Localisation in Homogeneous Transmission Medium

In a homogeneous medium (Fig. 8.6), fault localisation can be achieved using time-of-arrival analysis.

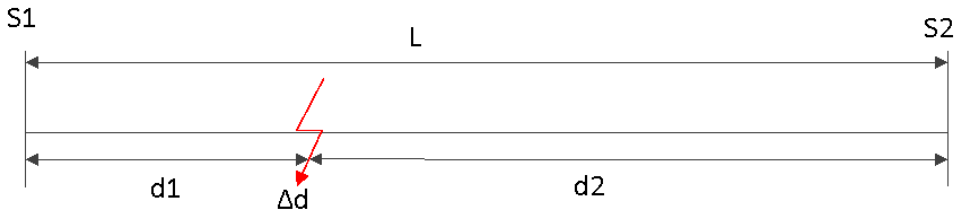

Figure 8.6: Homogeneous transmission medium

$$d_1 - d_2 = \Delta d \tag{8.3}$$

$$x - (L - x) = \Delta d \tag{8.4}$$

$$2x - L = \Delta d \tag{8.5}$$

$$x = \frac{L \pm \Delta d}{2} \tag{8.6}$$

$$\Delta d = v \cdot t \tag{8.7}$$

Fault Localisation in Inhomogeneous Transmission Medium

In practical HVDC systems, inhomogeneities affect propagation characteristics. These are illustrated in Fig. 8.7.

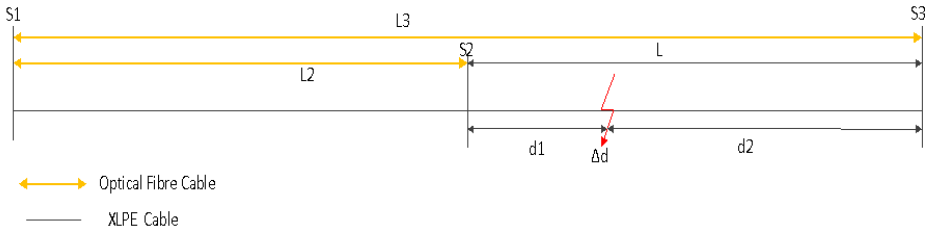

Figure 8.7: Inhomogeneous transmission medium

$$(V_{\text{xlpe}} \cdot \frac{d_2}{V_{\text{xlpe}}} + V_{\text{ofc}} \cdot \frac{L_3}{V_{\text{ofc}}}) - (V_{\text{xlpe}} \cdot \frac{d_1}{V_{\text{xlpe}}} + V_{\text{ofc}} \cdot \frac{L_2}{V_{\text{ofc}}}) = \Delta d \tag{8.8}$$

$$x = \frac{2L - \Delta d}{2} \tag{8.9}$$

$$\Delta d = \left(\Delta t - \left(\frac{L_3}{V_{\text{ofc}}} - \frac{L_2}{V_{\text{ofc}}}\right)\right) V_{\text{xlpe}} \tag{8.10}$$

$$x = \frac{2L - \left(\Delta t - \left(\frac{L_3}{V_{\text{ofc}}} - \frac{L_2}{V_{\text{ofc}}}\right)\right) V_{\text{xlpe}}}{2} \tag{8.11}$$

Fault Localisation Using Adjacent Sensors

Faults were simulated at 5 km, 10 km, and 15 km upstream of Sensor 2. The results are shown in Fig. 8.8, Fig. 8.9, and Fig. 8.10.

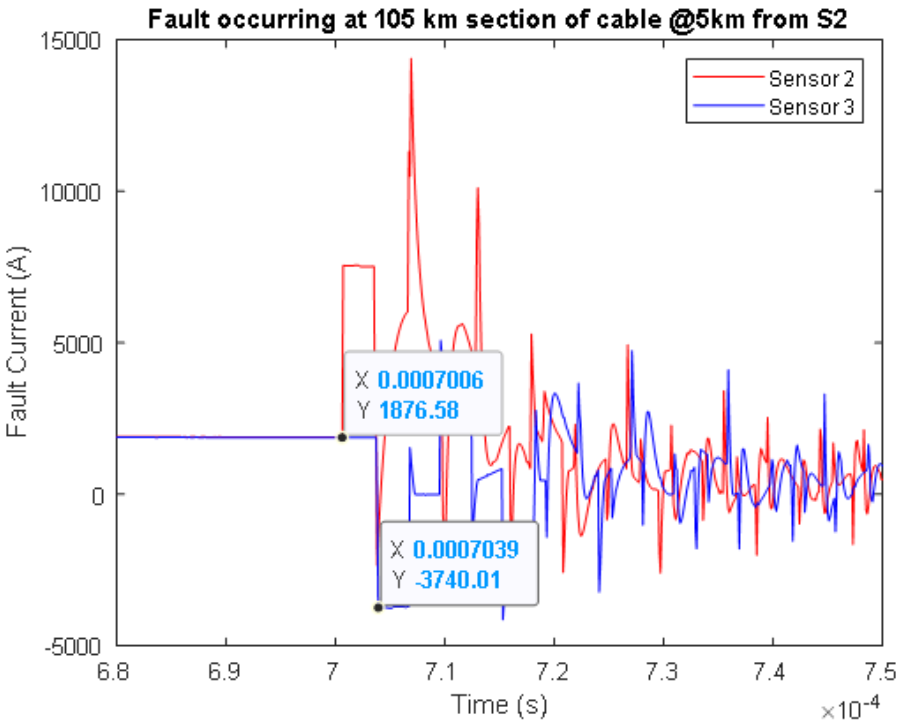

Figure 8.8: Fault at 5 km from Sensor 2

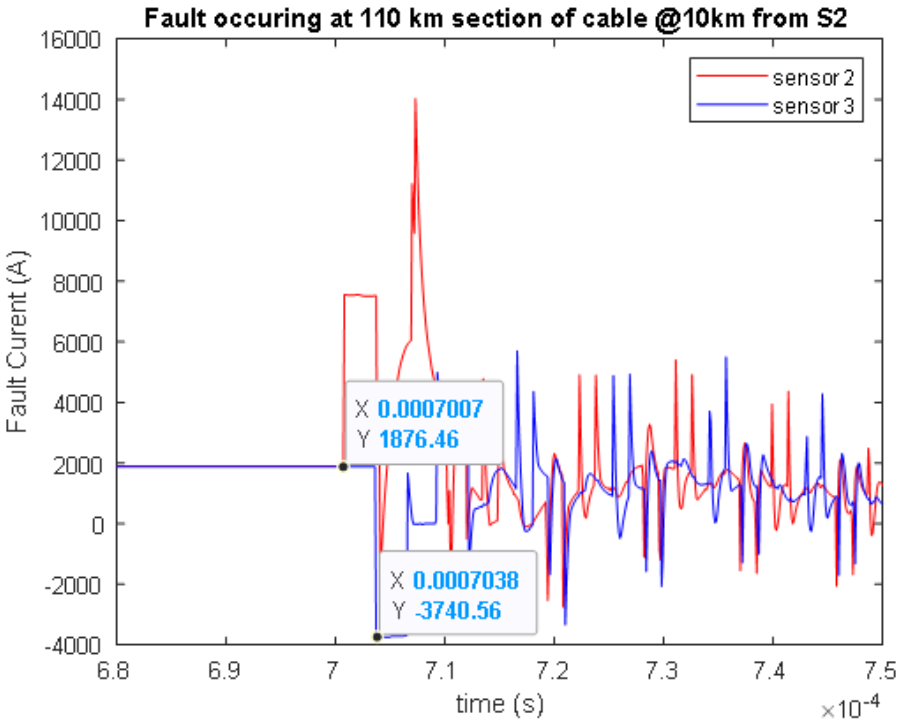

Figure 8.9: Fault at 10 km from Sensor 2

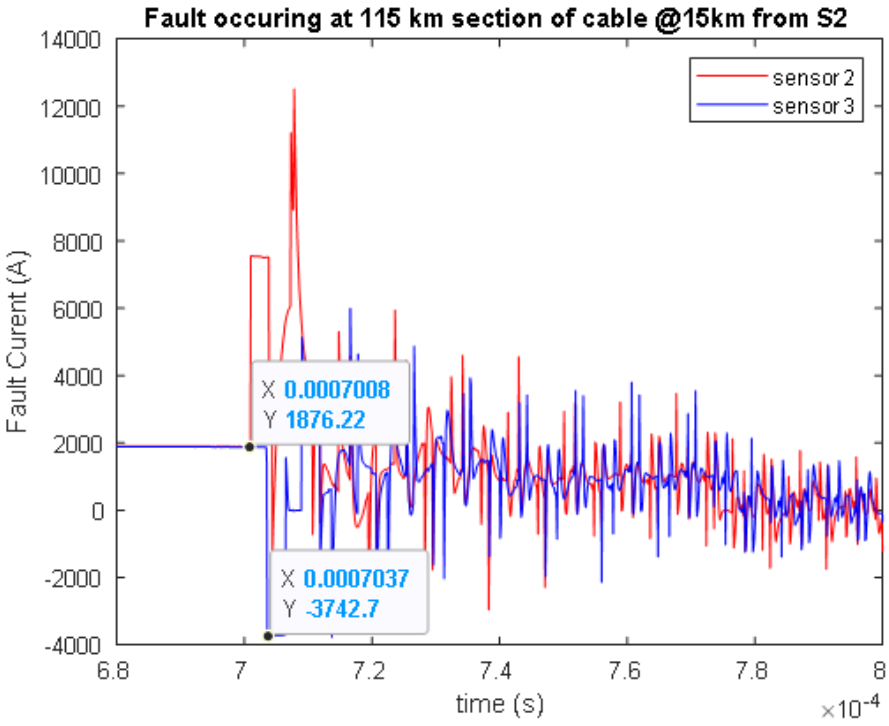

Figure 8.10: Fault at 15 km from Sensor 2

The estimated fault locations derived from phase shift analysis are summarised in Table 8.2.

Table 8.2: Fault location detection using phase shift signature

Distance (km)	Δt (s)	Δt_2 (s)	Δd (m)	Estimated (m)	Actual (m)
5	3.30×10^{-3}	2.80×10^{-3}	1.90×10^{5}	4.80×10^{3}	5.00×10^{3}
10	3.10×10^{-3}	2.60×10^{-3}	1.77×10^{5}	1.16×10^{4}	1.00×10^{4}
15	2.90×10^{-3}	2.40×10^{-3}	1.63×10^{5}	1.84×10^{4}	1.50×10^{4}

Fault Localisation Based on Sensors 1 and 2 Through a Homogeneous Transmission Medium

In addition to using phase shift information between adjacent sensors surrounding the fault, it was observed that fault localisation can also be achieved using the phase relationship between Sensor 1 and Sensor 2, as shown in Fig. 8.11, Fig. 8.12, and

Fig. 8.13, owing to the near-homogeneous nature of the XLPE cable connecting them. This highlights the versatility of the distributed sensing architecture, which provides multiple fault-localisation strategies. While polarity inversion and phase displacement between adjacent sensors provide spatial cues that identify the faulted region between upstream and downstream nodes, a consistent phase response between Sensor 1 and Sensor 2 in a uniform propagation medium also provides a predictable basis for fault position estimation.

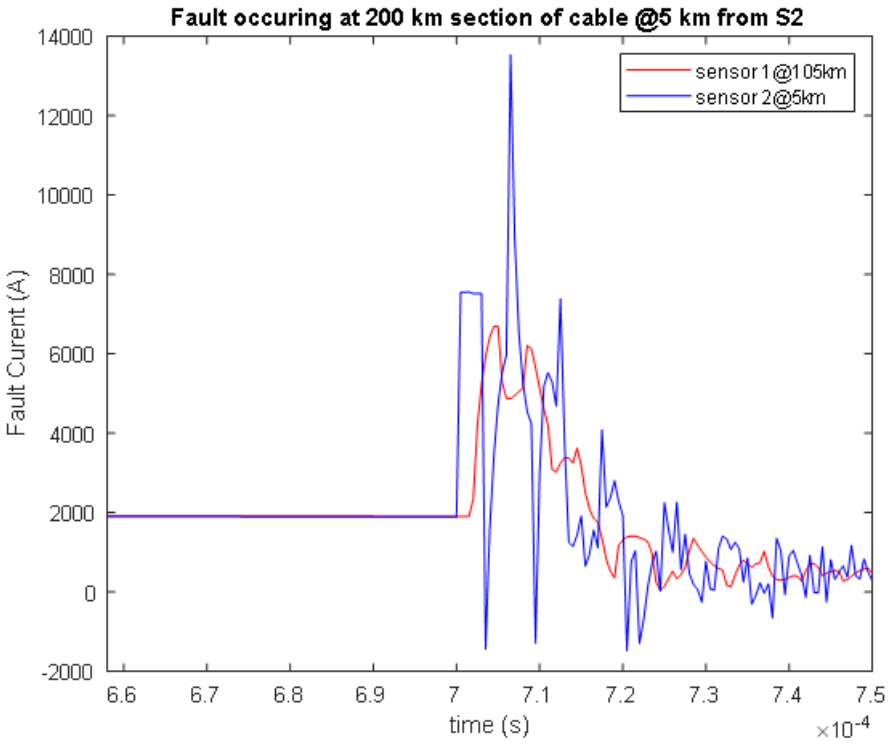

Figure 8.11: Fault at 105 km from Sensor 1

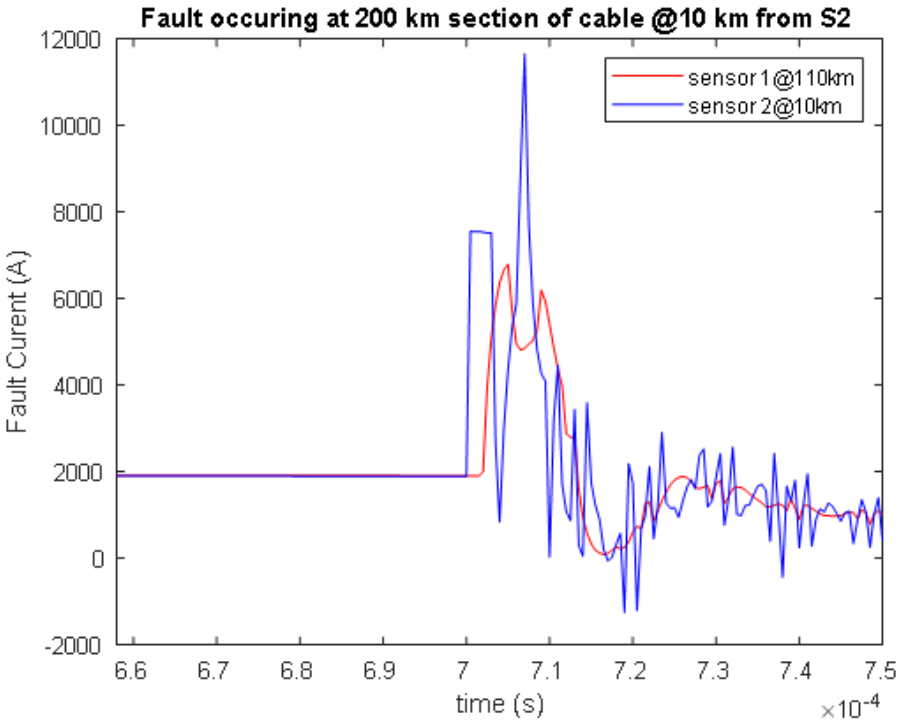

Figure 8.12: Fault at 110 km from Sensor 1

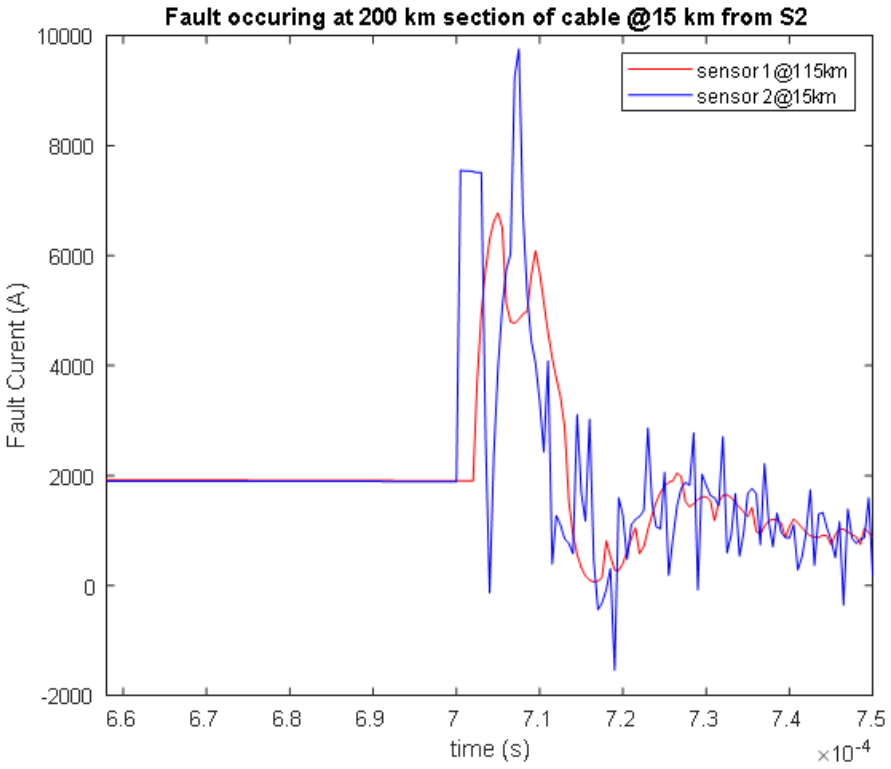

Figure 8.13: Fault at 115 km from Sensor 1

The estimated fault positions and corresponding errors are summarised in Table 8.3.

Table 8.3: Fault distance estimation using phase shift information

Fault to S2	Δt **(s)**	Δd **(m)**	**Estimated Distance from S1 (m)**	**Actual Distance from S1 (m)**	**Error (%)**
5 km	1.60×10^{-3}	1.09×10^{5}	1.044×10^{5}	1.05×10^{5}	0.57
10 km	1.80×10^{-3}	1.22×10^{5}	1.112×10^{5}	1.10×10^{5}	-1.09
15 km	2.00×10^{-3}	1.36×10^{5}	1.18×10^{5}	1.15×10^{5}	-2.61

8.4 Effect of Line Parameters and Insulation Condition

The propagation speed of an injected signal is strongly dependent on the permittivity and permeability of the insulation dielectric, as well as the cable inductance. These

properties are influenced by insulation condition, thermal loading, electrical stress, and ageing. The electrical conductivity of the insulation, as governed by the hopping model of dielectric behaviour, may be expressed as:

$$\sigma(E,T) = A \exp\left(\frac{-\phi q}{k_b T}\right) \frac{\sinh(B|E|)}{|E|} \tag{8.12}$$

where A and B are polymer constants, ϕ is the thermal activation energy, q is the electron charge (1.602×10^{-19} C), E is the electric field (V/m), k_b is the Boltzmann constant (1.38×10^{-23} J/K), and T is the temperature in kelvin.

The relationship between capacitance and dielectric permittivity may be written as:

$$Q = CV \tag{8.13}$$

$$C = \frac{\varepsilon A}{d}, \qquad \varepsilon = \varepsilon_0 \varepsilon_r \tag{8.14}$$

The insulation loss tangent, $\tan\delta$, which is widely used as an indicator of dielectric condition, is influenced by the electrical properties of the insulation material. In ageing polymeric insulation systems, changes in dielectric permittivity and conductivity modify both the capacitive and resistive components of the insulation current. An increase in relative permittivity increases the effective capacitance of the cable insulation, thereby increasing the displacement current. At the same time, degradation mechanisms such as thermal ageing, moisture ingress, and electrical stress can increase dielectric losses, which in turn increase the propagation velocity of electromagnetic waves, also influencing the electromagnetic wave propagation velocity along the cable, since the propagation speed is governed by the distributed line parameters L and C. Consequently, an increase in insulation capacitance reduces propagation velocity, thereby directly affecting time-of-flight-based fault localisation methods.

The propagation velocity of the electromagnetic wave along the transmission line is given by:

$$V = \frac{1}{\sqrt{LC}} \tag{8.15}$$

where L and C represent the inductance and capacitance per unit length of the cable, respectively. Consequently, any increase in insulation permittivity that raises the capacitance will reduce the propagation velocity of travelling-wave signals.

This phenomenon has important implications for fault localisation methods that rely on signal propagation characteristics, such as time-domain reflectometry (TDR). In TDR-based systems, the estimated fault distance is calculated using the measured signal travel time and an assumed propagation velocity. If the dielectric properties of the insulation change due to ageing or degradation, the propagation velocity may deviate from its nominal value, thereby introducing errors in the estimated fault location.

From an electrical perspective, the current flowing through the insulation can be separated into conduction current, I_R, which is governed by the insulation conductivity, and displacement current, I_C, which arises from the capacitive behaviour of the dielectric. The displacement current is directly related to capacitance and the rate of change of applied voltage, whereas the conduction current is governed by the insulation resistance. Degradation mechanisms that increase dielectric losses may therefore influence both current components and alter the effective loss tangent of the insulation system.

In practical HVDC transmission systems, the presence of multiple cable sections, splice joints, and transitions between different transmission media introduces impedance discontinuities along the propagation path. These discontinuities can cause partial reflections of travelling waves and give rise to multiple reflected signals when measured using TDR. In multi-terminal HVDC networks, where numerous joints may exist, such reflections can complicate TDR interpretation and reduce fault localisation accuracy.

By contrast, optical current sensing systems employ optical fibre as the signal transmission medium and are therefore largely unaffected by the electrical characteristics of the power cable. Optical fibres exhibit high thermal stability and immunity to electromagnetic interference, enabling measurement signals to propagate at a stable velocity

that is independent of the dielectric properties of the power cable insulation. This provides a more reliable basis for time-of-flight-based fault detection and localisation than purely electrical signal propagation methods.

Experimental investigations reported in [8], [9] provide further insight into the influence of thermal ageing on the dielectric properties of XLPE insulation. In the experiment illustrated in Fig. 8.14, XLPE cable samples were subjected to thermal loading at 120°C for extended durations while the relative permittivity was measured over a range of frequencies. The results indicate that between 0 and approximately 1440 h of thermal exposure, the relative permittivity remained relatively stable across the investigated frequency range. However, following prolonged ageing beyond this period, a noticeable increase in permittivity was observed at lower frequencies, reaching approximately 2.52, while the variation at higher frequencies remained less pronounced.

The initial permittivity measured at 50 Hz under unaged conditions was approximately 2.44 and served as the reference value for the analysis presented in Fig. 8.14. The observed increase in permittivity following prolonged thermal exposure is attributed to structural modifications within the XLPE insulation, including weakening of crystalline spherulites and enhanced dipolar polarisation mechanisms arising from ageing of the polymeric molecular chains [9].

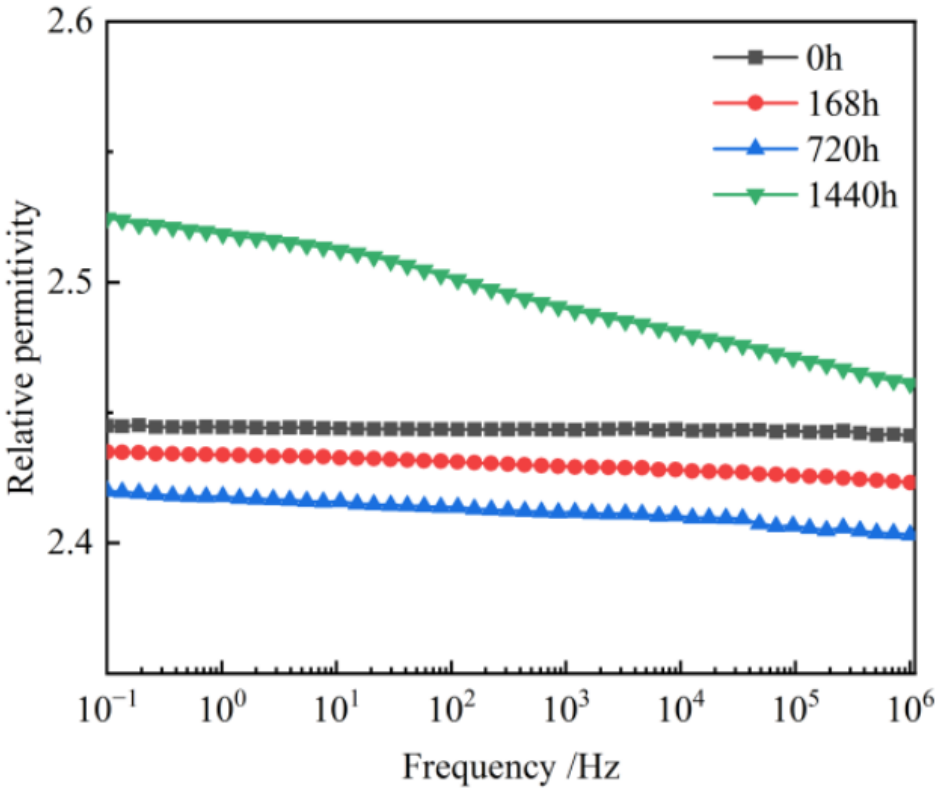

Figure 8.14: Insulation permittivity changes with frequency [9]

Figure 8.14 indicates that, over a sustained period of thermal cycling, changes occur in the morphological structure of the insulation, which in turn affect its dielectric properties and dielectric loss factor [8], [9].

8.4.1 Capacitance Effect on Propagation Speed

As illustrated in Fig. 8.16, even minor deviations in cable capacitance result in observable shifts in the reflected signal profile. In this analysis, the cable inductance was held constant while the capacitance was varied from the nominal datasheet values using recalculated values corresponding to changes in dielectric permittivity. Although these variations produced only a slight change in time-of-flight, they resulted in a disproportionately large error in fault location estimation. This highlights the limitation of relying on static line parameters, which may not adequately represent morphological and dielectric ageing of the cable insulation over time.

In contrast, optical fibre cables demonstrate superior thermal stability, retaining their structural and functional integrity under extreme temperature conditions. Studies have shown that standard optical fibres can maintain performance at temperatures exceeding 200°C, with some reports indicating stability up to 400°C [10]. Furthermore, regenerated fibre Bragg gratings (RFBGs) have been demonstrated to withstand temperatures in the range of 1300–1500°C while maintaining their sensing properties [11]. These characteristics make optical fibre-based sensing systems particularly suitable for harsh environments and provide a significant advantage over conventional electrical sensors.

For benchmarking, a time-domain reflectometry model, which remains a widely adopted offline industrial method, was employed to analyse the influence of cable capacitance variations on signal propagation speed. The model incorporated a signal generator with an amplitude of 100 units and a sampling frequency of 20 kHz (sample time: 5×10^{-5} s), as shown in Fig. 8.15. The line parameters were taken from the ABB HVDC cable datasheet [12]. The test configuration included two parallel cable sections and three splice joint segments, with each line section matched to its corresponding load impedance for reliable reflection analysis.

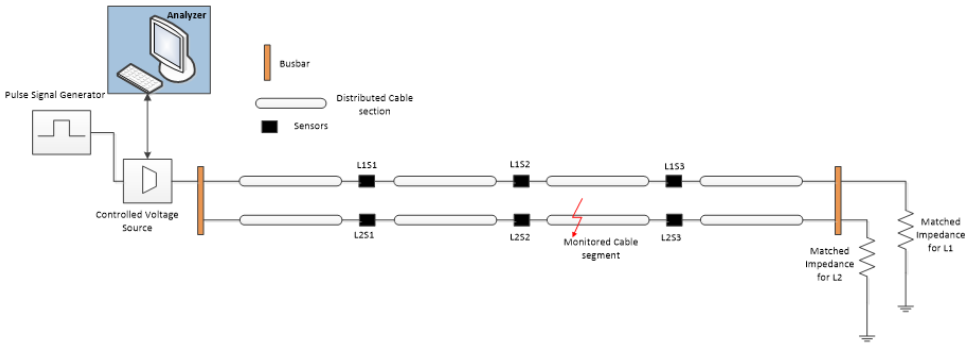

Figure 8.15: Propagation speed determination with TDR

Figure 8.15 shows the propagation speed determination using TDR.

The simulation result showing the effect of insulation capacitance variation on signal propagation is presented in Fig. 8.16.

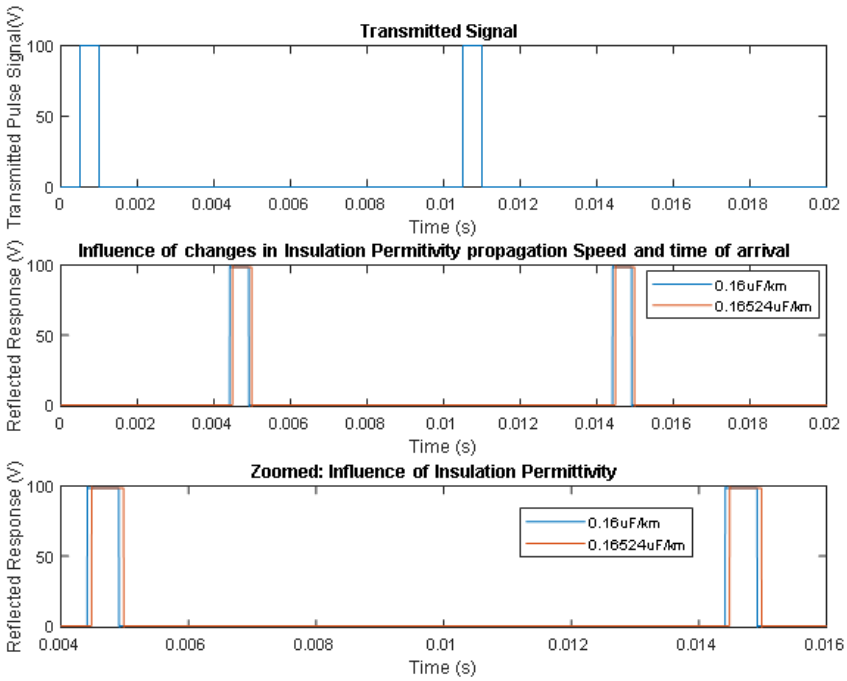

Figure 8.16: Effect of permittivity/capacitance changes on propagation speed and time of flight

As observed in Fig. 8.16, the incident and reflected pulse amplitudes are approximately equal. This condition is attributable to the zero fault resistance used in the simulation, which effectively models a solid ground fault. By contrast, if the fault resistance were assigned a high value, approaching infinity and thereby representing an open circuit or discontinuity, the reflected signal amplitude would be lower than that of the incident pulse because of reflection at a high-impedance discontinuity. This behaviour is consistent with the reflection coefficient relation:

$$\Gamma = \frac{Z_{\text{fault}} - Z_0}{Z_{\text{fault}} + Z_0}, \qquad Z_0 = \sqrt{\frac{L}{C}} \tag{8.16}$$

The matched impedance, Z_0, calculated from the line parameters was 91.85 Ω.

Table 8.4: Impact of capacitance changes on propagation speed and time

C (F)	Round-Trip (m)	v (m/s)	ToF (s)	Calculated Distance (m)	Error (m)	Actual Distance Error (m)
1.60×10^{-7}	300000	68000000	0.0044118	300000	–	–
1.6524×10^{-7}	300000	66953845	0.0044807	304688	4688	2344

The calculated distance values presented in Table 8.4 are obtained using the assumed propagation velocity and the measured time-of-flight of the reflected signal.

8.4.2 Achievable Fault Location Resolution

The sensor system sampling frequency strongly influences the achievable fault-location resolution, the dynamic performance of the sensing and signal-conditioning components, and the signal propagation velocity in the cable. The latter is governed by the distributed inductance and capacitance parameters, which define the travelling-wave propagation characteristics. Although the optical fibre itself introduces negligible propagation delay, the overall system response is primarily constrained by the interrogation, signal conditioning, and data acquisition stages, which therefore determine the achievable detection and control latency.

Consequently, the spatial resolution of fault localisation is inherently limited by the specifications and bandwidth of the measurement hardware employed. These factors impose practical limits on the minimum detectable distance to the fault point and therefore influence the attainable localisation accuracy in practical HVDC systems.

For example, fibre Bragg grating interrogators have been reported to achieve sampling rates up to 264 MHz [10], whereas commercially available instruments such as the Micron Optics SM690 offer a maximum sampling rate of 2 MHz for a single FBG channel without multiplexing [11].

To determine the spatial resolution achievable by the PZT transducer and the ac-

quisition system, the following relationship is used:

$$v = m_{\text{res}} \cdot f_{\text{acq}} \tag{8.17}$$

where v is the signal propagation speed in the medium (m/s), m_{res} is the attainable spatial resolution (m), and f_{acq} is the acquisition frequency (Hz). Rearranging gives:

$$m_{\text{res}} = \frac{v}{f_{\text{acq}}} \tag{8.18}$$

This shows that spatial resolution is inversely proportional to sampling frequency and directly proportional to signal propagation speed. Hence, for a given acquisition frequency, a lower propagation speed results in finer spatial resolution. In polymeric insulation systems such as XLPE and polyethylene (PE), the propagation velocity of electromagnetic waves is typically 51–58% and 65% of the speed of light in vacuum, respectively [13], [14], [15], [16]. The exact value depends on dielectric constant, temperature, and molecular cross-linking density, all of which influence the effective capacitance of the insulating medium.

For instance, assuming an acquisition rate of 1 MHz and a propagation speed of 1.53×10^8 m/s in XLPE, the corresponding spatial resolution is approximately 153 m, as summarised in Table 8.5. Increasing the acquisition frequency improves resolution proportionally; however, sensor noise, PZT bandwidth, and signal attenuation impose practical limits on achievable performance.

In this study, the PZT used in the low-voltage transducer has a resonant frequency of approximately 135 kHz, which inherently limits the effective sampling rate and overall measurement bandwidth. This bandwidth restriction corresponds to a spatial resolution of approximately 1.133 km, assuming an electromagnetic-wave propagation velocity of 51% of the speed of light in XLPE insulation. By contrast, higher-performance PZTs, such as the Thorlabs PN5FC1 with a resonant frequency of 2.1 MHz and capacitance of 10 nF [17], offer substantially improved speed and reduced hysteresis, enabling a much finer spatial resolution of approximately 82.5 m.

Table 8.5: Fault location resolution based on acquisition rate and signal propagation speed

Propagation Speed (m/s)	**Acquisition Rate (Hz)**	**Resolution (m)**	**Remark**
1.53×10^8	1.00×10^6	153	Acquisition rate based on Micron Optics SM690 interrogator sampling frequency and 51% of the speed of light propagation
6.8×10^7	1.00×10^6	68	Acquisition rate based on Micron Optics SM690 interrogator sampling frequency and propagation speed based on line parameters from ABB submarine cable datasheet
1.53×10^8	1.35×10^5	1133.3	Acquisition rate based on PZT resonance frequency of 135 kHz and 51% of the speed of light propagation
6.8×10^7	1.35×10^5	503.7	Acquisition rate based on PZT resonance frequency of 135 kHz and propagation speed based on line parameters from ABB submarine cable datasheet
1.53×10^8	3.20×10^4	4781	Acquisition rate based on IBSEN photonic interrogator sampling frequency and 51% of the speed of light propagation
6.8×10^7	3.20×10^4	2125	Acquisition rate based on IBSEN photonic interrogator sampling frequency and propagation speed based on line parameters from ABB submarine cable datasheet

When using commercially available FBG interrogation systems such as the IMON high-speed interrogator from Ibsen Photonics, operating at approximately 32.5 kHz, the spatial resolution reduces to approximately 4.7 km when a propagation speed of 51% of the speed of light is assumed. Nevertheless, because up to 30 sensors can be multiplexed on a single optical fibre line, fault localisation over a 100 km HVDC cable can still be achieved with a practical precision of approximately 3.3 km, which is adequate for many high-voltage transmission monitoring applications.

8.5 Distributed Photonic Sensing as a Data Source for AI-Based HVDC Network Management

Accurate measurement of state variables is fundamental to ensuring the sustainable, reliable, and secure operation of HVDC systems. Beyond its immediate operational significance, accurate measurement also forms the basis for the progressive integration of artificial intelligence (AI) and machine learning (ML) into modern HVDC network management. The proposed distributed photonic sensing system offers a distinct advantage by providing continuous, high-resolution data streams from multiple sensing locations distributed along the network. When aggregated at control and data centres, these data streams can support AI-driven frameworks for adaptive performance optimisation, active network management, and enhanced asset utilisation.

In conventional AC networks, data availability is comparatively mature due to the widespread deployment of current transformers, voltage transformers, and phasor measurement units, which collectively provide rich datasets for real-time monitoring and AI model development [18], [19]. By contrast, HVDC networks remain constrained by limited network visibility and insufficient measurement coverage, which hinders the deployment of intelligent, data-driven control mechanisms [20], [21].

The proposed distributed photonic sensing framework directly addresses these limitations by introducing a spatially distributed sensing architecture capable of capturing high-fidelity current and temperature measurements throughout the HVDC infrastructure within the uncertainty limits of the sensing system. Each sensing node, comprising

a hybrid PZT, fibre Bragg grating, and shunt interface, acts as a local observability point and provides a continuous optical data stream reflecting both steady-state and transient operating conditions.

When integrated, the outputs of these distributed nodes form a spatiotemporal map of the transmission system, thereby providing real-time insight into network dynamics. The availability of such datasets creates the foundation for advanced AI applications capable of recognising operating patterns, detecting incipient faults, and predicting insulation degradation or converter failures before they become critical. By leveraging this photonic data stream, AI models can support predictive maintenance, fault localisation, and adaptive control with greater robustness than conventional point-sensing methods.

In particular, AI-assisted active network management can utilise distributed sensing data to optimise power flow, regulate converter set-points, and maintain voltage stability across multi-terminal HVDC grids. During abnormal operating conditions, real-time AI inference can enable rapid fault classification and dynamic reconfiguration of protection schemes, thereby enhancing system resilience and reducing restoration times. Furthermore, the inherent temperature sensitivity of FBGs introduces an additional monitoring dimension that can be incorporated into multi-parameter AI models for condition-aware operation. By correlating electrical and thermal signatures, such models can identify degradation trends, estimate component lifetime, and recommend strategic maintenance interventions. Figure 8.17 illustrates the proposed workflow for distributed sensing applications in AI-enabled HVDC monitoring using DC-based OCS measurements [18], [22].

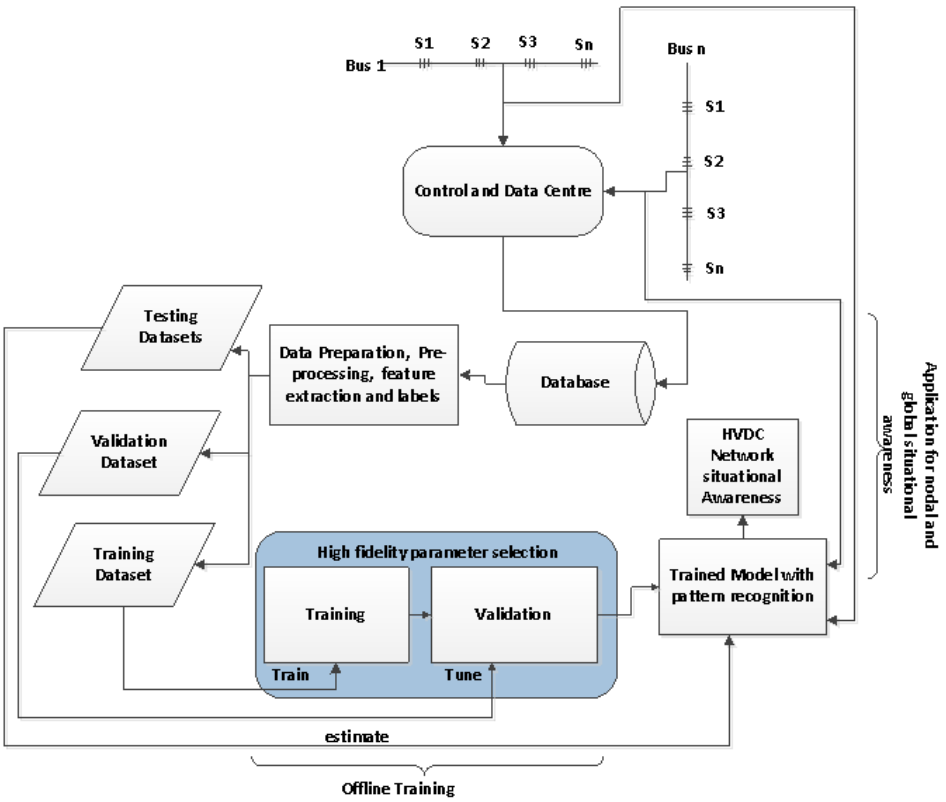

Figure 8.17: Proposed workflow diagram of AI-supported HVDC network algorithm

Ultimately, the integration of distributed photonic sensing has the potential to transform the HVDC network from a traditionally static infrastructure into an intelligent, self-aware system. This data-centric approach supports continuous learning from field conditions and aligns with the evolution toward autonomous HVDC operation, consistent with the principles of Industry 4.0 and the broader vision of a smart, interconnected, and adaptive energy ecosystem [23].

8.6 Conclusion

This chapter investigated the application of distributed optical current sensing for enhanced monitoring and protection of HVDC cable networks. A distributed sensing architecture based on instrumented splice joints incorporating hybrid shunt–PZT–FBG sensors was integrated within a simulated HVDC transmission environment to evaluate

its capability for fast fault detection, localisation, and insulation condition monitoring.

The results demonstrate that the use of optical fibre communication links significantly improves the speed of fault signal acquisition compared with conventional electrical sensing methods. The higher propagation velocity of optical signals allows transient fault signatures to be detected and communicated within a shorter time window, thereby enabling earlier activation of protection mechanisms and reducing the energy dissipated during fault events.

A key contribution of this work is the demonstration that fault localisation can be achieved using polarity inversion of fault currents between adjacent sensors. This polarity signature provides a simple and reliable spatial indicator of fault position, thereby enabling rapid identification of the faulted section of the HVDC line.

In addition, phase shift information extracted from distributed sensor measurements was shown to provide quantitative fault location estimation. Analytical expressions were derived for both homogeneous and inhomogeneous transmission media, enabling distance estimation under realistic HVDC cable configurations where propagation characteristics vary along the line.

The study further demonstrated that variations in line inductance and capacitance are directly linked to insulation condition, since dielectric ageing influences cable permittivity and hence signal propagation speed. By monitoring these changes through time-of-flight measurements, the distributed optical sensing system provides an additional mechanism for long-term insulation condition monitoring in HVDC cable systems.

Overall, the results confirm that distributed photonic sensing offers a powerful approach to improving the observability and protection performance of HVDC transmission systems. The ability to obtain high-speed, spatially distributed measurements along the transmission corridor provides significant advantages for fault detection, localisation, and condition assessment.

Future work should focus on large-scale deployment strategies, field validation under operational HVDC conditions, and integration with intelligent data-processing frameworks capable of utilising distributed sensing data for predictive maintenance and au-

tonomous network management.

Chapter 8 References

[1] Silvano Casoria (Hydro Quebec), *Thyristor based hvdc transmission system average model*, pp. 1–4.

[2] M. Barnes, D. van Hertem, S. P. Teeuwsen, and M. Callavik, "Hvdc systems in smart grids," *IEEE*, vol. 105, no. 11, pp. 9–16, 2017.

[3] ABB, *Abb review, hvdc special report*, pp. 6–21, 2014.

[4] SP Networks, *Angle-dc 2015 electricity network innovation competition*, pp. 6–18, 2015.

[5] R. P. P. Smeets and N. A. Belda, "High-voltage direct current fault current interruption: A technology review," *High Voltage*, Apr. 2021. DOI: 10.1049/hve2.12063.

[6] S. Khalid et al., "Technical assessment of hybrid hvdc circuit breaker components under M-HVDC faults," *Energies*, vol. 14, no. 23, pp. 4–8, Dec. 2021. DOI: 10.3390/en14238148.

[7] D. Tzelepis et al., "Single-ended differential protection in MTDC networks using optical sensors," *IEEE Transactions on Power Delivery*, vol. 32, no. 3, pp. 1605–1615, Jun. 2017. DOI: 10.1109/TPWRD.2016.2645231.

[8] H. Ghorbani, "Characterization of conduction and polarization properties of hvdc cable xlpe insulation materials," pp. 21–62, Ph.D. dissertation.

[9] K. Sohma and T. Hattori, *Heat-resistant thin optical fiber for sensing in high-temperature environments information & communications*, pp. 1–6.

[10] M. P. Fernández, L. A. B. Rossini, J. L. Cruz, M. V. Andrés, and P. A. C. Caso, "High-speed and high-resolution interrogation of fbg sensors using wavelength-to-time mapping and gaussian filters," *Optics Express*, vol. 27, no. 25, p. 36 815, Dec. 2019. DOI: 10.1364/OE.27.036815.

[11] Micron Optics, *Micron optics apex osa for interrogating fiber bragg grating sensors*, pp. 2–4, Atlanta, USA.

[12] ABB, *Xlpe submarine cable systems: Attachment to xlpe land cable systems – user's guide rev. 5*, [Online], pp. 3–8. Available: www.abb.com/cables.

[13] Thorne & Derrick, *Cable and cable fault locating – part 3*, [Online], Accessed: Nov. 9, 2024. Available: www.THORNEANDDERRICK.co.uk.

[14] RFI Technologies, *Coaxial cable dielectrics: Velocity of propagation and attenuation*, pp. 1–4.

[15] Industrial Fibre Optics, *Fiber optic speed of light apparatus instruction manual*, pp. 1–5, 2001.

[16] E. Ouatah, S. Megherfi, K. Haroun, and Y. Zebboudj, "Characteristics of partial discharge pulses propagation in shielded power cable," *Electric Power Systems Research*, 2013, pp. 2–6. DOI: 10.1016/j.epsr.2013.01.012.

[17] Thorlabs, *Thorlabs pn5fc1 pzt actuator*, [Online], Available: www.thorlabs.com/contact, 2020.

[18] A. B. Kilembe, R. I. Hamilton, and P. N. Papadopoulos, "Explainable machine learning: A shap value-based approach to locational frequency stability," *International Journal of Electrical Power and Energy Systems*, vol. 170, pp. 1–8, Sep. 2025. DOI: 10.1016/j.ijepes.2025.110885.

[19] P. N. Papadopoulos, S. Chatzivasileiadis, and A. Marot, "Can machine learning help keep the system secure?: Power systems and change addressing the increasing complexity and uncertainty during the energy transition," *IEEE Power and Energy Magazine*, vol. 22, no. 6, pp. 100–111, 2024. DOI: 10.1109/MPE.2024.3421388.

[20] Dr Othmane El Mountassir, *Hvdc transmission cables in the offshore wind industry: Reliability and condition monitoring*, [Online], pp. 2–8. Available: http://www.tennet.eu/nl/r and-mitsubishi-corporation-extend-partnership-in-ger-, 2015.

[21] ENTSO-E, *Entso-e aisbl recommendations to improve hvdc cable systems reliability*, pp. 1–4, 2019.

[22] A. Basavaraju, J. Du, F. Zhou, and J. Ji, "A machine learning approach to road surface anomaly assessment using smartphone sensors," *IEEE Sensors Journal*, vol. 20, no. 5, pp. 3–7, Mar. 2020. DOI: 10.1109/JSEN.2019.2952857.

[23] Deloitte Insight, *Introduction: Great awakening 2*, pp. 5–17.

Chapter 9

Conclusion, Technology Limitations, and Future Work

This thesis has presented the design, development, and laboratory validation of a distributed optical current sensor (OCS) for high-voltage direct current (HVDC) networks. The proposed sensing system enables accurate current measurement while supporting enhanced monitoring, protection, and control functionalities. The design aligns with relevant IEC requirements for DC current transformers (DCCTs) and addresses the inherent limitations of conventional HVDC current-sensing technologies, which are predominantly limited to terminal-based deployment.

9.1 Summary of Contributions

The primary contributions of this thesis are summarised as follows:

- Development of a distributed optical current sensing architecture capable of multiplexed deployment along HVDC transmission cables.
- Design and implementation of an ultra-low-power sensing system enabling self-sustained operation in electrically constrained environments.
- Design and Implementation of an ultralow power non-linear amplifier with no extra circuitry for gain setting selection

- Demonstration of reduced fault detection latency, with approximately 1 ms improvement over a 100 km HVDC cable, as presented in Chapter 8.
- Development of a Novel Segregated Piecewise Calibration Method in the Quadratic Regression Family
- Establishment of a unified sensing framework supporting both protection and condition monitoring through current and temperature measurement.
- Determination of fault and fault location by phase shift and inverted polarity signals from adjacent sensors.
- Validation of the feasibility of distributed sensing for enhanced wide-area monitoring, protection, and control (WAMPAC) applications in HVDC networks.

9.2 Conclusion

A key contribution of this research is the transition from terminal-based measurement-the current rise prior to the knee point, and reduces associated energy dissipation, thereby improving fault-mitigationsensors, lack inherent multiplexing capability and are therefore unsuitable for WAMPAC applications. In contrast, the proposed OCS enables spatially distributed measurements, significantly enhancing network observability.

The results presented in Chapter 8 demonstrate that distributed OCS deployment reduces fault detection latency by approximately 1 ms for a 100 km HVDC cable. This reduction enables earlier fault intervention, limits current rise prior to the knee point, and reduces associated energy dissipation, thereby improving fault mitigation performance.

In addition to protection applications, the OCS enables condition monitoring of HVDC cables. Continuous measurement of current and temperature distributions supports proactive thermal management. Furthermore, as demonstrated in Chapter 7, variations in signal propagation characteristics provide an indirect indicator of insula-

tion condition, enabling assessment of dielectric degradation through changes in effective capacitance.

Laboratory validation confirms that the proposed OCS operates as a multifunctional sensing platform that supports enhanced observability and WAMPAC-oriented studies in HVDC systems.

9.3 Specific Advantages of Optical Current Sensing for HVDC Networks

The proposed optical current sensing approach addresses key limitations associated with conventional technologies, including:

- Thermal drift affecting measurement accuracy
- Magnetic saturation in ferromagnetic-based sensors
- Susceptibility to electromagnetic interference (EMI)
- Deployment constraints related to size, weight, and power requirements
- Lack of multiplexing capability

A fundamental advantage of optical sensing is that signal propagation in optical fibre is independent of transmission line electrical parameters. Optical signals propagate at approximately 2×10^8 m/s (approximately 66.6% of the speed of light), which is significantly faster than electromagnetic propagation in HVDC cables. This enables reduced detection latency and improved system responsiveness.

9.3.1 Enhancing HVDC Network Visibility and Intelligent Grid Management

The OCS's distributed deployment capability significantly improves HVDC network observability. Unlike AC systems, HVDC networks require ultra-fast fault detection due to the absence of natural current zero-crossing and long transmission distances. These constraints necessitate high-performance monitoring solutions [1].

Conventional approaches rely on indirect or time-consuming diagnostic techniques, limiting real-time situational awareness [2]. The proposed distributed sensing architecture enables direct measurement at multiple locations, improving fault localisation and system state estimation.

9.3.2 Improving Spatial and Temporal Network Intelligence

Distributed sensing enhances both spatial and temporal resolution of network measurements. This enables:

- Active network management (ANM)
- Capacity curtailment to prevent thermal and electrical overloading
- Improved transmission system security
- Enhanced fault localisation accuracy

The availability of high-resolution data also supports the integration of artificial intelligence (AI) and machine learning (ML) for predictive and adaptive grid operation.

9.3.3 Dual-Sensing Capability: Current and Temperature Measurement

The proposed OCS enables simultaneous measurement of current and temperature, allowing:

- Detection of thermal threshold violations
- Monitoring of thermal loading dynamics
- Detection of current threshold violations
- Analysis of current loading profiles

This dual functionality provides a unified platform for monitoring electrical and thermal conditions.

9.3.4 Optical Current Sensor as a High-Speed Protection Enabler

HVDC protection requires rapid detection due to the absence of natural current zero-crossing and the fast rise of fault current. Although modern voltage source converter (VSC) systems incorporate fault ride-through (FRT) capabilities [3], fast and accurate detection remains essential.

The proposed OCS enhances protection performance through:

- High-speed response and signal propagation
- Proximity to fault locations via distributed deployment
- Immunity to electromagnetic interference
- Passive operation without external power supply
- Flexible installation along the transmission corridor

9.3.5 Optical Current Sensor as a Tool for Network Control

Conventional VSC-HVDC control relies on dq-frame transformations to enable proportional-integral (PI) control [4], [5], introducing computational complexity.

The proposed approach enables direct DC-side measurement using OCS technology, eliminating coordinate transformations and improving control efficiency and responsiveness.

9.4 Technology Limitations

Despite its advantages, the proposed OCS system is subject to practical limitations related to measurement range, temporal resolution, and system bandwidth.

9.4.1 Measurement Range Limitation

The measurement range is constrained by the limited supply voltage available from the ultra-low-power energy harvesting system. The amplifier output is restricted to approximately 5 V, limiting the measurable input range.

Under the current configuration:

- Non-linear mode supports transient currents up to approximately 7 kA
- Extended operation up to 14 kA is achievable with reduced nominal gain
- Linear mode is limited to approximately 4.4 kA

These constraints arise from the relationship between shunt resistance (50 $\mu\Omega$), amplifier gain, and available supply voltage.

9.4.2 Temporal Resolution and Bandwidth Limitation

The temporal resolution is limited by the sampling frequency of the optical interrogator. For the IMON interrogator, a sampling interval of approximately 30.7 μs introduces discretisation in time measurement.

This results in:

- Limited spatial resolution in travelling-wave-based fault localisation
- Additional detection latency in protection response

For a 100 km HVDC cable, the combined propagation and sampling delay is approximately 531 μs. While this remains within typical HVDC protection requirements, it contributes to the overall response time.

Additionally, finite system bandwidth can attenuate high-frequency components of transient signals, affecting wavefront detection accuracy.

9.5 Future Research Directions

Further work is required to enhance the applicability of the proposed sensing system across diverse HVDC configurations.

Key research directions include:

- Thermal characterisation and drift compensation
- Application in multi-terminal HVDC (MTDC) networks

- Integration with hybrid DC circuit breaker technologies
- Mechanical robustness under offshore and extreme conditions
- Integration with LCC and VSC-based HVDC systems
- Development of advanced signal processing and machine learning techniques

Future investigations will focus on large-scale validation and real-network deployment to further establish the effectiveness of distributed optical sensing for next-generation HVDC systems.

Chapter 9 References

[1] O. E. Mountassir, *Hvdc transmission cables in the offshore wind industry: Reliability and condition monitoring*, pp. 1–5. [Online]. Available: http://www.tennet.eu/nl/news/article and-mitsubishi-corporation-extend-partnership-in-ger-. Accessed: Jul. 12, 2025, 2015.

[2] ENTSO-E AISBL, *Recommendations to improve hvdc cable systems reliability*, pp. 2–7, 2019.

[3] A. Johnson, *Hvdc implementation fault ride through*, pp. 2–40.

[4] M. Eremia, C. Liu, and A. Edris, *Advanced Solutions in Power Systems: HVDC, FACTS, and Artificial Intelligence*. IEEE-Wiley, 2016, pp. 224–228.

[5] D. V. Hertem, O. Gomis-Bellmunt, and J. Liang, *HVDC Grids*. IEEE-Wiley, 2016, pp. 120–135.